

NASA/CR—1999-206599



Follow-on Low Noise Fan Aerodynamic Study Task 15—Final Report

Nathan J. Heidegger, Edward J. Hall, and Robert A. Delaney
Allison Engine Company, Indianapolis, Indiana

Prepared under Contract NAS3-27394 Task 15

National Aeronautics and
Space Administration

Lewis Research Center

February 1999

NASA Center for Aerospace Information
7121 Standard Drive
Hanover, MD 21076
Price Code: A07

Available from

National Technical Information Service
5285 Port Royal Road
Springfield, VA 22100
Price Code: A07

Preface

This report was prepared by Nathan J. Heidegger, Edward J. Hall, and Robert A. Delaney of the Allison Engine Company, Indianapolis, IN. The work was performed under NASA Contract NAS3-27394 from October 1996 to January 1998. Principal investigator for this program was Nathan J. Heidegger. The Allison Program Manager for this contract was Robert A. Delaney. The NASA Project Manager was Christopher J. Miller.

Acknowledgments

The authors would like to express their appreciation to the following people who contributed to this program: Kurt Weber and Bill Clark of Allison Engine Company and Christopher Rumsey and the other *CFL3D* developers at NASA Langley, for their insights into the formulation, modification, and implementation of the Spalart-Allmaras turbulence model; William Dalton and Dale Elliott of Allison Engine Company, and Gary Podboy of NASA Lewis Research Center for their assistance in understanding the Low-Noise Fan design and experimental rig configuration.

Contents

1	SUMMARY	1
2	INTRODUCTION	3
3	TURBULENCE MODEL DESCRIPTIONS	5
3.1	Introduction	5
3.2	Navier-Stokes Numerical Algorithm	5
3.3	Turbulence Modeling	6
3.4	Algebraic Baldwin-Lomax Turbulence Model	7
3.5	Baldwin-Lomax Model Modifications	8
3.5.1	Wake Parameter Modifications	8
3.5.2	Modified Coefficients	9
3.6	One-Equation Spalart-Allmaras Turbulence Model	10
3.6.1	Spalart-Allmaras Transport Equation for Implicit Solver	11
3.6.2	Derivation of the Spalart-Allmaras Transport Equation for Generalized Coordinates	12
3.6.3	Implicit Discretization of the Spalart-Allmaras Transport Equation	14
3.6.4	Linearization of the Spalart-Allmaras Transport Equation Source Term	16
3.7	Wall Distance Determination	19
3.8	ADPAC Turbulence Model Routine Modifications	19
4	VALIDATION OF THE SPALART-ALLMARAS MODEL	21
4.1	Introduction	21
4.2	Flat Plate	21
4.2.1	3-D Extension of the Flat Plate	24
4.3	NLR Symmetric Airfoil	25
4.4	Transonic Bump	34
4.5	Mark II Turbine Vane	34
4.6	Near-Wall Spacing Sensitivity Study	39
4.6.1	Flat Plate	39
4.6.2	Stator Midspan Passage	43
5	TURBULENCE MODEL EFFECTS ON WAKE PREDICTION	55
5.1	Introduction	55

5.2	Geometry Definition	55
5.3	Experimental Data	57
5.4	Grid Generation	58
5.5	Predicted Fan Performance	60
5.5.1	Spanwise Exit Profiles	63
5.6	Predicted Wake Region Comparison	66
5.6.1	Pitchwise Velocity Profiles	66
5.6.2	Axial Velocity Contours	72
5.6.3	Wake Centerlines	77
5.7	Wake Definition Study	96
5.7.1	Wake Structure and Description	96
5.7.2	Wake Correlations	96
5.7.3	Similarity Profiles	110
6	CONCLUSIONS	121

List of Figures

3.1	Variation of C_{cp} and C_{Kleb} with Coles wake factor (Π).	9
3.2	Schematic illustration of numerical solution sequence of Spalart-Allmaras turbulence model in the <i>ADPAC</i> flow solver.	20
4.1	Normalized flat plate boundary layer profiles of velocity (U/U_∞), shear stress (τ/τ_w), and kinematic eddy viscosity ($\nu_t/0.025U_\infty\delta^*$) at $Re_\theta \approx 10^4$ as calculated by <i>ADPAC</i> using both the Baldwin-Lomax and Spalart-Allmaras turbulence models.	22
4.2	Axial distributions along a flat plate of boundary layer thickness (δ), wall shear stress (τ_{wall}), and friction coefficient (C_f), compared with experimental data [25] and analytical expressions [24, 23].	23
4.3	Convergence histories of the flow equation residuals and turbulence model equation residuals for the flat plate case using three levels of multi-grid and employing a full multi-grid startup.	24
4.4	Three-dimensional mesh system made up of stacked 2-D slices. The grid indices (i,j,k) were rotated through to test each grid index as a solid wall.	25
4.5	Axial distributions along a flat plate of boundary layer thickness (δ), wall shear stress (τ_{wall}), and friction coefficient (C_f), comparing the 2-D and 3-D formulations (with and without multi-grid) of the Spalart-Allmaras model.	26
4.6	Geometry description of the NLR flat-plate airfoil model with the location of downstream experimental data stations and computational boundaries.	27
4.7	Details of the mesh used to collect the <i>ADPAC</i> solution for the NLR flat-plate airfoil model.	28
4.8	Distribution of y^+ values along a mesh line radiating away from the airfoil at approximately 38% chord.	29
4.9	Comparisons between NLR experimental data and numerical predictions of axial velocity profiles in the wake region downstream of the airfoil.	31
4.9	(concluded) Comparisons between NLR experimental data and numerical predictions of axial velocity profiles in the wake region downstream of the airfoil.	32
4.10	Comparison of centerline axial velocity distributions downstream of the airfoil between the NLR experimental data and numerical predictions.	33

4.11	Comparisons between NLR experimental data and numerical predictions of Reynolds stress profiles in the wake region downstream of the airfoil.	35
4.11	<i>(concluded)</i> Comparisons between NLR experimental data and numerical predictions of Reynolds stress profiles in the wake region downstream of the airfoil.	36
4.12	Contours of Mach number around the transonic bump test case as predicted by ADPAC using the Baldwin-Lomax model (<i>top</i>) and the Spalart-Allmaras model (<i>bottom</i>).	37
4.13	Comparison between experimental and predicted surface static pressure over a transonic bump.	38
4.14	Contours of Mach number (<i>left</i>) and turbulence level χ (<i>right</i>) for the Mark II turbine vane with an inlet χ value of 1.	40
4.15	Comparison between experimental and predicted surface static pressure and heat transfer coefficients around the Mark II turbine transonic vane.	41
4.16	Comparison of axial velocity distributions evaluated where $Re_\theta \approx 10^4$ for different near-wall spacings and turbulence models.	42
4.17	Distribution of friction coefficient ($C_f \times 100$) for different near-wall spacings and turbulence models.	44
4.18	Pictorial representation of the 3-D annular slice taken from the stator midspan.	45
4.19	Comparison of axial velocity [ft/s] contours for the midspan stator case on the 0.05x-spacing mesh using the Baldwin-Lomax turbulence model and Spalart-Allmaras turbulence model.	47
4.20	Pitchwise distributions of axial velocity on the 65-point mesh series at four downstream locations showing the effects of near-wall spacing and selection of turbulence model on the wake deficit shape.	49
4.21	Pitchwise distributions of axial velocity on the 121-point mesh series at four downstream locations showing the effects of near-wall spacing and the selection of turbulence model on the wake deficit shape.	50
4.22	Pitchwise distributions of axial velocity at four downstream locations showing the effects of the number of circumferential points (65 or 121) and the selection of turbulence model on the wake deficit shape.	51
4.23	Prediction of wake decay in terms of wake width (δ/P) and centerline velocity deficit (V_{dc}/V_{max}), showing the effects of near-wall spacing using the Baldwin-Lomax turbulence model on the 121-point mesh series.	52
4.24	Prediction of wake decay in terms of wake width (δ/P) and centerline velocity deficit (V_{dc}/V_{max}), showing the effects of near-wall spacing using the Spalart-Allmaras turbulence model on the 121-point mesh series.	52
4.25	Prediction of wake decay in terms of wake width (δ/P) and centerline velocity deficit (V_{dc}/V_{max}), showing a comparison between the two turbulence models used and the effect of circumferential point density (65 or 121).	53

5.1	Photograph of Low Noise Fan test rig installed in the NASA Lewis Low-Speed Wind Tunnel.	56
5.2	Diagram of the low-noise fan rotor in the translated bypass vane configuration.	56
5.3	Meridional outlines of the two different inlet flowpaths used with the the low-noise fan rotor: the Allison nacelle and the NASA experimental bellmouth.	57
5.4	Meridional view of the LNF blade showing the axial locations of the downstream measuring stations including the three NASA experimental test stations.	58
5.5	Radial and tangential location of LDV experimental data points at Station 1 (bold lines represent the actual flowpath radii).	59
5.6	Meridional grid plane showing mesh points along the blade surface and upstream and downstream H-grid extents.	60
5.7	Contours of near-wall y^+ values for the Low Noise Fan blade pressure side (<i>left</i>) and suction side (<i>right</i>).	61
5.8	Midspan radial slice of the Low-Noise Fan mesh generated using a H-grid technique using 97 points across the blade pitch.	62
5.9	Close-up views of the midspan leading edge (<i>left</i>) and trailing edge (<i>right</i>) of the fan rotor showing the spreading of grid lines to reduce shear.	63
5.10	Axial cross-sections downstream of the fan blade showing the mesh resolution used to collect numerical <i>ADPAC</i> solutions.	64
5.11	Performance map at 100% N_c constant speed for the LNF showing the impact of the turbulence model.	65
5.12	Radial exit profiles downstream of the LNF of absolute total pressure and static pressure [psia].	67
5.13	Radial exit profiles downstream of the LNF of absolute total temperature and static temperature [degrees Rankine].	68
5.14	Radial exit profiles downstream of the LNF of absolute axial velocity and absolute tangential velocity [ft/s].	69
5.15	Radial exit profiles downstream of the LNF of absolute radial velocity and absolute total velocity [ft/s].	70
5.16	Radial exit profiles downstream of the LNF of efficiency and loss coefficient.	71
5.17	Schematic of the Low-Noise Fan showing locations of wake data extraction from both the NASA LDV experimental data and the <i>ADPAC</i> numerical solutions.	72
5.18	Wake profiles at Station 1 extracted from the <i>ADPAC</i> solutions at five different spanwise locations and compared with the experimental LDV data.	73
5.19	Wake profiles at Station 2 extracted from the <i>ADPAC</i> solutions at five different spanwise locations and compared with the experimental LDV data.	74

5.20	Wake profiles at Station 3 extracted from the <i>ADPAC</i> solutions at five different spanwise locations and compared with the experimental LDV data.	75
5.21	Contours of axial velocity, V_x , [ft/s] at approximately 10% span taken from the <i>ADPAC</i> Baldwin-Lomax (std. coeff.) solution.	77
5.22	Contours of axial velocity, V_x , [ft/s] at approximately 10% span taken from the <i>ADPAC</i> Baldwin-Lomax (mod. coeff.) solution.	78
5.23	Contours of axial velocity, V_x , [ft/s] at approximately 10% span taken from the <i>ADPAC</i> Spalart-Allmaras solution.	78
5.24	Contours of axial velocity, V_x , [ft/s] at approximately 25% span taken from the <i>ADPAC</i> Baldwin-Lomax (std. coeff.) solution.	79
5.25	Contours of axial velocity, V_x , [ft/s] at approximately 25% span taken from the <i>ADPAC</i> Baldwin-Lomax (mod. coeff.) solution.	79
5.26	Contours of axial velocity, V_x , [ft/s] at approximately 25% span taken from the <i>ADPAC</i> Spalart-Allmaras solution.	80
5.27	Contours of axial velocity, V_x , [ft/s] at approximately 50% span taken from the <i>ADPAC</i> Baldwin-Lomax (std. coeff.) solution.	80
5.28	Contours of axial velocity, V_x , [ft/s] at approximately 50% span taken from the <i>ADPAC</i> Baldwin-Lomax (mod. coeff.) solution.	81
5.29	Contours of axial velocity, V_x , [ft/s] at approximately 50% span taken from the <i>ADPAC</i> Spalart-Allmaras solution.	81
5.30	Contours of axial velocity, V_x , [ft/s] at approximately 75% span taken from the <i>ADPAC</i> Baldwin-Lomax (std. coeff.) solution.	82
5.31	Contours of axial velocity, V_x , [ft/s] at approximately 75% span taken from the <i>ADPAC</i> Baldwin-Lomax (mod. coeff.) solution.	82
5.32	Contours of axial velocity, V_x , [ft/s] at approximately 75% span taken from the <i>ADPAC</i> Spalart-Allmaras solution.	83
5.33	Contours of axial velocity, V_x , [ft/s] at approximately 90% span taken from the <i>ADPAC</i> Baldwin-Lomax (std. coeff.) solution.	83
5.34	Contours of axial velocity, V_x , [ft/s] at approximately 90% span taken from the <i>ADPAC</i> Baldwin-Lomax (mod. coeff.) solution.	84
5.35	Contours of axial velocity, V_x , [ft/s] at approximately 90% span taken from the <i>ADPAC</i> Spalart-Allmaras solution.	84
5.36	Orientation of wake structure behind the Low Noise Fan blades as represented by contours of axial velocity.	85
5.37	Contours of axial velocity, V_x , [ft/s] at Station 1 taken from the NASA LDV experimental data.	86
5.38	Contours of axial velocity, V_x , [ft/s] at Station 1 taken from the <i>ADPAC</i> Baldwin-Lomax (std. coeff.) solution.	86

5.39	Contours of axial velocity, V_x , [ft/s] at Station 1 taken from the <i>ADPAC</i> Baldwin-Lomax (mod. coeff.) solution.	87
5.40	Contours of axial velocity, V_x , [ft/s] at Station 1 taken from the <i>ADPAC</i> Spalart-Allmaras solution.	87
5.41	Contours of axial velocity, V_x , [ft/s] at Station 2 taken from the NASA LDV experimental data.	88
5.42	Contours of axial velocity, V_x , [ft/s] at Station 2 taken from the <i>ADPAC</i> Baldwin-Lomax (std. coeff.) solution.	88
5.43	Contours of axial velocity, V_x , [ft/s] at Station 2 taken from the <i>ADPAC</i> Baldwin-Lomax (mod. coeff.) solution.	89
5.44	Contours of axial velocity, V_x , [ft/s] at Station 2 taken from the <i>ADPAC</i> Spalart-Allmaras solution.	89
5.45	Contours of axial velocity, V_x , [ft/s] at Station 3 taken from the NASA LDV experimental data.	90
5.46	Contours of axial velocity, V_x , [ft/s] at Station 3 taken from the <i>ADPAC</i> Baldwin-Lomax (std. coeff.) solution.	90
5.47	Contours of axial velocity, V_x , [ft/s] at Station 3 taken from the <i>ADPAC</i> Baldwin-Lomax (mod. coeff.) solution.	91
5.48	Contours of axial velocity, V_x , [ft/s] at Station 3 taken from the <i>ADPAC</i> Spalart-Allmaras solution.	91
5.49	Wake centerlines compared between the experimental LDV data and the <i>ADPAC</i> cases at Station 1	93
5.50	Wake centerlines compared between the experimental LDV data and the <i>ADPAC</i> cases at Station 2	94
5.51	Wake centerlines compared between the experimental LDV data and the <i>ADPAC</i> cases at Station 3	95
5.52	Schematic of wake position and velocity definitions relative to the rotor blade. .	97
5.53	Identification of wake measurements and measuring locations.	98
5.54	Correlation data of wake width and centerline velocity deficit from the experimental LDV data split into 10% interval ranges in blade span.	100
5.55	Wake width and centerline velocity deficit data from approximately 10% span extracted from the experimental LDV data set and the <i>ADPAC</i> numerical solutions. (See Figures 5.21, 5.22, and 5.23)	102
5.56	Wake width and centerline velocity deficit data from approximately 25% span extracted from the experimental LDV data set and the <i>ADPAC</i> numerical solutions. (See Figures 5.24, 5.25, and 5.26)	103

5.57	Wake width and centerline velocity deficit data from approximately 50% span extracted from the experimental LDV data set and the <i>ADPAC</i> numerical solutions. (See Figures 5.27, 5.28, and 5.29)	104
5.58	Wake width and centerline velocity deficit data from approximately 75% span extracted from the experimental LDV data set and the <i>ADPAC</i> numerical solutions. (See Figures 5.30, 5.31, and 5.32)	105
5.59	Wake width and centerline velocity deficit data from approximately 90% span extracted from the experimental LDV data set and the <i>ADPAC</i> numerical solutions. (See Figures 5.33, 5.34, and 5.35)	106
5.60	Curve fits of the wake width and centerline velocity deficit data from 10% to 90% blade span for each of the three different turbulence models. The ranges of experimental data from each of the NASA measuring stations are also included.	108
5.61	Curve fits of the wake width and centerline velocity deficit data from 10% to 90% blade span including the effects of c_d . The <i>ADPAC</i> solutions using the three different turbulence models are compared with correlation curves from the literature. The ranges of experimental data from each of the NASA measuring stations are also included.	109
5.62	Similarity profiles reduced from the experimental LDV data at all three measuring stations, plotted in 10% span intervals.	111
5.63	Similarity profiles reduced between 10% and 70% from the experimental LDV data at all three measuring stations, plotted in 10% span intervals.	112
5.64	Curve fitting analysis used to determine the minimum number of frequencies required to model the similarity profile data using a Fourier series.	113
5.65	Similarity profiles reduced from the experimental LDV data at Stations 1, 2, and 3 and plotted in 10% span intervals.	115
5.66	Similarity profiles reduced from the <i>ADPAC</i> Baldwin-Lomax (std. coeff.) solution at Stations 1, 2, and 3 and plotted in 10% span intervals.	116
5.67	Similarity profiles reduced from the <i>ADPAC</i> Baldwin-Lomax (mod. coeff.) solution at Stations 1, 2, and 3 and plotted in 10% span intervals.	117
5.68	Similarity profiles reduced from the <i>ADPAC</i> Spalart-Allmaras solution at Stations 1, 2, and 3 and plotted in 10% span intervals.	118
5.69	Comparison between curve fits of the experimental and numerical similarity profile data at Stations 1, 2, and 3 along with the theoretical Gaussian profile.	119

List of Tables

4.1	Values of near-wall spacing for the flat plate series along with y^+ densities and near-wall y^+ values evaluated at $Re_\theta \approx 10^4$	42
4.2	Values of near-wall spacing for the stator midspan series along with average near-wall y^+ values and y^+ ranges evaluated along both surfaces of the stator.	43
5.1	Values of the correlation coefficients (a, b, c) for the curve fit shown in Figure 5.60.	107
5.2	Values of the correlation coefficients (a, b, c) for the curve fits including the effects of c_d shown in Figure 5.61.	107

Notation

A list of the symbols and acronyms used throughout this document and their definitions is provided below for convenience.

Roman Symbols

c ... aerodynamic chord
 c_d ... drag coefficient
 c_p ... specific heat at constant pressure
 d ... distance to solid surface
 i ... first grid index of numerical solution
 j ... second grid index of numerical solution
 k ... third grid index of numerical solution
 k ... thermal conductivity
mod ... modified coefficients
 p ... pressure
 r ... radius or radial coordinate
 s ... streamwise coordinate
std ... standard coefficients
 t ... time
 u ... velocity
 u^+ ... boundary layer inner variable
 x ... axial coordinate
 y ... vertical or normal coordinate
 y^+ ... boundary layer inner variable
 z ... Cartesian coordinate normal to (x, y) plane

ADPAC ... Advanced Ducted Propfan Analysis Code
AST ... Advanced Subsonic Technology
B-L ... Baldwin-Lomax turbulence model
CFD ... computational fluid dynamics
Dest ... turbulence destruction term
 J ... Jacobian
LDV ... laser Doppler velocimetry

LE ... leading edge
 LNF ... Low Noise Fan
 M ... Mach number
 MG ... levels of multi-grid
 NLR ... Nationaal Lucht- En Ruimtevaartlaboratorium
 P ... blade pitch
PLOT3D ... post-processing 3-D visualization tool
 Pr ... Prandtl number
Prod ... turbulence production term
 R ... gas constant
 R_c ... pressure ratio
 Re ... Reynolds Number
 Re_θ ... Reynolds Number based on momentum thickness
 S ... vorticity
 S-A ... Spalart-Allmaras turbulence model
 T ... temperature
 TE ... trailing edge
 U_{tip} ... rotor tip speed
 V ... velocity
 V_{dc} ... wake centerline velocity deficit
 V_r ... velocity in the cylindrical coordinate system radial direction
 V_x ... velocity in the cylindrical coordinate system axial direction
 V_θ ... velocity in the cylindrical coordinate system circumferential direction
 Vol ... volume
 W ... relative velocity

Greek Symbols

β ... flow angle
 γ ... specific heat ratio
 δ ... boundary layer thickness
 δ ... wake width
 δ^* ... boundary layer displacement thickness
 ζ ... third generalized coordinate
 η ... efficiency
 η ... second generalized coordinate
 θ ... tangential coordinate
 κ ... Kármán constant (0.41)
 μ ... coefficient of viscosity
 μ_{eff} ... effective viscosity
 μ_{lam} ... physical (laminar) viscosity
 μ_t ... turbulent or eddy viscosity
 ν ... kinematic viscosity (μ/ρ)
 ν_t ... kinematic turbulent viscosity

$\tilde{\nu}$... transport variable
 ξ ... first generalized coordinate
 ρ ... density
 σ ... blade solidity
 σ ... turbulence model constant (2/3)
 τ ... shear stress
 ϕ ... diffusion term
 χ ... normalized turbulence quantity
 ω ... loss coefficient
 ω ... rotational speed
 ω ... vorticity
 ω_{param} ... loss parameter

Subscripts

[]_{*i,j,k*} ... grid point index of variable
[]_{*inner*} ... inner boundary layer
[]_{*max*} ... maximum value
[]_{*min*} ... minimum value
[]_{*outer*} ... outer boundary layer
[]_{*p*} ... pressure side
[]_{*r*} ... pertaining to the radial (*r*) cylindrical coordinate
[]_{*ref*} ... reference value
[]_{*s*} ... static value
[]_{*s*} ... suction side
[]_{*t*} ... total (stagnation) value
[]_{*t*} ... turbulent quantity
[]_{*x*} ... pertaining to the axial (*x*) cylindrical coordinate
[]_{*w*} ... wall value
[]_{*wall*} ... wall value
[]_{*θ*} ... pertaining to the circumferential (*θ*) cylindrical coordinate
[]_{*∞*} ... freestream value

Chapter 1

SUMMARY

The focus of NASA Contract NAS3-27394 Task 15 was to investigate the effects of turbulence models on the prediction of rotor wake structures. The *ADPAC* code was modified through the incorporation of the Spalart-Allmaras one-equation turbulence model. Suitable test cases were solved numerically using *ADPAC* employing the Spalart-Allmaras turbulence model and another prediction code (*OVERFLOW*) for comparison. A near-wall spacing study was also completed to determine the adequate spacing of the first computational cell off the wall. Solutions were also collected using two versions of the algebraic Baldwin-Lomax turbulence model in *ADPAC*.

The effects of the turbulence model on the rotor wake definition was examined by obtaining *ADPAC* solutions for the Low Noise Fan rotor-only steady-flow case using the standard algebraic Baldwin-Lomax turbulence model, a modified version of the Baldwin-Lomax turbulence model, and the one-equation Spalart-Allmaras turbulence model. The results from the three different turbulence modeling techniques were compared with each other and the available experimental data. These results include overall rotor performance, spanwise exit profiles, and contours of axial velocity taken along constant axial locations and along blade-to-blade surfaces.

Wake characterizations were also performed on the experimental and *ADPAC* predicted results including the definition of a wake correlation function. Correlations were evaluated for wake width and wake depth. Similarity profiles of the wake shape were also compared between all numerical solutions and experimental data.

Chapter 2

INTRODUCTION

Over the past several decades, there has been a continuous effort focused towards the reduction of aircraft engine noise. The noise created by modern turbofan engines is a concern of several parties: airline operators, aircraft passengers, airport officials, and airport-area residents, for example. The common goal of these groups is for quieter engines without losing performance. Recent noise reduction efforts have been coordinated through the Advanced Subsonic Technology (AST) Project, a partnership between NASA, the U.S. aviation industry, and the Federal Aviation Administration.

The AST project was initiated to develop high-payoff technologies that enable safe and economical global air transportation. One of the areas of interest of the project is the Engine Noise Reduction Element. The goal of this element is to reduce engine noise by 6 decibels by the year 2000 relative to 1992 technology [1]. Three areas of engine noise reduction are being investigated: active noise control for fans, jet noise, and advanced low noise fan designs. The work described within this report, performed by Allison Engine Company under Task 15 of NASA Contract NAS3-27394, supported the last of these three areas of research.

Much of the noise radiated from an operating high-bypass turbofan engine can be attributed to the fan rotor wake interaction with the downstream bypass stator. Downstream of the fan blades, a row of stator blades in the bypass duct are commonly employed to eliminate swirl in the bypass duct flow exiting the nozzle of the engine. There is a strong interaction caused by the swirling rotor wakes from the fan impacting upon the bypass stators. The tone created by this interaction is a function of several parameters including the number of blades in each row, the rotational speed of the engine, and the size, shape, and orientation of the wake structure as it travels downstream.

Through advanced design techniques, this wake interaction can be minimized to lower the overall noise signature of the engine. To validate the new designs, experimental testing is usually required; however, in addition to experimental testing, computational fluid dynamics (CFD) can also be used to predict the wake interaction. The modeling accuracy of the wake region can be dependent upon the turbulence model used within the flow solver code. The results presented in this report show the impact of the turbulence model on the predicted wake character behind a high-bypass engine fan blade. As confidence increases in the computational prediction of the rotor wake interaction with the

bypass stator, designers will be able to model the acoustic performance of several design configurations without relying as heavily on experimental testing. This should result in faster and less expensive design cycles, especially in the preliminary design stages, and quieter turbofan engines.

The research described in this report facilitates the transition from experimental to computational-based fan acoustic design. To achieve this goal, a proven, three-dimensional, Navier-Stokes based aerodynamic analysis tool (*ADPAC*) was employed to analyze rotor wakes from a modern low noise fan design. Predictions from the *ADPAC* code were performed using both an algebraic and a newly developed one-equation turbulence model based on the Spalart-Allmaras formulation [2].

This report begins with a chapter that includes a brief overview of the *ADPAC* prediction code and detailed sections on the turbulence models used during this study. This chapter also presents a discussion on the incorporation of the one-equation Spalart-Allmaras model into *ADPAC*. This is followed by a chapter containing the validation cases used to evaluate the *ADPAC* implementation of the Spalart-Allmaras model. The numerical results compared with the experimental data are presented in the next chapter following brief discussions of the fan rotor geometry and grid generation. Conclusions drawn from the calculations are summarized in the final chapter.

Chapter 3

TURBULENCE MODEL DESCRIPTIONS

3.1 Introduction

Due to the complexity of modeling turbulent flows, directly calculating the net contributions resulting from turbulent velocity fluctuations requires excessive computational resources for even the most basic engineering application. Therefore, models simulating the turbulence quantities are needed as closure to the approximations made in the reduction of the Reynolds-averaged Navier-Stokes equations. The formulations and algorithms used to obtain the flow solutions included in this report are outlined within this chapter. The flow prediction code is briefly presented first, followed by descriptions of the turbulence models and their incorporation into *ADPAC*.

3.2 Navier-Stokes Numerical Algorithm

The aerodynamic predictions for the cases described in this study were obtained using the *ADPAC* analysis code. The *ADPAC* code is a general purpose turbomachinery aerodynamic design analysis tool which has undergone extensive development, testing, and verification [3, 4, 5, 6, 7]. Detailed code documentation is also available for the *ADPAC* program [8, 9, 10, 11]. A brief description of the theoretical basis for the *ADPAC* analysis is given below, and the interested reader is referred to the cited references for additional details.

The *ADPAC* analysis solves a time-dependent form of the three-dimensional Reynolds-averaged Navier-Stokes equations using a proven time-marching numerical formulation. Solutions may be obtained using either a rotating cylindrical coordinate system for annular flows, or a stationary Cartesian coordinate frame for linear cascades or other non-cylindrical geometries. The numerical technique employs proven numerics based on a finite-volume, explicit multi-grid Runge-Kutta time-marching solution algorithm derived from the developmental efforts of Jameson, Adamczyk, and others [12, 13, 14, 15]. Steady-state flows are obtained as the time-independent limit of the time-marching procedure. Several steady-state convergence acceleration techniques (local time stepping,

implicit residual smoothing, and multi-grid) are available to improve the overall computational efficiency of the analysis. An attractive feature of the *ADPAC* code is the versatility and generality of mesh systems upon which the analysis may be performed. The *ADPAC* code permits the use of a multiple-block mesh discretization which provides extreme flexibility for analyzing complex geometries. The block gridding technique enables the coupling of complex, multiple-region domains with common (non-overlapping) grid interface boundaries.

3.3 Turbulence Modeling

As a result of computer limitations regarding storage and execution speed, the effects of turbulence are introduced through an appropriate turbulence model and solutions are performed on a numerical grid designed to capture the macroscopic (rather than the microscopic) behavior of the flow.

The *ADPAC* code employs the Reynolds-averaged form of the Navier-Stokes equations. Correlation terms of the form $\overline{\rho u'v'}$ which result from the Reynolds-averaging procedure require closure through application of a turbulence model in the numerical solution procedure. The effects of turbulence are introduced into the numerical scheme by utilizing the Boussinesq approximation [16],

$$\tau_t = -\overline{\rho u'v'} = \mu_t \frac{\partial \bar{u}}{\partial y} \quad (3.1)$$

where μ_t is the turbulent eddy viscosity, resulting in an effective calculation viscosity defined as:

$$\mu_{eff} = \mu_{lam} + \mu_t \quad (3.2)$$

The simulation is therefore performed using an effective viscosity which combines the effects of the physical (laminar) viscosity and the effects of turbulence through the turbulence model and the turbulent viscosity μ_t . The turbulent flow thermal conductivity term is also treated as the combination of the laminar and turbulence quantities as:

$$k_{eff} = k_{lam} + k_t \quad (3.3)$$

For turbulent flows, the turbulent thermal conductivity k_t is determined from a turbulent Prandtl number Pr_t such that

$$Pr_t = \frac{c_p \mu_t}{k_t} \quad (3.4)$$

The turbulent Prandtl number is normally chosen to have a value of 0.9.

In this study, two different types of turbulence models were used to compute the eddy viscosity used in the Boussinesq approximation described above. The Baldwin-Lomax model is an example of an algebraic turbulence model due to the algebraic nature by which the turbulent viscosity is calculated. Algebraic models are generally the simplest models available for computational aerodynamic analysis, and are "tuned" based on correlations with flat plate turbulent boundary layer data. Unfortunately, the simplicity of the modeling approach limits the useful application to flows which consist primarily of well behaved (non-separated) wall bounded shear layers.

To overcome this limitation, a one-equation turbulence model was added to *ADPAC* based on the work of Spalart and Allmaras [2, 17, 18]. One-equation models generally overcome some of the limitations of algebraic models and resolve the μ_t field more accurately, but require substantially greater coding and computer resources to implement. Both models are described in greater detail in the sections which follow.

3.4 Algebraic Baldwin-Lomax Turbulence Model

A relatively standard version of the Baldwin-Lomax [19] turbulence model is implemented for the algebraic model used in the *ADPAC* analysis. This model is computationally efficient, and has been successfully applied to a wide range of geometries and flow conditions. The Baldwin-Lomax model specifies that the turbulent viscosity be based on an inner and outer layer of the boundary layer flow region as:

$$\mu_t = \begin{cases} (\mu_t)_{inner}, & y \leq y_{crossover} \\ (\mu_t)_{outer}, & y > y_{crossover} \end{cases} \quad (3.5)$$

where y is the normal distance to the nearest wall, and $y_{crossover}$ is the smallest value of y at which values from the inner and outer models are equal. The inner and outer model turbulent viscosities are defined as:

$$(\mu_t)_{inner} = \rho l^2 |\omega| \quad (3.6)$$

$$(\mu_t)_{outer} = K C_{cp} \rho F_{wake} F_{Kleb} y \quad (3.7)$$

Here, the term l is the Van Driest damping factor

$$l = \kappa y (1 - e^{(-y^+ / A^+)}) \quad (3.8)$$

ω is the vorticity magnitude, and F_{wake} is defined as:

$$F_{wake} = y_{max} F_{max} \quad (3.9)$$

where the quantities y_{max} , F_{max} are determined from the function

$$F(y) = y |\omega| [1 - e^{(-y^+ / A^+)})] \quad (3.10)$$

The term y^+ is defined as

$$y^+ = y \left(\sqrt{\frac{\rho |\omega|}{\mu_{lam}}} \right)_{wall} \quad (3.11)$$

The quantity F_{max} is the maximum value of $F(y)$ that occurs across the boundary layer profile, and y_{max} is the location of F_{max} . The determination of F_{max} and y_{max} is perhaps the most difficult aspect of this model for three-dimensional flows. The profile of $F(y)$ can have several local maxima, and it is often difficult to establish which values should be used. In this case, F_{max} is taken as the maximum value of $F(y)$ between a y^+ value of 100 and 1200. The function F_{Kleb} is the Klebanoff intermittency factor given by

$$F_{Kleb}(y) = [1 + 5.5 \left(\frac{C_{Kleb} y}{y_{max}} \right)^6]^{-1} \quad (3.12)$$

and the remainder of the terms are constants defined as:

$$\begin{aligned} A^+ &= 26 & C_{cp} &= 1.6 & C_{Kleb} &= 0.3 \\ \kappa &= 0.4 & K &= 0.0168 \end{aligned}$$

In practice, the turbulent viscosity is limited such that it never exceeds 1000 times the laminar viscosity.

In order to properly utilize this turbulence model, a fairly large number of grid cells must be present in the boundary layer flow region, and perhaps of greater importance, the spacing of the first grid cell off of a wall should be small enough to accurately account for the inner “law of the wall” turbulent boundary layer profile region ($y^+ \leq 5$). Unfortunately, this constraint is often not satisfied due to grid-induced problems related to mesh shear and excessive expansion ratios or due to the excessive computational costs of calculating on very fine meshes.

Practical applications of the Baldwin-Lomax model for three-dimensional viscous flow must be made with the limitations of the model in mind. The Baldwin-Lomax model was designed for the prediction of wall bounded turbulent shear layers, and is not likely to be well suited for flows with massive separations or large vortical structures. There are, unfortunately, a number of applications for turbomachinery where this model is likely to be invalid.

3.5 Baldwin-Lomax Model Modifications

3.5.1 Wake Parameter Modifications

Modifications in the Baldwin-Lomax turbulence model’s calculation of the F_{wake} parameter were tried and evaluated. The change in the parameter evaluation was targeted towards improving the turbulence model’s prediction accuracy in wake regions of the flow. To briefly review, the original Baldwin-Lomax formulation of $(\mu_t)_{outer}$ is defined as:

$$(\mu_t)_{outer} = K C_{CP} \rho F_{wake} F_{Kleb} y \quad (3.13)$$

In contrast to Equation 3.9, F_{wake} is now completely defined as in [19]:

$$F_{wake} = \min \left(\frac{y_{max} F_{max}}{C_{wk} y_{max} U_{dif}^2}, \frac{F_{max}}{F_{max}} \right) \quad (3.14)$$

Here U_{dif} is the difference between the maximum and minimum velocity in the profile given by:

$$U_{dif} = (\sqrt{u^2 + v^2 + w^2})_{max} - (\sqrt{u^2 + v^2 + w^2})_{min} \quad (3.15)$$

Minor modifications were made to the Baldwin-Lomax turbulence model in *ADPAC* to evaluate U_{dif} in the circumferential direction (k -dir) along a constant grid index line. Using this evaluation of the F_{wake} parameter for wake regions limits the user to a grid topology of an H-mesh through the blade passage. Runs with the modified parameter also appeared to have convergence difficulties. Due to these limitations and difficulties encountered in adapting this F_{wake} modification to an arbitrary geometry often encountered when using *ADPAC*, these changes were not included in the final release of the code, and alternative modifications to the Baldwin-Lomax model were investigated.

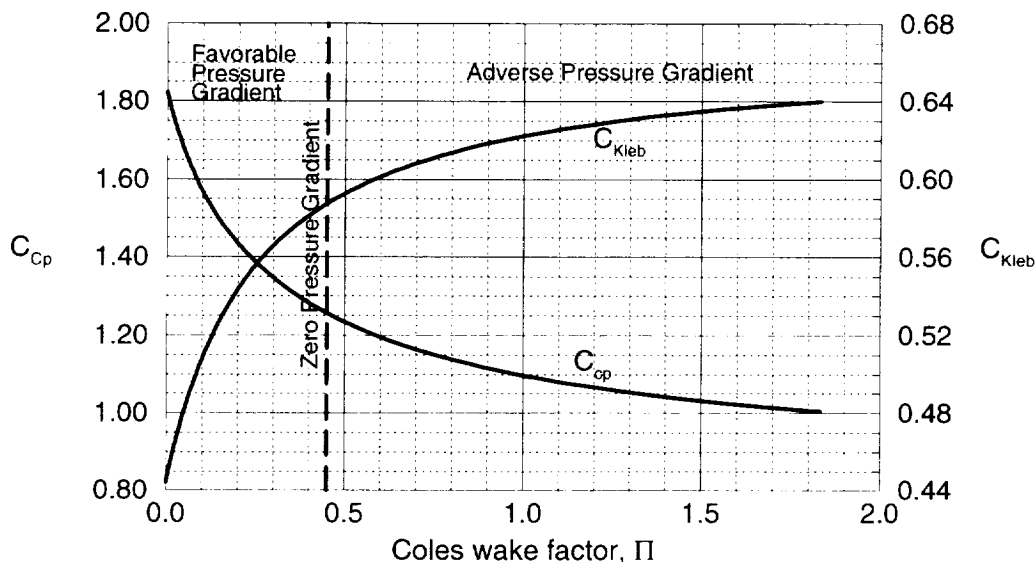


Figure 3.1: Variation of C_{cp} and C_{Kleb} with Coles wake factor (Π).

3.5.2 Modified Coefficients

In an effort to improve the Baldwin-Lomax model for turbomachinery applications, changes were made to the values of two of the model's coefficients to account for the adverse pressure gradients. The model modifications were treated in a similar manner as work presented by Turner and Jennions [21]. In their paper, these modification to the algebraic model produced results for a transonic fan almost as good as those obtained using a two-equation $k-\epsilon$ model. Based on a sensitivity analysis by Granville [20], the option to modify the coefficients in the standard Baldwin-Lomax turbulence model was added to *ADPAC*. The coefficients to be varied are C_{cp} and C_{Kleb} ; the standard values for these two coefficients are $C_{cp} = 1.6$ and $C_{Kleb} = 0.3$ [19].

The variation of these model coefficients with respect to pressure gradient is shown in Figure 3.1 [20]; the values for C_{cp} are read off the left-hand y-axis and range from 1.0 to 1.80, and the values for C_{Kleb} are read off the right-hand y-axis and range from 0.44 to 0.64. The plot shows regions for both favorable and adverse pressure gradients, such that the values of the coefficients can be chosen properly for either compressor or turbine applications.

This modification to *ADPAC* was accomplished through the addition of two new input keywords: **CCP** and **CKLEB**. The default values are set in the code to the standard Baldwin-Lomax values listed above, and are only changed if the **CCP** or **CKLEB** input lines are read in from the *ADPAC* input file. Values entered by the user for these coefficients are checked to ensure they are reasonable. The results presented in this report contain solutions collected with the standard Baldwin-Lomax values (1.6, 0.3) and a modified set of coefficient values (1.0, 0.64) for C_{cp} and C_{Kleb} , respectively.

3.6 One-Equation Spalart-Allmaras Turbulence Model

The turbulence model was modified slightly from its original presentation by Spalart and Allmaras [2] for incorporation into *ADPAC*. The equations and constants comprising the turbulence model are presented below, including the modifications for *ADPAC*.

The equation to calculate the eddy viscosity (μ_t) is given by:

$$\mu_t = \rho \tilde{\nu} f_{v1}, \quad \text{where } f_{v1} = \frac{\chi^3}{\chi^3 + c_{v1}^3}, \quad \text{and } \chi \equiv \frac{\tilde{\nu}}{\nu}, \quad (3.16)$$

ν is the kinematic viscosity, and $\tilde{\nu}$ is the working variable in the transport equation outlined below. The parameter χ is a convenient nondimensional term that is used to set boundary conditions and closely approximates the ratio of turbulent viscosity μ_t to laminar viscosity μ . The original Spalart-Allmaras formulation of the $\tilde{\nu}$ transport equation is presented below:

$$\begin{aligned} \frac{D\tilde{\nu}}{Dt} = & \underbrace{c_{b1} [1 - f_{t2}] \tilde{S} \tilde{\nu}}_{\text{production}} + \underbrace{\frac{1}{\sigma} \left[\nabla \cdot ((\nu + \tilde{\nu}) \nabla \tilde{\nu}) + c_{b2} (\nabla \tilde{\nu})^2 \right]}_{\text{diffusion}} \\ & - \underbrace{\left[c_{w1} f_w - \frac{c_{b1}}{\kappa^2} f_{t2} \right] \left[\frac{\tilde{\nu}}{d} \right]^2}_{\text{destruction}} + \underbrace{f_{t1} \Delta U^2}_{\text{trip}} \end{aligned} \quad (3.17)$$

where the substantial derivative is defined as:

$$\frac{D\tilde{\nu}}{Dt} = \frac{\partial(\tilde{\nu})}{\partial t} + \nabla \cdot (\tilde{\nu} \vec{V}) \quad (3.18)$$

The auxiliary equations needed to complete the model include:

$$\tilde{S} \equiv S + \frac{\tilde{\nu}}{\kappa^2 d^2} f_{v2}, \quad f_{v2} = 1 - \frac{\chi}{1 + \chi f_{v1}}, \quad S = |\nabla \times \vec{V}| \quad (\text{vorticity magnitude}) \quad (3.19)$$

where d is the distance to the nearest viscous wall, and

$$f_w = g \left[\frac{1 + c_{w3}^6}{g^6 + c_{w3}^6} \right]^{1/6}, \quad g = r + c_{w2}(r^6 - r), \quad r \equiv \frac{\tilde{\nu}}{\tilde{S} \kappa^2 d^2} \quad (3.20)$$

Since f_w reaches a constant for large values of r , r is upper bounded by the value of 10.

$$f_{t2} = c_{t3} \exp(-c_{t4} \chi^2) \quad (3.21)$$

The capability of the Spalart-Allmaras turbulence model to incorporate a trip function is currently not part of the *ADPAC* implementation, but is presented below for completeness. The trip function f_{t1} is represented by:

$$f_{t1} = c_{t1} g_t \exp \left(-c_{t2} \frac{\omega_t^2}{\Delta U^2} [d^2 + g_t^2 d_t^2] \right) \quad (3.22)$$

$$g_t \equiv \min \left(0.1, \frac{\Delta U}{\omega_t \Delta x} \right) \quad (3.23)$$

where: d_t is the distance to the trip, ω_t is the wall vorticity at the trip, ΔU is the difference between the velocity at the current point and the trip location, and Δx is the grid spacing along the wall at the trip point.

The original constants for this model are listed below:

$$\begin{array}{llll} c_{b1} = 0.1355 & \sigma = 2/3 & c_{b2} = 0.622 & \kappa = 0.41 \\ c_{w1} = \frac{c_{b1}}{\kappa^2} + \frac{1+c_{b2}}{\sigma} & c_{w2} = 0.3 & c_{w3} = 2 & c_{v1} = 7.1 \\ c_{t1} = 1 & c_{t2} = 2 & c_{t3} = 1.1 & c_{t4} = 2 \end{array}$$

In a reprint [17] of the original model formulation [2], Spalart and Allmaras recommended the following modifications to two of the constants:

$$c_{t3} = 1.2 \quad c_{t4} = 0.5 \quad (3.24)$$

Additional modifications were also noted to help prevent \tilde{S} from going negative [18]. In this update of the model, the $f_{v2}(\chi)$ term is redefined below where c_{v2} is equal to 5:

$$f_{v2} = \left(1 + \frac{\chi}{c_{v2}}\right)^{-3} \quad (3.25)$$

3.6.1 Spalart-Allmaras Transport Equation for Implicit Solver

In order to match the finite volume approach coded in *ADPAC*, it is better to place the original transport equation presented by Spalart and Allmaras in a “conservative” form using $\rho\tilde{\nu}$ as the dependent variable instead of $\tilde{\nu}$ only. Multiply both sides of Equation 3.18 by ρ and make use of continuity:

$$\rho \frac{D\tilde{\nu}}{Dt} = \frac{D(\rho\tilde{\nu})}{Dt} - \tilde{\nu} \frac{D\rho}{Dt} = \frac{D(\rho\tilde{\nu})}{Dt} = \rho(\text{RHS})$$

For convenience, the numerical solution of the Spalart-Allmaras turbulence transport equation is based on the slightly altered conservation statement given below:

$$\begin{aligned} \frac{D(\rho\tilde{\nu})}{Dt} &= \rho c_{b1} [1 - f_{t2}] \tilde{S} \tilde{\nu} + \frac{\rho}{\sigma} \left[\nabla \cdot ((\nu + \tilde{\nu}) \nabla \tilde{\nu}) + c_{b2} (\nabla \tilde{\nu})^2 \right] \\ &\quad - \rho \left[c_{w1} f_w - \frac{c_{b1}}{\kappa^2} f_{t2} \right] \left(\frac{\tilde{\nu}}{d} \right)^2 + \rho f_{t1} \Delta U^2 \end{aligned} \quad (3.26)$$

Before proceeding, it is useful to rearrange the diffusion terms by noting the identity:

$$\nabla \cdot (\tilde{\nu} \nabla \tilde{\nu}) = (\nabla \tilde{\nu})^2 + \tilde{\nu} (\nabla^2 \tilde{\nu}) \quad (3.27)$$

such that the governing transport equation can be restated as:

$$\begin{aligned} \frac{D(\rho\tilde{\nu})}{Dt} &= \rho c_{b1} [1 - f_{t2}] \tilde{S} \tilde{\nu} + \frac{\rho}{\sigma} \left[\nabla \cdot ((\nu + (1 + c_{b2})\tilde{\nu}) \nabla \tilde{\nu}) - c_{b2} \tilde{\nu} \nabla^2 \tilde{\nu} \right] \\ &\quad - \rho \left[c_{w1} f_w - \frac{c_{b1}}{\kappa^2} f_{t2} \right] \left(\frac{\tilde{\nu}}{d} \right)^2 + \rho f_{t1} \Delta U^2 \end{aligned} \quad (3.28)$$

3.6.2 Derivation of the Spalart-Allmaras Transport Equation for Generalized Coordinates

The numerical solution is developed in terms of a Cartesian coordinate system (a similar procedure applies to develop the equations for a cylindrical coordinate solution). We note in advance that the solution of the turbulence transport equation is performed uncoupled from the solution of the flow equations. In this sense, then, the fluid properties can be treated as constants in the numerical solution of the turbulence transport equation.

Expressed in a Cartesian reference frame, the governing transport equation can be expanded in the following form:

$$\begin{aligned} & \frac{\partial(\rho\tilde{\nu})}{\partial t} + \frac{\partial(\rho u\tilde{\nu})}{\partial x} + \frac{\partial(\rho v\tilde{\nu})}{\partial y} + \frac{\partial(\rho w\tilde{\nu})}{\partial z} = \\ & \rho c_{b1} [1 - f_{t2}] \tilde{S}\tilde{\nu} \\ & + \frac{\rho}{\sigma} \left[\frac{\partial}{\partial x} \left((\nu + (1 + c_{b2})\tilde{\nu}) \frac{\partial\tilde{\nu}}{\partial x} \right) + \frac{\partial}{\partial y} \left((\nu + (1 + c_{b2})\tilde{\nu}) \frac{\partial\tilde{\nu}}{\partial y} \right) + \frac{\partial}{\partial z} \left((\nu + (1 + c_{b2})\tilde{\nu}) \frac{\partial\tilde{\nu}}{\partial z} \right) \right. \\ & \left. - c_{b2}\tilde{\nu} \left(\frac{\partial}{\partial x} \left(\frac{\partial\tilde{\nu}}{\partial x} \right) + \frac{\partial}{\partial y} \left(\frac{\partial\tilde{\nu}}{\partial y} \right) + \frac{\partial}{\partial z} \left(\frac{\partial\tilde{\nu}}{\partial z} \right) \right) \right] \\ & - \rho \left[c_{w1}f_w - \frac{c_{b1}}{\kappa^2}f_{t2} \right] \left(\frac{\tilde{\nu}}{d} \right)^2 + \rho f_{t1}\Delta U^2 \end{aligned}$$

In order to extract the numerical solution of this equation on an arbitrary grid system, a generalized coordinate transformation is defined as:

$$\xi = \xi(x, y, z) \quad \eta = \eta(x, y, z) \quad \zeta = \zeta(x, y, z) \quad (3.29)$$

The governing transport equation can be expanded according to the chain rule of differentiation. For example:

$$\frac{\partial}{\partial x} = \frac{\partial\xi}{\partial x} \frac{\partial}{\partial\xi} + \frac{\partial\eta}{\partial x} \frac{\partial}{\partial\eta} + \frac{\partial\zeta}{\partial x} \frac{\partial}{\partial\zeta} \quad (3.30)$$

One problem with employing this type of transformation is that the resulting equation is no longer in conservative form. It can be shown, however, that the conservative property can be recovered (see e.g. [22]) by dividing the resulting equation by the Jacobian (J) of the coordinate transformation and adding and subtracting like terms to recover the conservative property. In addition, for the present application, since the grid system is non-deforming, $\partial J/\partial t = 0$. Finally, to simplify the numerical solution, all cross-derivative

diffusion terms ($\frac{\partial}{\partial \xi} \left(\frac{\partial \tilde{\nu}}{\partial \eta} \right)$, for example) are eliminated from the final transformed equation. Based on these principles, the following transformed equation can be derived:

$$\begin{aligned}
& \frac{\partial \left(\frac{\rho \tilde{\nu}}{J} \right)}{\partial t} + \frac{\partial \left(\frac{\rho V_{\xi} \tilde{\nu}}{J} \right)}{\partial \xi} + \frac{\partial \left(\frac{\rho V_{\eta} \tilde{\nu}}{J} \right)}{\partial \eta} + \frac{\partial \left(\frac{\rho V_{\zeta} \tilde{\nu}}{J} \right)}{\partial \zeta} = \\
& \frac{\rho c_{b1}}{J} [1 - f_{t2}] \tilde{S} \tilde{\nu} + \\
& \frac{\rho}{\sigma J} \left[\xi_x \frac{\partial}{\partial \xi} \left(\phi \xi_x \frac{\partial \tilde{\nu}}{\partial \xi} \right) + \eta_x \frac{\partial}{\partial \eta} \left(\phi \eta_x \frac{\partial \tilde{\nu}}{\partial \eta} \right) + \zeta_x \frac{\partial}{\partial \zeta} \left(\phi \zeta_x \frac{\partial \tilde{\nu}}{\partial \zeta} \right) + \right. \\
& \xi_y \frac{\partial}{\partial \xi} \left(\phi \xi_y \frac{\partial \tilde{\nu}}{\partial \xi} \right) + \eta_y \frac{\partial}{\partial \eta} \left(\phi \eta_y \frac{\partial \tilde{\nu}}{\partial \eta} \right) + \zeta_y \frac{\partial}{\partial \zeta} \left(\phi \zeta_y \frac{\partial \tilde{\nu}}{\partial \zeta} \right) + \\
& \xi_z \frac{\partial}{\partial \xi} \left(\phi \xi_z \frac{\partial \tilde{\nu}}{\partial \xi} \right) + \eta_z \frac{\partial}{\partial \eta} \left(\phi \eta_z \frac{\partial \tilde{\nu}}{\partial \eta} \right) + \zeta_z \frac{\partial}{\partial \zeta} \left(\phi \zeta_z \frac{\partial \tilde{\nu}}{\partial \zeta} \right) \\
& \left. - c_{b2} \tilde{\nu} \left(\xi_x \frac{\partial}{\partial \xi} \left(\xi_x \frac{\partial \tilde{\nu}}{\partial \xi} \right) + \eta_x \frac{\partial}{\partial \eta} \left(\eta_x \frac{\partial \tilde{\nu}}{\partial \eta} \right) + \zeta_x \frac{\partial}{\partial \zeta} \left(\zeta_x \frac{\partial \tilde{\nu}}{\partial \zeta} \right) + \right. \right. \\
& \xi_y \frac{\partial}{\partial \xi} \left(\xi_y \frac{\partial \tilde{\nu}}{\partial \xi} \right) + \eta_y \frac{\partial}{\partial \eta} \left(\eta_y \frac{\partial \tilde{\nu}}{\partial \eta} \right) + \zeta_y \frac{\partial}{\partial \zeta} \left(\zeta_y \frac{\partial \tilde{\nu}}{\partial \zeta} \right) + \\
& \left. \left. \xi_z \frac{\partial}{\partial \xi} \left(\xi_z \frac{\partial \tilde{\nu}}{\partial \xi} \right) + \eta_z \frac{\partial}{\partial \eta} \left(\eta_z \frac{\partial \tilde{\nu}}{\partial \eta} \right) + \zeta_z \frac{\partial}{\partial \zeta} \left(\zeta_z \frac{\partial \tilde{\nu}}{\partial \zeta} \right) \right) \right] \\
& - \frac{\rho}{J} \left[c_{w1} f_w - \frac{c_{b1}}{\kappa^2} f_{t2} \right] \left(\frac{\tilde{\nu}}{d} \right)^2 + \frac{\rho f_{t1}}{J} \Delta U^2
\end{aligned} \tag{3.31}$$

where, for convenience, the following contravariant velocities are employed:

$$\begin{aligned}
V_{\xi} &= u \xi_x + v \xi_y + w \xi_z \\
V_{\eta} &= u \eta_x + v \eta_y + w \eta_z \\
V_{\zeta} &= u \zeta_x + v \zeta_y + w \zeta_z
\end{aligned} \tag{3.32}$$

and the diffusion term (ϕ) is defined as:

$$\phi = \nu + (1 + c_{b2}) \tilde{\nu} \tag{3.33}$$

Here, for convenience, the terms ξ_x , ξ_y refer to the derivative terms $\frac{\partial \xi}{\partial x}$, $\frac{\partial \xi}{\partial y}$, etc.

3.6.3 Implicit Discretization of the Spalart-Allmaras Transport Equation

A representative, discrete analog to the transformed equation employing implicit time discretization can be expressed as:

$$\begin{aligned}
 & \left[\frac{\partial \left(\frac{\rho \tilde{\nu}}{J} \right)}{\partial t} \right]^{(n+1)} + \\
 & \left[\frac{\partial \left(\frac{\rho V_{\xi} \tilde{\nu}}{J} \right)}{\partial \xi} \right]^{(n+1)} + \left[\frac{\partial \left(\frac{\rho V_{\eta} \tilde{\nu}}{J} \right)}{\partial \eta} \right]^{(n+1)} + \left[\frac{\partial \left(\frac{\rho V_{\zeta} \tilde{\nu}}{J} \right)}{\partial \zeta} \right]^{(n+1)} = \\
 & \left[\frac{\rho c_{b1}}{J} [1 - f_{t2}] \tilde{S} \tilde{\nu} \right]^{(n+1)} + \\
 & \frac{\rho}{\sigma J} \left[\xi_x \frac{\partial}{\partial \xi} \left(\phi \xi_x \frac{\partial \tilde{\nu}}{\partial \xi} \right) + \eta_x \frac{\partial}{\partial \eta} \left(\phi \eta_x \frac{\partial \tilde{\nu}}{\partial \eta} \right) + \zeta_x \frac{\partial}{\partial \zeta} \left(\phi \zeta_x \frac{\partial \tilde{\nu}}{\partial \zeta} \right) + \right. \\
 & \left. \xi_y \frac{\partial}{\partial \xi} \left(\phi \xi_y \frac{\partial \tilde{\nu}}{\partial \xi} \right) + \eta_y \frac{\partial}{\partial \eta} \left(\phi \eta_y \frac{\partial \tilde{\nu}}{\partial \eta} \right) + \zeta_y \frac{\partial}{\partial \zeta} \left(\phi \zeta_y \frac{\partial \tilde{\nu}}{\partial \zeta} \right) + \right. \\
 & \left. \xi_z \frac{\partial}{\partial \xi} \left(\phi \xi_z \frac{\partial \tilde{\nu}}{\partial \xi} \right) + \eta_z \frac{\partial}{\partial \eta} \left(\phi \eta_z \frac{\partial \tilde{\nu}}{\partial \eta} \right) + \zeta_z \frac{\partial}{\partial \zeta} \left(\phi \zeta_z \frac{\partial \tilde{\nu}}{\partial \zeta} \right) \right. \\
 & \left. - c_{b2} \tilde{\nu} \left(\xi_x \frac{\partial}{\partial \xi} \left(\xi_x \frac{\partial \tilde{\nu}}{\partial \xi} \right) + \eta_x \frac{\partial}{\partial \eta} \left(\eta_x \frac{\partial \tilde{\nu}}{\partial \eta} \right) + \zeta_x \frac{\partial}{\partial \zeta} \left(\zeta_x \frac{\partial \tilde{\nu}}{\partial \zeta} \right) + \right. \right. \\
 & \left. \left. \xi_y \frac{\partial}{\partial \xi} \left(\xi_y \frac{\partial \tilde{\nu}}{\partial \xi} \right) + \eta_y \frac{\partial}{\partial \eta} \left(\eta_y \frac{\partial \tilde{\nu}}{\partial \eta} \right) + \zeta_y \frac{\partial}{\partial \zeta} \left(\zeta_y \frac{\partial \tilde{\nu}}{\partial \zeta} \right) + \right. \right. \\
 & \left. \left. \xi_z \frac{\partial}{\partial \xi} \left(\xi_z \frac{\partial \tilde{\nu}}{\partial \xi} \right) + \eta_z \frac{\partial}{\partial \eta} \left(\eta_z \frac{\partial \tilde{\nu}}{\partial \eta} \right) + \zeta_z \frac{\partial}{\partial \zeta} \left(\zeta_z \frac{\partial \tilde{\nu}}{\partial \zeta} \right) \right) \right]^{(n+1)} \\
 & - \left[\frac{\rho}{J} \left[c_{w1} f_w - \frac{c_{b1}}{\kappa^2} f_{t2} \right] \left(\frac{\tilde{\nu}}{d} \right)^2 \right]^{(n+1)} + \left[\frac{\rho f_{t1}}{J} \Delta U^2 \right]^{(n+1)} \quad (3.34)
 \end{aligned}$$

Here the superscript $(n + 1)$ indicates the time level of the discrete numerical solution.

The discrete representations of the individual terms are analyzed separately based on the requirements of the numerical scheme. First, the time derivative term is discretized using a first order accurate implicit discretization as:

$$\left[\frac{\partial \left(\frac{\rho \tilde{\nu}}{J} \right)}{\partial t} \right]^{(n+1)} \approx \left[\frac{\left(\frac{\rho \tilde{\nu}}{J} \right)_{(i,j,k)}^{(n+1)} - \left(\frac{\rho \tilde{\nu}}{J} \right)_{(i,j,k)}^{(n)}}{\Delta t} \right] \quad (3.35)$$

In this representation, Δt is the discrete time step interval and the subscript (i, j, k) represents the indices of the discrete solution in the numerical grid. A finite volume numerical strategy is employed in this analysis which mimics the numerical techniques used in the solution of the Navier-Stokes equations in the *ADPAC* code. In this respect, the term $1/J$ is regarded as the cell volume, and the discrete representations of the dependent variable ($\tilde{\nu}$) are taken to lie at cell centers denoted by the indices i, j, k . These indices correspond to the ξ, η, ζ coordinate directions along the structured numerical mesh coordinates. It is also useful to develop the solution in what is referred to as “delta” form, whereby the solver approximates the change in the variable of interest, rather than the actual value of the variable itself. These interpretations lead to:

$$\left[\frac{\partial \left(\frac{\rho \tilde{\nu}}{J} \right)}{\partial t} \right]^{(n+1)} \approx \left(\frac{Vol}{\Delta t} \right) \Delta(\rho \tilde{\nu})_{(i,j,k)}^{(n+1)} \quad (3.36)$$

where $\Delta(\rho \tilde{\nu})^{(n+1)} = (\rho \tilde{\nu})^{(n+1)} - (\rho \tilde{\nu})^{(n)}$.

Time-linearization of the convection terms employs a Taylor series expansion in time as follows:

$$\left[\frac{\partial}{\partial \xi} \left(\frac{\partial \rho V_\xi \tilde{\nu}}{J} \right) \right]^{(n+1)} \approx \left[\frac{\partial}{\partial \xi} \left(\frac{\partial \rho V_\xi \tilde{\nu}}{J} \right) \right]^{(n)} + \frac{\partial}{\partial t} \left[\frac{\partial}{\partial \xi} \left(\frac{\partial \rho V_\xi \tilde{\nu}}{J} \right) \right]^{(n)} \Delta t + \dots \quad (3.37)$$

The convection terms employ a spatial upwind numerical discretization operator defined as:

$$\left[\frac{\partial \left(\frac{\rho V_\xi \tilde{\nu}}{J} \right)}{\partial \xi} \right]^{(n+1)} \approx \begin{cases} V_\xi [(\rho \tilde{\nu})_{(i,j,k)} - (\rho \tilde{\nu})_{(i-1,j,k)}] & V_\xi \geq 0 \\ V_\xi [(\rho \tilde{\nu})_{(i+1,j,k)} - (\rho \tilde{\nu})_{(i,j,k)}] & V_\xi < 0 \end{cases} \quad (3.38)$$

Similar operators apply for convective derivatives in the η and ζ directions. Here it has been assumed that the spatial increments in the transformed coordinate system $\Delta \xi, \Delta \eta, \Delta \zeta$ are all equal to one. An upwind difference is used for simplicity, stability, and to enhance diagonal dominance of the implicit coefficient matrix.

In practice, this operator is implemented in a combined form as:

$$\left[\frac{\partial \left(\frac{\rho V_\xi \tilde{\nu}}{J} \right)}{\partial \xi} \right]^{(n)} \approx V_\xi \left(\frac{1}{2} (1 + \text{sign}(V_\xi)) ((\rho \tilde{\nu})_{(i,j,k)}^{(n)} - (\rho \tilde{\nu})_{(i-1,j,k)}^{(n)}) + \frac{1}{2} (1 - \text{sign}(V_\xi)) ((\rho \tilde{\nu})_{(i+1,j,k)}^{(n)} - (\rho \tilde{\nu})_{(i,j,k)}^{(n)}) \right) \quad (3.39)$$

where the sign function is defined as:

$$\text{sign}(V_\xi) = \begin{cases} 1 & V_\xi \geq 0 \\ -1 & V_\xi < 0 \end{cases} \quad (3.40)$$

Implicit representation of the diffusion terms again utilizes a Taylor series expansion in time as follows:

$$\left(\xi_x \frac{\partial}{\partial \xi} \left(\phi \xi_x \frac{\partial \tilde{\nu}}{\partial \xi}\right)\right)^{(n+1)} \approx \left(\xi_x \frac{\partial}{\partial \xi} \left(\phi \xi_x \frac{\partial \tilde{\nu}}{\partial \xi}\right)\right)^{(n)} + \frac{\partial}{\partial t} \left[\left(\xi_x \frac{\partial}{\partial \xi} \left(\phi \xi_x \frac{\partial \tilde{\nu}}{\partial \xi}\right)\right)^{(n)}\right] \Delta t + \dots \quad (3.41)$$

Exchanging the spatial and temporal operators and implementing the discrete representations of the various derivatives results in the following equation:

$$\left(\xi_x \frac{\partial}{\partial \xi} \left(\phi \xi_x \frac{\partial \tilde{\nu}}{\partial \xi}\right)\right)^{(n+1)} \approx \left(\xi_x \frac{\partial}{\partial \xi} \left(\phi \xi_x \frac{\partial \tilde{\nu}}{\partial \xi}\right)\right)^{(n)} + \xi_x \frac{\partial}{\partial \xi} \left(\phi \xi_x \frac{\partial}{\partial \xi} \Delta(\rho \tilde{\nu})^{(n+1)}\right) \quad (3.42)$$

The spatial gradient operator in the diffusion terms are approximated using central differences in the following manner:

$$\begin{aligned} \xi_x \frac{\partial}{\partial \xi} \left[\phi \xi_x \frac{\partial \tilde{\nu}}{\partial \xi}\right]^{(n)} \approx \\ (\xi_x)_{(i,j,k)} \left(\phi_{(i+\frac{1}{2},j,k)} (\xi_x)_{(i+\frac{1}{2},j,k)} [(\rho \tilde{\nu})_{(i+1,j,k)} - (\rho \tilde{\nu})_{(i,j,k)}] \right. \\ \left. - \phi_{(i-\frac{1}{2},j,k)} (\xi_x)_{(i-\frac{1}{2},j,k)} [(\rho \tilde{\nu})_{(i,j,k)} - (\rho \tilde{\nu})_{(i-1,j,k)}]\right) \end{aligned} \quad (3.43)$$

In practice, the diffusion coefficient terms (ϕ) are limited to non-negative values only for numerical stability.

3.6.4 Linearization of the Spalart-Allmaras Transport Equation Source Term

The success of the implicit solution of the Spalart-Allmaras transport equation turbulence model is based heavily on the manner with which source (turbulence production and destruction) terms are linearized. Four linearization strategies are discussed in the original paper describing the Spalart-Allmaras model [2]. The method employed here corresponds roughly to method four in that reference. The strategy is to try to linearize, as completely as possible, the production and destruction source terms with respect to the dependent variable $\tilde{\nu}$. The complex, highly nonlinear nature of these terms makes this a difficult task. It is also desirable from a numerical standpoint to only linearize those terms which contribute positive elements to the implicit coefficient matrix (increasing diagonal dominance). This is desirable to aid in the accuracy and stability of the numerical scheme.

If we describe the turbulence production term as *Prod* and the turbulence destruction term as *Dest*, then we seek to describe a linearization for the combination *Prod* – *Dest* whereby the derivative (*Prod* – *Dest*)' is negative (and therefore contributes to diagonal dominance of the coefficient matrix. In this discussion, the production and diffusion terms are represented by:

$$Prod = \frac{\rho c_{b1}}{J} [1 - f_{t2}] \tilde{S} \tilde{\nu} \quad Dest = \frac{\rho}{J} \left[c_{w1} f_w - \frac{c_{b1}}{\kappa^2} f_{t2} \right] \left(\frac{\tilde{\nu}}{d} \right)^2 \quad (3.44)$$

Following the technique described by Spalart and Allmaras, the production term is written in terms of P , a function of $\rho\tilde{\nu}$, as:

$$Prod = P \cdot (\rho\tilde{\nu}) \quad (3.45)$$

and therefore:

$$Prod' = P + P' \cdot (\rho\tilde{\nu}) \quad (3.46)$$

Here the superscript $()'$ indicates differentiation with respect to $(\rho\tilde{\nu})$. In this case, we can see immediately that:

$$P = \frac{c_{b1}}{J} [1 - f_{t2}] \tilde{S} \quad (3.47)$$

and also that:

$$P' = \frac{1}{\rho J} c_{b1} \tilde{S}(-f'_{t2}) + \frac{1}{\rho J} c_{b1} [1 - f_{t2}] \tilde{S}' \quad (3.48)$$

One can then construct the additional derivative terms one element at a time to complete the linearization. A summary of each of the derivative terms is given below:

$$(f_{v2})' = \frac{-3}{\nu c_{v2}} \left(1 + \frac{\tilde{\nu}}{\nu c_{v2}} \right)^{-4}$$

$$(\tilde{S})' = \frac{1}{\kappa^2 d^2} (f_{v2} + \tilde{\nu}(f_{v2})')$$

$$(f_{t2})' = \frac{-2c_{t4}\chi f_{t2}}{\nu}$$

$$(P)' = \frac{-c_{b1}\tilde{S}(f_{t2})'}{\rho J} + \frac{c_{b1}}{\rho J} [1 - f_{t2}](\tilde{S})'$$

$$(r)' = \frac{r}{\tilde{\nu}} \left(1 - \tilde{\nu} \frac{(\tilde{S})'}{\tilde{S}} \right)$$

$$(g)' = (r)'(1 + c_{w2}(6r^5 - 1))$$

$$(f_w)' = \frac{f_w(g)'}{g} \left(1 - \frac{g^6}{g^6 + c_{w3}^6} \right)$$

$$(D)' = \frac{Dest}{(\rho\tilde{\nu})^2} - \frac{\tilde{\nu}}{\rho d^2 J} \left[c_{w1}(f_w)' - \frac{c_{w1}}{\kappa^2} (f_{t2})' \right]$$

The source term linearization terms can be represented by the combination $(P' - D')$. In practice, the numerical solver only implements this linearization for those points where the combination contributes to the diagonal dominance of the coefficient matrix. That is, the exact linearization is modified to $POS(P' - D')$ where the POS operator indicates that the term contributes to diagonal dominance in the coefficient matrix.

After applying the discrete representations of the governing equation, and collecting terms, the following implicit equation for the dependent variable $\Delta(\rho\tilde{\nu})$ can be developed:

$$[I + \frac{\Delta t}{Vol}(M_{(i+1)} + M_{(i-1)} + M_{(j+1)} + M_{(j-1)} + M_{(k+1)} + M_{(k-1)})](\Delta\rho\tilde{\nu}) = \frac{\Delta t}{Vol}[RHS_{(i,j,k)}] \quad (3.49)$$

The term $RHS_{(i,j,k)}$ represents the collection of all terms which can be computed from known data at time level (n) . Here, $M_{(i+1)}$ represents matrix elements corresponding to $(\Delta\rho\tilde{\nu})_{(i+1,j,k)}$, $M_{(j+1)}$ represents matrix elements corresponding to $(\Delta\rho\tilde{\nu})_{(i,j+1,k)}$, etc. The left hand side implicit matrix operator consists of a complex, irregular coefficient matrix which is difficult to solve directly. Instead, this complex matrix is approximately factored as follows:

$$\begin{aligned} & [I + \frac{\Delta t}{Vol}(M_{(i+1)} + M_{(i-1)})] \\ & [I + \frac{\Delta t}{Vol}(M_{(j+1)} + M_{(j-1)})] \\ & [I + \frac{\Delta t}{Vol}(M_{(i+1)} + M_{(i-1)})](\Delta\rho\tilde{\nu}) = \\ & \frac{\Delta t}{Vol}[RHS_{(i,j,k)}] \end{aligned} \quad (3.50)$$

Now each of the factored matrix components ($[I + \frac{\Delta t}{Vol}(M_{(i+1)} + M_{(i-1)})]$ for example) have a tridiagonal matrix structure representing the discrete solution along one of the three coordinate directions. The complete system can then be solved through sequential reduction of the individual tridiagonal matrices. That is,

$$\begin{aligned} (\Delta\rho\tilde{\nu})^{**} &= [I + \frac{\Delta t}{Vol}(M_{(i+1)} + M_{(i-1)})]^{-1} \frac{\Delta t}{Vol}[RHS_{(i,j,k)}] \\ (\Delta\rho\tilde{\nu})^* &= [I + \frac{\Delta t}{Vol}(M_{(j+1)} + M_{(j-1)})]^{-1} (\Delta\rho\tilde{\nu})^{**} \\ (\Delta\rho\tilde{\nu}) &= [I + \frac{\Delta t}{Vol}(M_{(k+1)} + M_{(k-1)})]^{-1} (\Delta\rho\tilde{\nu})^* \\ (\rho\tilde{\nu})^{(n+1)} &= (\rho\tilde{\nu})^{(n)} + (\Delta\rho\tilde{\nu}) \end{aligned} \quad (3.51)$$

In this application, the coefficient terms resulting from the linearization of the source terms in the governing equation are included in the first matrix reduction step described above. Spalart and Allmaras describe methods by which errors associated with the approximate factorization can be reduced or eliminated through iteration. For the applications tested here, these modifications were not deemed necessary.

3.7 Wall Distance Determination

Since this turbulence model, as do many, requires the distance to the nearest viscous wall to be known, a searching routine was developed to calculate this minimum distance for all computational cells in the mesh. Due to the flexibility of the multi-block capability and parallelization of *ADPAC*, this task was not as straight forward as might first appear. The *ADPAC* boundary conditions are interrogated to find all viscous surface definitions (**SSVI**). The x , y , and z locations of the face center of each face comprising the viscous surface are stored in a long 1-D array. For multiple processor applications, information needs to be sent across the network to a single processor to compile the array and the complete list broadcast back to all the processors. The distance from the cell center of each of the volumes making up each mesh block are then calculated with the minimum distance stored as d .

Despite the length of time needed to calculate the distance field, this calculation only needs to be performed once and the resulting values will be included in the turbulence model restart file, eliminating the need to execute the distance finding routine on the restart of a simulation. In fact it may be advisable to initially run *ADPAC* with zero iterations to calculate the near-wall distance field. These results can be checked in the *PLOT3D* output file (*case.p3d1eq*) after which the solution can be restarted.

3.8 ADPAC Turbulence Model Routine Modifications

The specification of inlet boundary conditions and initial conditions for the turbulence model transport variable ($\tilde{\nu}$) is handled by specifying a value of the non-dimensional variable χ ($\tilde{\nu}/\nu$). By specifying χ , the user does not need to account for variations in $\tilde{\nu}$ caused by changes in **PREF**, **TREF**, **DIAM**, or any other reference quantity used for non-dimensionalization. It was found in the cases tested, that a small initial value of χ does not provide a strong enough trigger for the production term and causes the solution to converge to the trivial solution ($\tilde{\nu} = 0.0$), resulting in a laminar flow field. Through numerical experimentation, most of the test cases presented in the following chapter were run using an initial value of χ equal to 20 with inlet values being specified at $\chi_{in} = 1$. At this point, no direct relationship between χ_{in} and the percentage turbulence level (Tu) has been derived.

An illustration of the implicit solution sequence for the Spalart-Allmaras turbulence model transport equation in the *ADPAC* flow solver are given in Figure 3.2. With the implicit flow solver, the flow and turbulence transport equations are completely uncoupled and the individual solutions occur sequentially during a given iteration.

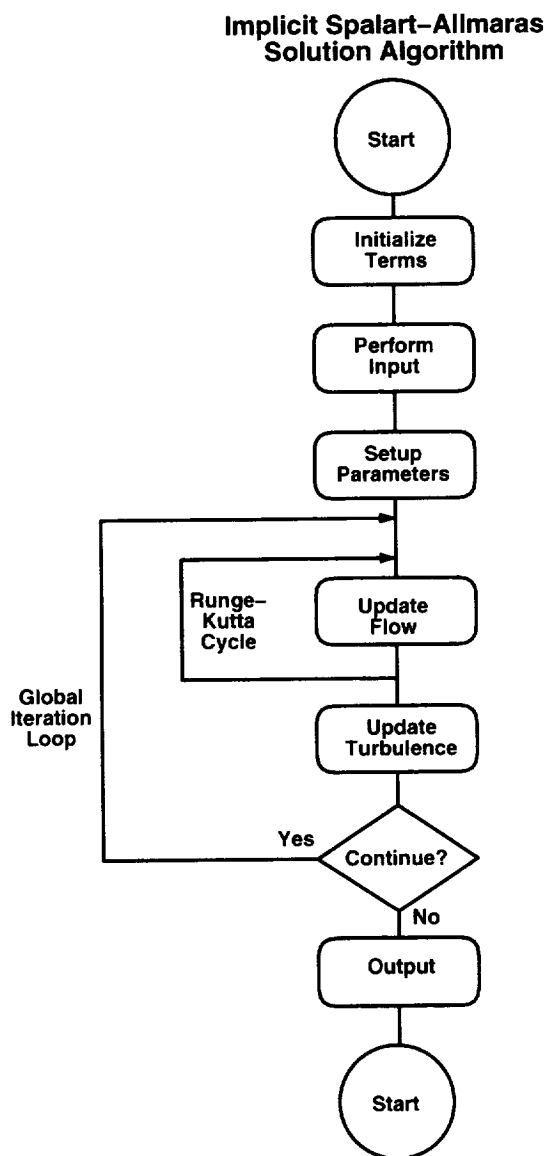


Figure 3.2: Schematic illustration of numerical solution sequence of Spalart-Allmaras turbulence model in the *ADPAC* flow solver.

Chapter 4

VALIDATION OF THE SPALART-ALLMARAS MODEL

4.1 Introduction

As the one-equation turbulence model was being incorporated into the *ADPAC* routines, test cases were run to ensure the model was accurately coded. Results presented within this section include the following validation cases: a subsonic flat plate, a subsonic symmetric airfoil, a transonic bump, and a transonic turbine cascade. Comparisons are made between the results obtained using the algebraic Baldwin-Lomax model and the one-equation Spalart-Allmaras model. The subsonic symmetric airfoil case was also solved using a separate prediction code with the Spalart-Allmaras model and those results are compared with the results from *ADPAC*.

The sensitivity of the turbulence field predicted by the Spalart-Allmaras model to the near-wall spacing used in the computational mesh was also addressed. A 2-D flat plate and a 3-D stator midspan passage were analyzed using several variations of near-wall spacing. The results from the near-wall spacing study generated guidelines for future mesh generation when the Spalart-Allmaras model is to be employed.

4.2 Flat Plate

The most fundamental test case used in developing and testing turbulence models is the simple flat plate. A 9-foot flat plate was solved using *ADPAC* for a Mach 0.2 freestream flow using both the Baldwin-Lomax algebraic turbulence model and the Spalart-Allmaras one-equation turbulence model. A computational mesh was generated with 77 points along the plate and 49 points normal to the plate. The mesh expansion ratios were less than 1.23 in both directions and the near-wall spacing of the first cell along the viscous wall resulted in y^+ values less than 1 for the majority of the plate ($x > 0.0042$ ft). For points extremely close to the leading edge, the y^+ values were all below to 2.5. Figure 4.1 shows the normalized boundary layer profiles of velocity (U/U_∞), shear stress (τ/τ_w), and kinematic eddy viscosity ($\nu_t/0.025U_\infty\delta^*$) from the *ADPAC* solutions at a location along the plate where the Reynolds number based on momentum thickness (Re_θ) was approximately

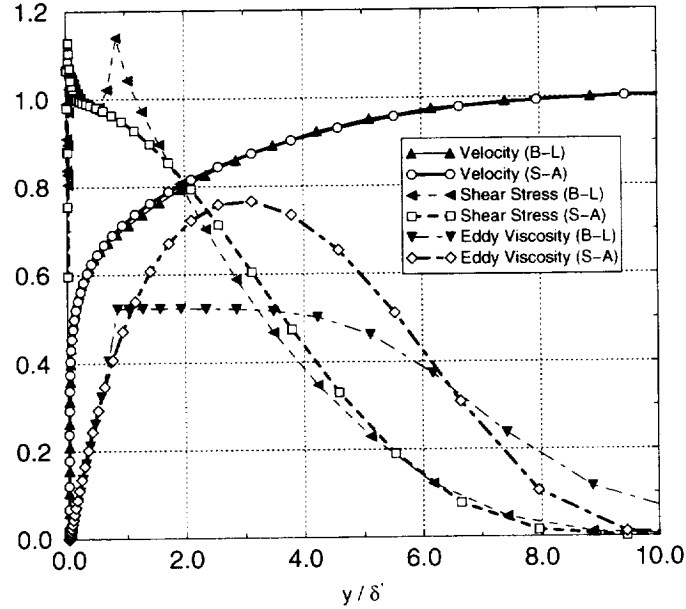


Figure 4.1: Normalized flat plate boundary layer profiles of velocity (U/U_∞), shear stress (τ/τ_w), and kinematic eddy viscosity ($\nu_t/0.025U_\infty\delta^*$) at $Re_\theta \approx 10^4$ as calculated by *ADPAC* using both the Baldwin-Lomax and Spalart-Allmaras turbulence models.

10,000. The filled symbols represent results using the Baldwin-Lomax model and the open symbols with the thicker lines are results using the Spalart-Allmaras model. For the one-equation results, this figure mirrors a plot presented in the original Spalart-Allmaras paper [2]. The difference between the Baldwin-Lomax results and Spalart-Allmaras results are most prominent in the outer portion of the boundary layer. Both models closely predict the eddy viscosity distribution in the near wall region ($y/\delta^* < 1$); however, in the outer portion of the boundary layer, the Baldwin-Lomax model encounters a discontinuity due to switching from the inner-layer equation to the outer-layer equation [23], while the Spalart-Allmaras model results predict a more continuous distribution of eddy viscosity.

Axial distributions of boundary layer thickness, wall shear stress, and friction coefficient are presented in Figure 4.2. Comparisons can be made between the two *ADPAC* turbulence models, analytical expressions [24, 23] and experimental data [25]. Since both the Baldwin-Lomax and the Spalart-Allmaras model were calibrated to predict the flat plate boundary layer during their development, no significant differences should be noticed between the two numerical solutions which appears to be the case. The minor discrepancy between the numerical predictions of boundary layer thickness (δ) and the analytical expression can be attributed to the singularity cell at the inlet boundary and viscous wall intersection.

The flat plate test case was also used to validate the multi-grid acceleration of the turbulence model equation. Solving the turbulence equation using the explicit algorithm without multi-grid, the solution appears to reach convergence at approximately 15,000 iterations where the residual values level off. When multi-grid is employed including a “full” multi-grid start-up procedure, convergence is reached in approximately 4000

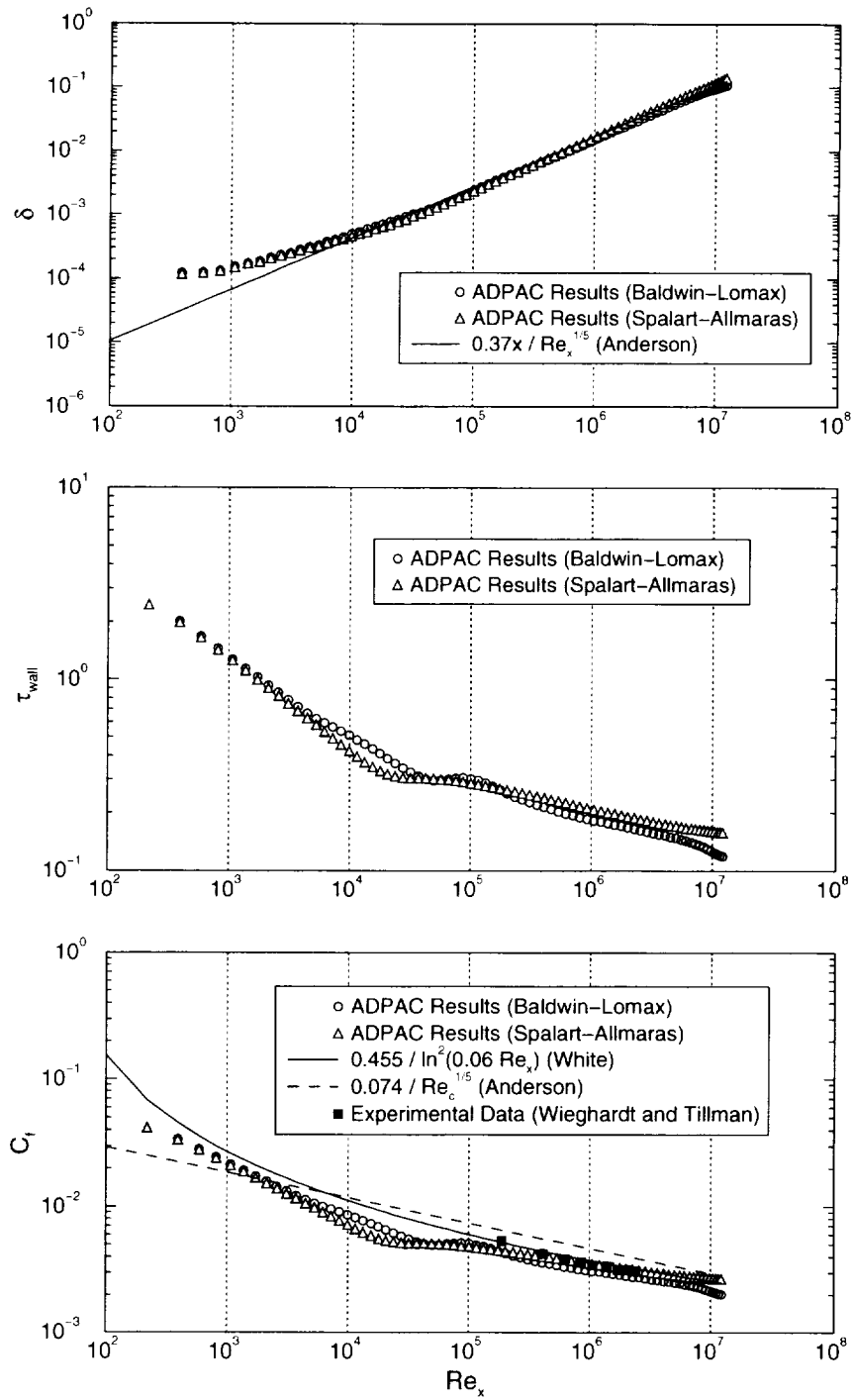


Figure 4.2: Axial distributions along a flat plate of boundary layer thickness (δ), wall shear stress (τ_{wall}), and friction coefficient (C_f), compared with experimental data [25] and analytical expressions [24, 23].

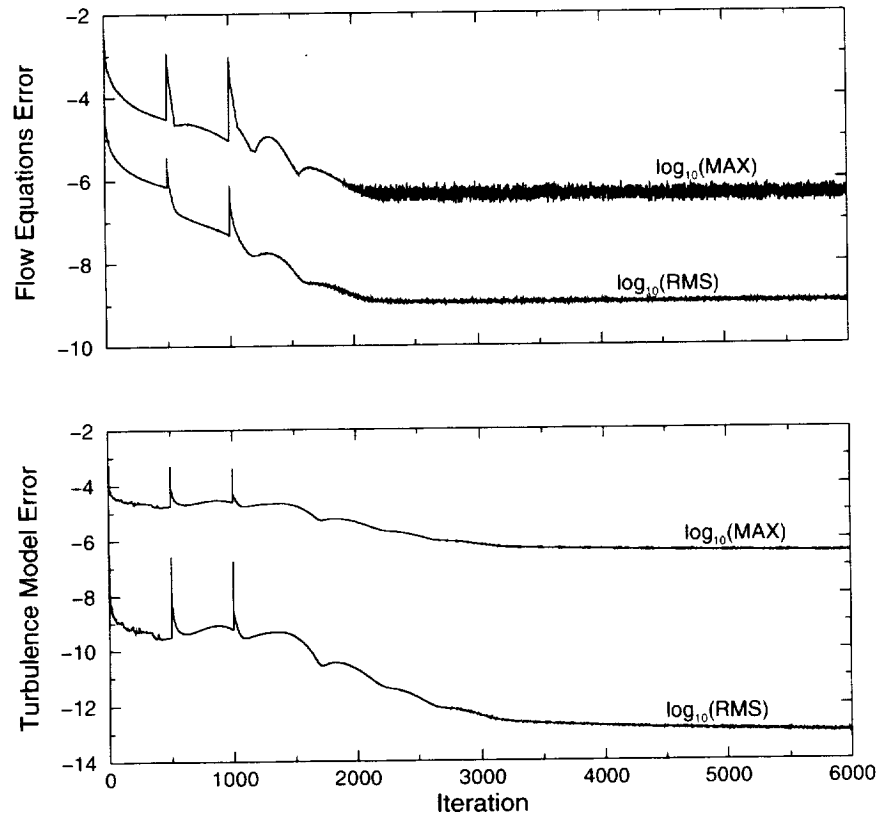


Figure 4.3: Convergence histories of the flow equation residuals and turbulence model equation residuals for the flat plate case using three levels of multi-grid and employing a full multi-grid startup.

iterations as shown in Figure 4.3. The corresponding axial distributions were plotted for the multi-grid solution and exactly matched the non-multi-grid solution. It is interesting to note the characteristic of the turbulence model equation convergence; after initially decreasing slightly, the turbulence model error actually increases while the flow gradients are being established, and then decreases until it levels off at a converged state. This ramp up and down in the convergence history has been seen in other codes running with the Spalart-Allmaras model. The spikes in the convergence histories occurring at 500 and 1000 iterations are related to the full multi-grid startup procedure when the solution data are interpolated to the next finer mesh level.

4.2.1 3-D Extension of the Flat Plate

In order to ensure consistency between the 2-D routines and 3-D routines, the 2-D flat plate mesh used above was extended into the third dimension as shown in Figure 4.4. Three different flat plate meshes were tested; the physical location (x, y, z) of the mesh points remained the same, however the grid indices (i, j, k) were rotated through such that in each case the outward normal of the viscous plate was a different grid index. This was

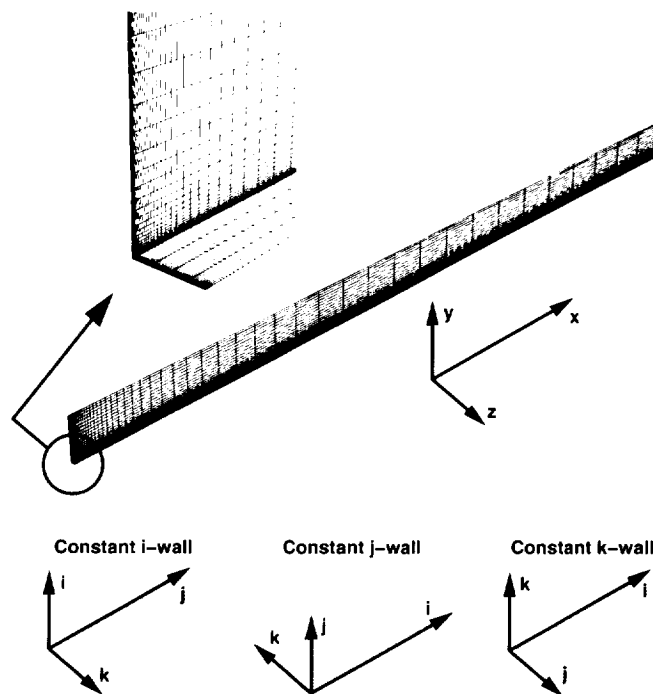


Figure 4.4: Three-dimensional mesh system made up of stacked 2-D slices. The grid indices (i,j,k) were rotated through to test each grid index as a solid wall.

done to make sure the routines were coded exactly the same in each coordinate direction.

These flat plate cases were run with and without multi-grid acceleration resulting in six runs. The results from these runs are shown in Figure 4.5 along with the 2-D results. All the results collapse onto a single line running through the 2-D results represented by the symbols. This indicates that the Spalart-Allmaras turbulence model appears to be coded similarly in each of the coordinate directions.

4.3 NLR Symmetric Airfoil

Through searching the literature, a symmetric flat-plate airfoil tested at the National Aerospace Laboratory (NLR, The Netherlands) [26] was found to be a very suitable test case. The NLR test case was one of the four test cases used by Goldberg in his paper describing the implementation of the $k-\mathcal{R}$ turbulence model [27]. The NLR test case provides a simple 2-D flat-plate airfoil geometry with extensive measurements of both mean and fluctuating quantities in the 2-D wake shed from the airfoil. Goldberg states that this case is “particularly illuminating since the (turbulence) model is expected to detect automatically the switch from wall-bounded to wake flow and build the eddy viscosity field accordingly.”

Figure 4.6 shows the flat-plate airfoil geometry and the location of the computational freestream boundary. The data stations where wake data was measured in the experiment are also shown and correspond to where the numerical data were extracted

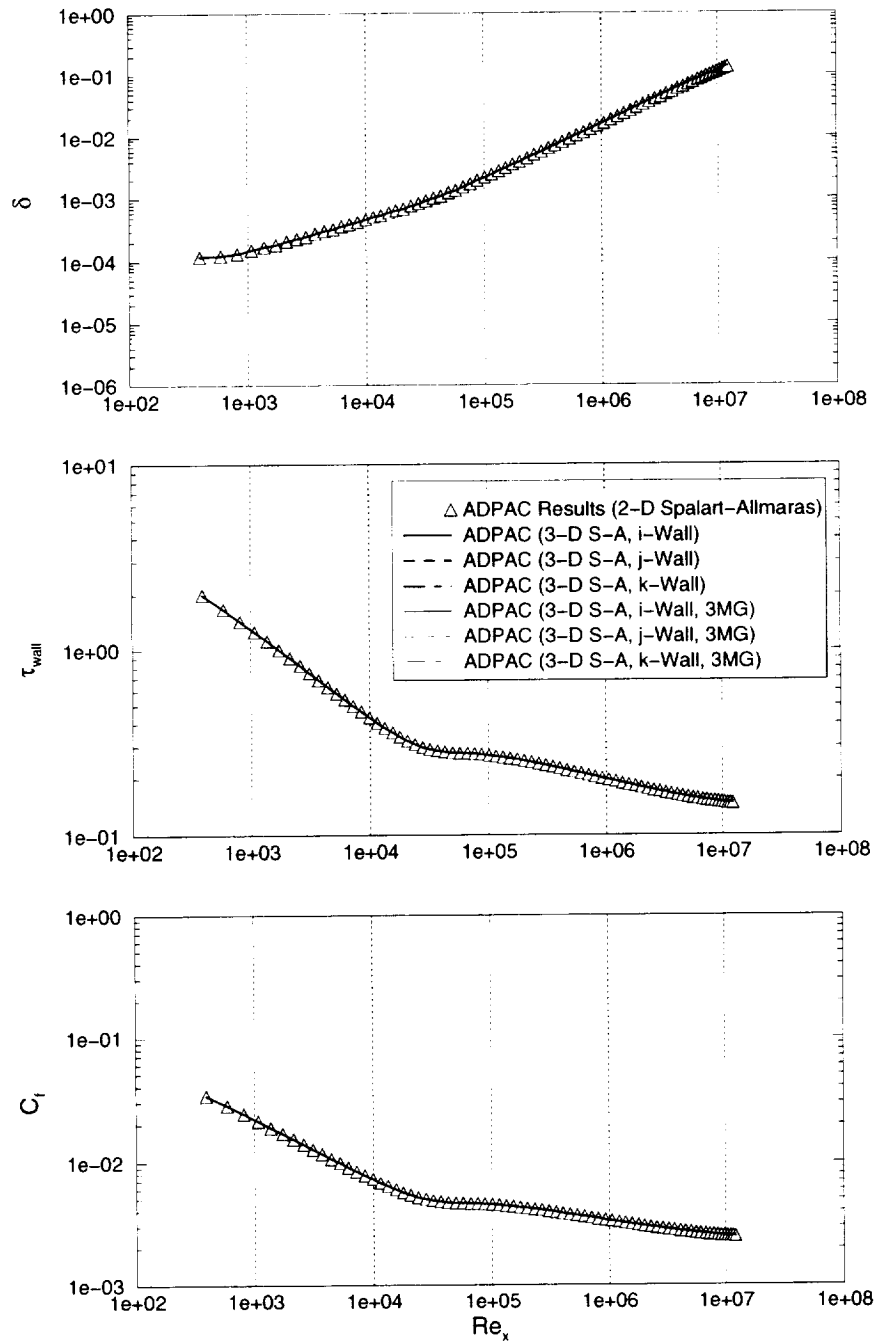


Figure 4.5: Axial distributions along a flat plate of boundary layer thickness (δ), wall shear stress (τ_{wall}), and friction coefficient (C_f), comparing the 2-D and 3-D formulations (with and without multi-grid) of the Spalart-Allmaras model.

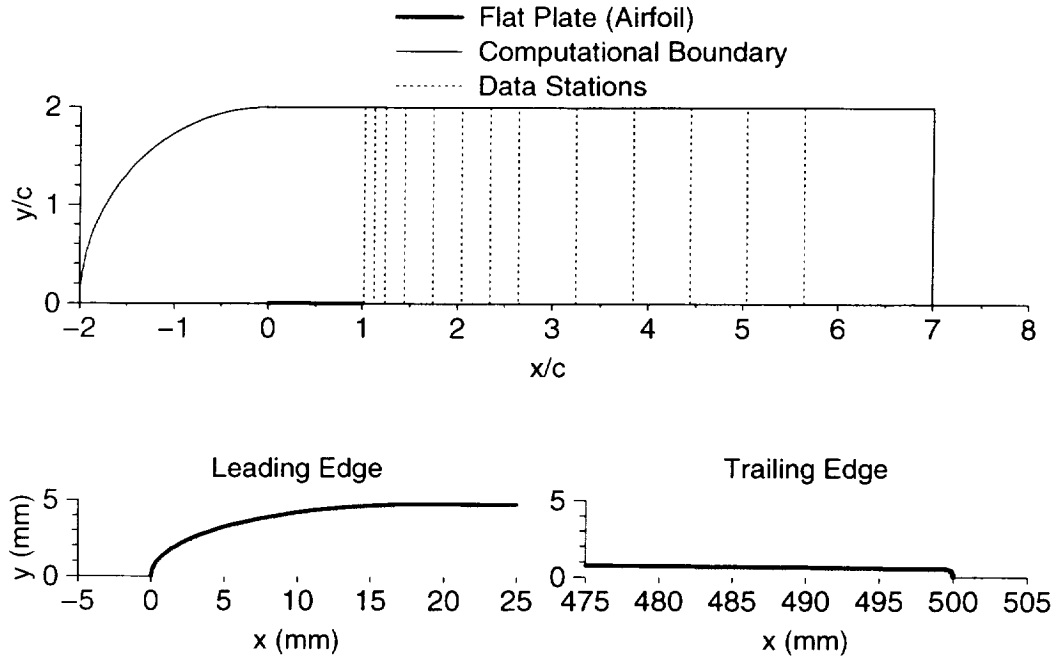


Figure 4.6: Geometry description of the NLR flat-plate airfoil model with the location of downstream experimental data stations and computational boundaries.

for comparisons. The leading edge of the airfoil is defined by the following equation of a half-ellipse:

$$y = \sqrt{22.5625 - \left(\frac{x - 19}{4}\right)^2}, \quad x \leq 19 \text{ mm}$$

and is connected with straight lines to the trailing edge where the radius is 1.1 mm. The leading and trailing edge regions of the airfoil are shown in Figure 4.6.

A C-type mesh topology was selected to grid around the airfoil as shown in the top of Figure 4.7. Extremely tight mesh spacing was used near the airfoil surface (0.01 mm) in order to ensure multiple points inside the viscous sublayer. An additional mesh block was added in the centerline wake region in order to increase the mesh resolution and decrease the grid shear; this block can be seen near the trailing edge in the bottom of Figure 4.7. The total number of mesh points used in both blocks was 29,906 with cell expansion ratios of less than 1.45 in the axial direction and less than 1.15 in the normal direction. Values of y^+ were calculated throughout the entire flow field from the *ADPAC* solution. These values are plotted versus mesh index in Figure 4.8 for a typical mesh line radiating away from the airfoil at approximately $0.38 x/c$. The near-wall value of y^+ is less than 1.0 and there are five points within the viscous sublayer ($y^+ < 5$).

Prior to the implementation of the Spalart-Allmaras turbulence model into *ADPAC*, this test case was solved using the *OVERFLOW* code which already had the Spalart-Allmaras model available. The *OVERFLOW* code, an out-growth of the *F3D/Chimera* code developed by Steger at NASA Ames Research Center, is a

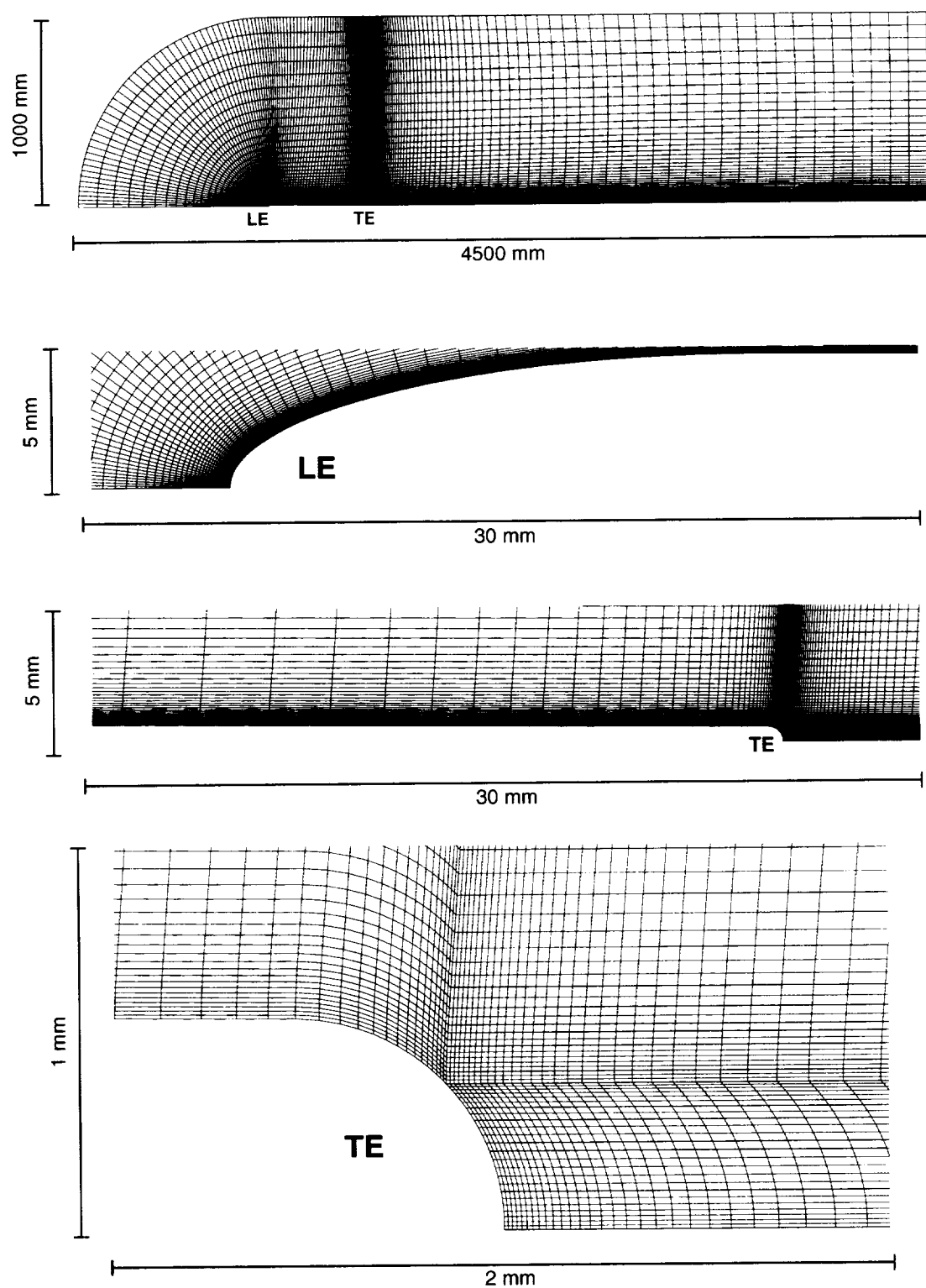


Figure 4.7: Details of the mesh used to collect the *ADPAC* solution for the NLR flat-plate airfoil model.

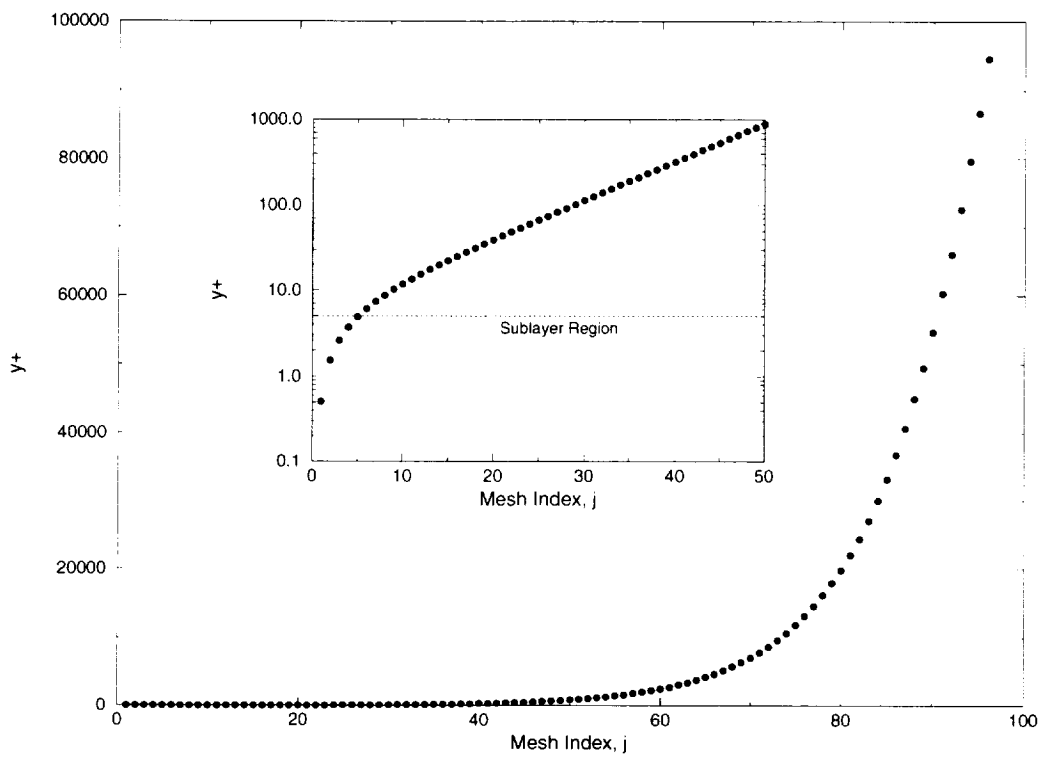


Figure 4.8: Distribution of y^+ values along a mesh line radiating away from the airfoil at approximately 38% chord.

Navier-Stokes code which utilizes overlapped grids [28]. When the *OVERFLOW* code was used with the Spalart-Allmaras model, the results improved dramatically over the *ADPAC* results using the Baldwin-Lomax model in the ability to predict the wake shape. This was a significant motivating factor to incorporate the Spalart-Allmaras model into *ADPAC* to improve wake prediction.

The NLR report contained detailed measurements of axial velocity taken across the 2-D wake region downstream of the airfoil at the 13 stations shown in Figure 4.6 and listed in Figure 4.9; these stations ranged in x/c values from 1.016 to 5.644. Figure 4.9 compares the *ADPAC* -predicted velocity profiles with the NLR experimental data. The experimental data taken on the lower side of the airfoil ($y < 0$) was reflected generating the doubling of experimental data points at each y/c location. The convergence of the *ADPAC* numerical solution was determined when these velocity profiles remained the same through additional iterations. Due to the extremely tight mesh spacing used and the low convection speed of the wake, the number of iterations needed to propagate the wake decay profile downstream was approximately 50,000 using *ADPAC* with multi-grid.

Attention should be drawn to the differences between the *ADPAC* Baldwin-Lomax results (thin solid line), the *OVERFLOW* Spalart-Allmaras results (thick dot-dash line), and the *ADPAC* Spalart-Allmaras results (thick solid line). The *ADPAC* velocity profiles obtained using the Baldwin-Lomax model match fairly well the experimental data from 0.01 y/c upwards. However near the centerline of the wake ($y/c < 0.01$), the wake deficit does not mix out; this is typical of the Baldwin-Lomax turbulence model designed for wall-bounded flows and not free shear flows. With the addition of the Spalart-Allmaras turbulence model, the *ADPAC* predicted results dramatically shift to match the data extremely well at every downstream axial location. In a comparison between the two solutions using the Spalart-Allmaras model, the *ADPAC* results appear to predict the wake shape slightly better than the *OVERFLOW* predictions. This and other subtle differences between the two flow prediction codes may be due to differences in their respective internal numerics and/or boundary condition treatments.

Figure 4.10 shows a comparison of the centerline axial velocity (wake deficit) downstream of the airfoil for all the collected solutions. Solutions using a simple mixing-length turbulence model in *ADPAC* and the one-equation Baldwin-Barth turbulence model [29] in *OVERFLOW* are also included for comparison. Both the Baldwin-Lomax and mixing-length models in *ADPAC* significantly under-predict the centerline velocity, while the Baldwin-Barth model in *OVERFLOW* does a slightly better job of predicting the wake decay but still falls short. The two solutions using the Spalart-Allmaras turbulence model do the best jobs of predicting the decay in wake deficit.

In addition to the mean flow velocities, the shear stresses resulting from the fluctuating velocity component were also compared. The shear stress was evaluated from the converged *ADPAC* flow and eddy viscosity fields using the following relation:

$$-\overline{u'v'} = \frac{\mu_t}{\rho} \left(\frac{\partial u}{\partial y} + \frac{\partial v}{\partial x} \right) \quad (4.1)$$

Figure 4.11 presents the normalized Reynolds stress profiles at the same downstream measuring stations shown previously. The Baldwin-Lomax model predicts the stress levels slightly better than the Spalart-Allmaras model *immediately* behind the airfoil

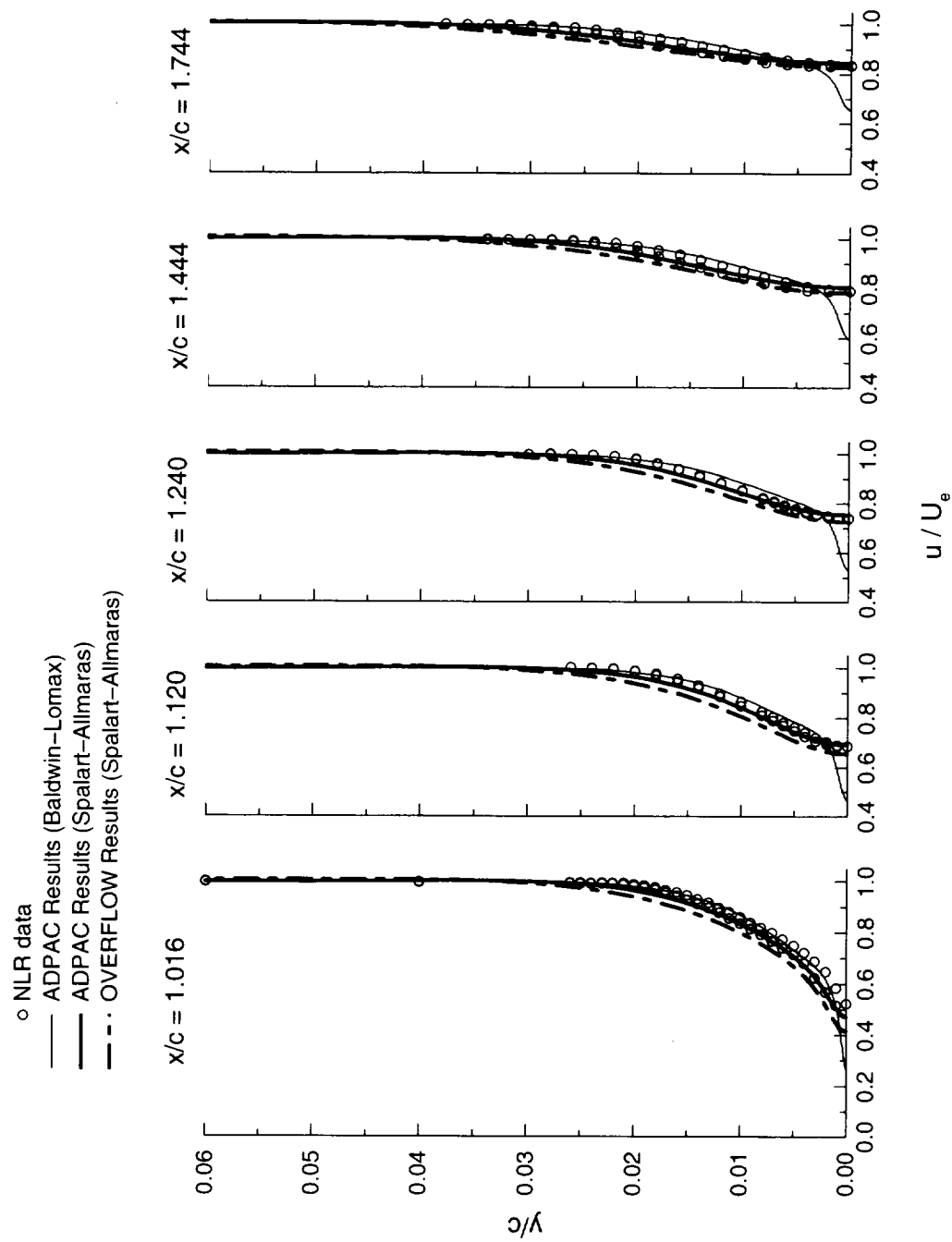


Figure 4.9: Comparisons between NLR experimental data and numerical predictions of axial velocity profiles in the wake region downstream of the airfoil.

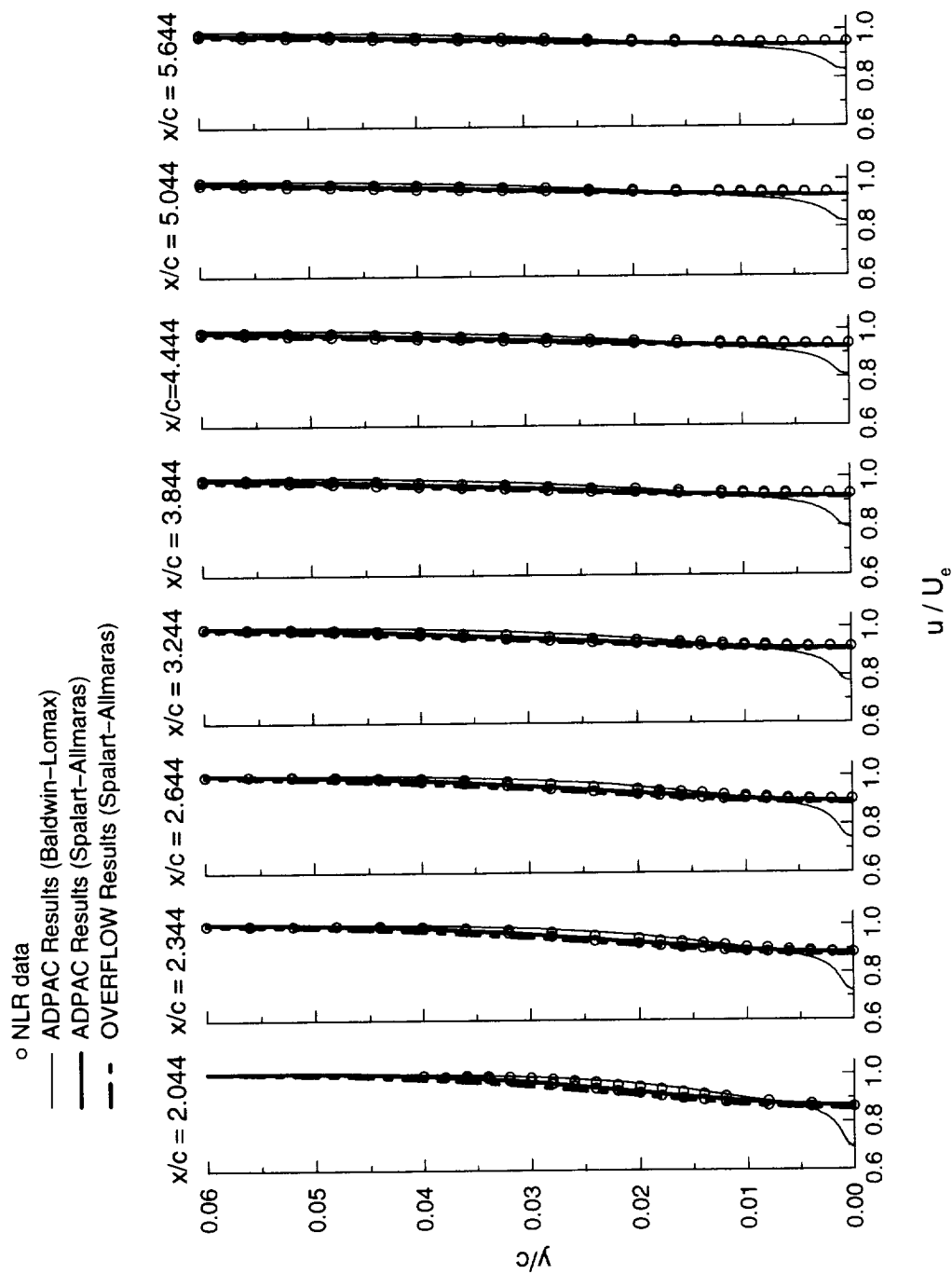


Figure 4.9: (concluded) Comparisons between NLR experimental data and numerical predictions of axial velocity profiles in the wake region downstream of the airfoil.

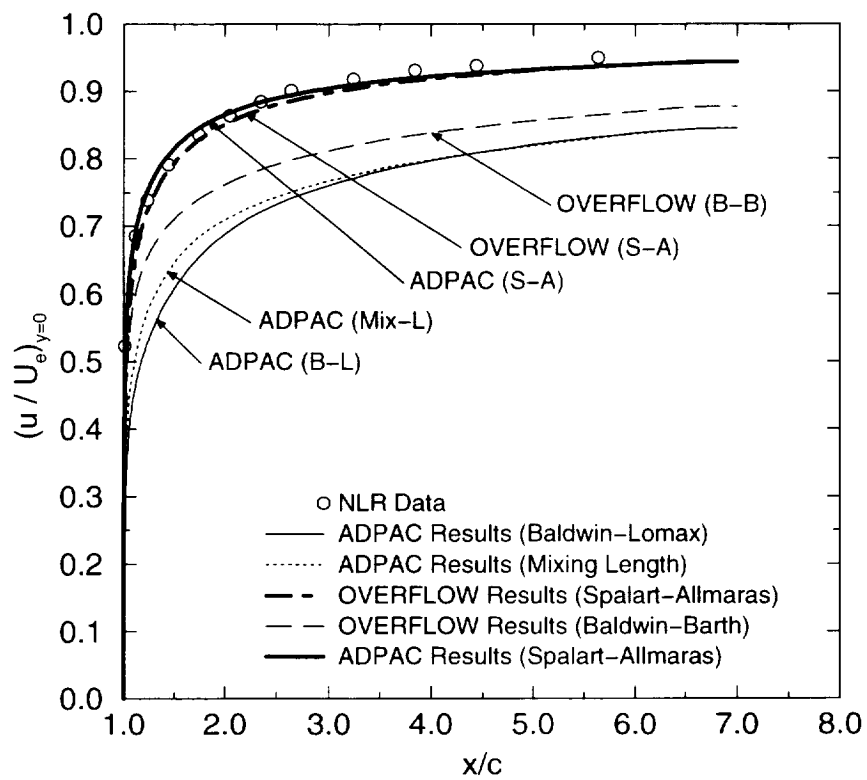


Figure 4.10: Comparison of centerline axial velocity distributions downstream of the airfoil between the NLR experimental data and numerical predictions.

trailing edge. However, the advantage clearly shifts to the one-equation model shortly thereafter. The improved representation of the outer portion of the boundary layer eddy viscosity distribution afforded by the Spalart-Allmaras model (as shown in Figure 4.1 for the flat plate case, $1.0 \leq y/\delta^* \leq 5.0$) appears to carry on downstream, resulting in an improved representation of the wake. The *ADPAC* Baldwin-Lomax results are similar to those presented by Goldberg [27] for the NLR airfoil, and the *ADPAC* Spalart-Allmaras results closely follow his $k-\mathcal{R}$ results. From these results, it is evident that the use of the Spalart-Allmaras model results in an improved capability for predicting the wake structure when compared to the Baldwin-Lomax model.

4.4 Transonic Bump

The third test case presented is transonic flow over an axisymmetric bump [30]. High subsonic flow (Mach 0.875) accelerates over a bump on a circular cylinder creating a shock wave with a recirculation zone behind the shock. Figure 4.12 compares the predicted Mach number contours between the Baldwin-Lomax and Spalart-Allmaras models. The Baldwin-Lomax model predicts a slightly stronger shock located farther aft on the bump when compared to the Spalart-Allmaras model results, primarily due to differences in the recirculating region downstream of the shock.

The static pressure distributions for this case are shown in Figure 4.13. As seen in the contour plots, the *ADPAC* Baldwin-Lomax results appear to place the shock farther downstream when compared to the experimental data and the results miss the size of the recirculation region. The *ADPAC* Spalart-Allmaras results show an improvement in the prediction of the pressure distribution: not only is the shock location moved upstream closer to the experimental location, but the recirculation region is well defined and matches very closely with the experimental data. The small bump in the middle of the recirculation region occurs at the trailing edge of the bump ($x/c = 1.0$) and is related to the sharp corner in the mesh.

4.5 Mark II Turbine Vane

The Mark II turbine vane cascade [31] was selected to determine the effect of freestream turbulence specification on heat transfer. Although the level of freestream turbulence is determined by the inlet specification of χ , no direct relationship between χ_{in} and the percentage turbulence level (Tu) has been derived. The *ADPAC* Spalart-Allmaras solutions were collected on a coarse mesh (193x33) using five different values of inlet turbulence over a large range ($\chi_{in} = 1, 10, 20, 100, 500$). Previous *ADPAC* results using the Baldwin-Lomax model are also included from both the coarse and fine (385x49) meshes [7].

To better visualize the flow field and the turbulence field, contour plots of Mach number and turbulence level χ are shown in Figure 4.14 with an inlet χ value of 1. The flow around the turbine vane has a small supersonic region on the suction side of the airfoil. The resulting shock triggers the turbulent boundary layer as can be seen in the increase in χ intensity immediately behind the shock location. The level of turbulence

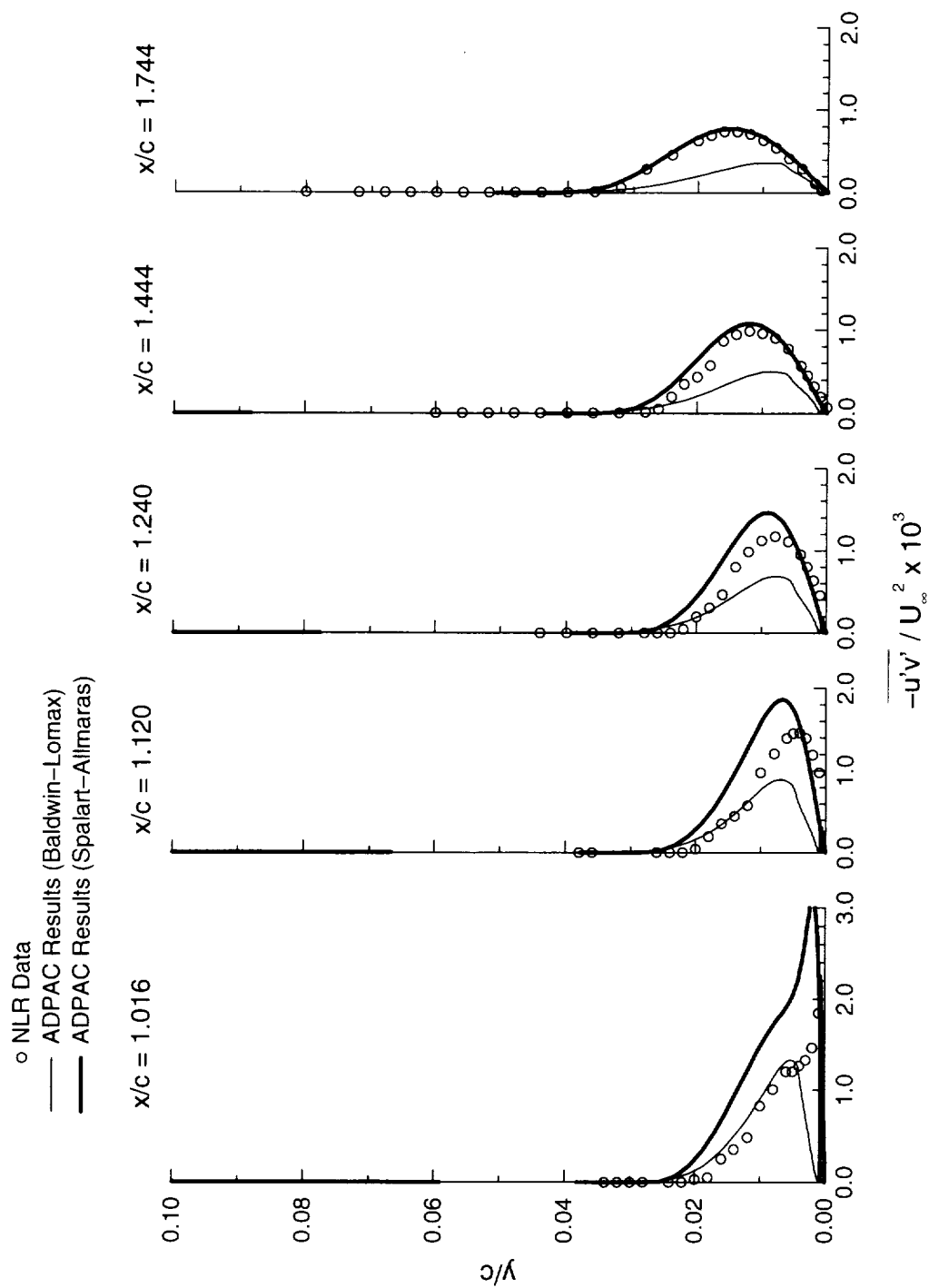


Figure 4.11: Comparisons between NLR experimental data and numerical predictions of Reynolds stress profiles in the wake region downstream of the airfoil.

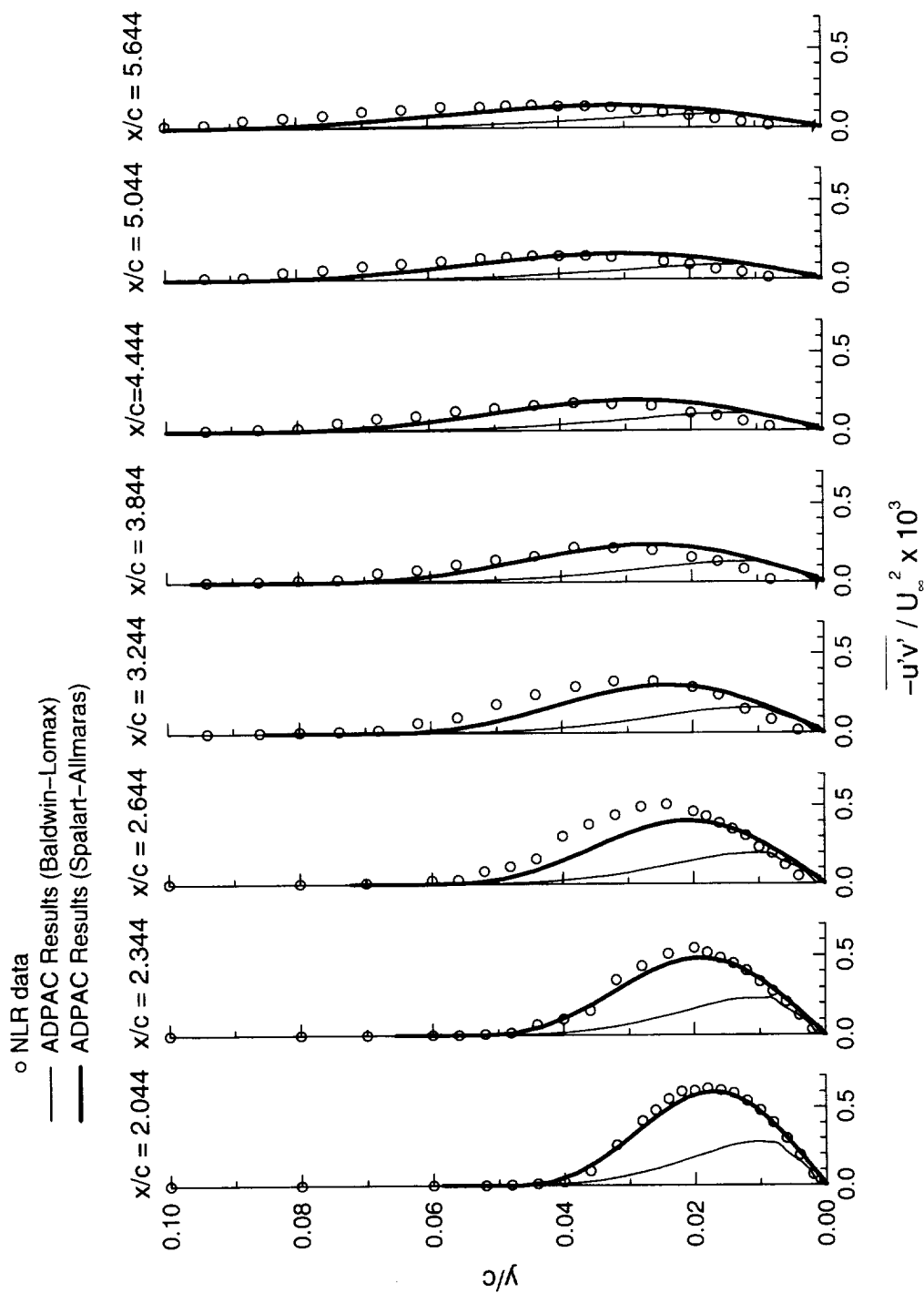


Figure 4.11: (concluded) Comparisons between NLR experimental data and numerical predictions of Reynolds stress profiles in the wake region downstream of the airfoil.

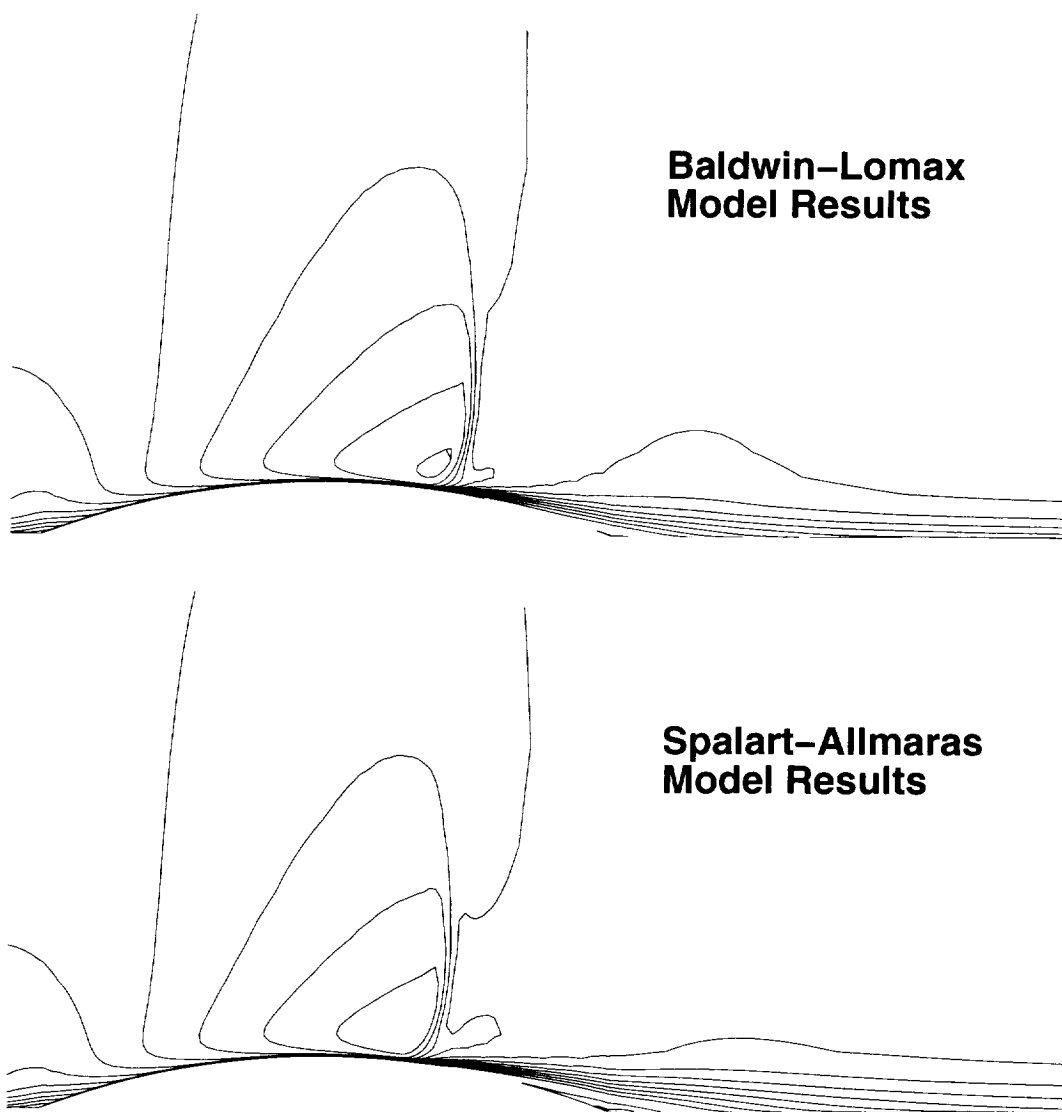


Figure 4.12: Contours of Mach number around the transonic bump test case as predicted by ADPAC using the Baldwin-Lomax model (*top*) and the Spalart-Allmaras model (*bottom*).

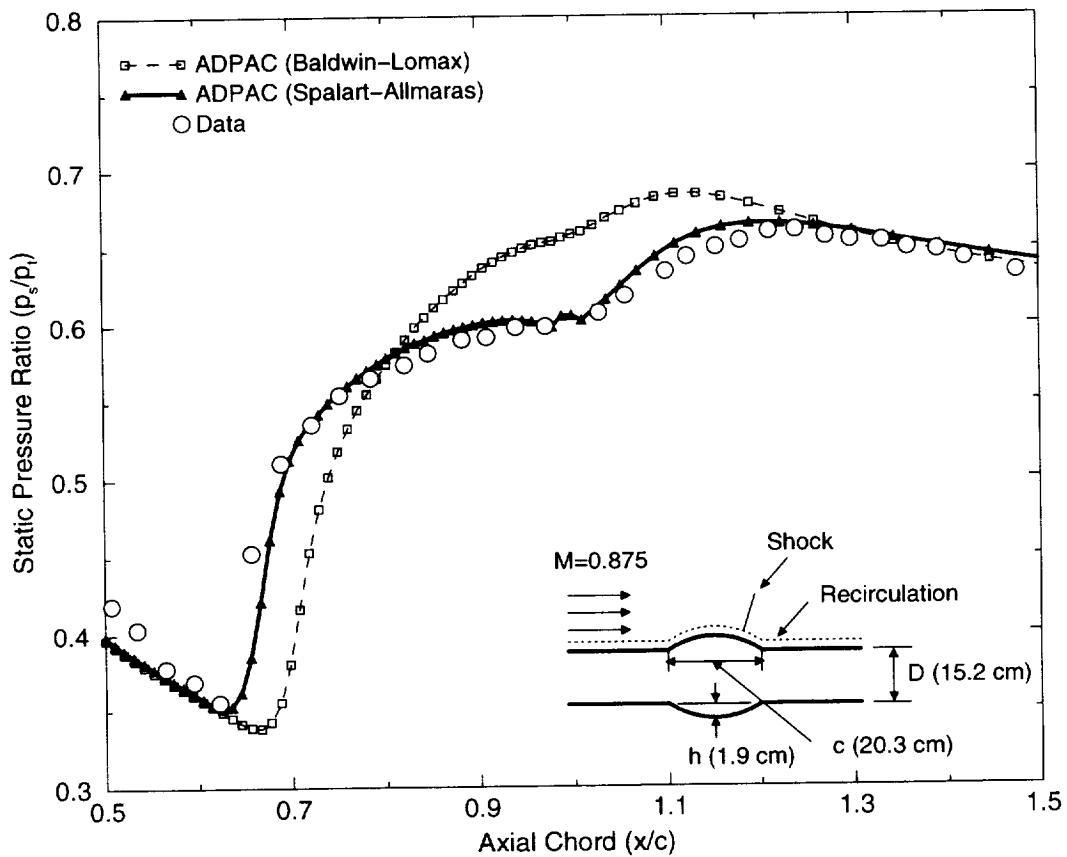


Figure 4.13: Comparison between experimental and predicted surface static pressure over a transonic bump.

peaks at a value of χ near 250 in the center of the wake which can be seen exiting the lower portion of the computational domain and re-entering it above.

Distributions of airfoil static pressure and heat transfer coefficient are shown in Figure 4.15. The level of inlet χ has negligible effects on the pressure distribution; however, the freestream turbulence has a greater effect on the level of heat transfer coefficient. While all of the Spalart-Allmaras results are reasonable and lie close to the experimental data, as the inlet value of χ is increased the heat transfer coefficient is also increased as would be expected.

4.6 Near-Wall Spacing Sensitivity Study

Two simple geometries were used to determine the sensitivity to near-wall spacing for each of the turbulence models (Baldwin-Lomax and Spalart-Allmaras). The 2-D geometry selected was a simple flat plate, and the 3-D geometry was a midspan slice of a compressor stator. The detailed results from each of these test cases will be presented below in their respective sections.

4.6.1 Flat Plate

The flat plate grid used previously during the Spalart-Allmaras model incorporation and validation stages was considered the baseline near-wall spacing (1x). Using the same number of grid points, the near-wall spacing was changed creating a series of flat plate meshes with increasing near-wall distance. Table 4.1 lists the series of meshes used and the corresponding physical distance to the first grid point away from the viscous wall. The axial distribution of grid points along the plate remained unchanged throughout the generation of this mesh series.

ADPAC solutions were collected on each of the meshes using both the algebraic Baldwin-Lomax turbulence model and the one-equation Spalart-Allmaras turbulence model. As part of the post-processing of these several cases, distributions of y^+ values were evaluated from the converged flow and viscosity fields. Table 4.1 also contains information of the grid density near the wall in terms of y^+ values. The number of mesh cells with y^+ values less than 5 and 10, respectively, taken at a location along the plate where the Reynolds number based on momentum thickness was approximately 10,000 are listed in the table. The value of the y^+ is also listed for the first cell center off the wall.

At the same axial location ($Re_\theta \approx 10^4$), axial velocity profiles are compared in Figure 4.16 for different near-wall spacings and turbulence models. For both the Baldwin-Lomax and Spalart-Allmaras turbulence models, the flow solution appears to be near-wall spacing independent for meshes tighter than the 10x spacing. For mesh spacings greater than 5x the velocity distribution curves begin to deviate from the coalescence of results from the more tightly clustered meshes. When compared to the y^+ values listed in Table 4.1, this suggests that at least one grid cell should be centered within the linear sublayer of the boundary layer ($y^+ \leq 3$).

Figure 4.17 compares the distributions of friction coefficient (C_f) for each of the flat plate cases analyzed. Again, as was seen in the velocity distributions, meshes with

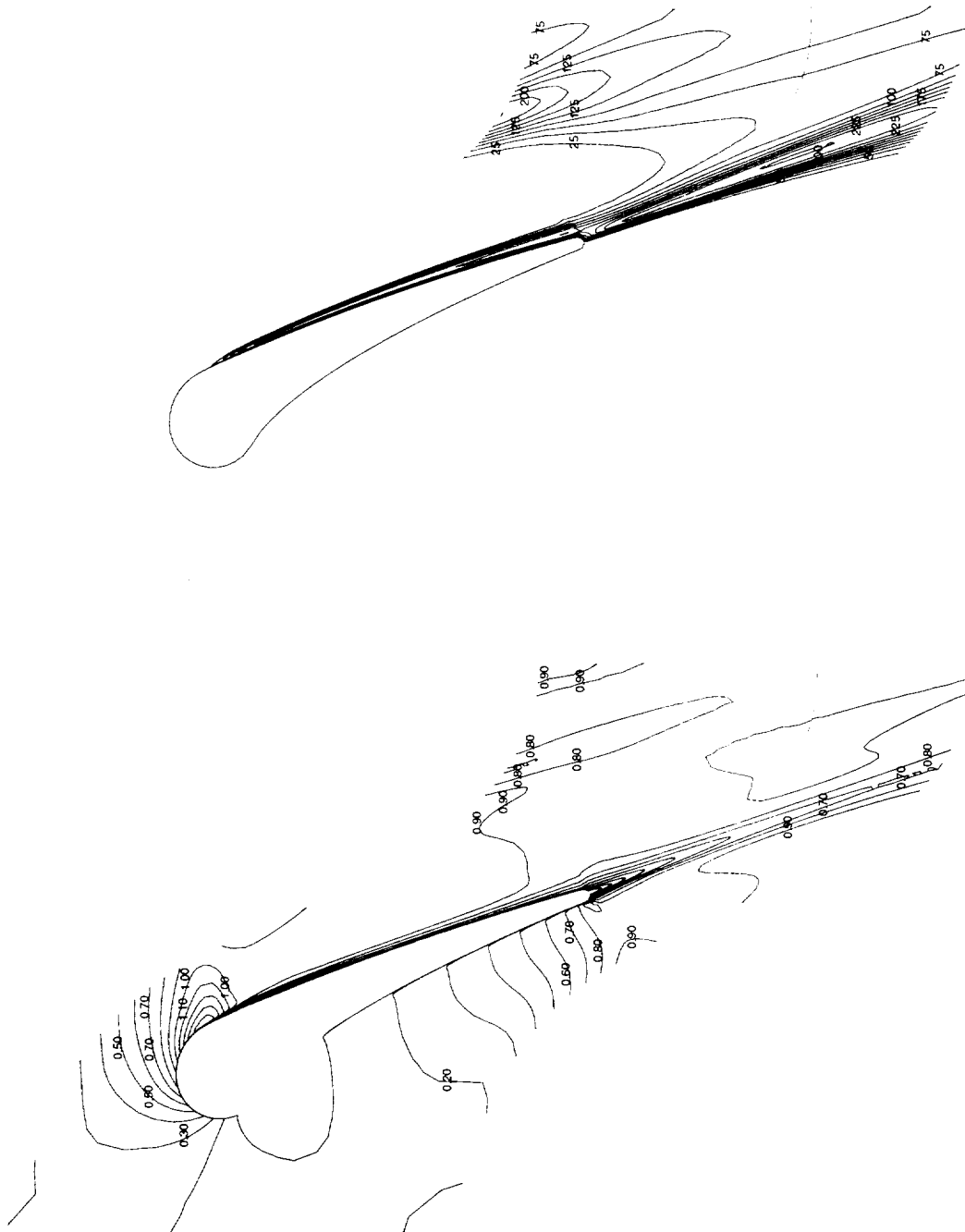


Figure 4.14: Contours of Mach number (*left*) and turbulence level χ (*right*) for the Mark II turbine vane with an inlet χ value of 1.

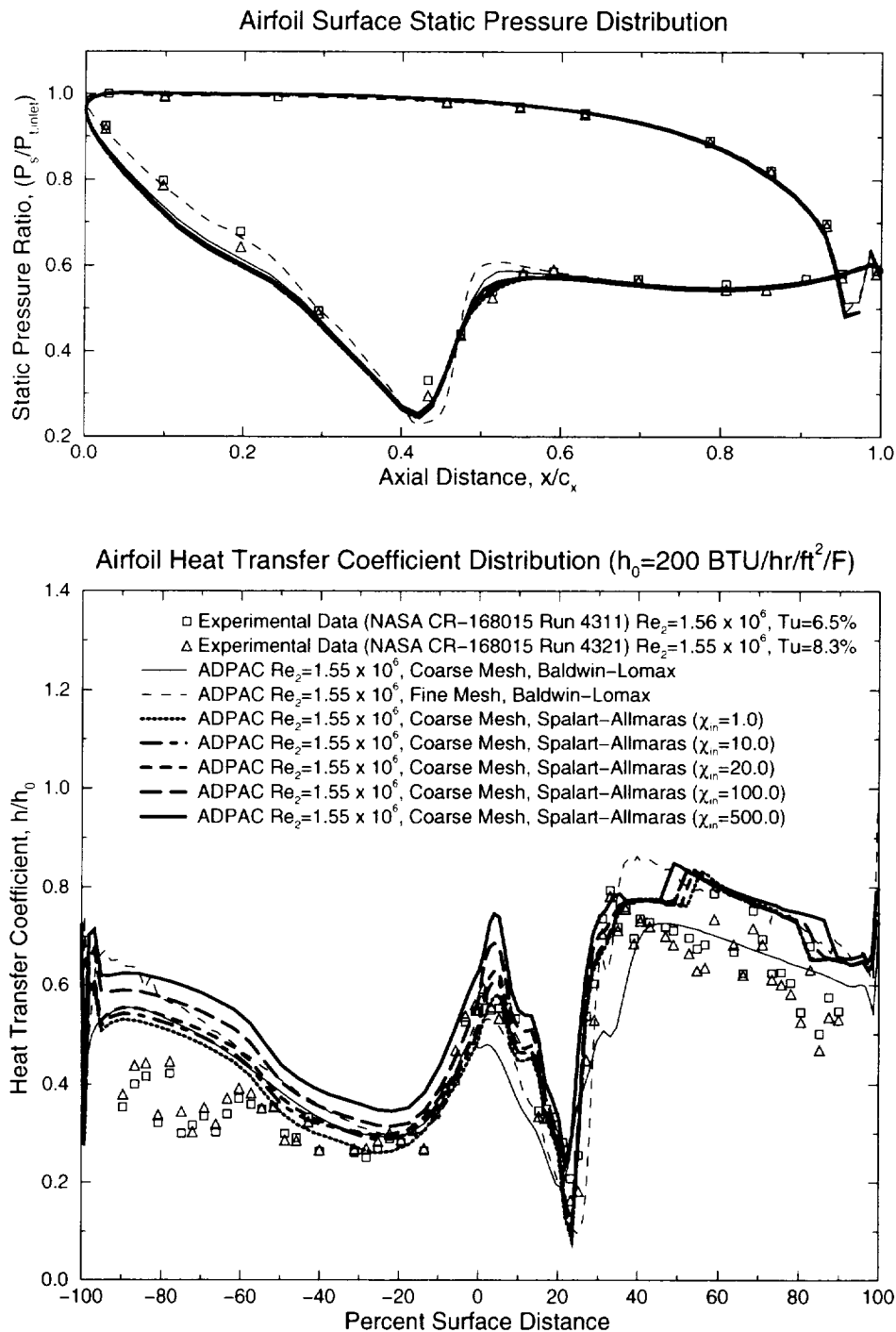


Figure 4.15: Comparison between experimental and predicted surface static pressure and heat transfer coefficients around the Mark II turbine transonic vane.

Spacing Name	Physical Spacing (ft)	# Points $y^+ < 5$ ($Re_\theta = 10^4$)	# Points $y^+ < 10$ ($Re_\theta = 10^4$)	First y^+ Value ($Re_\theta = 10^4$)
0.2x	0.000004	8	11	0.11
1x	0.00002	3	6	0.54
2x	0.00004	2	4	1.08
5x	0.0001	1	2	2.58
10x	0.0002	1	1	4.66
20x	0.0004	0	1	7.79
50x	0.001	0	0	14.20
100x	0.002	0	0	21.43

Table 4.1: Values of near-wall spacing for the flat plate series along with y^+ densities and near-wall y^+ values evaluated at $Re_\theta \approx 10^4$.

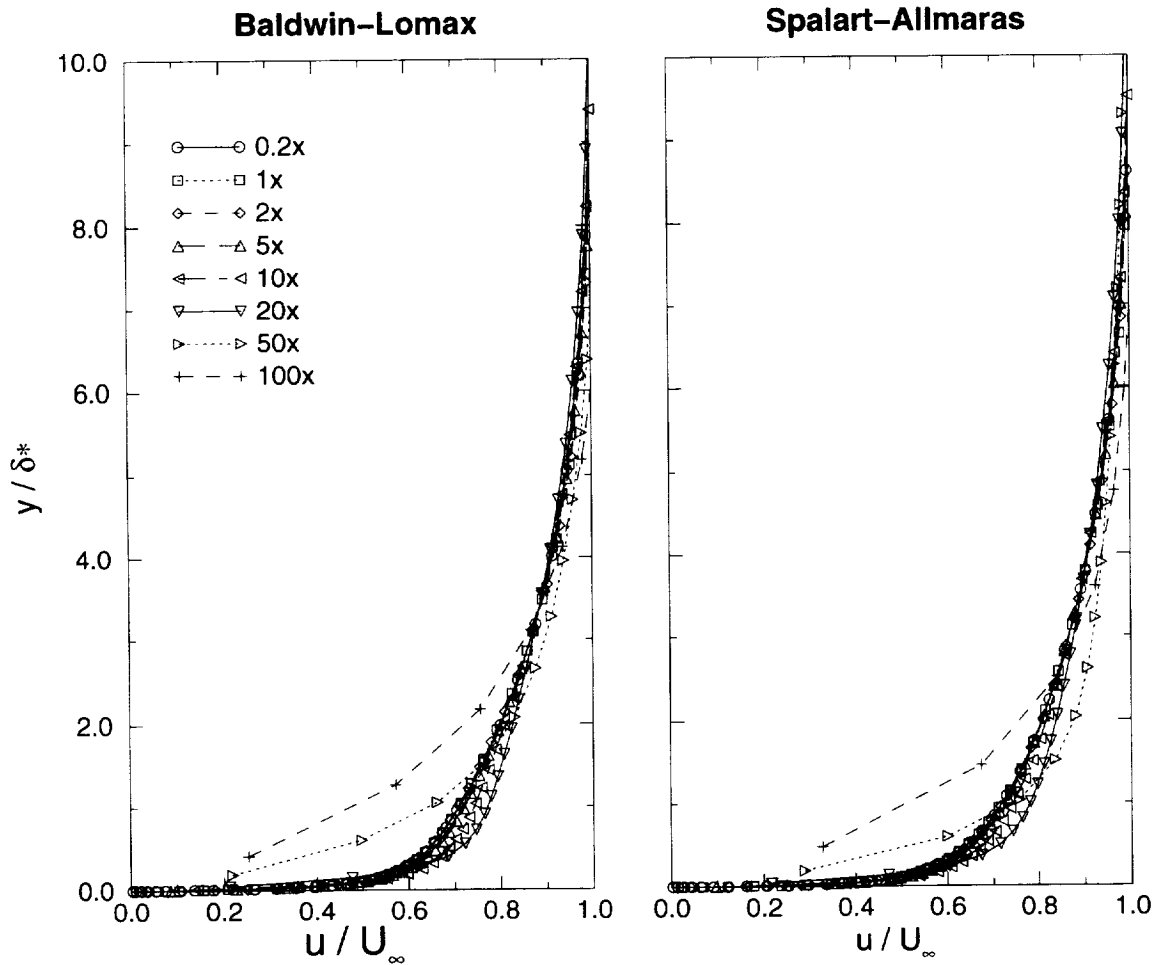


Figure 4.16: Comparison of axial velocity distributions evaluated where $Re_\theta \approx 10^4$ for different near-wall spacings and turbulence models.

Spacing Name	Physical Spacing (1 / 1000 in)	Average y^+ Value (First Cell)	y^+ Range (min – max) (First Cell)
0.05x	0.0065	0.26	0.02 – 0.70
0.2x	0.026	0.97	0.09 – 2.45
1x	0.13	4.11	0.40 – 9.01
2x	0.26	6.80	0.48 – 13.67

Table 4.2: Values of near-wall spacing for the stator midspan series along with average near-wall y^+ values and y^+ ranges evaluated along both surfaces of the stator.

spacings larger than 5x appear to deviate significantly from the mesh-independent solutions. In a comparison between the two turbulence models, the Spalart-Allmaras model results asymptote to a level closer to the experimental data [25] than do the Baldwin-Lomax model results for the mesh-independent solutions. This can be traced back to differences in predicted near-wall normal velocity gradient ($\partial u / \partial y$). The discrepancy between the *ADPAC* solutions and experimental data for the first 2 feet of the plate may be related to the treatment of the leading edge.

4.6.2 Stator Midspan Passage

In order to test the near-wall spacing effects on a 3-D problem and to evaluate its effects on the wake prediction, a narrow, annular passage was modeled from the midspan of a rear-stage compressor stator blade as shown in Figure 4.18. The stator geometry was extracted from the Allison AST Candidate 10-stage axial compressor design that had been used in a previous stator seal cavity leakage study [32]. The upper and lower mesh boundaries were held at constant radius and modeled as inviscid solid walls. Using the guidelines established from the flat plate with respect to near-wall y^+ values, a series of four 3-D meshes were created with the physical near-wall spacings (in 0.001 inches) listed in Table 4.2. For reference, the chord of the stator is approximately 0.62 inches. The table also lists the average and range of y^+ value for the first cell along the entire stator midspan surface. It should be noted that the 1x spacing listed for the stator midspan case (0.00013”) is different than the 1x spacing used for the flat plate cases. (The 1x notation merely refers to a baseline clustering value that might be used depending upon the geometry application.)

For each mesh generated, *ADPAC* solutions were collected using both the Baldwin-Lomax and Spalart-Allmaras turbulence models. The size of the H-grids used were 161 points axially (65 along the blade surface) and either 65 or 121 points circumferentially (blade-to-blade). The two numbers of circumferential points (65 or 121) were used to determine the effect of mesh density in the wake region without effecting the near-wall spacing; that is, both the 0.2x meshes have the same near-wall spacing regardless if the mesh has 65 or 121 points circumferentially. The number of radial points was 9 for the 65-point meshes and 5 for the 121-point meshes, which was not critical as there were no significant gradients in the radial direction.

As one of the primary goals of this research is to determine the effect of turbulence

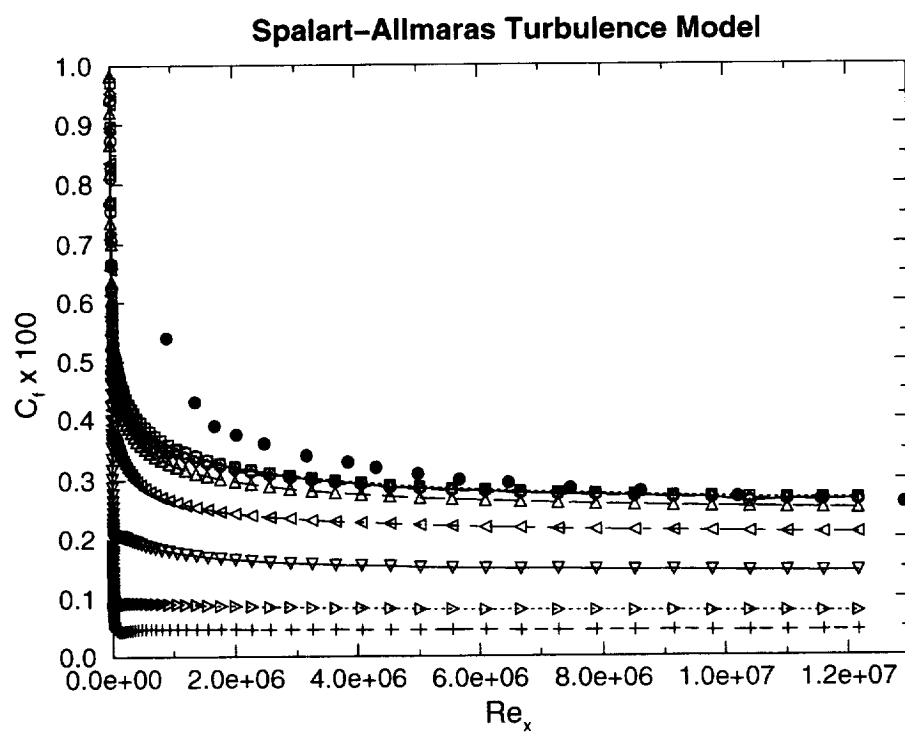
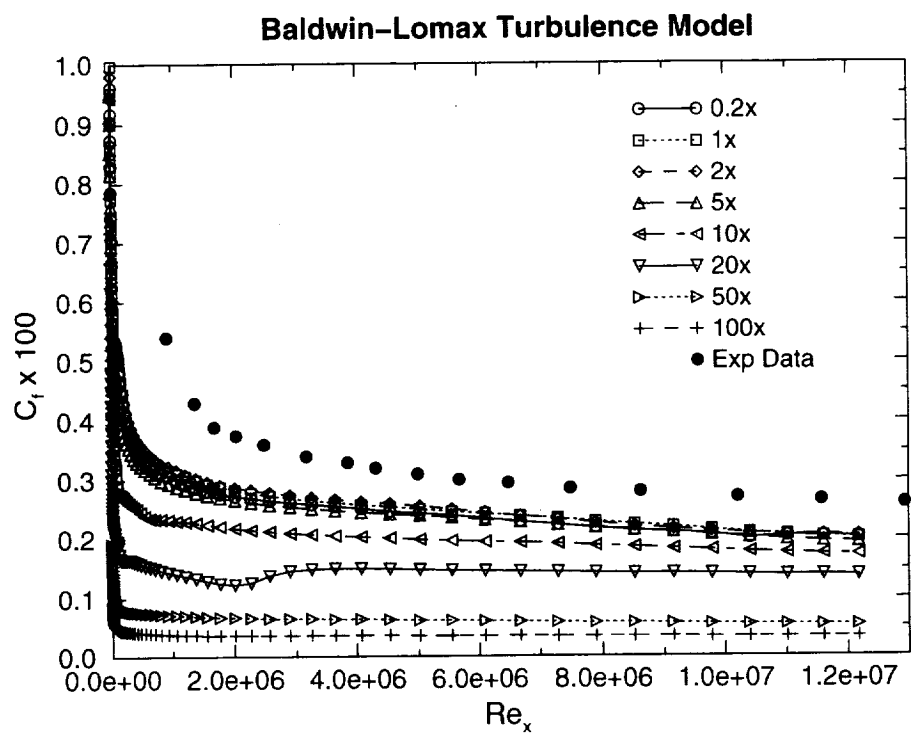


Figure 4.17: Distribution of friction coefficient ($C_f \times 100$) for different near-wall spacings and turbulence models.

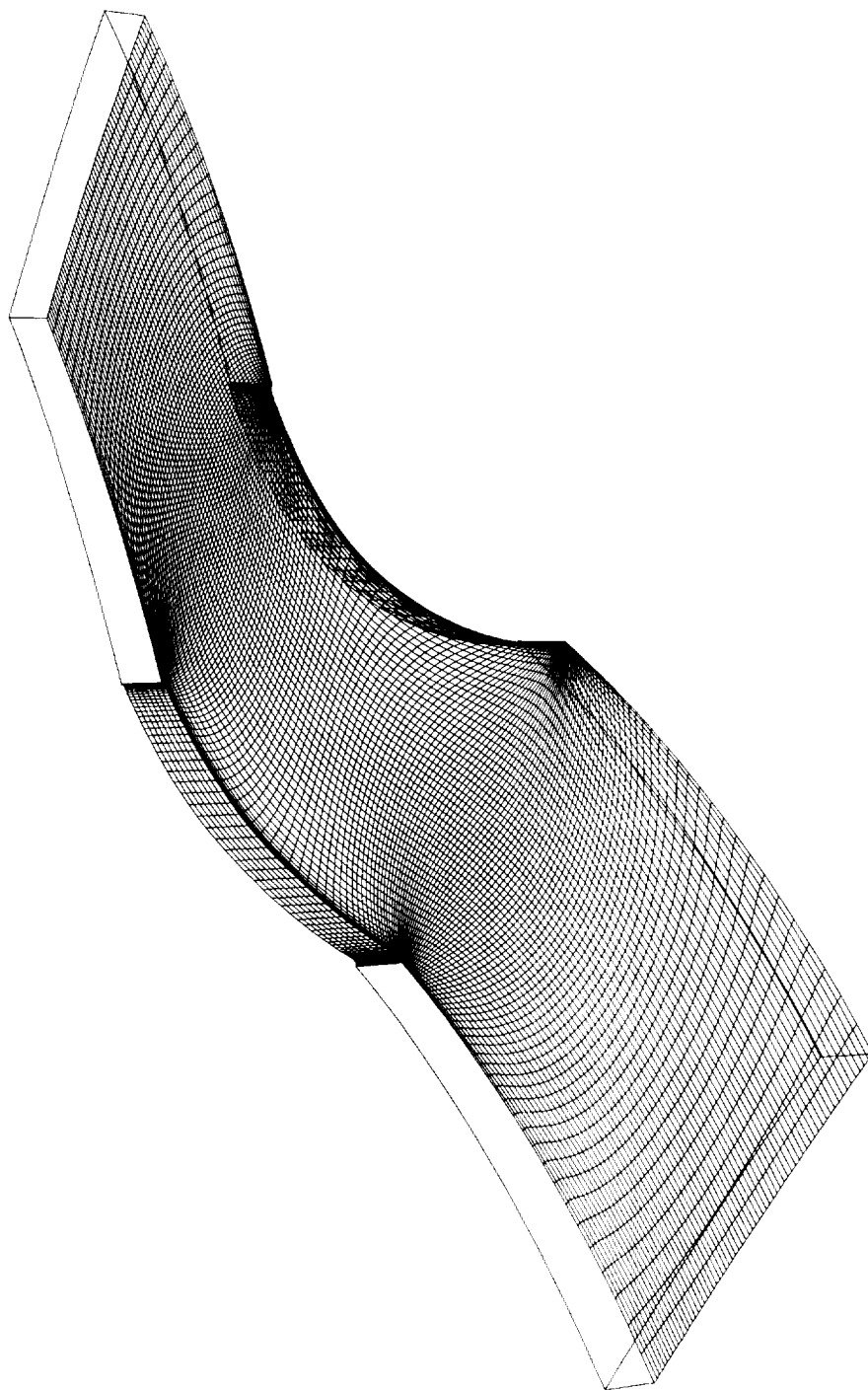


Figure 4.18: Pictorial representation of the 3-D annular slice taken from the stator midspan.

models on the wake prediction capability of *ADPAC*, all the results comparing near-wall spacing differences will be focused in the wake region. Figure 4.19 shows contours of axial velocity through the stator midspan section. Both solutions shown in the figures were collected using the tightest mesh spacing ($0.05x$) with 121 points in the circumferential direction. In the inter-blade region, the contour levels appear to be similar between the two solutions; however, in the wake region, some significant differences can be seen. The Spalart-Allmaras solution shows a larger velocity deficit immediately behind the stator blade which continually decreases as the wake propagates downstream. Whereas, the Baldwin-Lomax solution shows a wake pattern that decays only until approximately 0.25 chords downstream of the trailing edge and then remains constant, merely convecting downstream as reflected in the parallel contour lines exiting the mesh domain.

Comparisons can also be made between the pitchwise velocity distributions at various stations downstream of the stator blade. Figures 4.20 and 4.21 show these distributions for the various near-wall spacings analyzed for the 65-point mesh series and 121-point mesh series, respectively. Axial velocity distribution cross-sections were taken at 10%, 25%, 50%, and 75%-chord downstream of the stator trailing edge. The $2x$ mesh spacing was not analyzed in the 121-point series due to its similarity to the $1x$ case in the 65-point series. The discussion of the near-wall spacing results will be limited to the 121-point mesh series due to the similarity of the trends with the 65-point series. This discussion is followed by a comparison between the 65-point and 121-point mesh solutions collected using the finest near-wall spacing.

As was noted in the contour plots above, probably the most striking difference between the two turbulence models is the difference in the level of the velocity deficit immediately behind the stator blade. At $x/c = 1.10$ in (top plot in Figure 4.21), the velocity deficit predicted with the Spalart-Allmaras model is approximately 40% larger than the deficit predicted using the Baldwin-Lomax model on the finest near-wall spacing ($0.05x$). The Spalart-Allmaras wake prediction of the velocity deficit decays further downstream, while the wake shape predicted by the Baldwin-Lomax model essentially has the same shape from $x/c = 1.25$ on downstream. At $x/c = 1.75$, the Spalart-Allmaras wake shape has decayed approximately to the same size as the quasi-constant downstream wake shape predicted using Baldwin-Lomax model.

With respect to near-wall spacing, as the spacing is decreased two primary effects can be seen on the wake shape regardless of turbulence model used: the width of the wake increases and the exit flow angle of the stator cascade is altered slightly (reflected in the shift of wake centerlines). These two effects may be directly related to the predicted size of the suction-side boundary layer which is tied to near-wall spacing. As the boundary layer is resolved better with decreasing near-wall spacing, the suction-side boundary layer spreads out while the pressure-side boundary layer remains constant in size. This is shown in the wake velocity plots as the predicted results of pressure-side of the wake (left-hand side of the wake deficit bucket) pretty much lie on top of one another at the $x/c = 1.10$ location, while the suction-side of the wake predictions (right-hand side of the wake deficit bucket) expand in circumferential size. This growth in suction-side boundary layer size as the near-wall resolution is increased also shifts the exit velocity "upwards" with respect to the contour plots presented earlier in Figure 4.19; that is, a thicker suction-side boundary layer results in less turning by the vane. Changes in the exit velocity flow angle account for the shift in wake centerline location, which is then amplified further as the wake

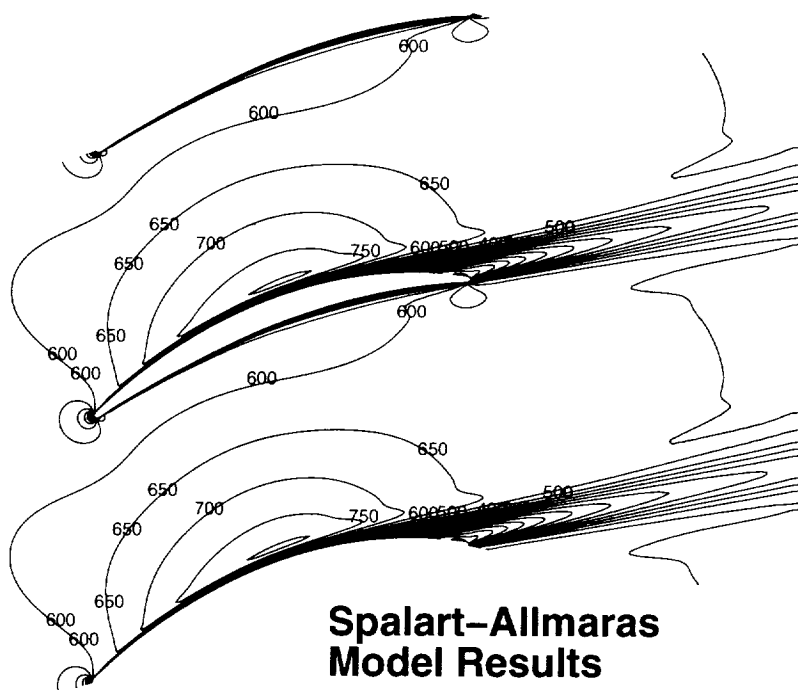
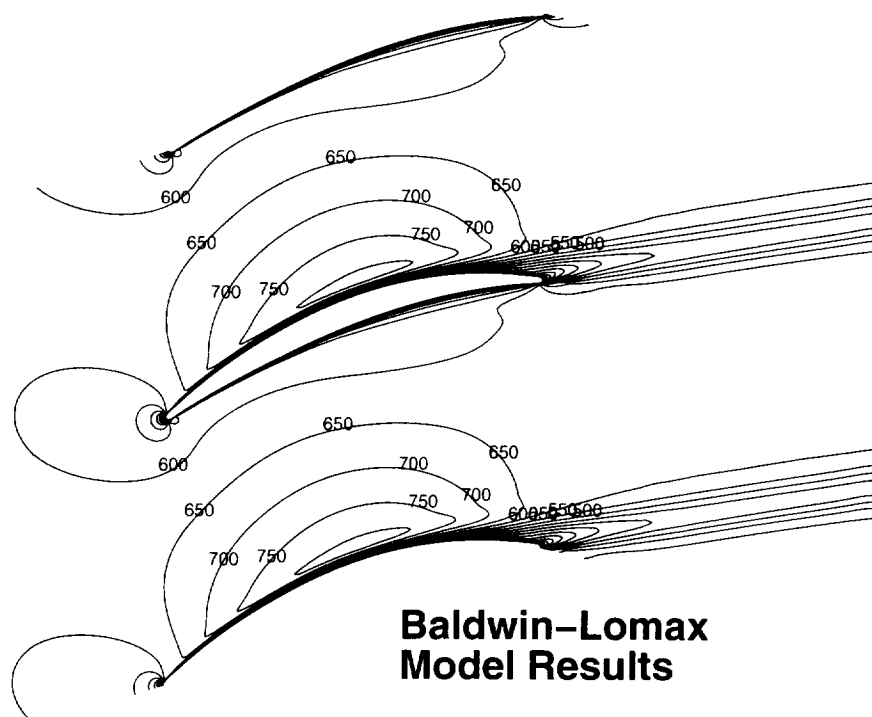


Figure 4.19: Comparison of axial velocity [ft/s] contours for the midspan stator case on the 0.05x-spacing mesh using the Baldwin-Lomax turbulence model and Spalart-Allmaras turbulence model.

travels downstream.

Figure 4.22 compares wake shapes from the 65-point series and the 121-point series on the tightest near-wall spacing mesh (0.05x). No significant differences are initially obvious. At the closest data station to the stator blade ($x/c = 1.10$), the Spalart-Allmaras predicted wake deficit is slightly deeper using 121 points; however, this is due to better resolution in the limited region when the wake is very narrow. Downstream this difference is unnoticeable from $x/c = 1.25$ onward. In the Baldwin-Lomax solutions when more points are used circumferentially (121), it appears the wake decays even less, as seen at $x/c = 1.75$ for example, before reaching its quasi-constant shape which convects unchanged downstream.

The wake shape can be described by two parameters: the wake width at half-height normalized by blade pitch (δ/P) and the velocity deficit magnitude normalized by the maximum velocity (V_{dc}/V_{max}). Figures 4.23 and 4.24 shows curves of these parameters taken from the 121-point mesh series for the Baldwin-Lomax and Spalart-Allmaras turbulence models, respectively. From these figures, the two finest meshes (0.2x and 0.05x) appear to approximate the same solution for the wake deficit parameter. With respect to the wake width, the rate of decay appears to be the same for all mesh spacing shown; however, the initial predicted wake width at the trailing edge ($x/c = 1.00$) increased in size with *decreasing* near-wall spacing. Granted that the solution may still be changing slightly when the near-wall spacing is decreased beyond the 0.2x level, the slight gains made in the predicted solution may not offset the need for more mesh points near the airfoil resulting in longer solution run times.

Several of the differences between the wake predictions of the two turbulence models mentioned previously can be summarized quantitatively in Figure 4.25. Figure 4.25 shows a comparison of the wake shape parameters between the two different turbulence models taken from *ADPAC* solutions solved on the finest mesh (0.05x). The bold lines in the figure represent results from the 121-point mesh series and the thinner lines are results from the 65-point series. The most significant difference between the two turbulence model predictions is the decay rate of the velocity deficit. The Baldwin-Lomax predicted wake deficit decays very quickly and reaches a plateau of approximately 0.30 at a location of $x/c = 1.35$. As noted above, this deficit level remains constant and the wake will continue to propagate downstream without significantly decaying any further. In contrast, the Spalart-Allmaras model predicted wake deficit decreases at a slower rate and appears to continue to decay as the wake exits the mesh domain. This trend is also apparent in the top plot of wake width; the Baldwin-Lomax prediction has reached a level value of wake width, while the Spalart-Allmaras model is still allowing for the wake to mix out and widen.

The differences shown in Figure 4.25 due to the number of circumferential points (65 or 121) appear to have a greater impact on the Baldwin-Lomax model than on the Spalart-Allmaras model, primarily related to wake width prediction. From these results, it can be justified that when using the one-equation Spalart-Allmaras turbulence model 65 points should be adequate mesh resolution to describe the wake decay without adding considerably to the analysis run time. With respect to near-wall spacing, it appears that for spacing-independent results all of the cell centers next to a viscous surface should be located within a y^+ value of approximately five ($y^+ \leq 5$).

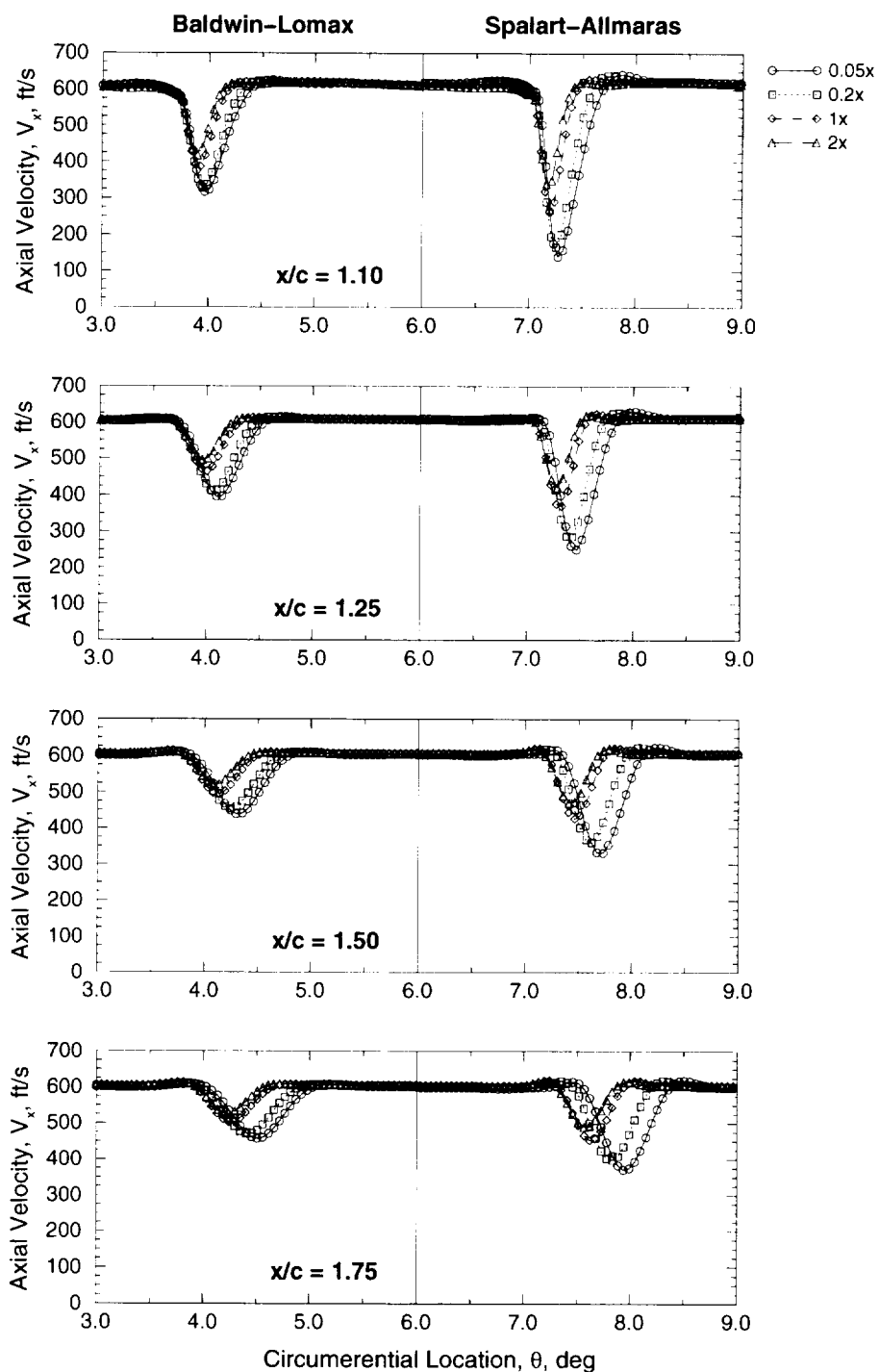


Figure 4.20: Pitchwise distributions of axial velocity on the 65-point mesh series at four downstream locations showing the effects of near-wall spacing and selection of turbulence model on the wake deficit shape.

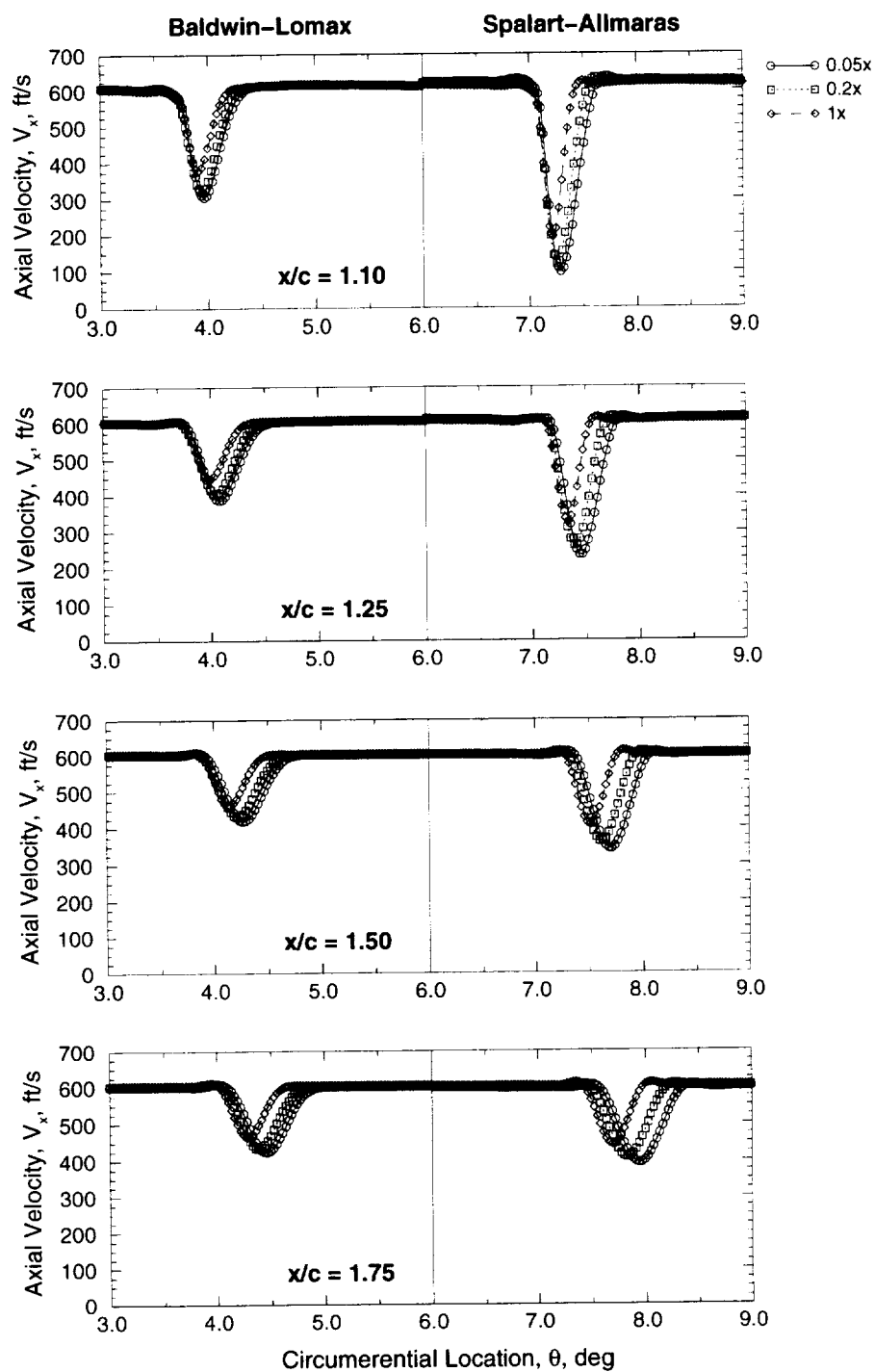


Figure 4.21: Pitchwise distributions of axial velocity on the 121-point mesh series at four downstream locations showing the effects of near-wall spacing and the selection of turbulence model on the wake deficit shape.

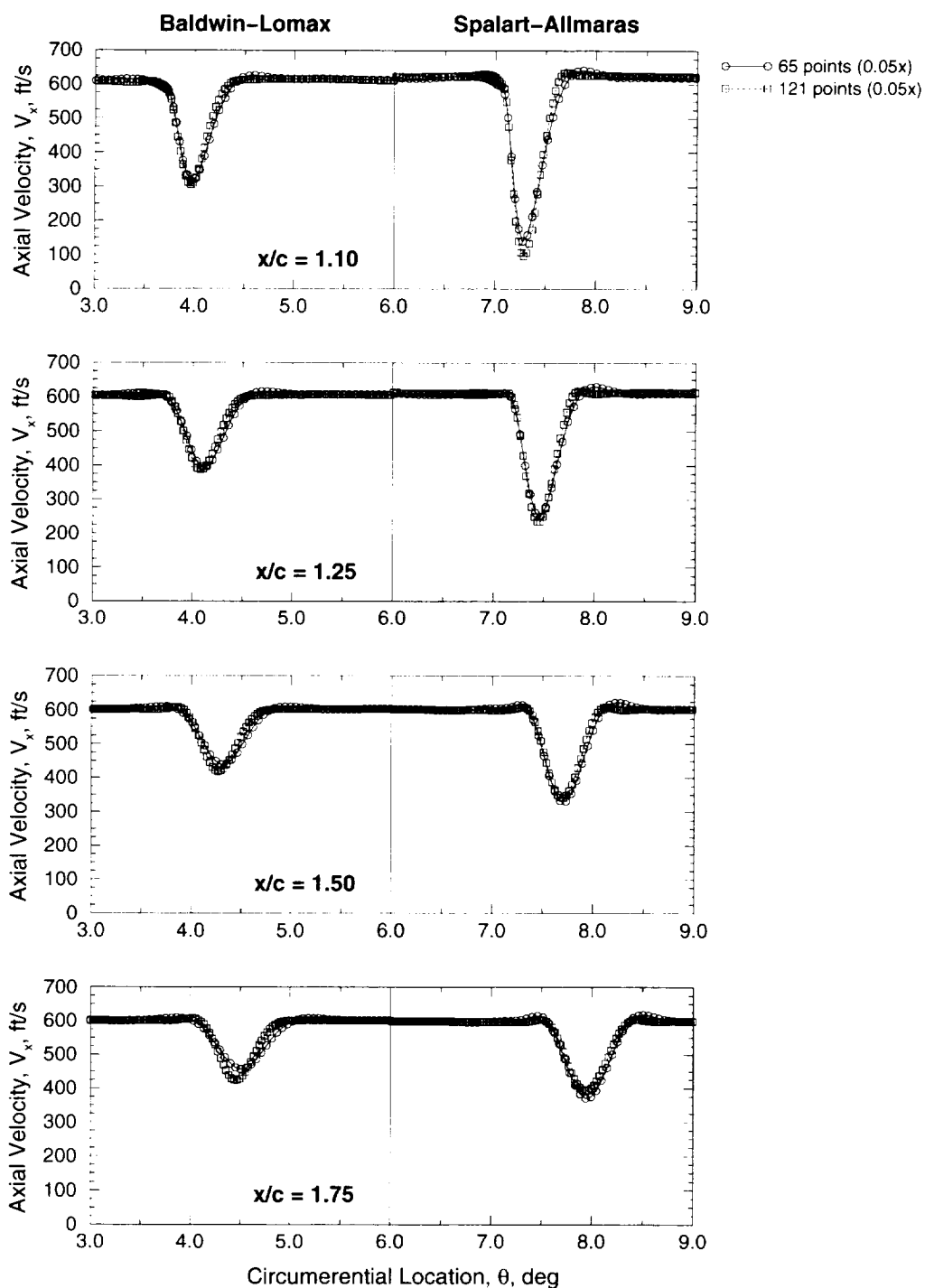


Figure 4.22: Pitchwise distributions of axial velocity at four downstream locations showing the effects of the number of circumferential points (65 or 121) and the selection of turbulence model on the wake deficit shape.

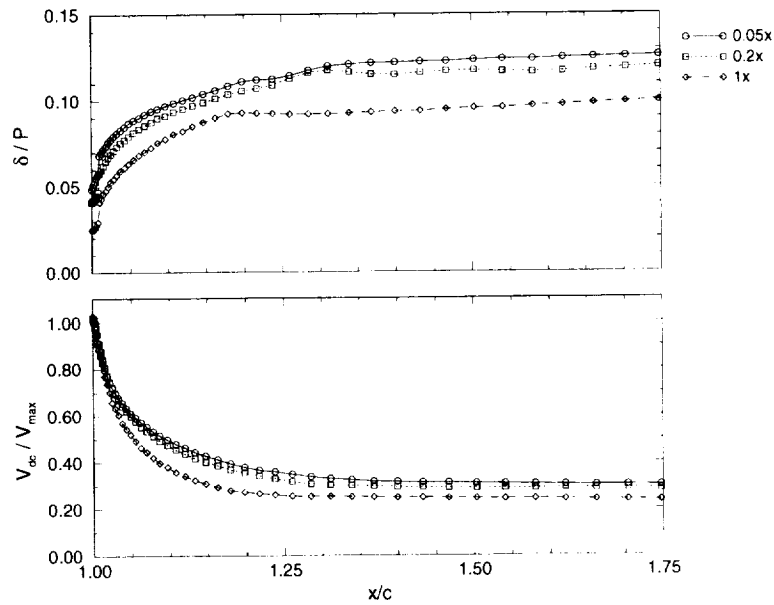


Figure 4.23: Prediction of wake decay in terms of wake width (δ/P) and centerline velocity deficit (V_{dc}/V_{max}), showing the effects of near-wall spacing using the Baldwin-Lomax turbulence model on the 121-point mesh series.

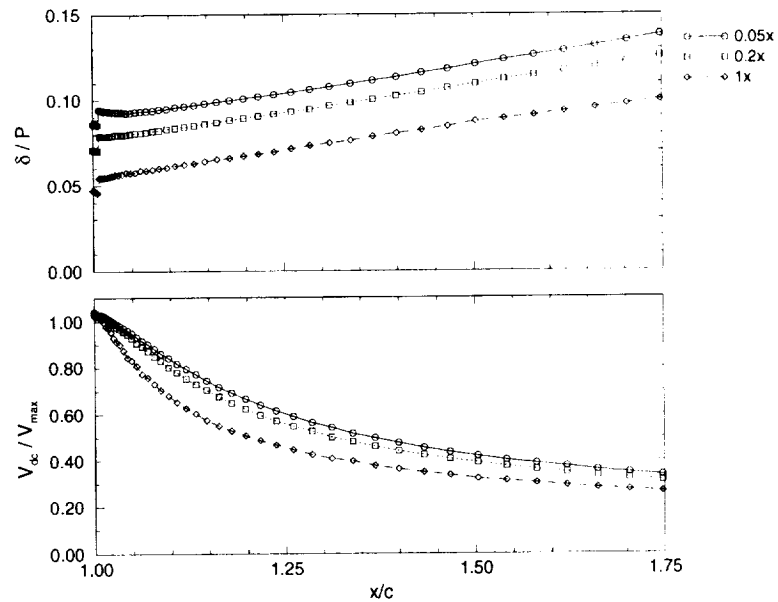


Figure 4.24: Prediction of wake decay in terms of wake width (δ/P) and centerline velocity deficit (V_{dc}/V_{max}), showing the effects of near-wall spacing using the Spalart-Allmaras turbulence model on the 121-point mesh series.

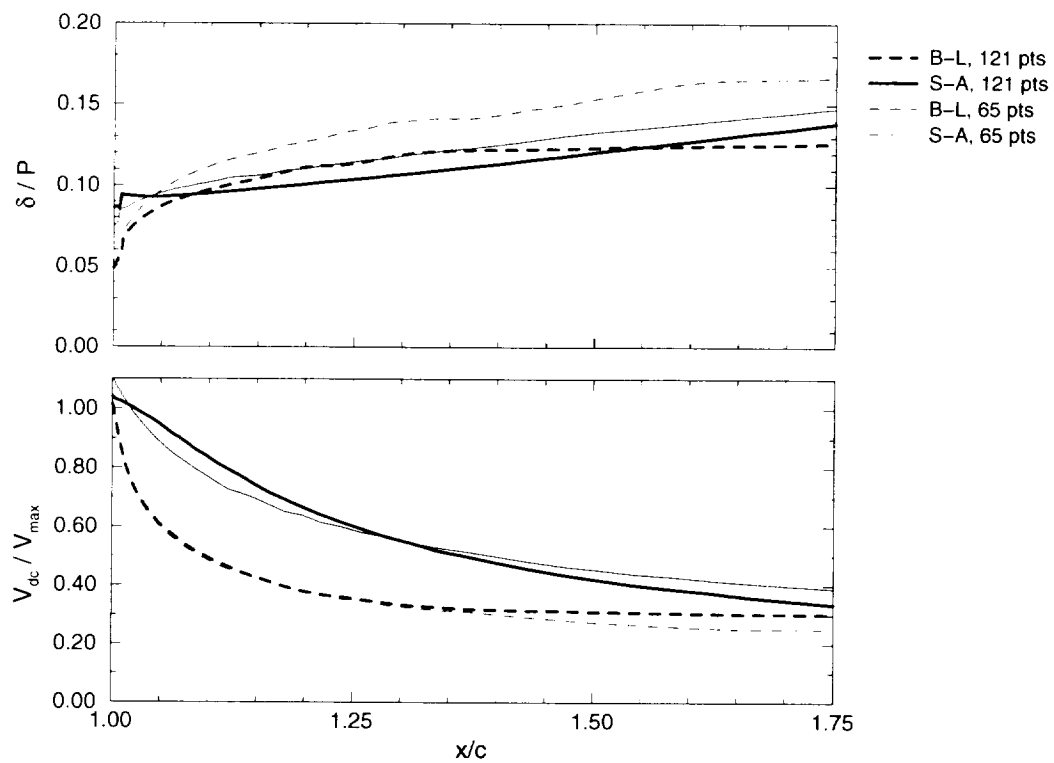


Figure 4.25: Prediction of wake decay in terms of wake width (δ/P) and centerline velocity deficit (V_{dc}/V_{max}), showing a comparison between the two turbulence models used and the effect of circumferential point density (65 or 121).

Chapter 5

TURBULENCE MODEL EFFECTS ON WAKE PREDICTION

5.1 Introduction

One of the advantages to using CFD prediction codes to analyze turbomachinery is the capability to test many different geometric and aerodynamic configurations relatively quickly. If the numerical models in these aerodynamic codes are proven accurate enough, more detailed data beyond the basic fan blade performance numbers can be derived from the numerical simulations. Part of this additional data is the wake definition as it travels downstream through the bypass duct of a turbofan engine. By accurately predicting the shape of the fan rotor wakes, predictions can be made of the level of the acoustic signature of the engine. This chapter addresses the effects of different turbulence models on the prediction of the wake definition. The fan blade configuration and experimental data are briefly described followed by a section on the mesh generation used in the numerical simulations. Results from the *ADPAC* solutions are presented both in terms of overall fan performance and a more detailed section over the wake region definition. The chapter concludes with a section on wake correlations and similarity profiles of the wakes.

5.2 Geometry Definition

The geometry model used in this numerical study was the Allison/NASA Low Noise Fan (LNF). The Low Noise Fan is a low tip speed, moderate pressure rise fan stage designed specifically for the demonstration of noise reduction concepts [33]. The 18-bladed fan rotor is a fixed-pitch configuration providing a pressure ratio of 1.378 at the design point with a mass flow of approximately 103 lbm/s. The fan blade has a diameter of 22 inches with a 0.30 hub-to-tip ratio and a 100% design rotational speed of 10417.4 RPM resulting in a tip speed of 1000 ft/s. Figure 5.1 displays the LNF rig in the NASA testing facility. The drawing in Figure 5.2 shows a meridional view of the Low Noise Fan and was used as reference for the definition of the hub and casing flowpaths.

In order to match the experimental data, the upstream inlet flowpath was modeled after the experimental rig. After receiving geometry definitions for the bellmouth from

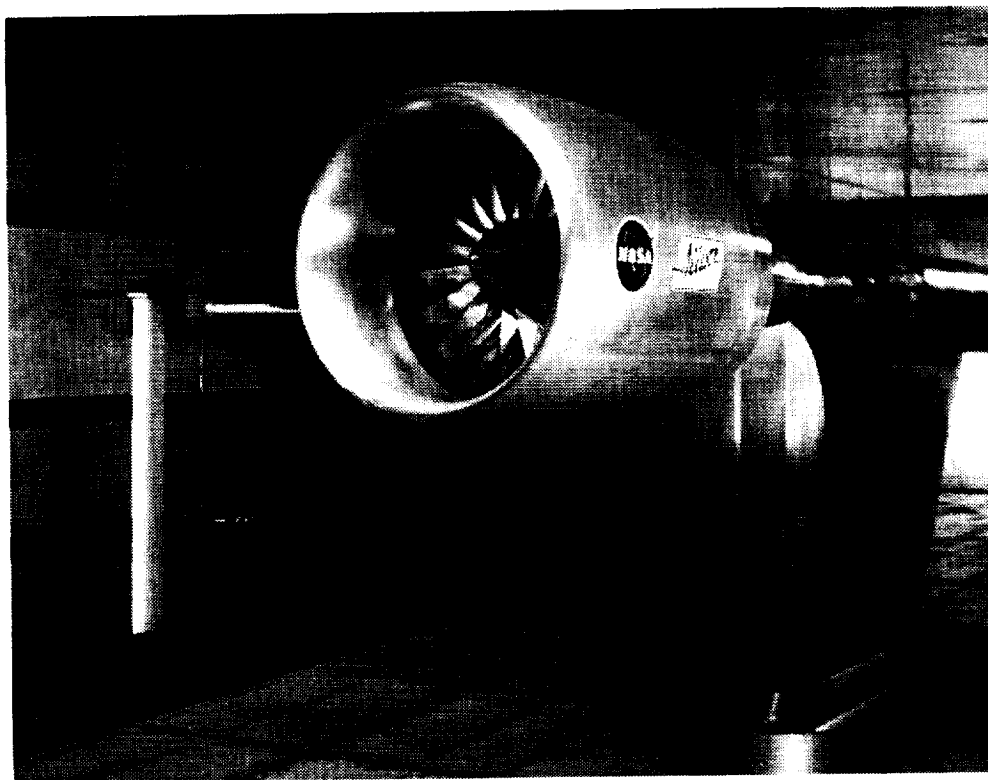


Figure 5.1: Photograph of Low Noise Fan test rig installed in the NASA Lewis Low-Speed Wind Tunnel.

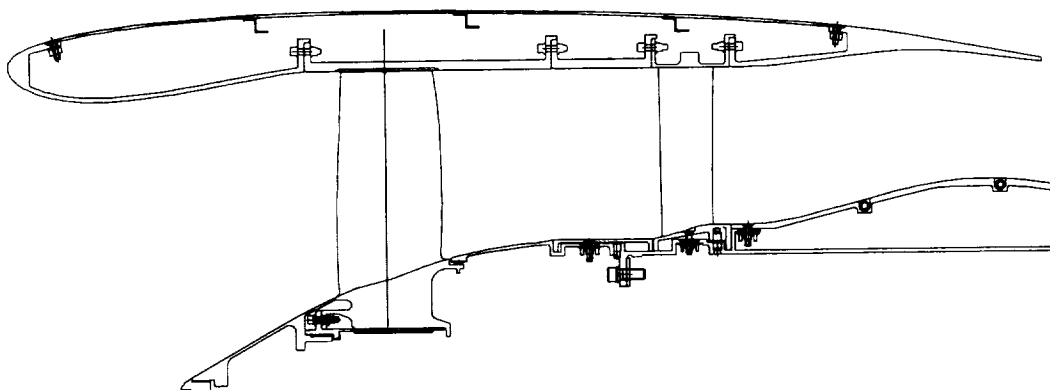


Figure 5.2: Diagram of the low-noise fan rotor in the translated bypass vane configuration.

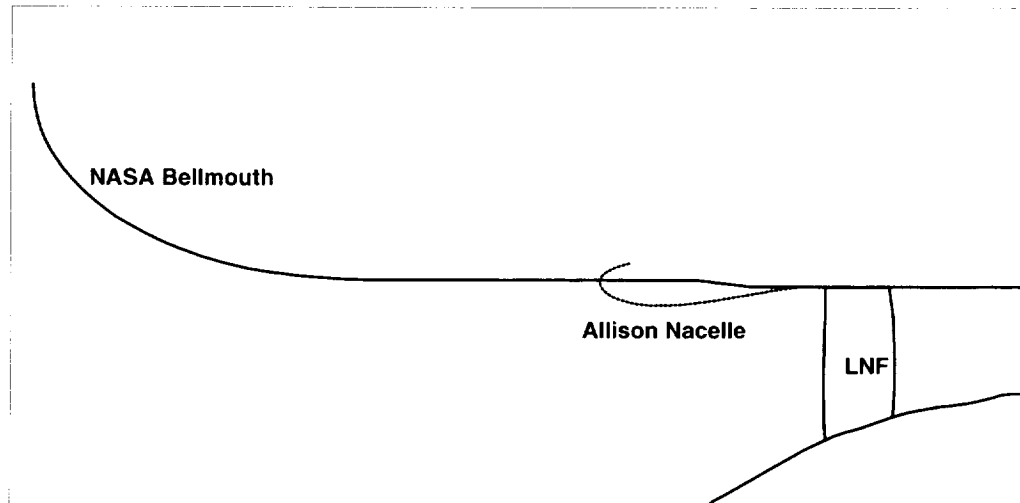


Figure 5.3: Meridional outlines of the two different inlet flowpaths used with the the low-noise fan rotor: the Allison nacelle and the NASA experimental bellmouth.

NASA and the coupling ring from Allison, a completed outer flowpath definition shown in Figure 5.3 was determined. Also shown as a dashed line in Figure 5.3 is the geometry definition of the nacelle for the low-noise fan assembly.

5.3 Experimental Data

As part of the larger Low Noise Fan effort, experimental tests were performed under a variety of conditions and geometric configurations [34]. In addition to overall performance measurements, detailed flow velocity measurement were obtained using laser Doppler velocimetry (LDV) equipment. The LDV data were collected at an off-design point where the mass flow through the fan was 92.5 lbm/s. These data were forwarded to the authors from NASA Lewis Research Center in *PLOT3D* format to be used in evaluating the wake prediction capability of *ADPAC*.

Figure 5.4 shows the downstream measuring planes from which data are presented. The three measuring stations used during the NASA LDV experiment are shown as solid black lines and labeled as Stations 1, 2, and 3. Station 1 is located 1.2 inches downstream of the tip trailing edge, Station 2 is 2.7 inches downstream, and Station 3 is 3.4 inches downstream. Numerical data was interpolated from the *ADPAC* solutions to the same axial locations for comparison. The single dashed line identifies the fan exit location (**E**) from which the blade performance was calculated, the spanwise exit profiles extracted, and the sample mesh cross-section generated (see Figure 5.10). This axial plane was chosen from a grid convenience perspective. To give an example of the resolution of the LDV measurements, Figure 5.5 shows the radial and tangential LDV measurement locations at Station 1. This matrix of measurements contains 28 radial locations and 51 tangential locations, and it is very typical of Stations 2 and 3. The high density in the tangential direction is extremely useful when defining wake profiles. Due to experimental

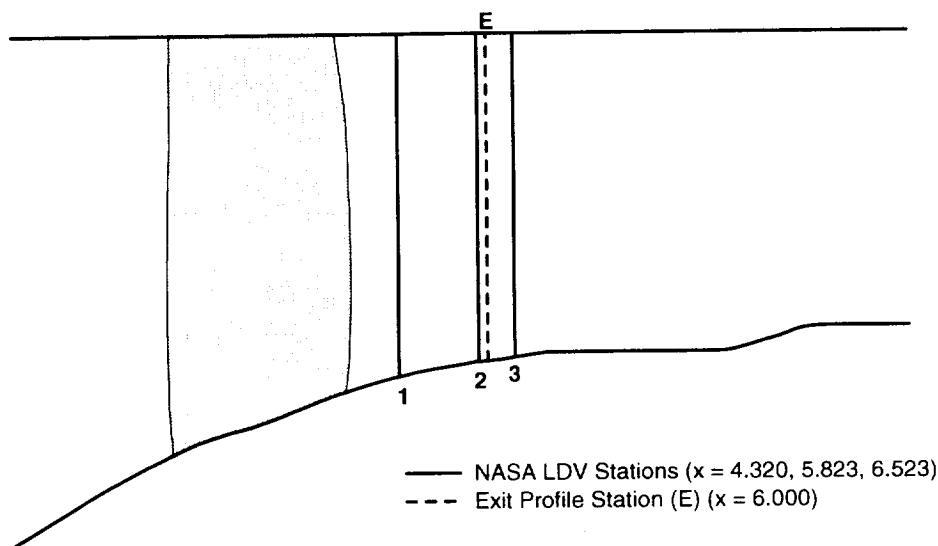


Figure 5.4: Meridional view of the LNF blade showing the axial locations of the downstream measuring stations including the three NASA experimental test stations.

limitations, the lowest radial line occurs at approximately 4.3% span and the upper-most at 98.6% span.

5.4 Grid Generation

A single-block H-grid through the fan rotor was selected as the mesh topology to be used for the turbulence model comparison. This simple meshing structure was chosen to help identify and solve possible difficulties and/or development issues with the implementation of the one-equation Spalart-Allmaras turbulence model. Even though all the LNF results presented in this report are from H-grid mesh topologies, the one-equation turbulence model has been successfully used on a variety of mesh combinations, including O-grid and C-grid topologies. A second H-grid was also used to model the tip clearance region on top of the fan rotor. This clearance was modeled at the design value of 0.020"; however, the experimental rig was run at a much tighter clearance.

The downstream boundary of the mesh was extended several chords downstream of the fan rotor, past the location of the bypass vane installation. The hub flowpath definition used for the H-grid was taken from the vane configuration shown in Figure 5.2 since that was the configuration run when the LDV data was taken. The meridional distribution of the mesh points along the blade surface slice is shown in Figure 5.6.

Several different grid resolutions were used during the grid generation process. All of the meshes had 161 points in the axial direction (including 65 points along the blade chordwise) and 53 points radially (including 5 points in the tip clearance). The number of circumferential mesh points was increased from 49 to 65 and finally to 97 in order to adequately resolve the wake definition and to provide sufficient near-wall spacing for the Spalart-Allmaras model without excessively increasing the cell expansion ratios. The total

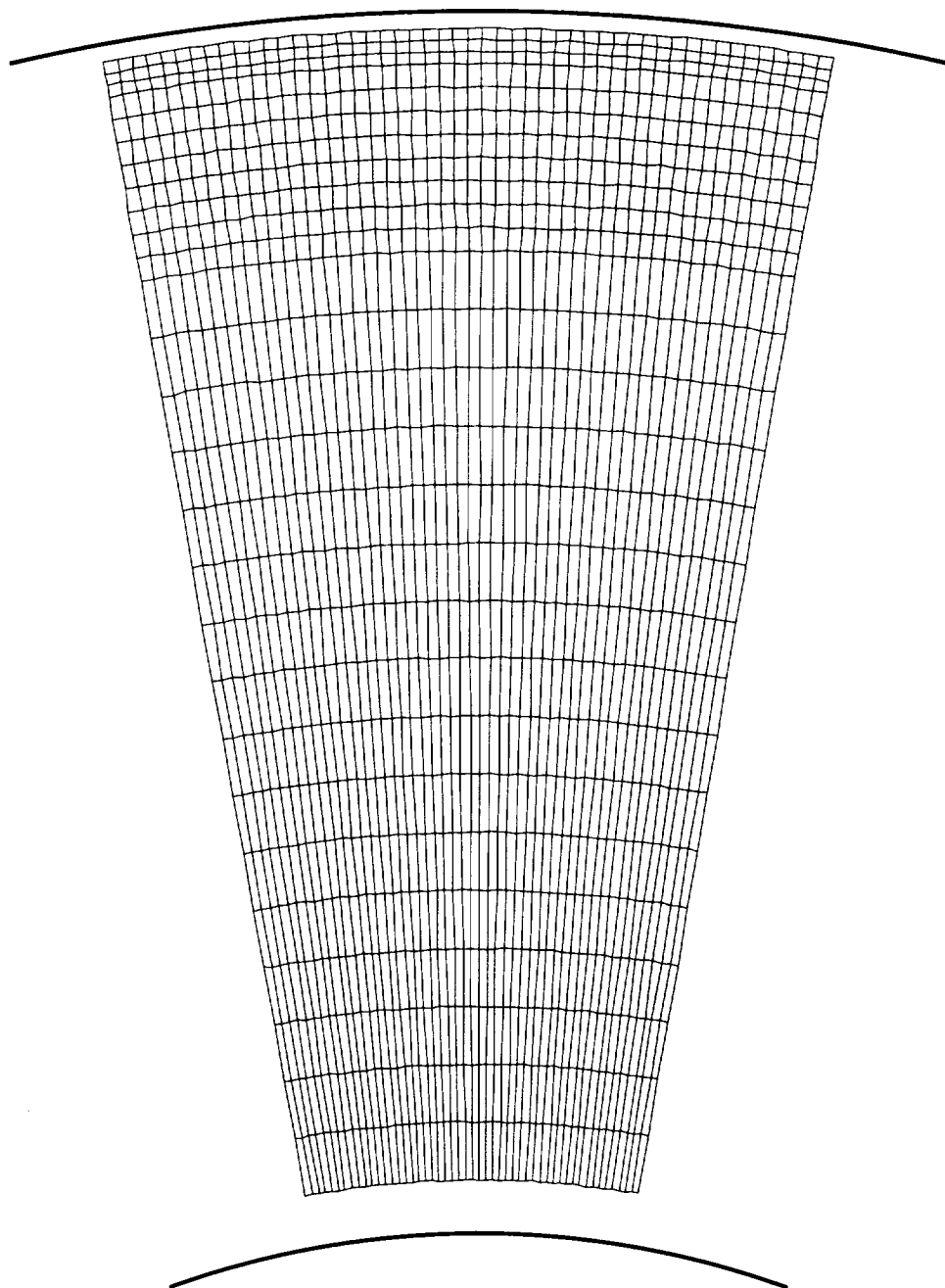


Figure 5.5: Radial and tangential location of LDV experimental data points at Station 1 (bold lines represent the actual flowpath radii).

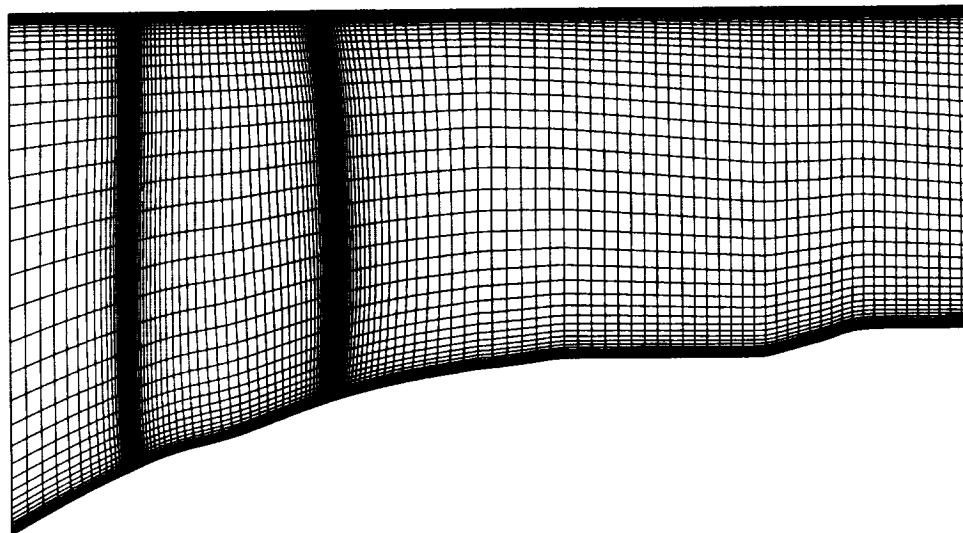


Figure 5.6: Meridional grid plane showing mesh points along the blade surface and upstream and downstream H-grid extents.

number of mesh points including the tip clearance grid block was 831,926 points; all of the *ADPAC* results for the LNF presented in this report were collected using this mesh.

The near-wall spacing was constrained to 0.0003 inches along the blade surfaces which resulted in the near-wall y^+ distributions shown in Figure 5.7. The vast majority of the y^+ values are well under 5, only points along the leading edge where the boundary layer is essentially non-existent do the y^+ values creep slightly above 5. From the results of the near-wall spacing study presented in the previous chapter, this mesh resolution should be adequate to ensure a grid-independent solution with the Spalart-Allmaras turbulence model.

As shown in a midspan distribution of mesh points (Figure 5.8), the circumferential points along a constant axial grid index do *not* all share the same physical axial location (e.g., the grid lines “bow” out around the blade region). This mesh generation approach greatly reduces grid shear near the blade leading and trailing edges as shown in Figure 5.9. An axial cross-section from the mesh is shown in Figure 5.10; the location of the cross-section is downstream of the fan blade and corresponds to the location from which the spanwise exit profiles were calculated.

5.5 Predicted Fan Performance

Using the H-grid described above, converged *ADPAC* solutions were collected using the algebraic Baldwin-Lomax turbulence model with two sets of coefficients and the one-equation Spalart-Allmaras turbulence model. As described in the previous chapter about the turbulence model details, the two sets of Baldwin-Lomax model coefficients used were for the standard case: $C_{cp} = 1.6$ and $C_{Kleb} = 0.3$ (identified as std. coeff.); and for the modified coefficients: $C_{cp} = 1.0$ and $C_{Kleb} = 0.64$ (identified as mod. coeff.).

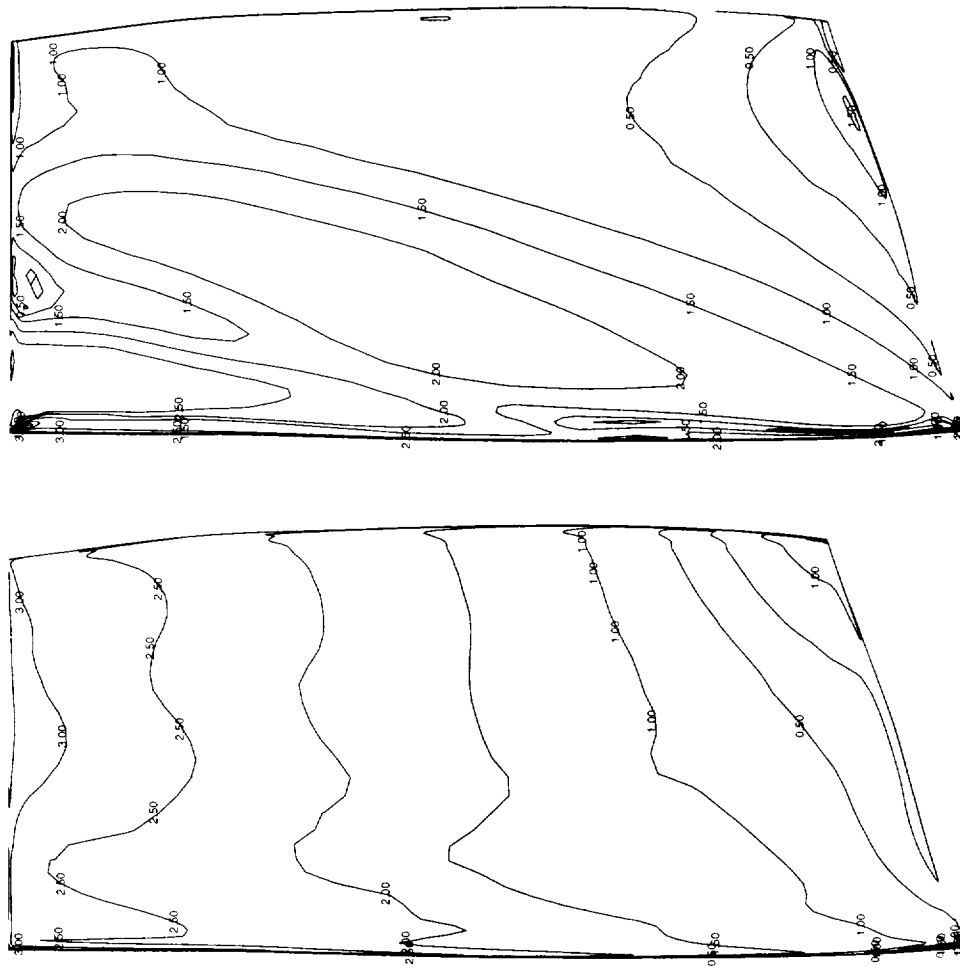


Figure 5.7: Contours of near-wall y^+ values for the Low Noise Fan blade pressure side (*left*) and suction side (*right*).

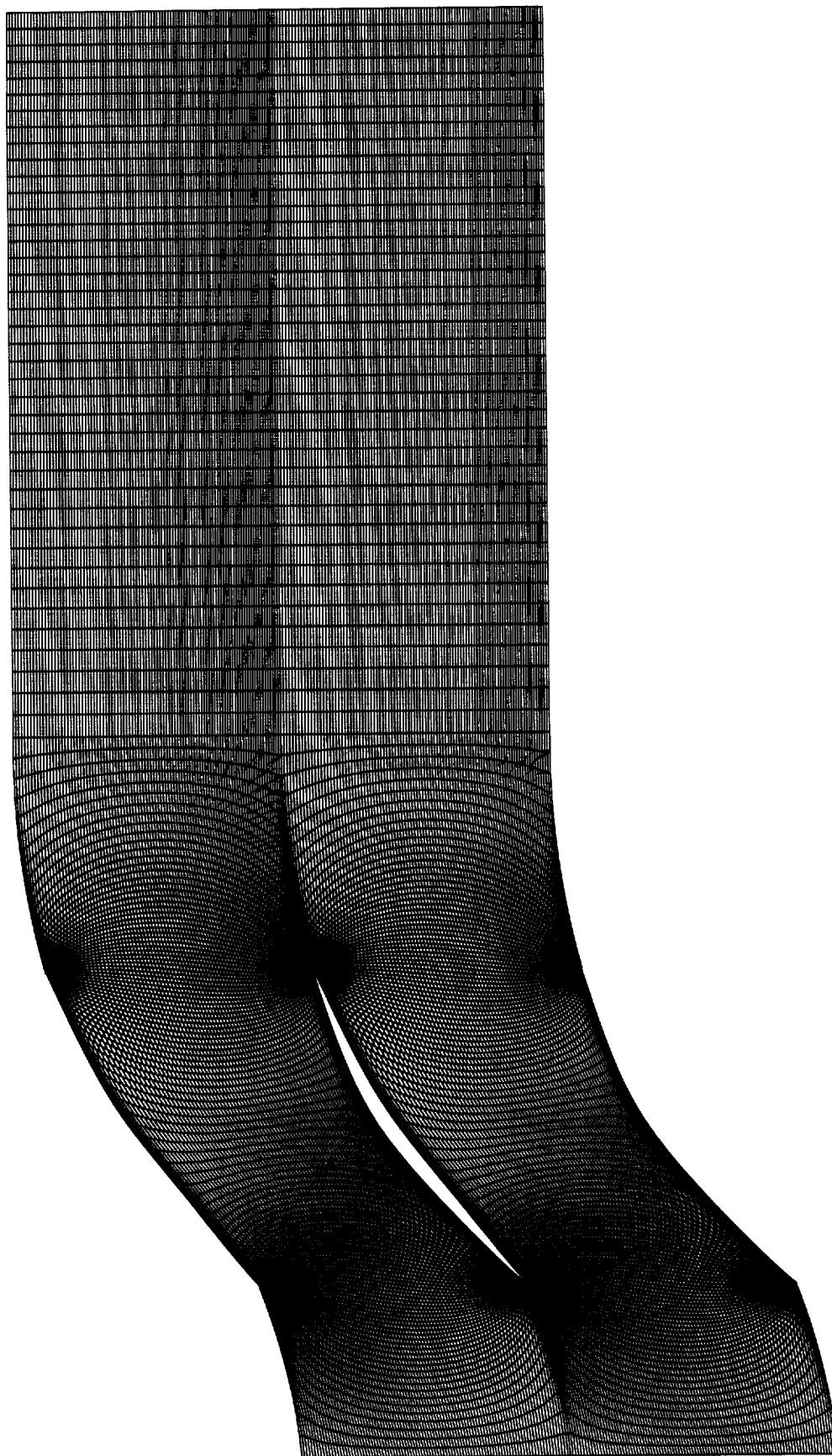


Figure 5.8: Midspan radial slice of the Low-Noise Fan mesh generated using a H-grid technique using 97 points across the blade pitch.

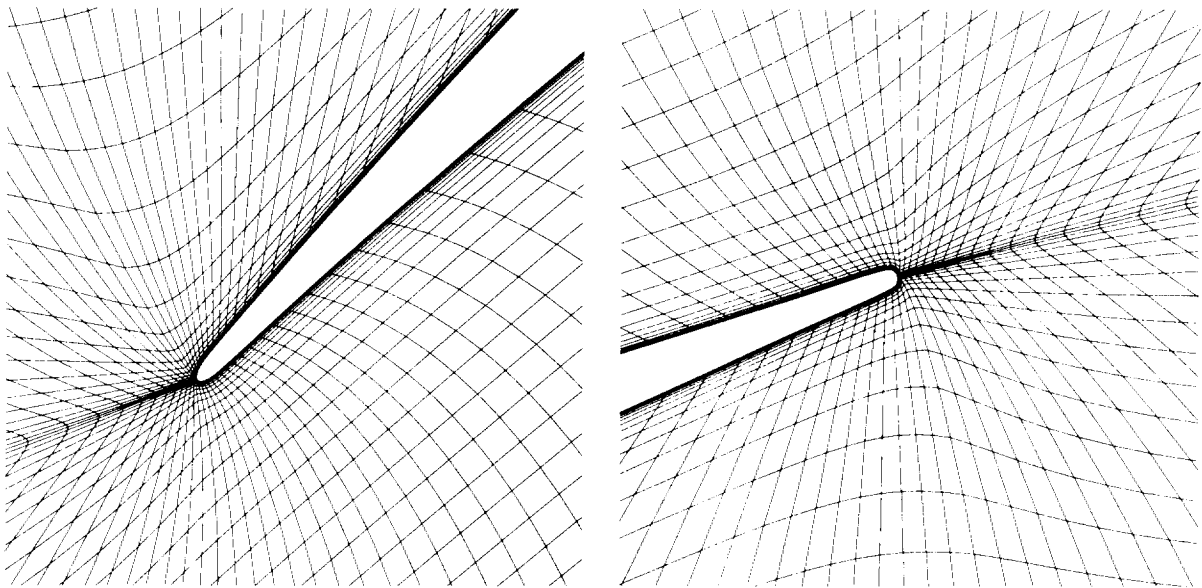


Figure 5.9: Close-up views of the midspan leading edge (*left*) and trailing edge (*right*) of the fan rotor showing the spreading of grid lines to reduce shear.

Figure 5.11 shows the total pressure ratio and efficiency calculated from each of the *ADPAC* solutions compared with the NASA experimental data. All the *ADPAC* solutions were calculated using a fixed mass flow exit boundary condition set at 92.5 lbm/s to match the flow conditions during the LDV wake data experiment. The blade performance was calculated across the mesh inlet plane and the downstream measuring station (identified as **E** in Figure 5.4).

The predicted pressure ratio and efficiency were both higher than the experimental data when the standard Baldwin-Lomax model coefficients were used. When the coefficients were modified to account for the adverse pressure gradient, the predicted pressure ratio was lowered slightly and the effect was mostly negligible with respect to lowering predicted efficiency. When the Spalart-Allmaras was used, the pressure ratio dropped further to just below 1.40, and the predicted efficiency was lowered closer to the experimental data.

5.5.1 Spanwise Exit Profiles

Spanwise exit profiles were calculated from the *ADPAC* solutions and are presented in Figures 5.12 through 5.16. The results from solutions collected with the standard Baldwin-Lomax coefficients are shown with a thin solid line, those using the modified coefficients are shown with by a dashed line, and those using the Spalart-Allmaras model are shown with a thick solid line.

As was reflected in the overall blade performance, the Spalart-Allmaras results of total pressure are lower across the span compared to the two Baldwin-Lomax solutions in Figure 5.12. Using the Spalart-Allmaras turbulence model, the small overshoot in total pressure, centered at approximately 2% span, was eliminated. No significant differences

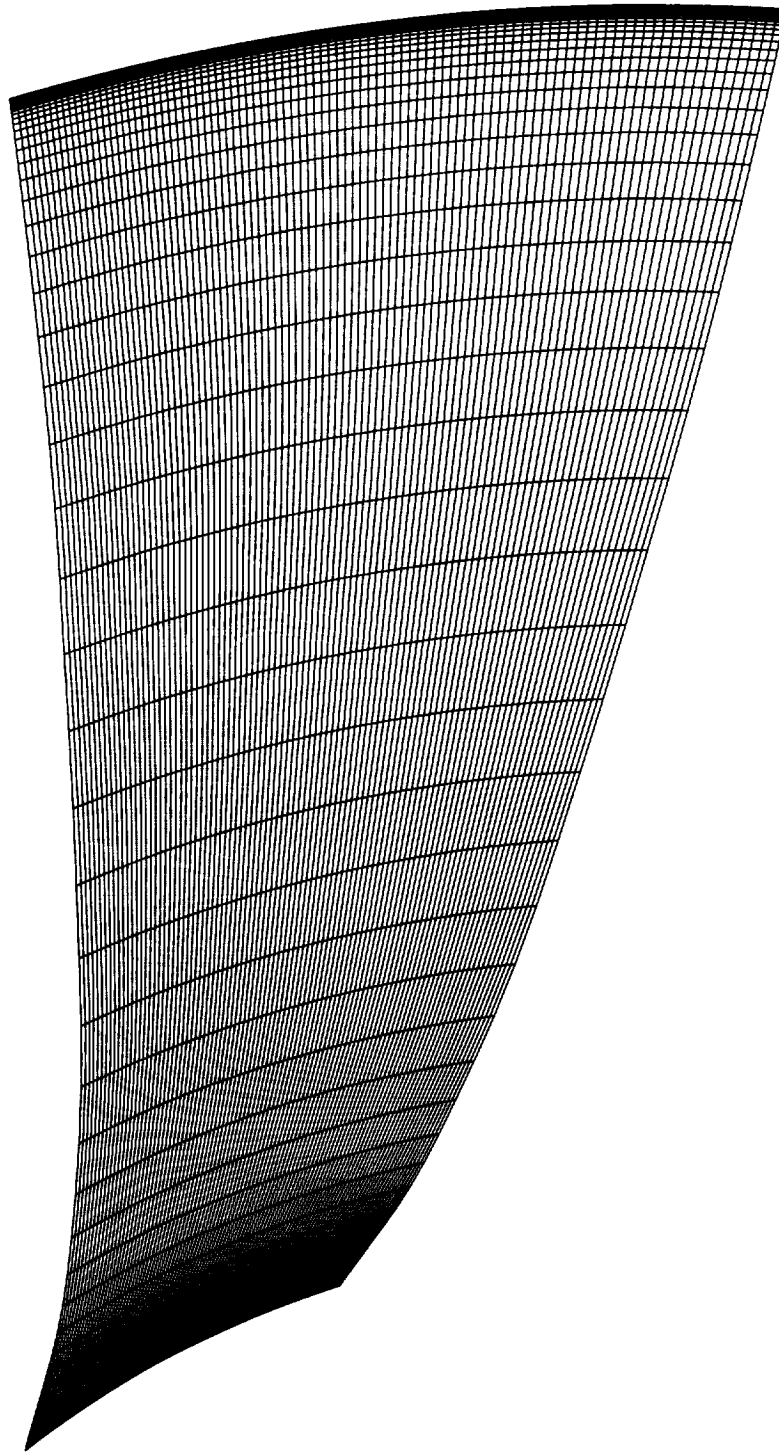


Figure 5.10: Axial cross-sections downstream of the fan blade showing the mesh resolution used to collect numerical *ADPAC* solutions.

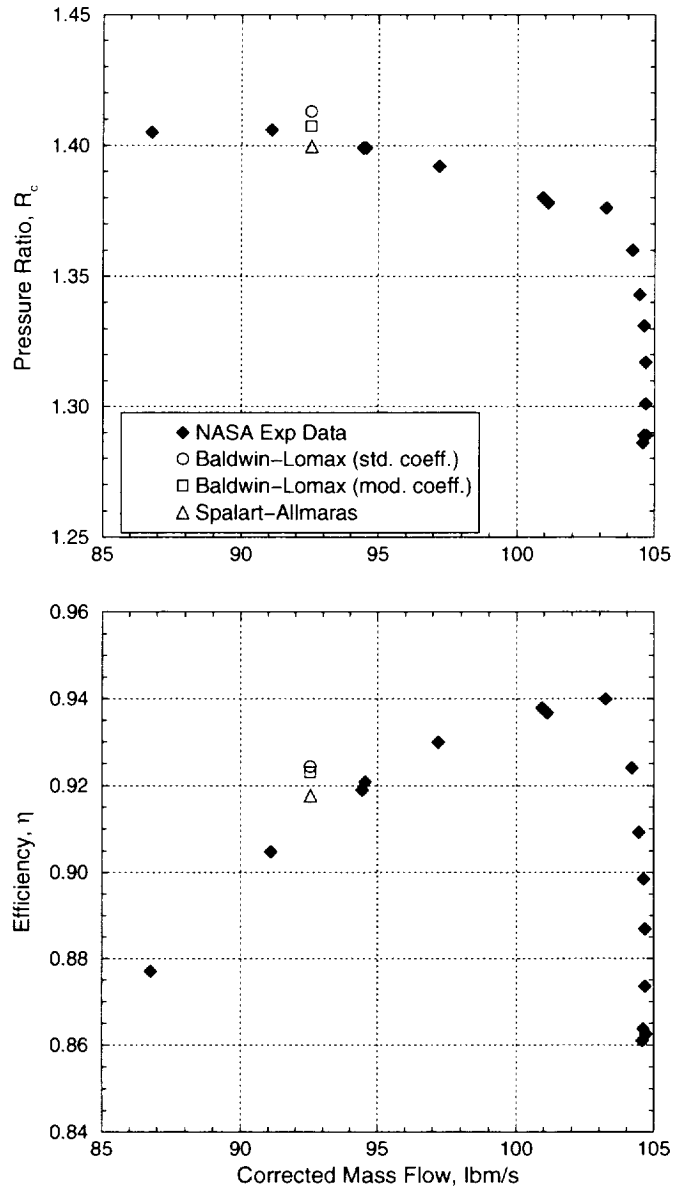


Figure 5.11: Performance map at 100% N_c constant speed for the LNF showing the impact of the turbulence model.

were noticed in the temperature distributions in Figure 5.13.

The profiles of axial and tangential velocities appeared to show the greatest impact in variation in turbulence model, as shown in Figure 5.14. Even though the *ADPAC* solutions were all run to a specified exit mass flow, there were small variations in density related to the pressure ratio variations between the three cases. While the axial velocity distributions appear to vary significantly between the three *ADPAC* solutions due to the expanded scale on the plot, the mass-averaged axial velocities at the exit plane only varied within 1% of each other. With the differences in both axial and tangential velocity, the mass-averaged absolute flow angle calculated at this downstream axial station varied between 39.07 degrees (B-L std), 38.55 degrees (B-L mod), and 38.30 (S-A). Figure 5.15 shows the distributions of radial velocity and absolute total velocity. By eliminating the overshoot near the hub in total pressure and axial velocity, the radial distribution of efficiency and loss coefficient become much more smoothly defined in the hub region, shown in Figure 5.16.

5.6 Predicted Wake Region Comparison

5.6.1 Pitchwise Velocity Profiles

The experimental LDV data from the NASA rig test were compared with the *ADPAC* solutions for the fan rotor at 100% corrected speed. The measurement of the wake (axial velocity deficit) was compared at five radial stations at three different axial stations downstream of the fan rotor shown schematically in Figure 5.17. The *ADPAC* numerical solutions were interpolated to match the locations at which the experimental data were measured (e.g., no interpolation was done to the LDV data). Radial slices were extracted at the experimental radial measuring stations closest to 10%, 25%, 50%, 75% and 90% span. The exact radial location of each slice is listed on the plots.

In order to align the numerical and experimental profiles in the circumferential direction, the tangential location of the axial velocity deficit centerlines taken at Station 1 along the 50% radial span from the Baldwin-Lomax (std. coeff.) case was matched to the corresponding experimental LDV wake centerline. This tangential shift was then applied to *all* other numerical profiles. The *ADPAC* profiles were also mirrored in the circumferential direction to account for the difference in rotation direction between the experimental rig and numerical results. Profiles of axial velocity are shown in Figures 5.18, 5.19, and 5.20, for the three measuring stations, respectively.

In general, the *ADPAC* results matched fairly well with the majority of experimental results; however, some significant differences between the *ADPAC* results and the experimental data and between the different *ADPAC* turbulence model results exist. In the Station 1 midspan region shown in middle three plots of Figure 5.18, the *ADPAC* results are closely aligned with each other and the data. The predicted results show a larger velocity deficit than is shown in the experimental data; this is especially apparent at the 90% span location. At this radial location, the three *ADPAC* results also predict a wider wake region. The pressure-side of the predicted wake appears to align circumferentially with the experimental data, but the larger wake deficit pushes the suction-side of the wake off (to the left) the experimental data.

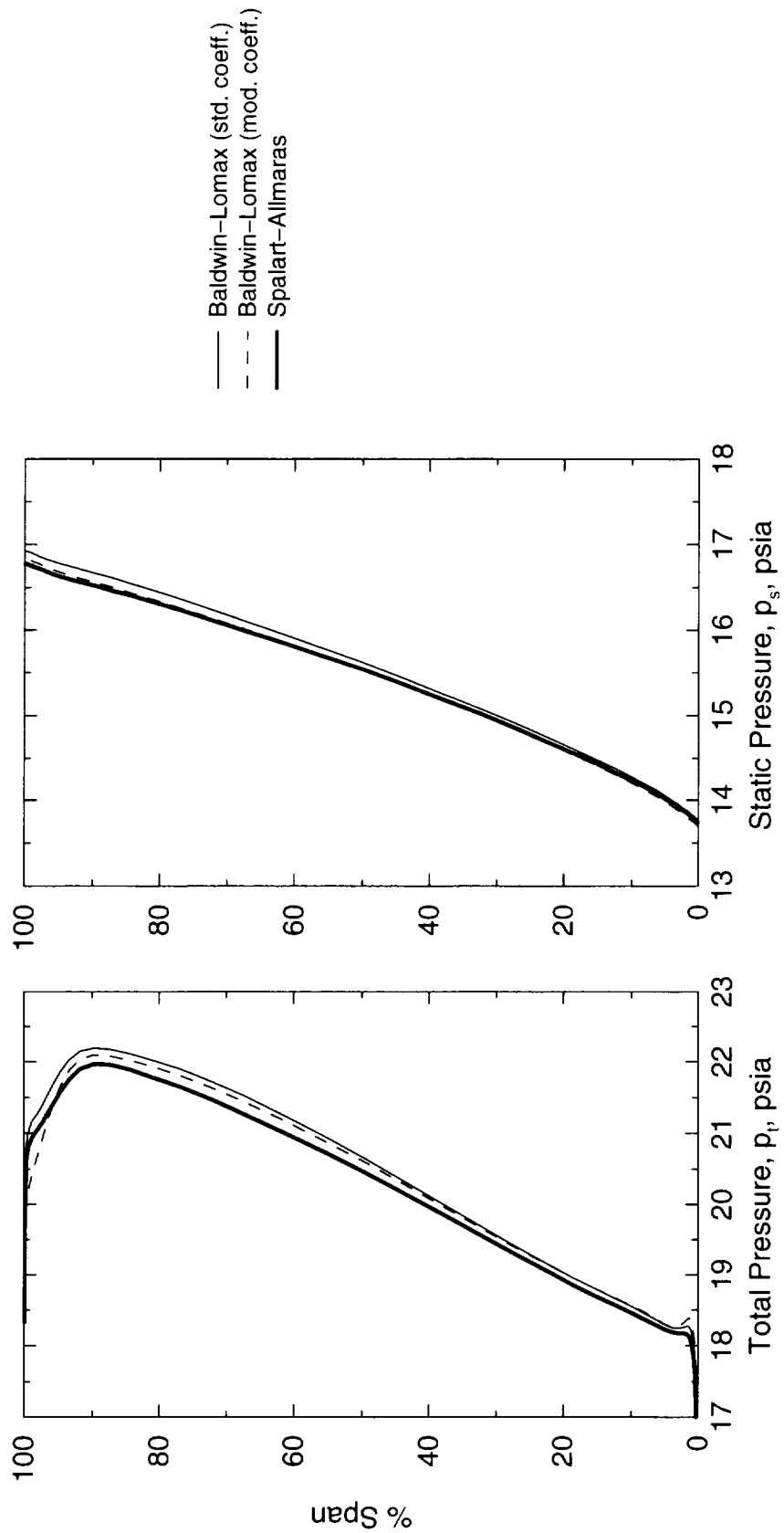


Figure 5.12: Radial exit profiles downstream of the LNF of absolute total pressure and static pressure [psia].

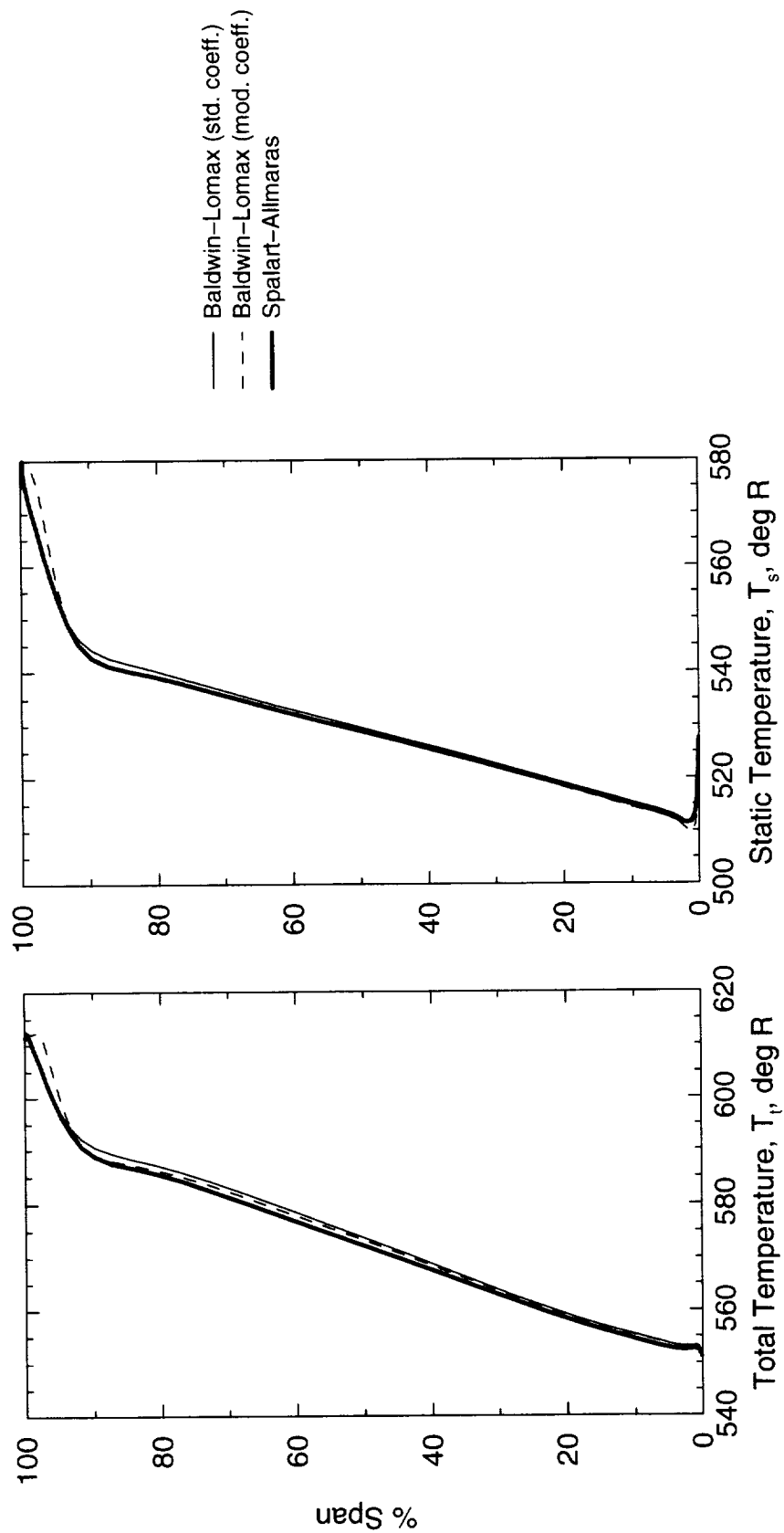


Figure 5.13: Radial exit profiles downstream of the LNF of absolute total temperature and static temperature [degrees Rankine].

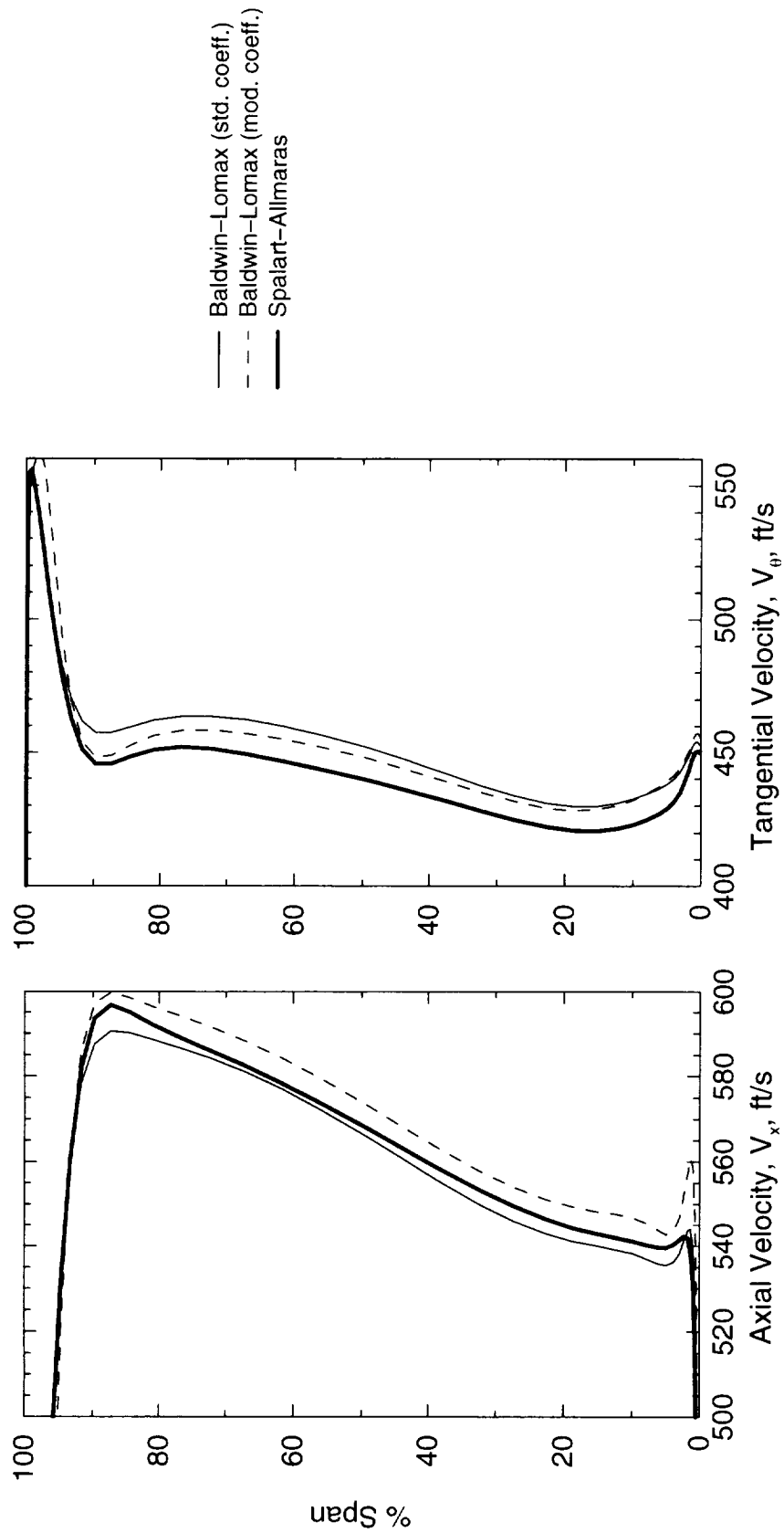


Figure 5.14: Radial exit profiles downstream of the LNF of absolute axial velocity and absolute tangential velocity [ft/s].

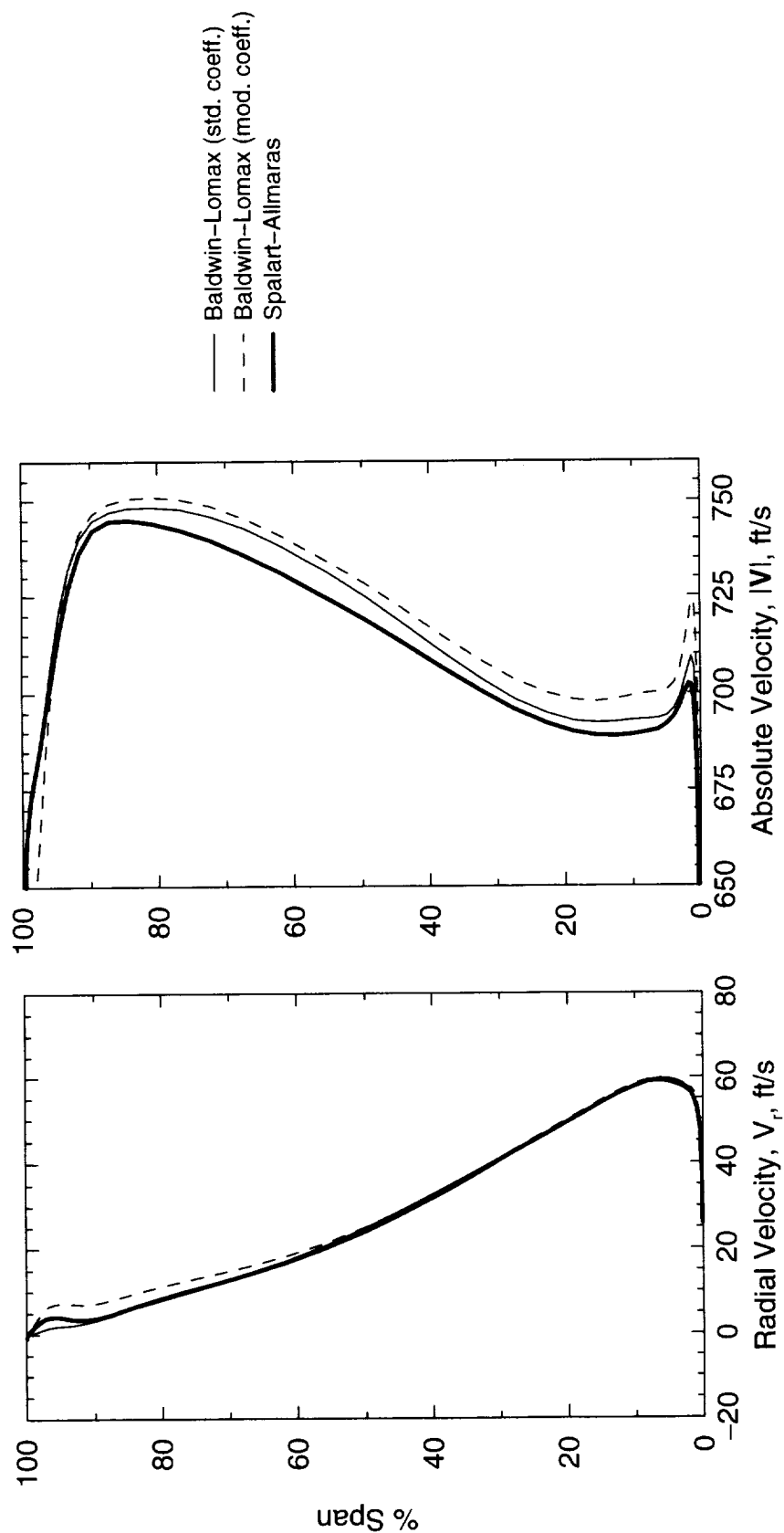


Figure 5.15: Radial exit profiles downstream of the LNF of absolute radial velocity and absolute total velocity [ft/s].

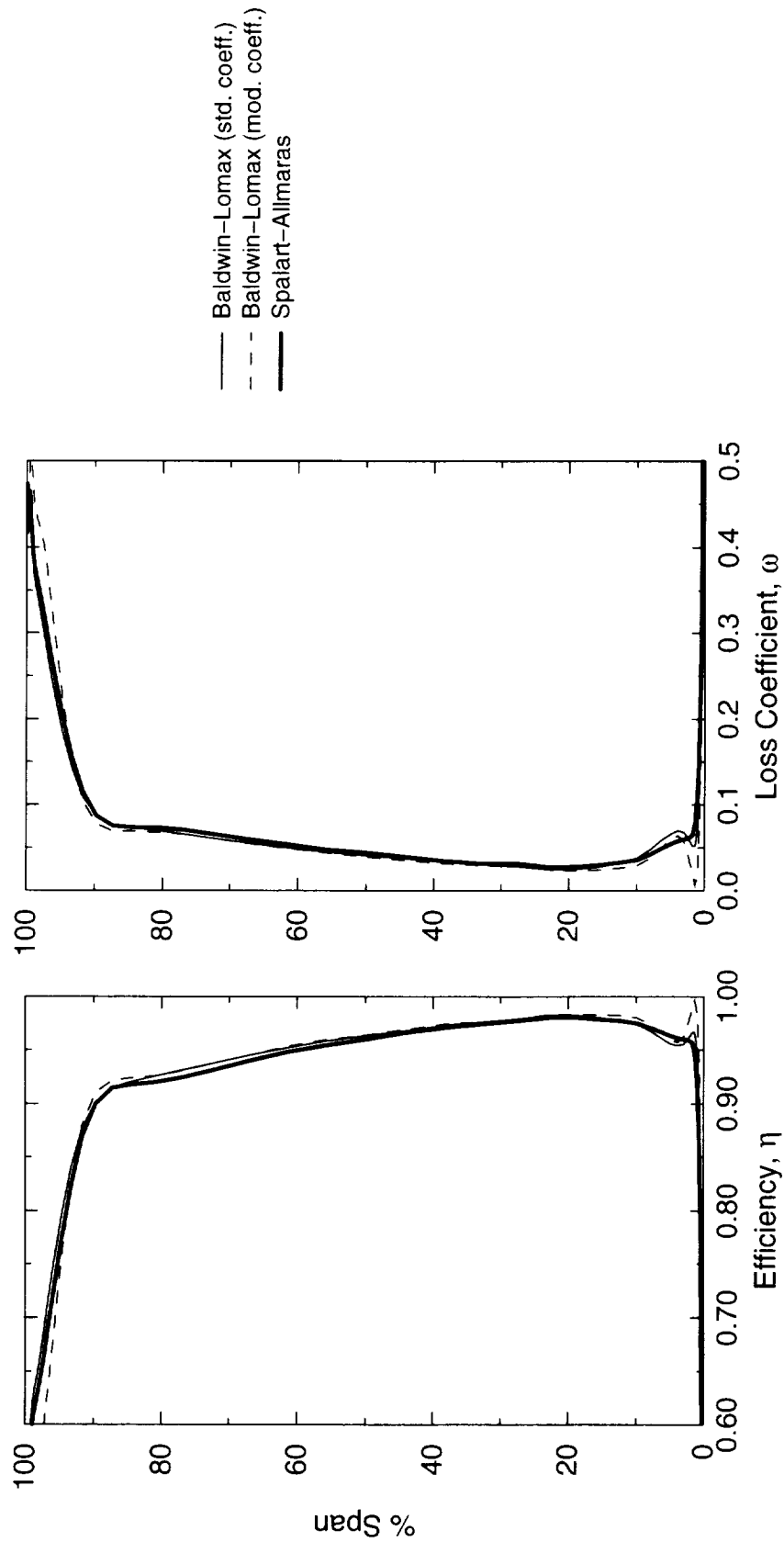


Figure 5.16: Radial exit profiles downstream of the LNF of efficiency and loss coefficient.

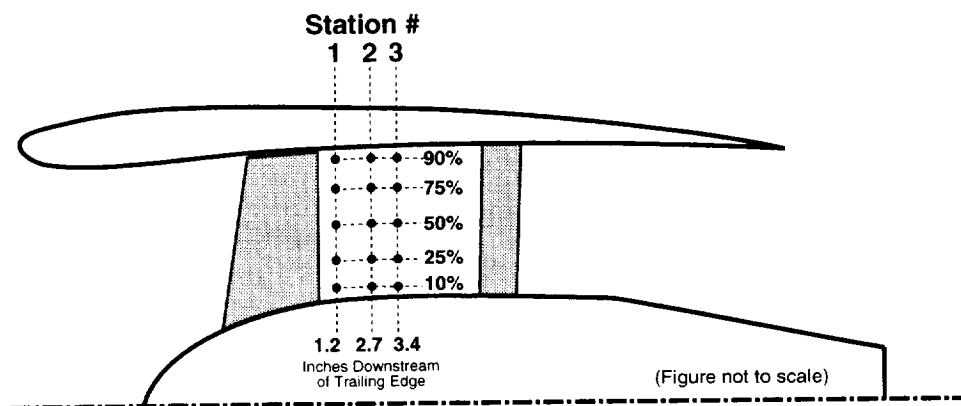


Figure 5.17: Schematic of the Low-Noise Fan showing locations of wake data extraction from both the NASA LDV experimental data and the *ADPAC* numerical solutions.

The experimental results and the numerical solutions differ in the circumferential position wake centerline most noticeably at 10% span. This shift in wake centerline location is addressed in a following section comparing the wake centerline shapes. Also at this lower span location, the differences caused by the selection of *ADPAC* turbulence model is most obvious. The wake deficit predicted using the standard coefficients in the Baldwin-Lomax model was approximately one-half the size of the experimental data. When the modified coefficients were used in the Baldwin-Lomax model, the wake deficit increased, almost matching the Spalart-Allmaras predicted wake deficit and better approximating the experimental data. These trends continue downstream through Stations 2 and 3, in Figures 5.19 and 5.20, respectively.

5.6.2 Axial Velocity Contours

As presented in the previous section, comparisons were made of axial velocity distributions across the pitch of the blade between the experimental LDV data and the *ADPAC* solutions. In order to better interpret differences in the experimental and numerical results, contour plots of axial velocity were taken at five different radial span locations. Figures 5.21 through 5.35 show “blade-to-blade” contours of predicted axial velocity, V_x , from just upstream of the rotor blade trailing edge to just downstream of the last measuring station.

The numerical data shown in these figures was taken from the radial mesh slice whose average percentage-span value most closely matched 10%, 25%, 50%, 75%, and 90% span, respectively; the contour values are in ft/s and are plotted x vs. $\bar{r}\theta$, where \bar{r} is the average radius of the mesh slice. On each of the blade-to-blade contour plots, three bold vertical lines were positioned at the axial locations corresponding to the three experimental measuring stations (1.2”, 2.7”, and 3.4” downstream of the tip trailing edge). The plots are presented on the page such that the blade rotation is downward on the page (i.e., the pressure side is the lower side of the blade, the suction side is the upper). To compare with the plots presented previously and figures to appear later within this report, the circumferential angle increases going *down* the plot; the suction side of the blade is at

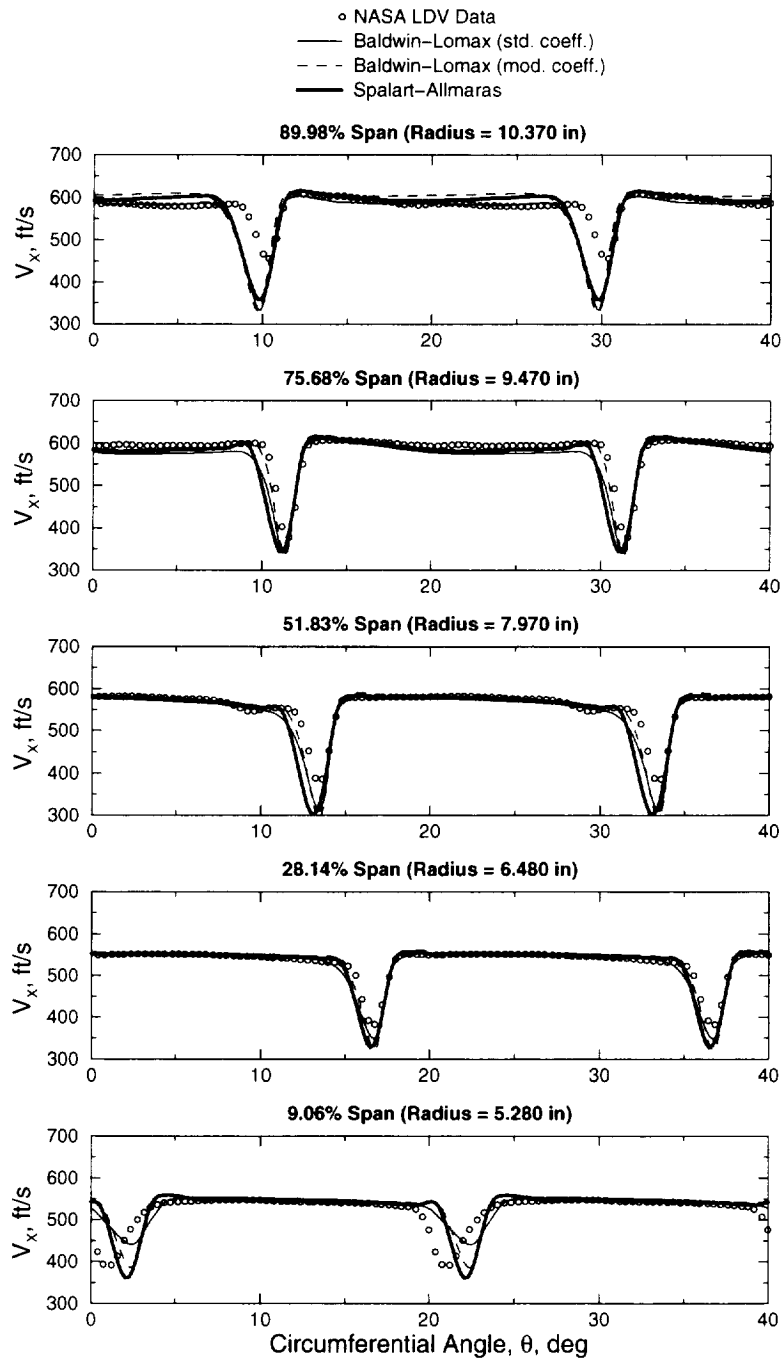


Figure 5.18: Wake profiles at **Station 1** extracted from the *ADPAC* solutions at five different spanwise locations and compared with the experimental LDV data.

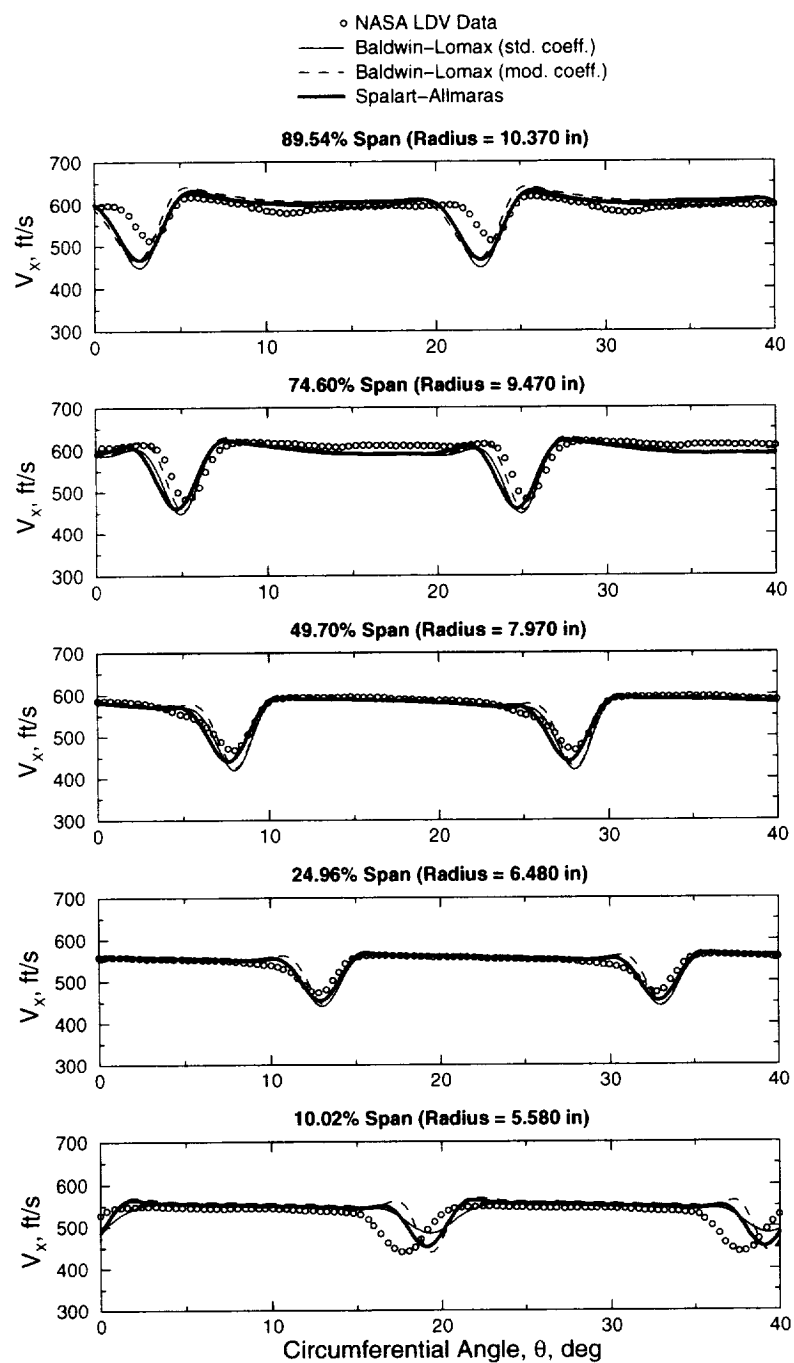


Figure 5.19: Wake profiles at **Station 2** extracted from the *ADPAC* solutions at five different spanwise locations and compared with the experimental LDV data.

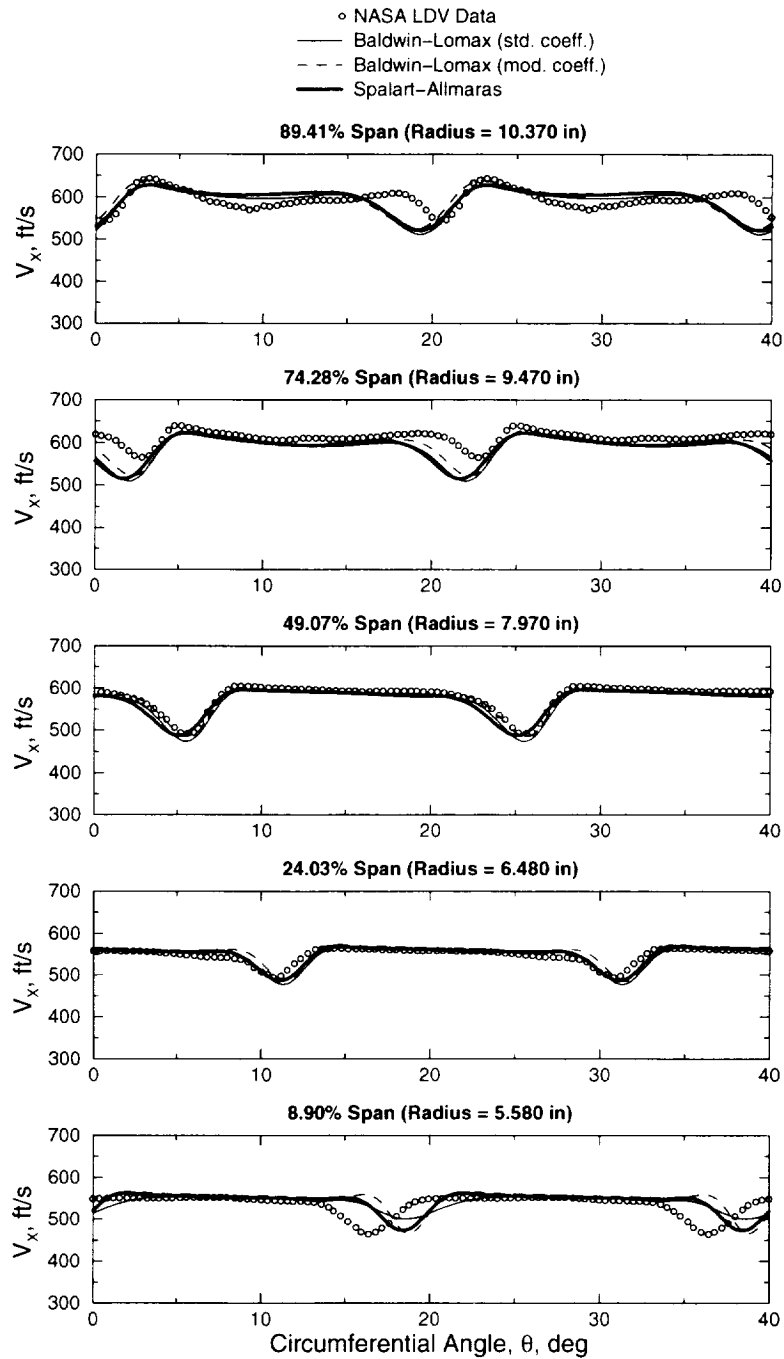


Figure 5.20: Wake profiles at **Station 3** extracted from the *ADPAC* solutions at five different spanwise locations and compared with the experimental LDV data.

a lower circumferential angle than the corresponding pressure side of the same blade.

As was seen with the previous line data of axial velocity, there is little difference between the two Baldwin-Lomax *ADPAC* contour plots at each blade span location with a possible exception at 10%. The greatest difference between the Baldwin-Lomax results and the Spalart-Allmaras results appears to occur along the suction-side (upper) portion of the trailing edge region. The minimum velocity levels in the Spalart-Allmaras results are consistently 150 to 200 ft/s lower in the trailing edge region than the levels predicted by the two Baldwin-Lomax models. This is very similar to the results found during the near-wall spacing study presented in the previous chapter. Even though the Spalart-Allmaras model predicts lower axial velocities at the trailing edge, by Station 1 the velocity levels are closer to the Baldwin-Lomax results. This is indicative of different decay rate and pattern in the wake definition which is addressed in more detail later within this report.

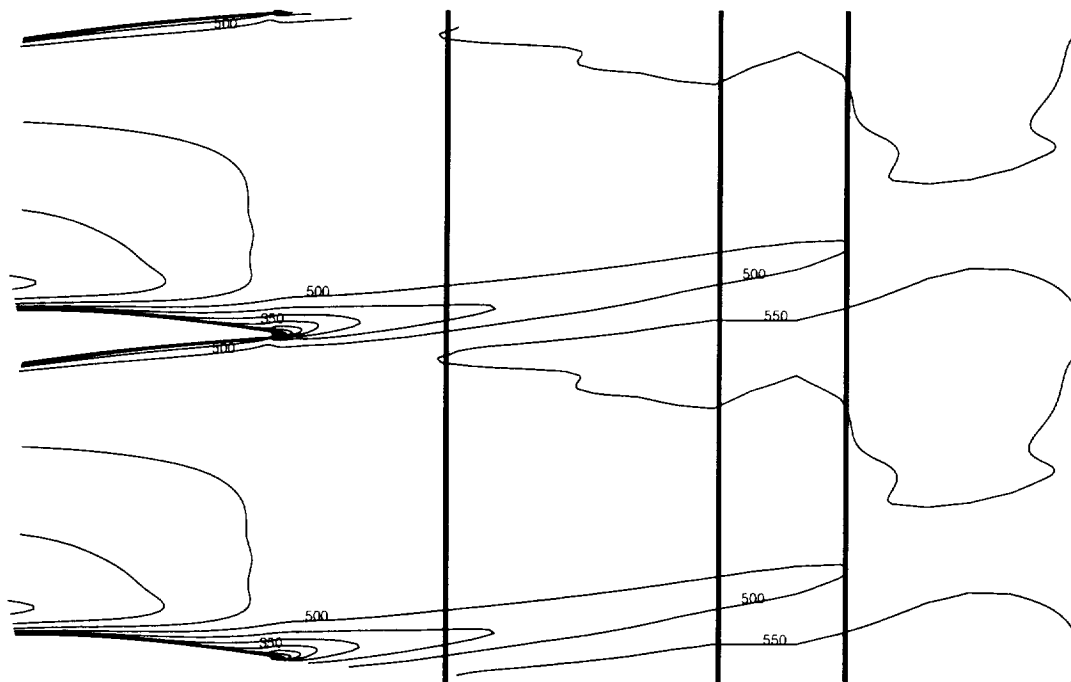


Figure 5.21: Contours of axial velocity, V_x , [ft/s] at approximately 10% span taken from the *ADPAC* Baldwin-Lomax (std. coeff.) solution.

5.6.3 Wake Centerlines

No blade-to-blade contour plots were made from the experimental data due to inadequate axial data resolution; however, at the constant axial measuring stations, several comparisons can be made. Figure 5.36 shows the Low Noise Fan blades with a constant axial slice displaying axial velocity contours. The blades are rotating in a counter-clockwise fashion in this figure. Figures 5.37 through 5.48 show contour plots of axial velocity taken from the experimental data and the *ADPAC* solutions; these contour plots are displayed as viewed from the front of the engine with respect to Figure 5.36. Data in Figures 5.37 to 5.40 were extracted at Station 1, Figures 5.41 to 5.44 at Station 2, and Figures 5.45 to 5.48 at Station 3. The single passage data were duplicated and rotated one blade pitch (20 deg) to present a complete wake structure regardless of the boundary of the data (represented by the very thin lines). Whereas the *ADPAC* results span the entire radial extent of the passage, the experimental data is limited near the endwalls; the actual radial locations of the hub and case for the experimental contour plots are shown with thicker lines similar to Figure 5.5.

The predicted shape and location of the wake in the $r - \theta$ plane are similar to the measured data. As was shown in the pitchwise velocity distributions, the velocity levels outside the wake region are similar between the experimental and numerical data. Within the wake region, the *ADPAC* results show a larger magnitude of axial velocity deficit. Another difference between the experimental data and the numerical data is the size and location of the rotor tip vortex. The rotor tip vortex in the experimental data is larger and extends lower into the flow stream than the predicted tip vortex shape; this may be due to the previously stated differences in the tip clearance.

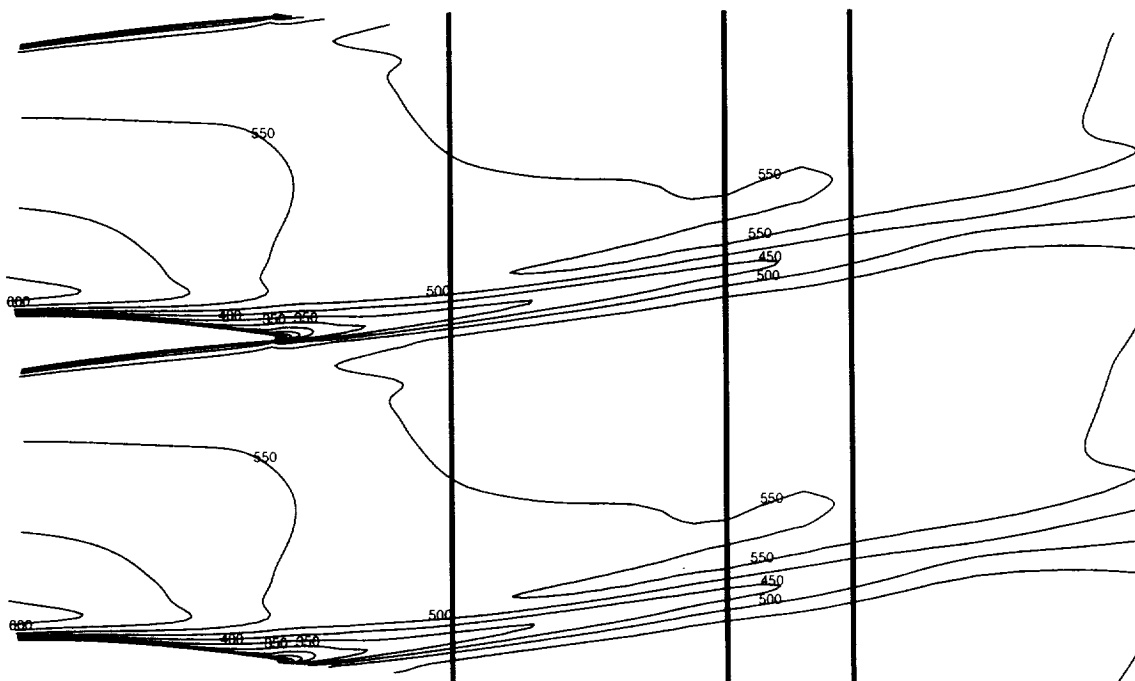


Figure 5.22: Contours of axial velocity, V_x , [ft/s] at approximately 10% span taken from the ADPAC Baldwin-Lomax (mod. coeff.) solution.

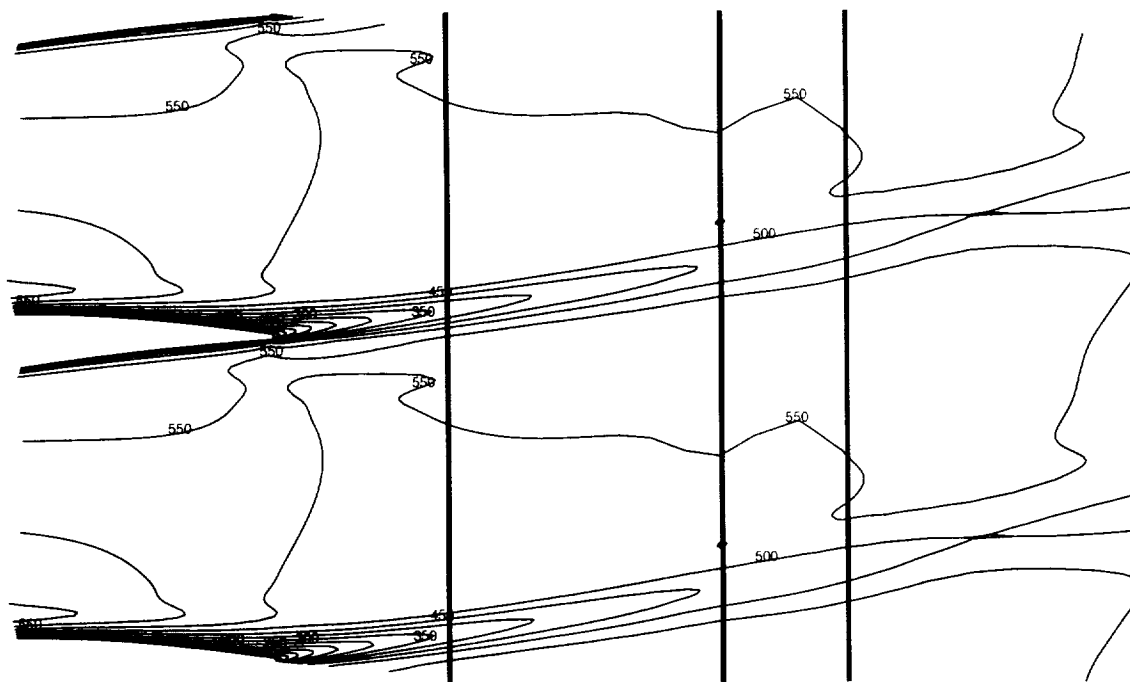


Figure 5.23: Contours of axial velocity, V_x , [ft/s] at approximately 10% span taken from the ADPAC Spalart-Allmaras solution.

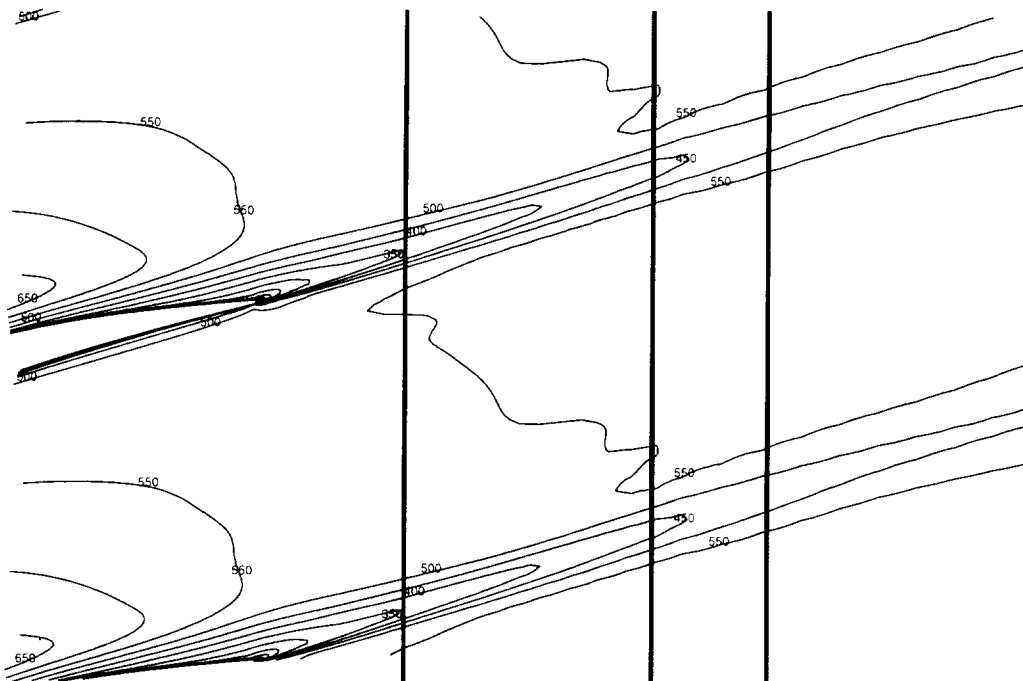


Figure 5.24: Contours of axial velocity, V_x , [ft/s] at approximately 25% span taken from the ADPAC Baldwin-Lomax (std. coeff.) solution.

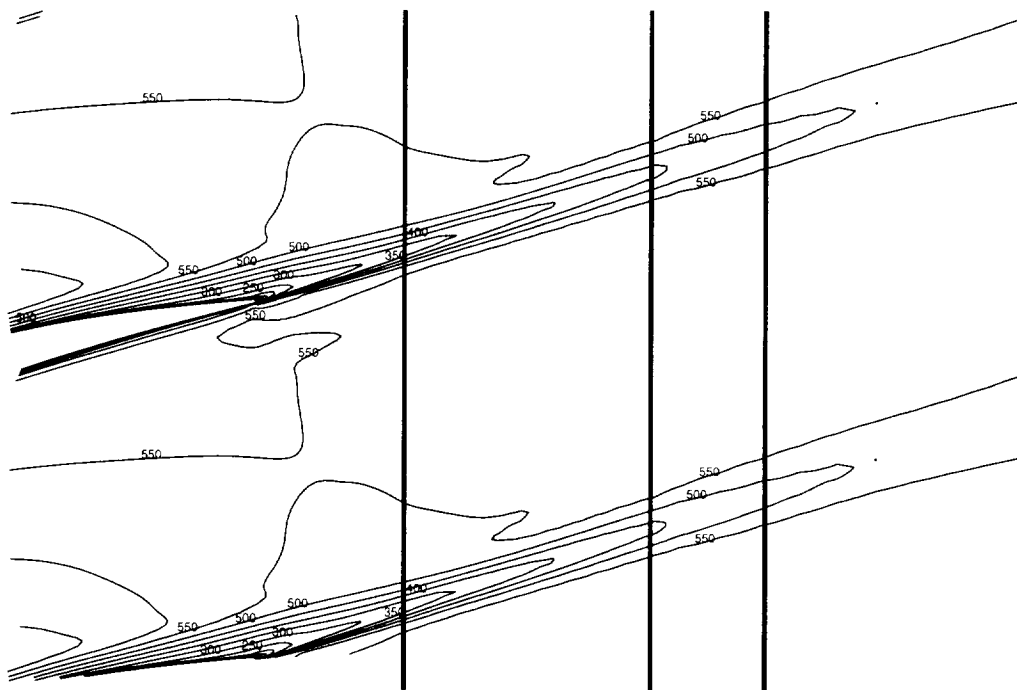


Figure 5.25: Contours of axial velocity, V_x , [ft/s] at approximately 25% span taken from the ADPAC Baldwin-Lomax (mod. coeff.) solution.

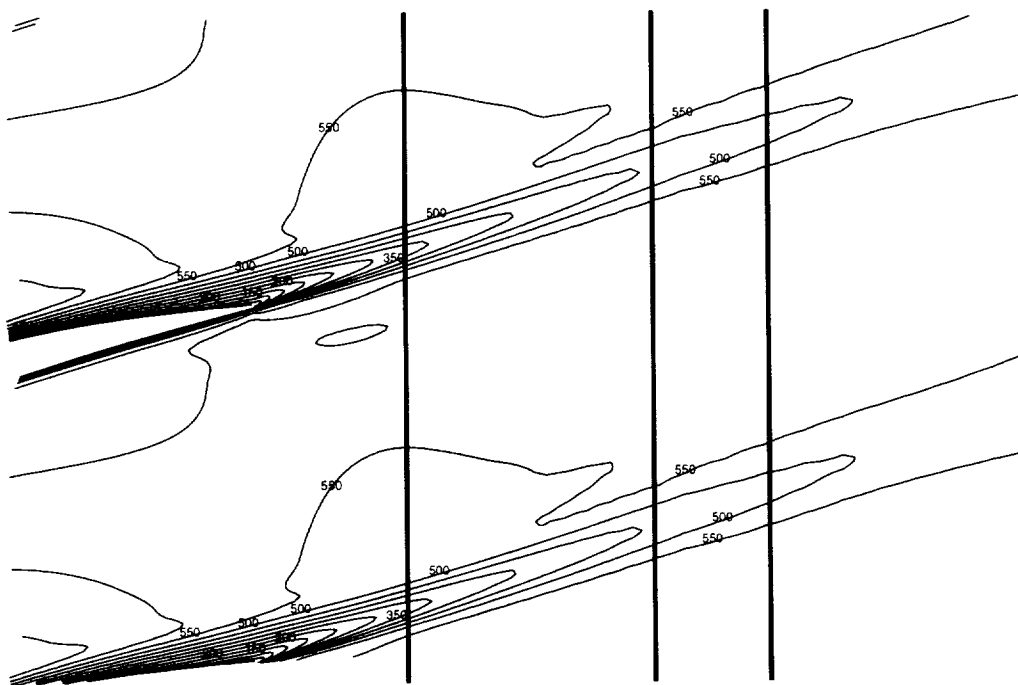


Figure 5.26: Contours of axial velocity, V_x , [ft/s] at approximately 25% span taken from the ADPAC Spalart-Allmaras solution.

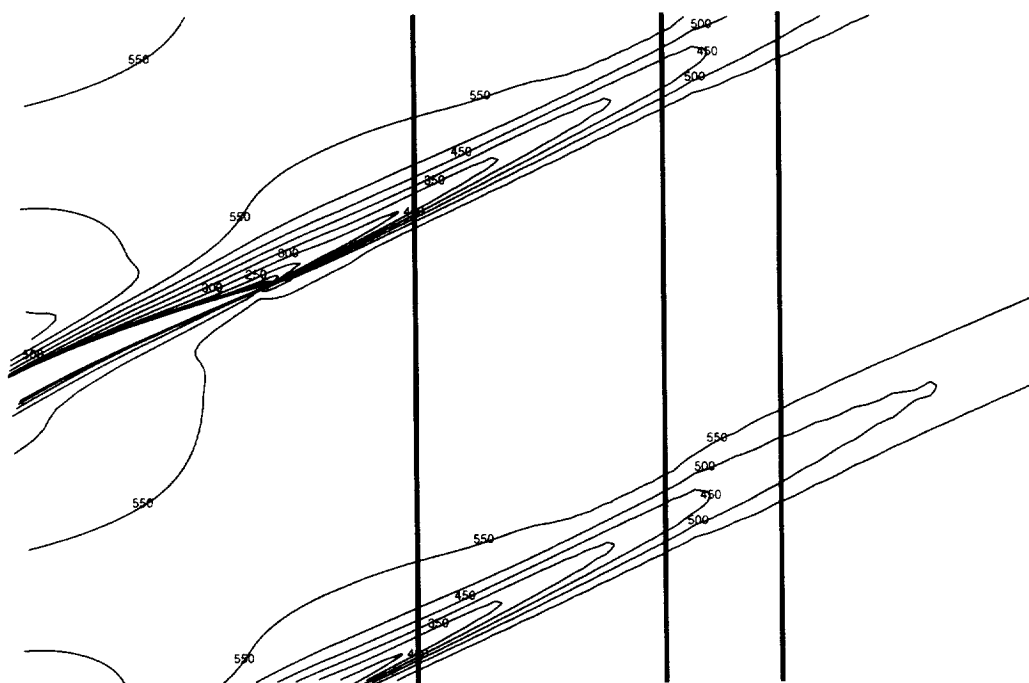


Figure 5.27: Contours of axial velocity, V_x , [ft/s] at approximately 50% span taken from the ADPAC Baldwin-Lomax (std. coeff.) solution.

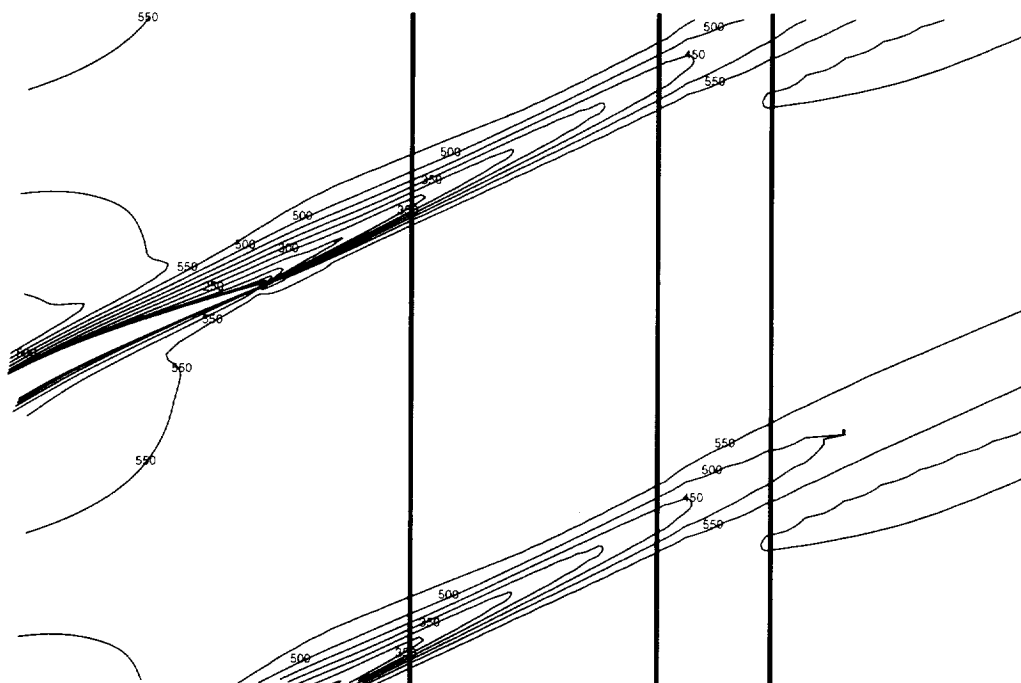


Figure 5.28: Contours of axial velocity, V_x , [ft/s] at approximately 50% span taken from the ADPAC Baldwin-Lomax (mod. coeff.) solution.

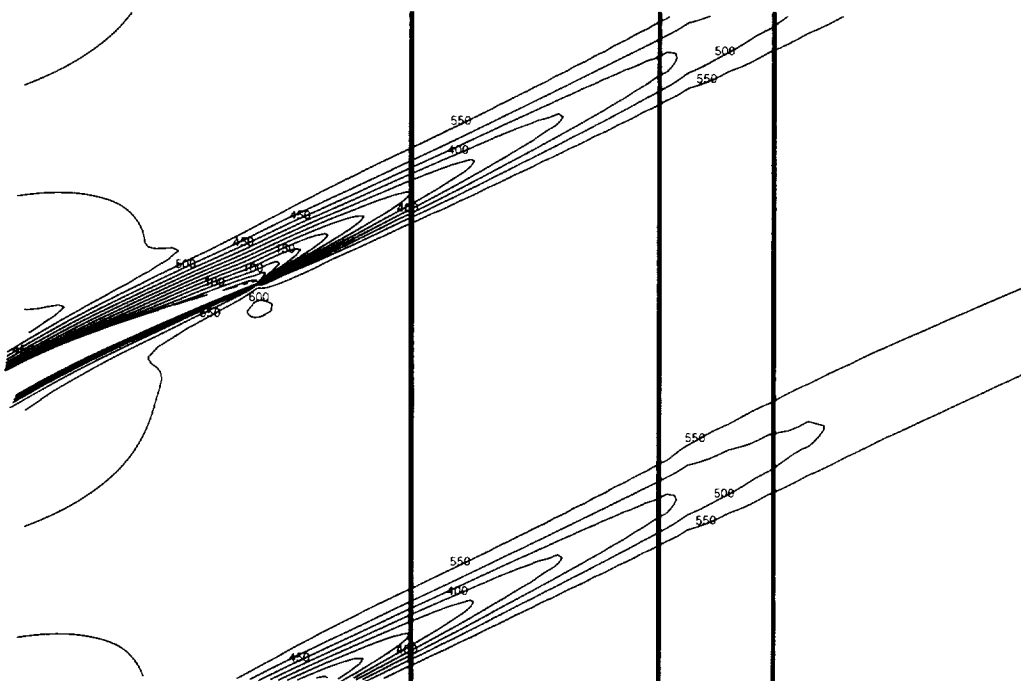


Figure 5.29: Contours of axial velocity, V_x , [ft/s] at approximately 50% span taken from the ADPAC Spalart-Allmaras solution.

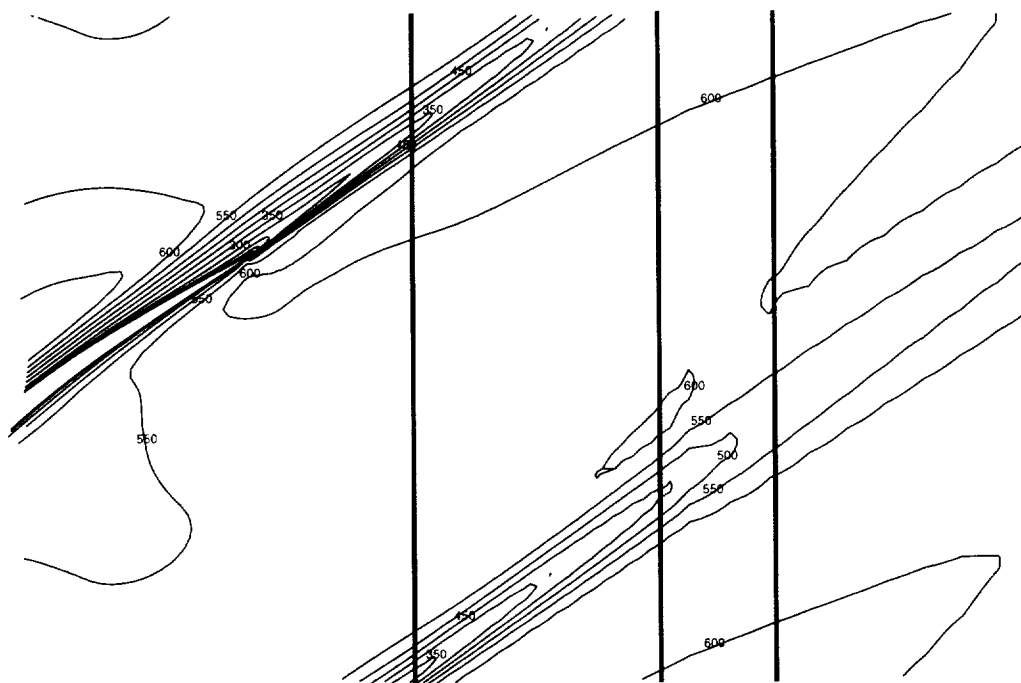


Figure 5.30: Contours of axial velocity, V_x , [ft/s] at approximately 75% span taken from the ADPAC Baldwin-Lomax (std. coeff.) solution.

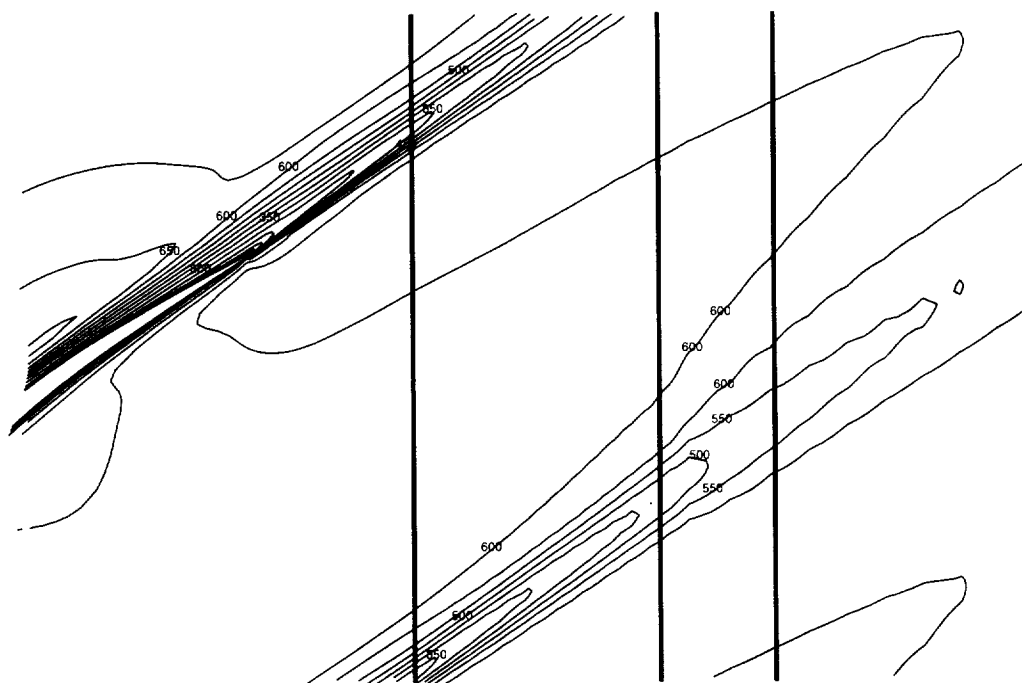


Figure 5.31: Contours of axial velocity, V_x , [ft/s] at approximately 75% span taken from the ADPAC Baldwin-Lomax (mod. coeff.) solution.

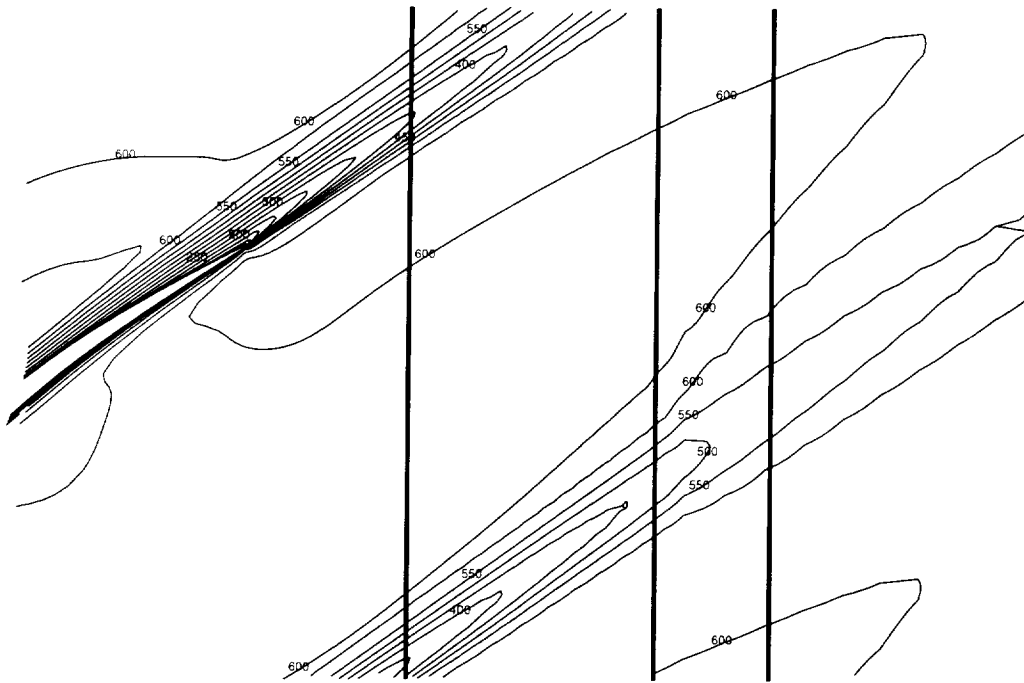


Figure 5.32: Contours of axial velocity, V_x , [ft/s] at approximately 75% span taken from the ADPAC Spalart-Allmaras solution.

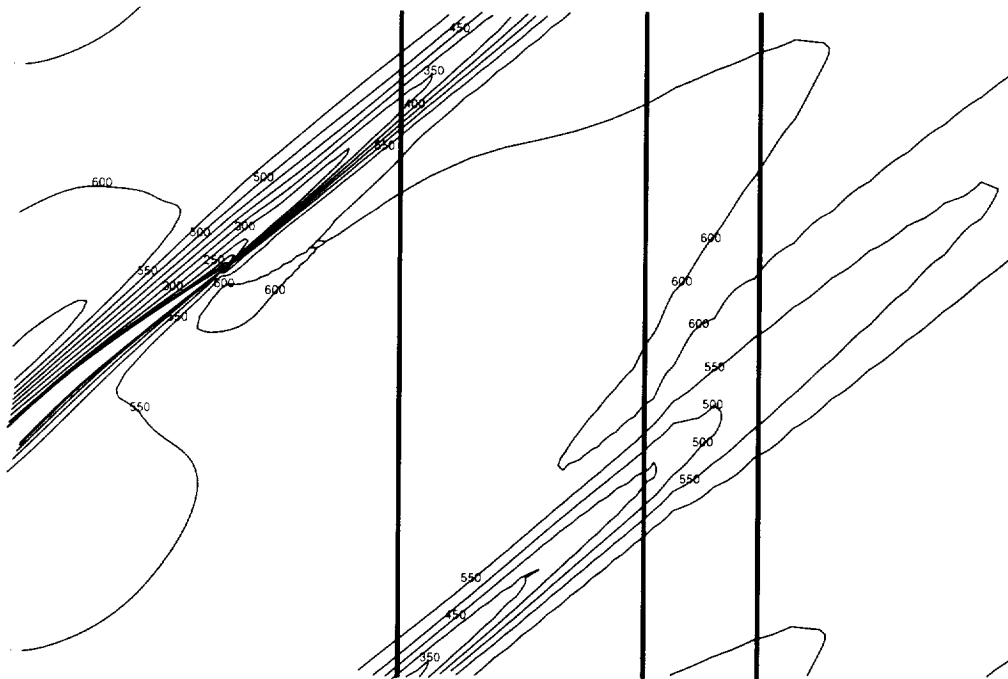


Figure 5.33: Contours of axial velocity, V_x , [ft/s] at approximately 90% span taken from the ADPAC Baldwin-Lomax (std. coeff.) solution.

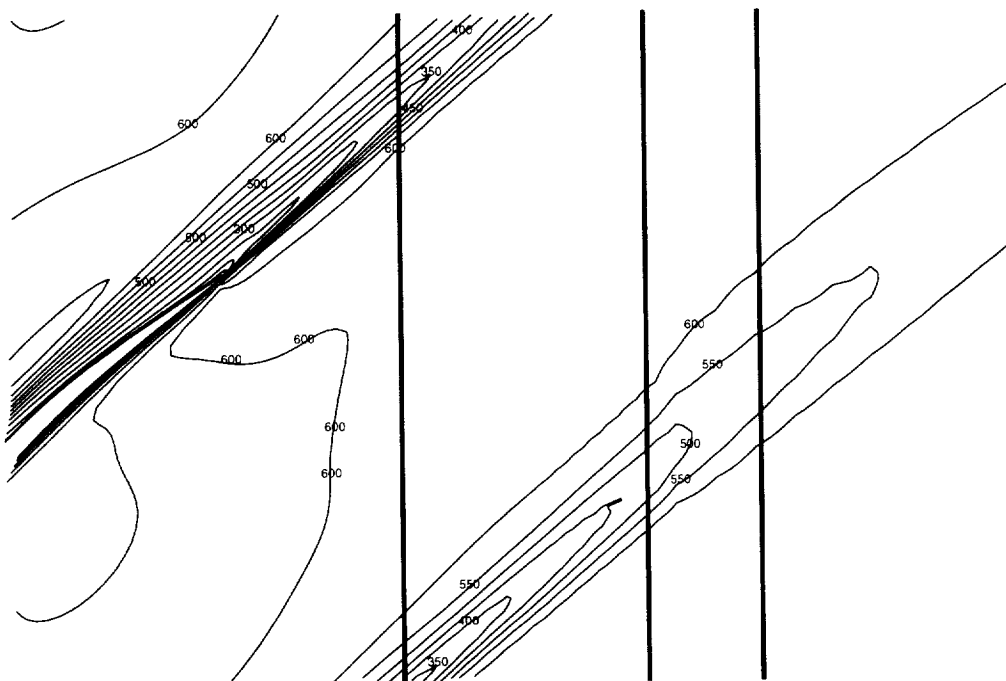


Figure 5.34: Contours of axial velocity, V_x , [ft/s] at approximately 90% span taken from the ADPAC Baldwin-Lomax (mod. coeff.) solution.

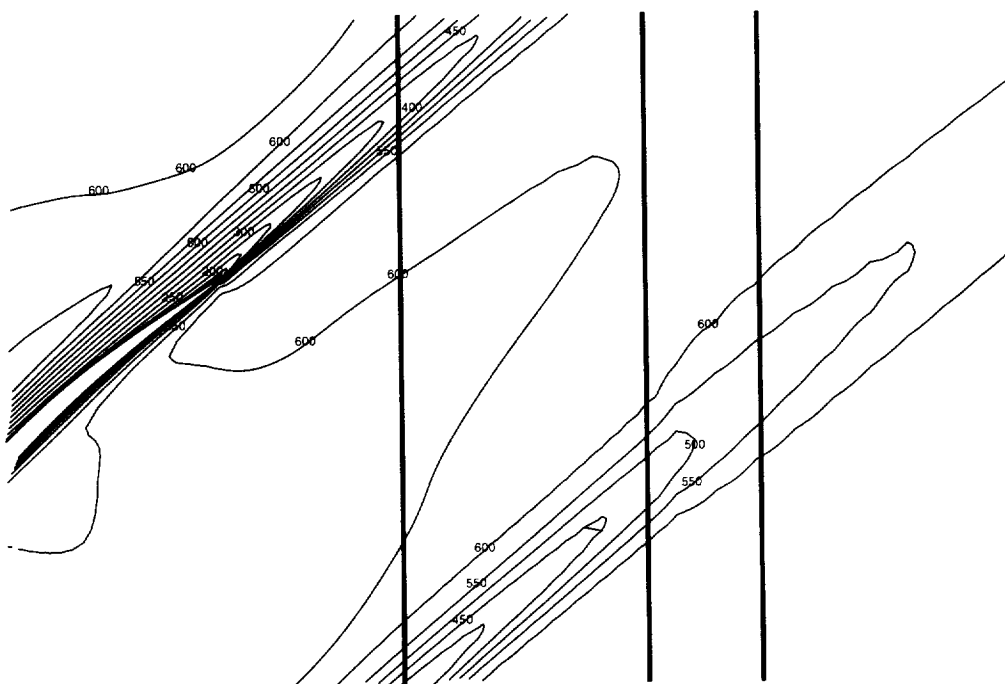


Figure 5.35: Contours of axial velocity, V_x , [ft/s] at approximately 90% span taken from the ADPAC Spalart-Allmaras solution.

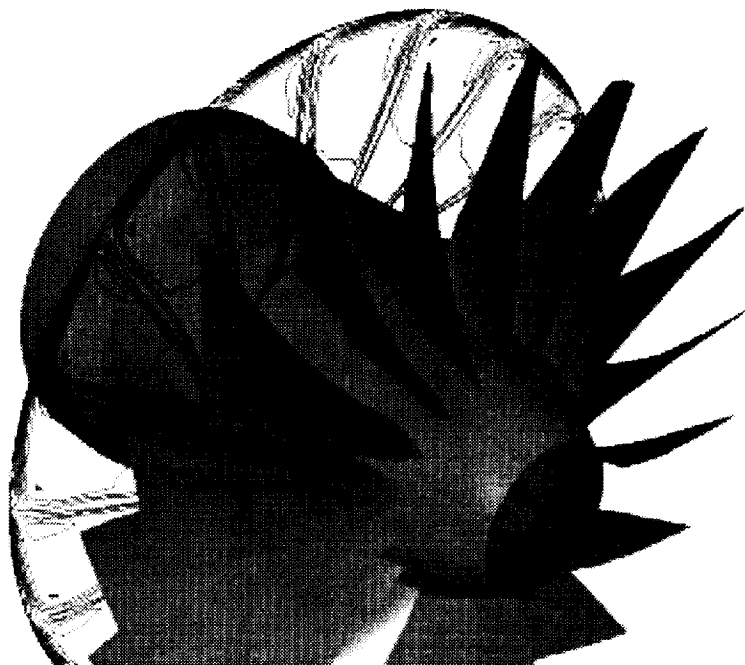


Figure 5.36: Orientation of wake structure behind the Low Noise Fan blades as represented by contours of axial velocity.

Both the experimental and numerical data were decomposed to take a constant axial slice of solution data and determine the minimum axial velocity location along each constant radial mesh slice. This essentially locates the wake centerline in the $r - \theta$ plane. Comparisons between the experimental data and the three *ADPAC* solutions are shown in Figures 5.49, 5.50, and 5.51 for Stations 1, 2, and 3, respectively. In these figures, the filled circles represent the NASA experimental data, the open circles represent the *ADPAC* Baldwin-Lomax solution with standard coefficients, the open squares represent the *ADPAC* Baldwin-Lomax solution with the modified coefficients, and the open triangles represent the Spalart-Allmaras solution. The data bounds for the *ADPAC* solutions extend radially from the hub surface to the outer casing; the LDV data bounds are limited radially to approximately 4% to 98% span. Concentric circles at approximately 10%, 25%, 50%, 75%, and 90% span are also included on each plot showing where the pitchwise data were extracted. For comparison to plots presented earlier, the circumferential angle is measured positively going counter-clockwise around the circle (i.e., the suction side is on the right side of the wake centerline and the pressure side is on the left).

In order to align the wake centerlines, the Baldwin-Lomax (std. coeff.) data were rotated until the circumferential location of the midspan (50%) wake centerline at Station 1 matched. The same tangential shift was then applied to *all* data sets at all the remaining measuring stations. This is the same procedure used to align the line data in the previous sections.

The *ADPAC* prediction of the location of the wake centerline appears to be very good, especially in the mid-span of the passage when compared with the experimental LDV data. From the hub to approximately 80% span, there is little difference between the

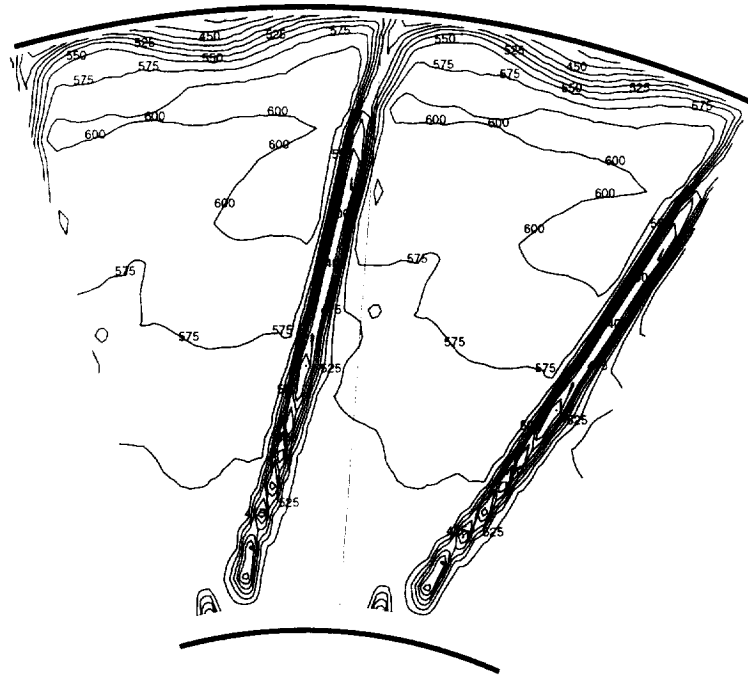


Figure 5.37: Contours of axial velocity, V_x , [ft/s] at **Station 1** taken from the NASA LDV experimental data.

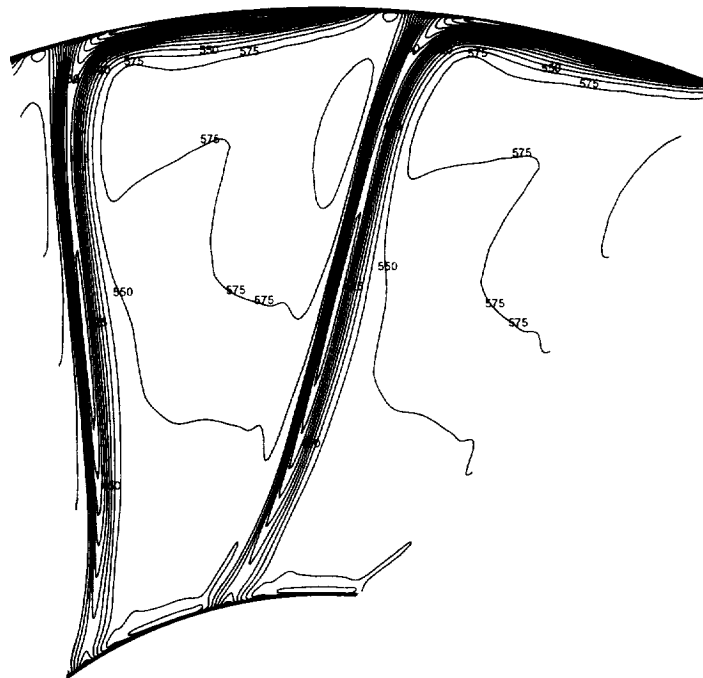


Figure 5.38: Contours of axial velocity, V_x , [ft/s] at **Station 1** taken from the ADPAC Baldwin-Lomax (std. coeff.) solution.

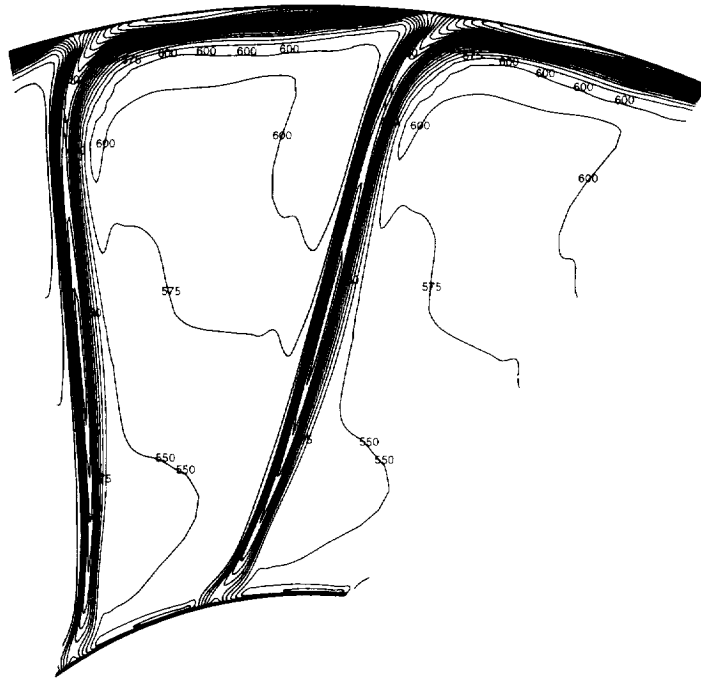


Figure 5.39: Contours of axial velocity, V_x , [ft/s] at **Station 1** taken from the *ADPAC* Baldwin-Lomax (mod. coeff.) solution.

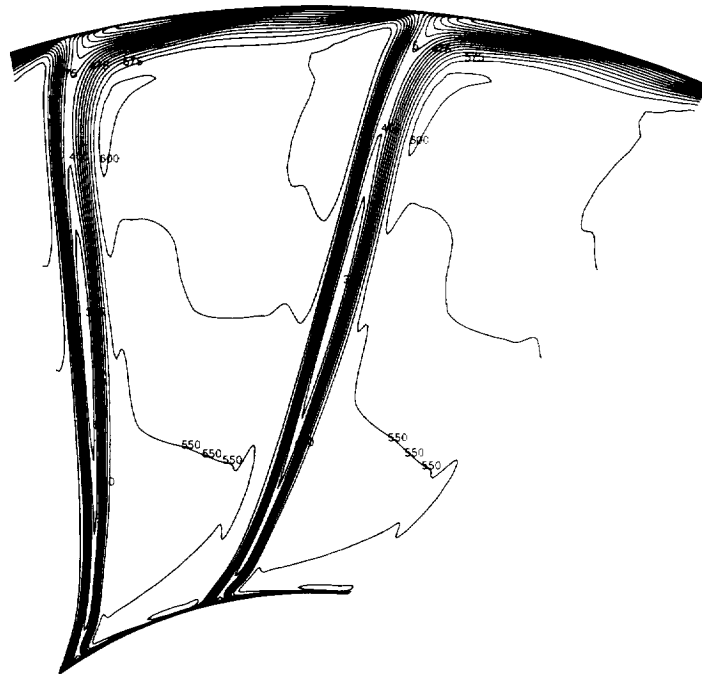


Figure 5.40: Contours of axial velocity, V_x , [ft/s] at **Station 1** taken from the *ADPAC* Spalart-Allmaras solution.

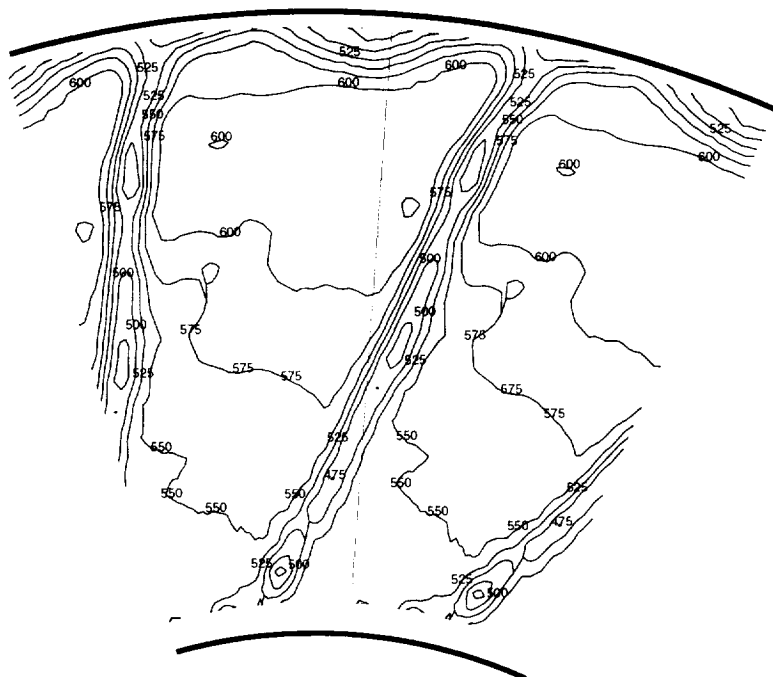


Figure 5.41: Contours of axial velocity, V_x , [ft/s] at **Station 2** taken from the NASA LDV experimental data.

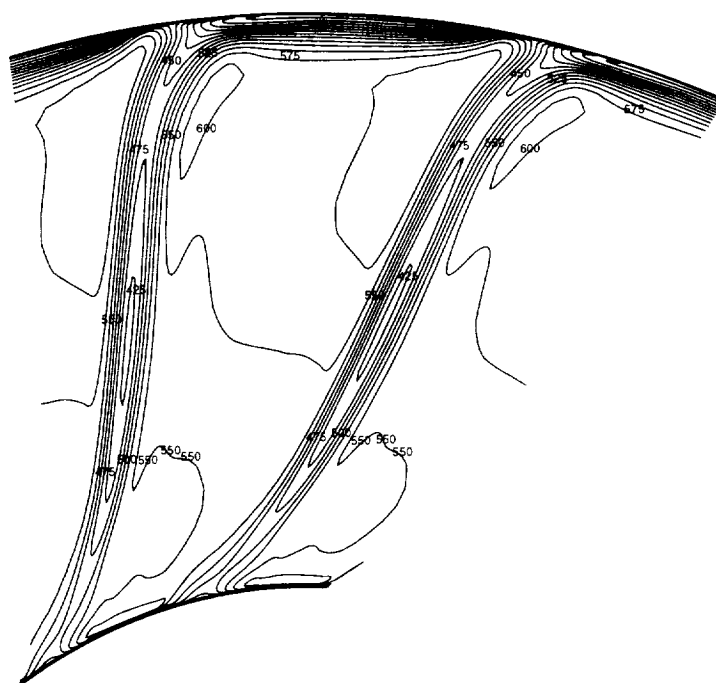


Figure 5.42: Contours of axial velocity, V_x , [ft/s] at **Station 2** taken from the ADPAC Baldwin-Lomax (std. coeff.) solution.

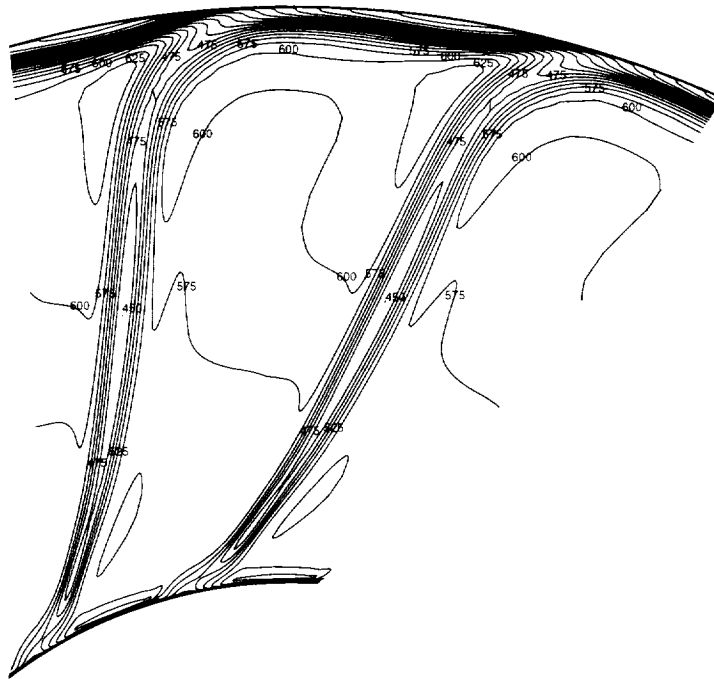


Figure 5.43: Contours of axial velocity, V_x , [ft/s] at **Station 2** taken from the *ADPAC* Baldwin-Lomax (mod. coeff.) solution.

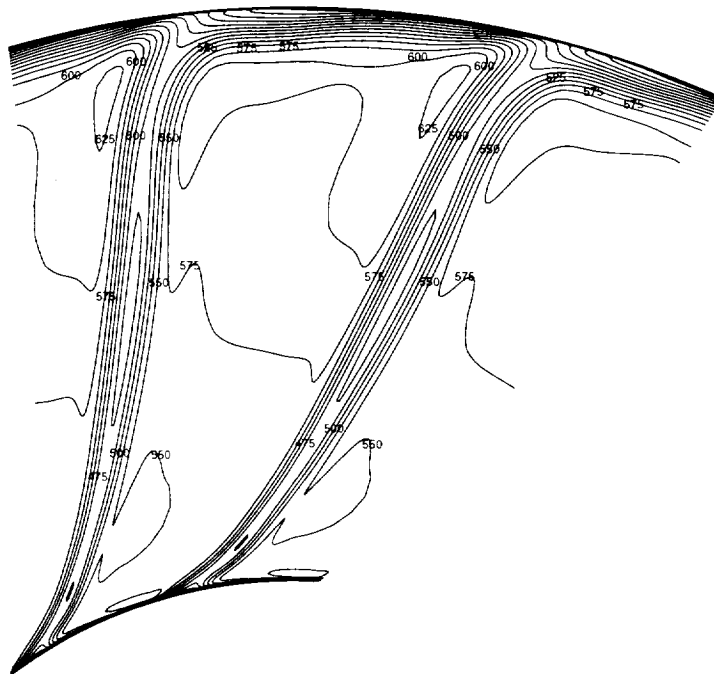


Figure 5.44: Contours of axial velocity, V_x , [ft/s] at **Station 2** taken from the *ADPAC* Spalart-Allmaras solution.

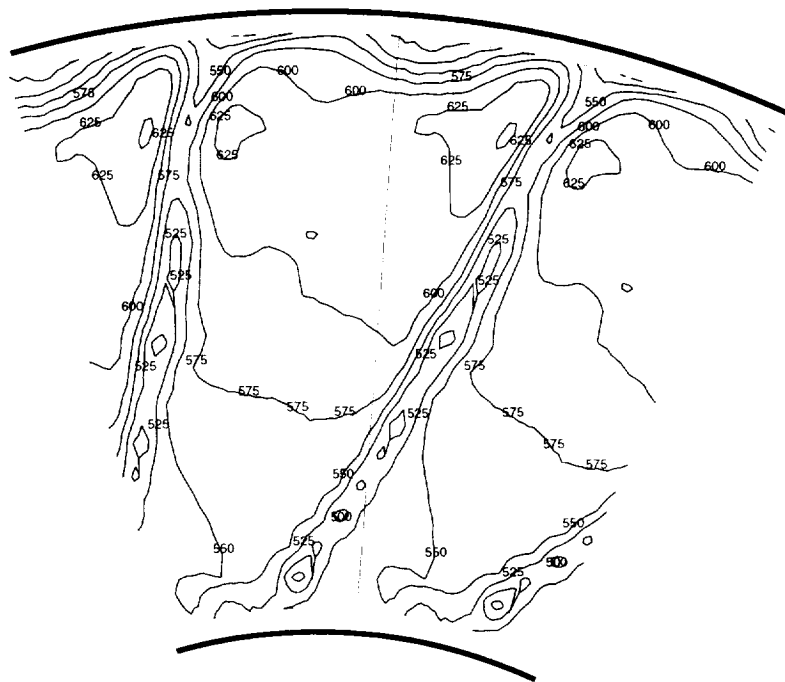


Figure 5.45: Contours of axial velocity, V_x , [ft/s] at **Station 3** taken from the NASA LDV experimental data.

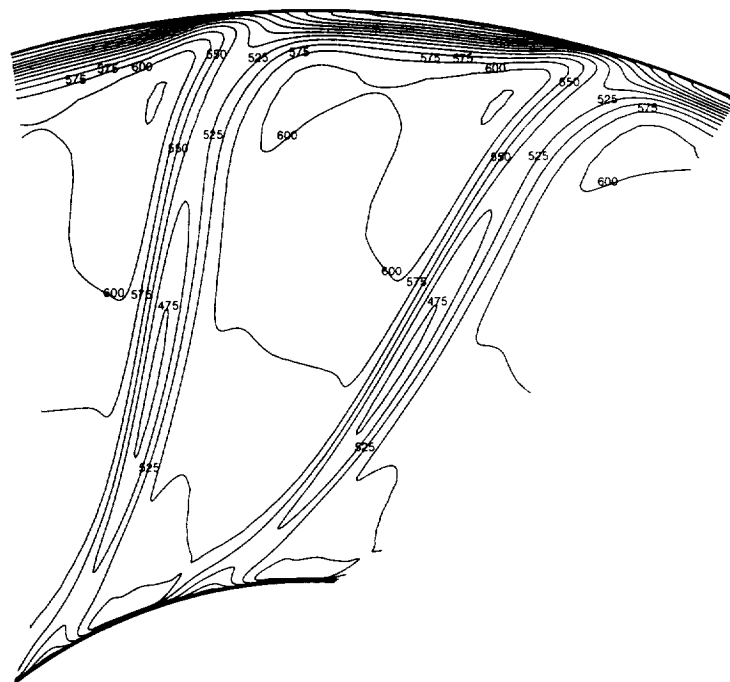


Figure 5.46: Contours of axial velocity, V_x , [ft/s] at **Station 3** taken from the ADPAC Baldwin-Lomax (std. coeff.) solution.

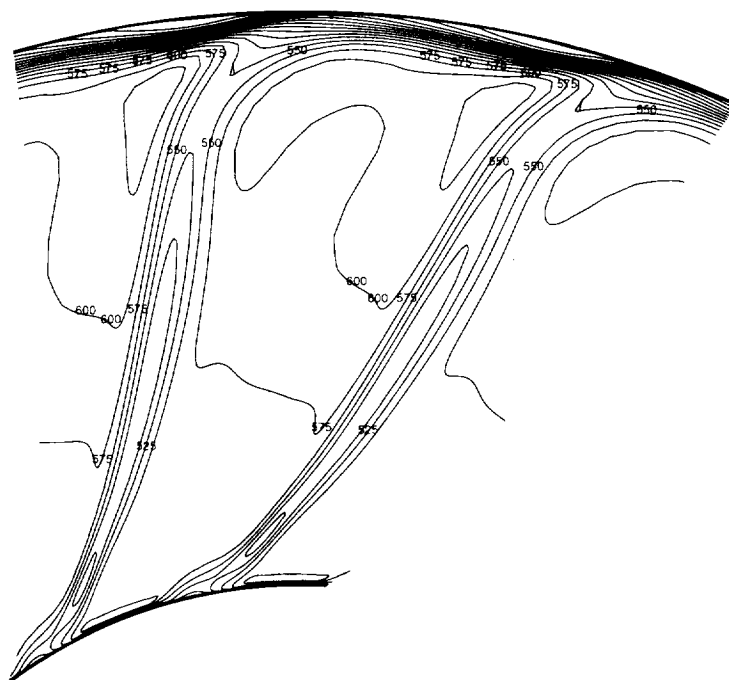


Figure 5.47: Contours of axial velocity, V_x , [ft/s] at **Station 3** taken from the *ADPAC* Baldwin-Lomax (mod. coeff.) solution.

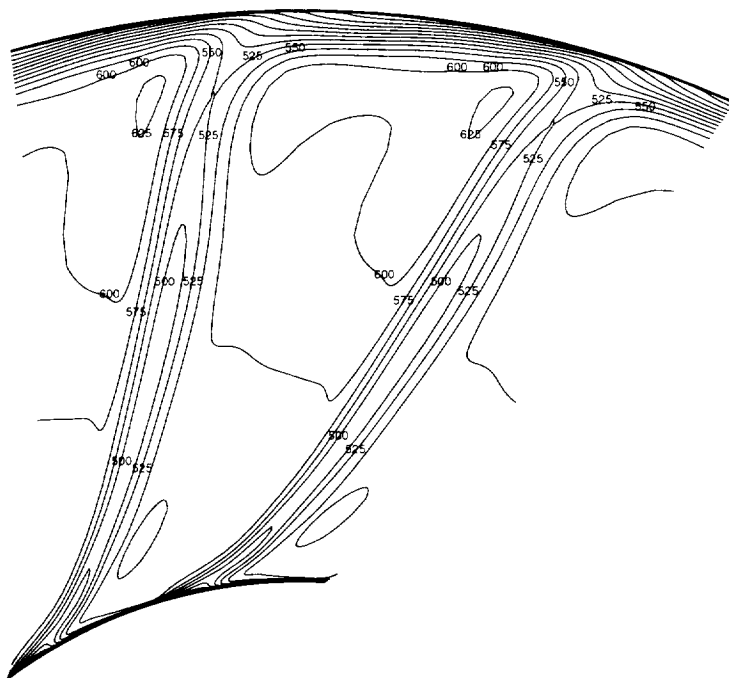


Figure 5.48: Contours of axial velocity, V_x , [ft/s] at **Station 3** taken from the *ADPAC* Spalart-Allmaras solution.

ADPAC solutions. The results from the modified coefficient Baldwin-Lomax case appears to always be slightly to the left (more swirl) of the other two *ADPAC* solutions. This is most likely caused by the small variation in exit flow angle mentioned earlier in the fan performance section, as the shift becomes larger at stations further downstream.

In the upper 20% portion of the span, differences can be seen among the predicted wake centerlines growing more noticeable further downstream (Stations 2 and 3). Near the outer casing, the differences in the location of the tip vortex can be seen clearly. The experimental symbols that represent the center of the tip vortex occur consistently lower radially than the numerical predictions (e.g., the circumferential “break” in the minimum velocity from the wake centerline to the tip vortex occurs at a lower radius in the experimental data compared to the *ADPAC* predictions) and the difference grows at stations further downstream. Again, a possible explanations for this difference are the aforementioned tip clearance discrepancy. At Station 3, there is a significant difference between the three *ADPAC* solutions in the tip region. The prediction of the tip vortices appears to be sensitive to the turbulence model used and is a possible area for further investigation, but was not included in the scope the the current work.

In the hub region, another discrepancy between the shape of the experimental and numerical wake centerline exists. From midspan down, the experimental data slowly veers off to the suction side and at approximately 10% span the experimental data appears to “bend” and shift tangentially about 10-20 degrees. The last experimental data point (at the lowest radius) appears to match back up with the *ADPAC* predicted wake shape. Therefore, the tangential shift in the axial velocity deficit near the hub highlighted in the previous section comparing the pitchwise velocity profiles may not have been seen if the data were sliced at the lowest radial experimental measuring radius.

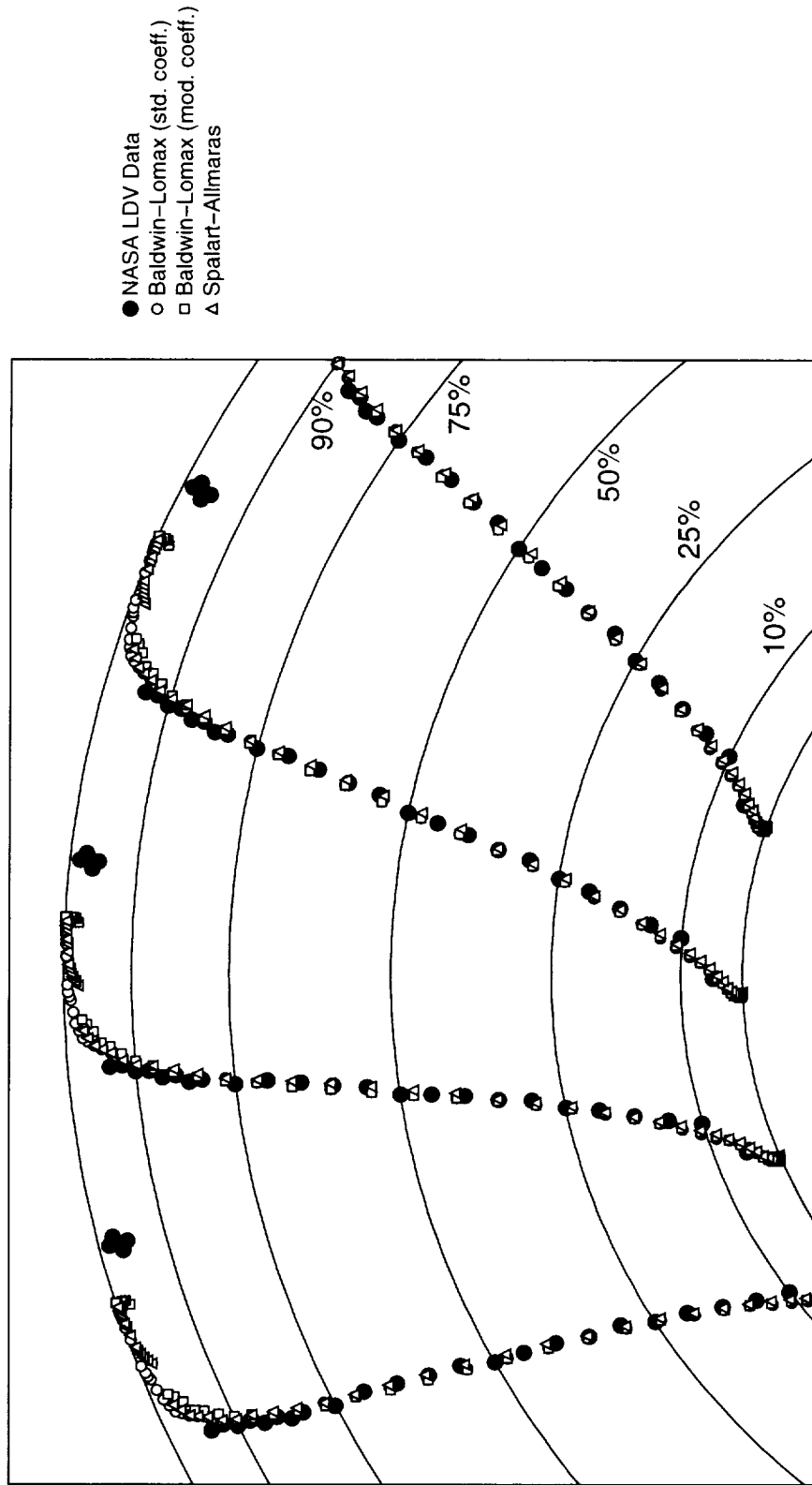


Figure 5.49: Wake centerlines compared between the experimental LDV data and the ADPAC cases at **Station 1**.

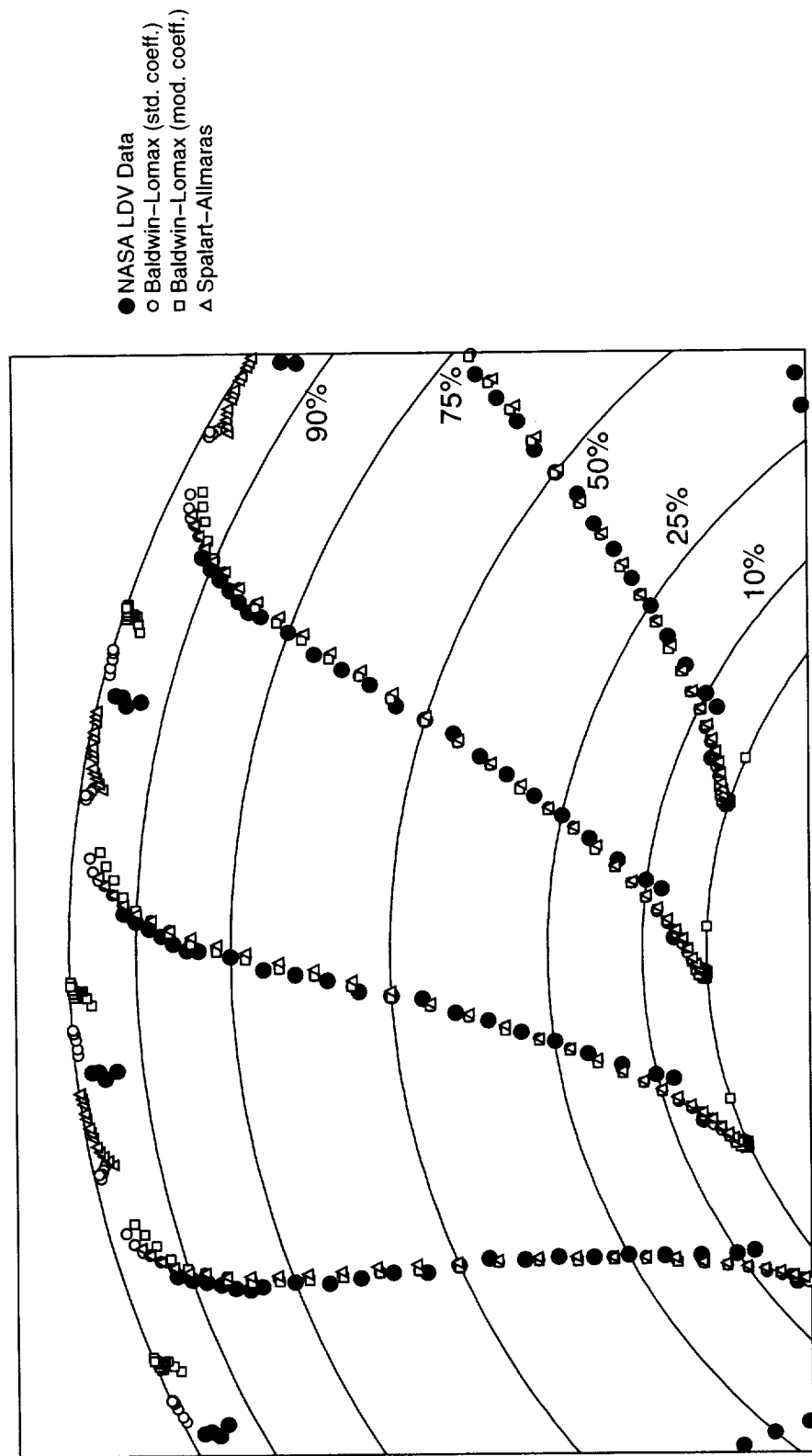


Figure 5.50: Wake centerlines compared between the experimental LDV data and the ADPAC cases at **Station 2**.

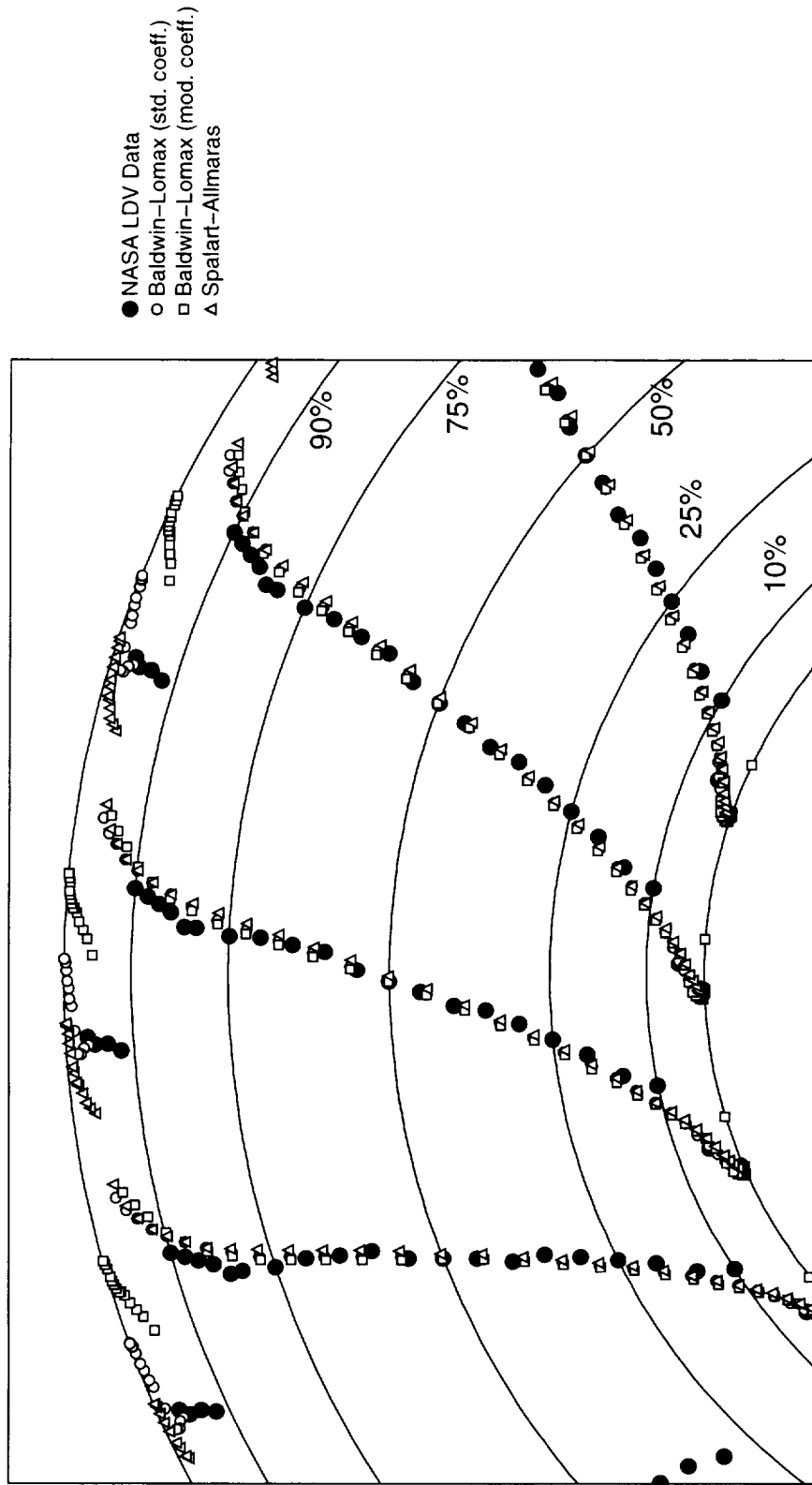


Figure 5.51: Wake centerlines compared between the experimental LDV data and the ADPAC cases at **Station 3**.

5.7 Wake Definition Study

5.7.1 Wake Structure and Description

Prior to the description of the data reduction and the presentation of the correlation results, the terms used in many of the correlation equations need to be identified and related to the wake shape. Figure 5.52 shows a schematic representation of a blade-to-blade rotor passage including the wake regions and velocity triangles. The velocities designated with the letter V are in the absolute reference frame, and those with W are in the relative frame. A velocity distribution downstream of the rotor trailing edge has been superimposed on the figure to identify various velocity levels including the minimum velocity (W_{min}) and the mid-pitch velocity (W_o). The pressure and suction sides of the wake region are also noted.

In Figure 5.53, a data sample of the velocity distribution from approximately 50% span is shown in the upper portion of the figure. Below the data, a schematic shows the various wake shape dimensions. The majority of the terms used in the wake correlations following in this report are shown in this figure. The centerline velocity deficit of the wake is defined as:

$$W_{dc} = W_o - W_{min}$$

where W_o is the relative streamwise velocity at the circumferential location one-half pitch from the wake centerline position ($\theta_c \pm P/2$) which is assumed to be a "freestream" reference velocity. The wake width (δ) is defined as the circumferential width between the two points where the velocity distribution crosses the $W_{dc}/2$ value. This width can be sub-divided into a pressure-side and suction-side half-width, δ_p and δ_s , respectively. Also shown in the figure is the normalized tangential distance used in the similarity profile, η , defined as:

$$\eta = \theta/(\delta/2)$$

5.7.2 Wake Correlations

To determine correlations for the wake width and centerline velocity deficit, a method of data reduction similar to that used by Majjigi and Gliebe [35] was used and is briefly described below. The correlation includes a weak influence of the drag coefficient (c_d). Using spanwise distributions of design data for the Low Noise Fan (LNF) [33], a spanwise profile of c_d was evaluated by:

$$c_d = \frac{\bar{\omega}_p \cos^3 \beta_M}{\sigma \cos^2 \beta_1}$$

where,

$$\beta_M = \tan^{-1} \left(\frac{\tan \beta_1 + \tan \beta_2}{2} \right)$$

and β_1 and β_2 are the relative inlet and exit flow angles, respectively, $\bar{\omega}_p$ is the profile loss coefficient, and σ is the blade solidity.

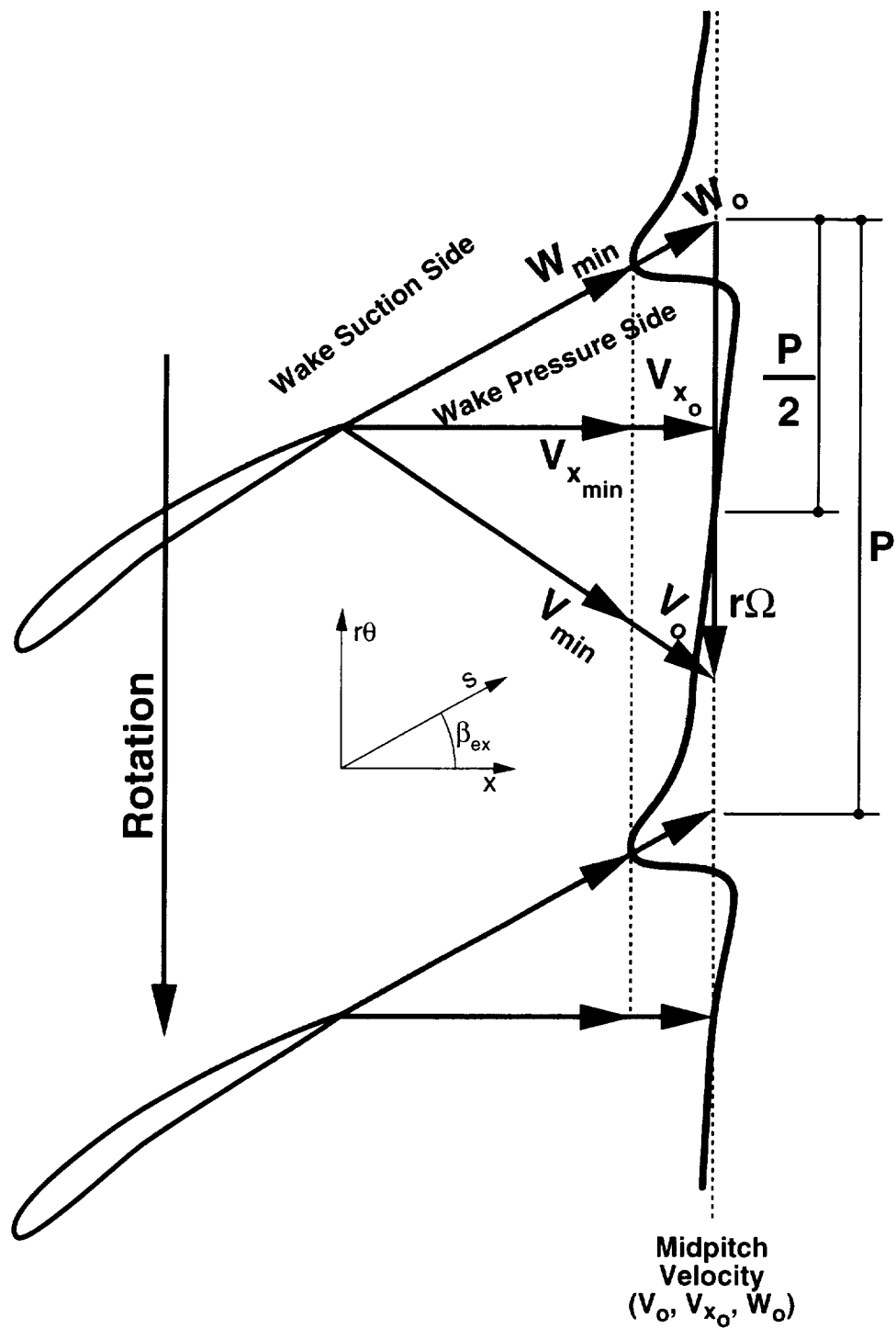


Figure 5.52: Schematic of wake position and velocity definitions relative to the rotor blade.

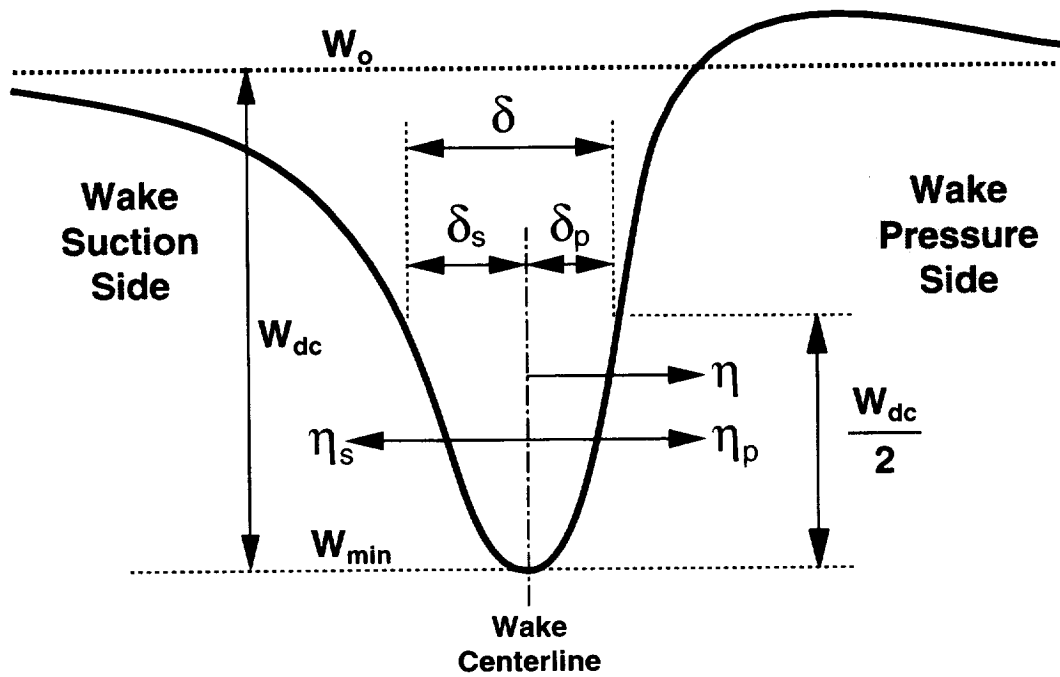
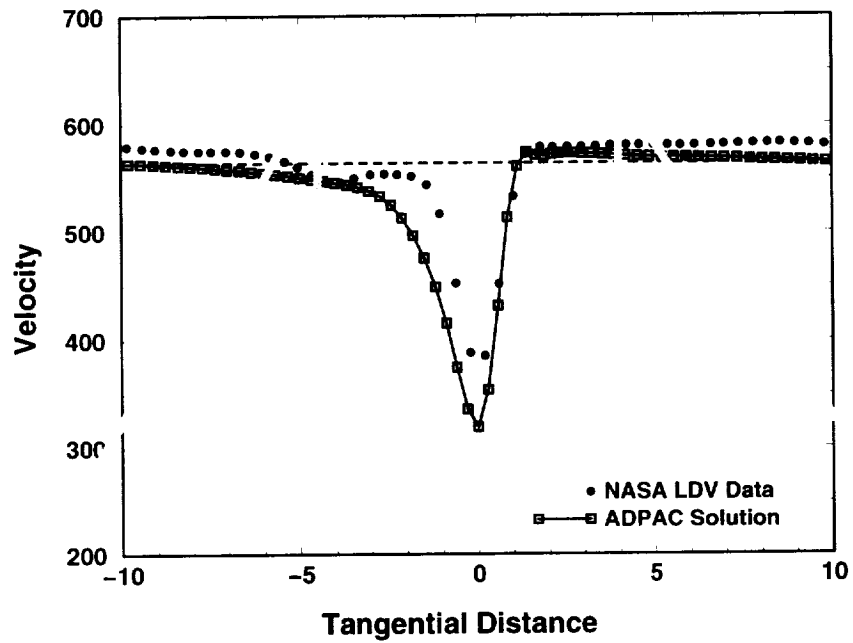


Figure 5.53: Identification of wake measurements and measuring locations.

In the Majjigi and Gliebe report [35], the data was correlated using the following form:

$$y = \delta/P = \frac{ax + b}{cx + 1}, \quad x = \frac{s}{c} \frac{1}{c_d^{1/8}}$$

where a , b , and c are the fitted coefficients. For the wake width correlation, y is the wake width normalized by the blade pitch (δ/P) and x is the streamwise distance normalized by the aerodynamic chord modified by the drag coefficient. For the velocity deficit correlation:

$$y = \frac{W_{dc}}{W_o} \frac{1}{c_d^{1/4}} = \frac{ax + b}{cx + 1}, \quad x = \frac{s}{c}$$

where y is the the velocity deficit normalized by the mid-pitch velocity and modified by the drag coefficient ($W_{dc}/W_o \times 1/c_d^{1/4}$) and x is the streamwise distance normalized by the aerodynamic chord (s/c).

Some of the figures in this report of the wake correlations include the curve fits found by Majjigi and Gliebe [35] and by Topol and Philbrick in a more recent study [36] using the same correlation techniques. In order to determine the coefficients (a , b , c), a non-linear curve fitting routine was written using the Levenberg-Marquart method [37].

To determine the general scatter of the data, the experimental LDV data measured at Stations 1, 2, and 3, were plotted in 10% span intervals in Figure 5.54. From examination of the data, the data points from 10% span to 90% span are grouped close together, and the points in the outer 10% span regions appear more scattered. The LDV data points in the outer 10% endwall regions were shaded. This scatter in the endwall regions near the hub and the case is primarily due to the breakdown of the clean wake profile (as diagramed in Figure 5.53) from the interaction between the wake, the tip clearance vortex, and the endwall boundary layers. Based on this and other more quantitative results from curve fits, the wake correlation functions will be fit using only the data in the 10% to 90% span region.

With respect to matching the previously determined correlation curves found in the literature, both the experimental and numerical LNF results agree better with the curves in the velocity deficit correlation (*lower plot*) than in the wake width correlation (*upper plot*). It should be noted that the two literature curve fits also agree better in the velocity deficit correlation than in the wake width correlation, possibly an indication of a higher sensitivity to blade geometry or blade loading in the wake width correlation.

In order to determine the detailed differences between the *ADPAC* turbulence models in predicting wakes, the wake shape parameters were evaluated at five spanwise locations (10%, 25%, 50%, 75%, and 90%) and are plotted in Figures 5.55 through 5.59. By examining the data prior to curve fitting, variations in the prediction capability can be determined before being “washed-out” in the curve fits. Since all the data contained in one plot were taken from approximately the same spanwise location, the dependence on c_d is assumed to be negligible and was not included in this series of five figures.

The mesh slices from which the wake parameters were taken are the same locations used to plot the blade-to-blade axial velocity contours in Figures 5.21 to 5.35; the corresponding contour plots are referenced in the caption of the figures. The experimental data included in each plot was take from a range of $\pm 10\%$ about the specific span location.

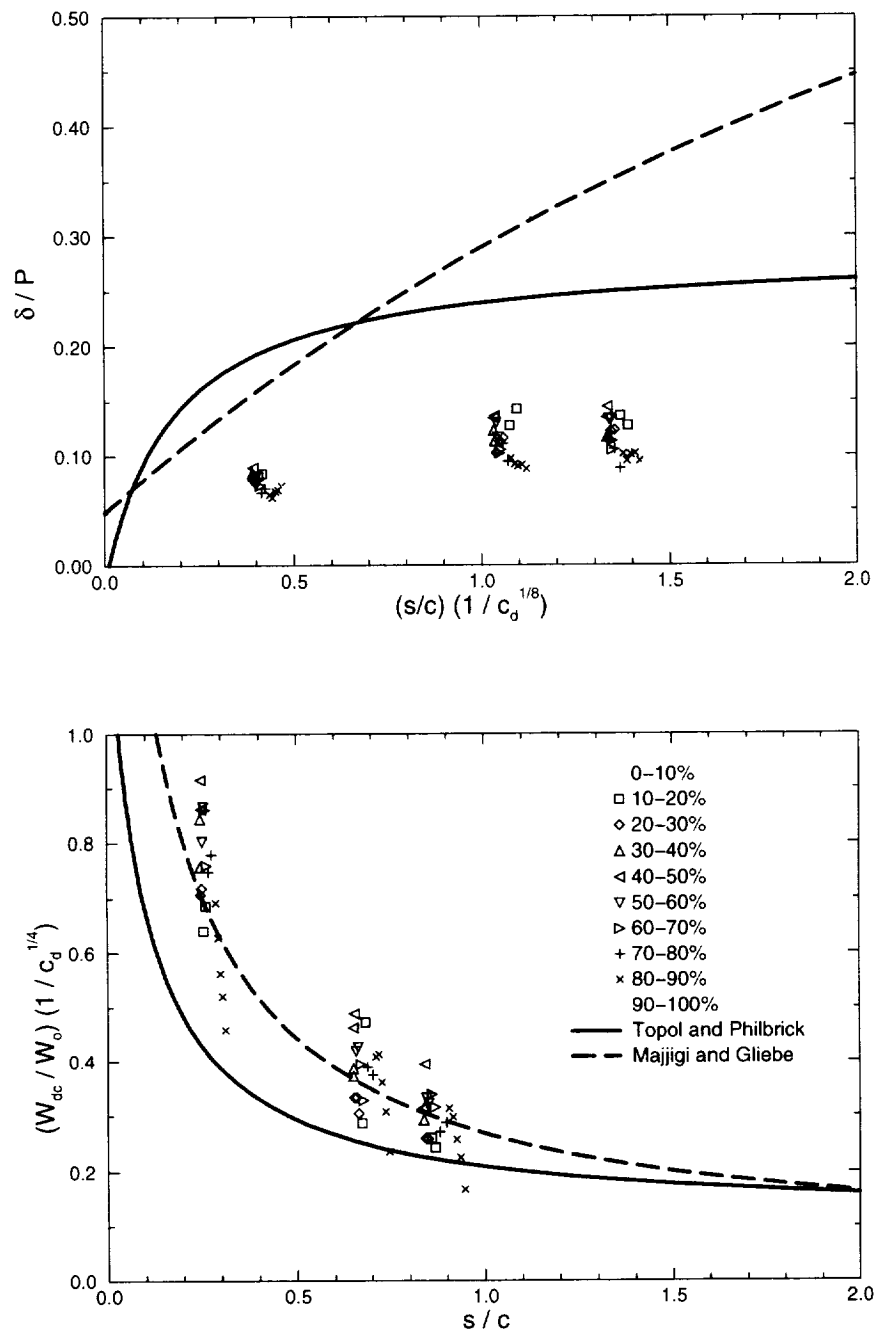


Figure 5.54: Correlation data of wake width and centerline velocity deficit from the experimental LDV data split into 10% interval ranges in blade span.

For all the span locations except the 10% location, the three *ADPAC* solutions lie fairly close together. At the 10% span location (Figure 5.55), the largest difference between the *ADPAC* solutions is seen in the prediction of wake width decay. The standard coefficient Baldwin-Lomax model results show the wake width growing rapidly downstream and the velocity deficit also decaying quickly; this is most likely the result of the Baldwin-Lomax prediction of the hub boundary layer merging into the lower span of the wake.

At the three middle span locations (25%, 50%, and 75% in Figures 5.56, 5.57, and 5.58), some general trends can be identified. With respect to the wake width prediction, the *ADPAC* results all pass through the first two stations of experimental data, but drift slightly above the final measuring station data. Also, the Spalart-Allmaras results are mostly higher than the Baldwin-Lomax (std. coeff.) results which are in turn higher than the Baldwin-Lomax (mod. coeff.) results. In the velocity deficit plots, a significant difference between the Spalart-Allmaras model results and both of the Baldwin-Lomax model results is displayed. The Baldwin-Lomax results, regardless of coefficients used, drop off rapidly immediately behind the blade trailing edge and then abruptly change decay rates. In contrast, the Spalart-Allmaras results shows a smoother decay rate away from the fan blade. These line plots quantify the differences noted previously in the blade-to-blade contour plots. It is interesting to note that by the first measuring station, the three models are approximately back together which is the reason no significant differences were apparent in the pitchwise velocity plots at Station 1.

Each of the data sets from 10% to 90% span was fitted to the correlation function using the method described above. The coefficients of the curve fits are listed in Table 5.1 and the curves are plotted in Figure 5.60 along with the experimental data. The experimental data is shown by a vertical bar with caps representing the range of data from 10% to 90% span at each of the three measuring stations (labeled as **1**, **2**, and **3**). The curve fits from the three *ADPAC* solutions lie closely together with little differences. As was seen in the previous plots at each of the five spanwise locations, the Spalart-Allmaras results predict a slightly larger wake width over the two Baldwin-Lomax results, and all the *ADPAC* solutions pass high through the experimental data ranges. With respect to the velocity deficit, the sharp change in decay rate shown in the Baldwin-Lomax results previously has been smoothed out by the curve fit; however, the two Baldwin-Lomax curve fits still do predict a faster decay rate in velocity deficit than does the Spalart-Allmaras curve fit.

The three *ADPAC* curve fits for wake correlations are compared in Figure 5.61 with those found in the literature. These curve fits included the effect of c_d in the correlation and the corresponding curve fit coefficients are listed in Table 5.2. The two curve fits from the literature [36, 35] are shown on the plots using thick lines with symbols. The correlation form for the wake width (δ) appears to be not as well suited as for the centerline velocity deficit. The two curve fits from the literature and the group of three *ADPAC* curve fits vary greatly in predicting the trend of wake width decay. All of the curve fits with respect to velocity deficit appear to reasonably follow the same trend with the *ADPAC* results matching closely to the correlation presented by Majjigi and Gliebe. While it appears to be a point of discrepancy and interest, further investigations into determining the correct parameters to normalize correlation functions across geometry and flow condition ranges lies outside the scope of this work.

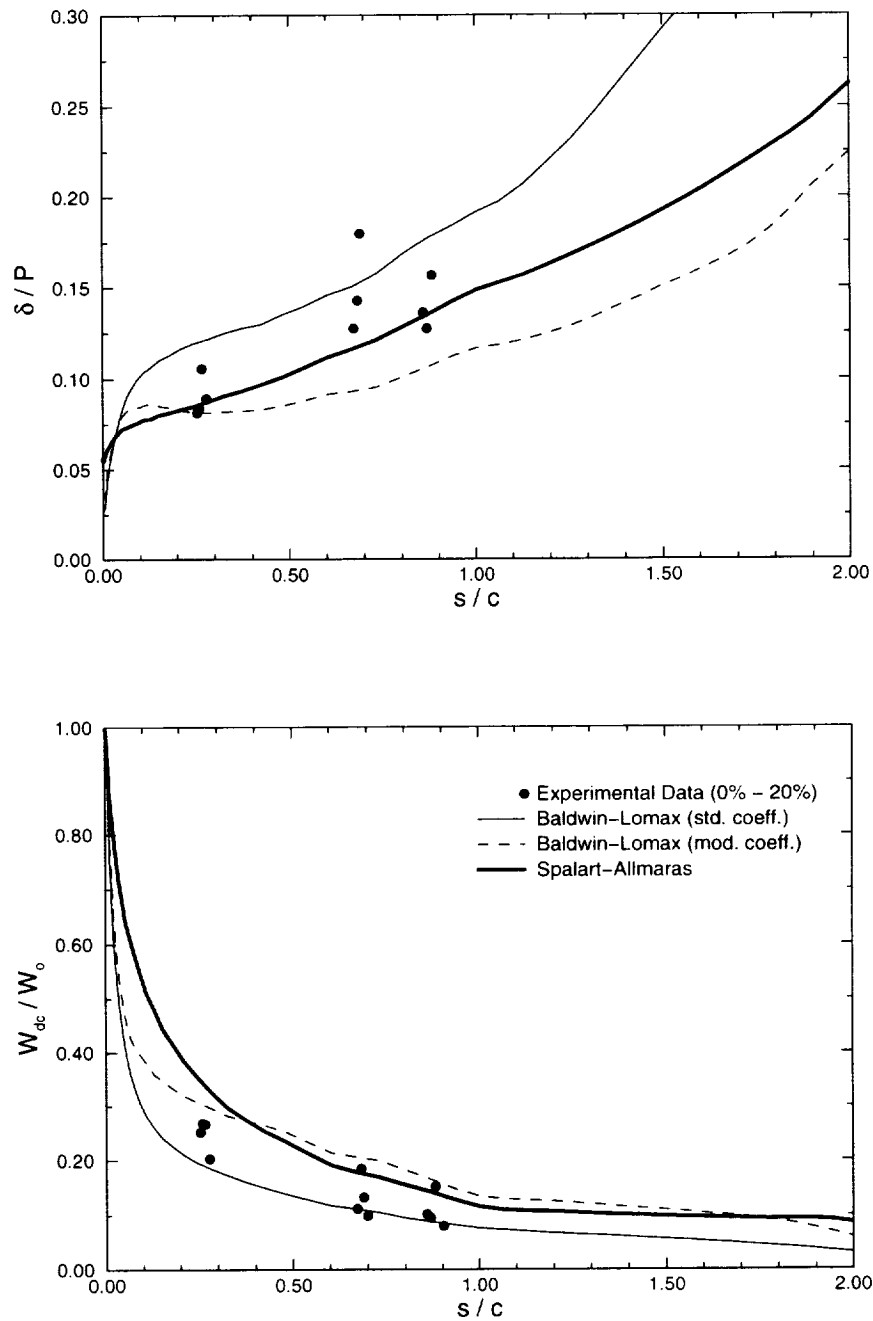


Figure 5.55: Wake width and centerline velocity deficit data from approximately 10% span extracted from the experimental LDV data set and the *ADPAC* numerical solutions. (See Figures 5.21, 5.22, and 5.23)

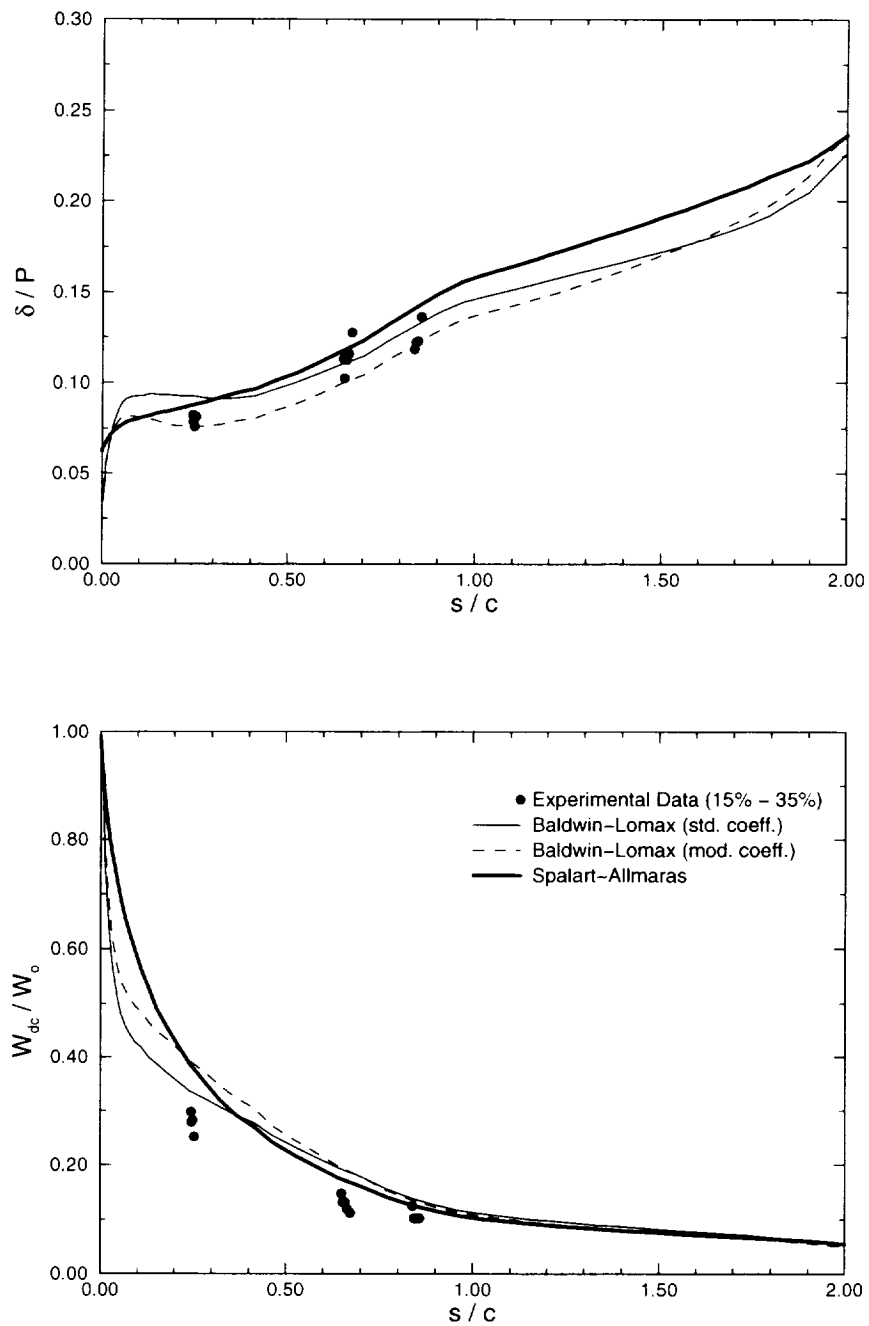


Figure 5.56: Wake width and centerline velocity deficit data from approximately 25% span extracted from the experimental LDV data set and the *ADPAC* numerical solutions. (See Figures 5.24, 5.25, and 5.26)

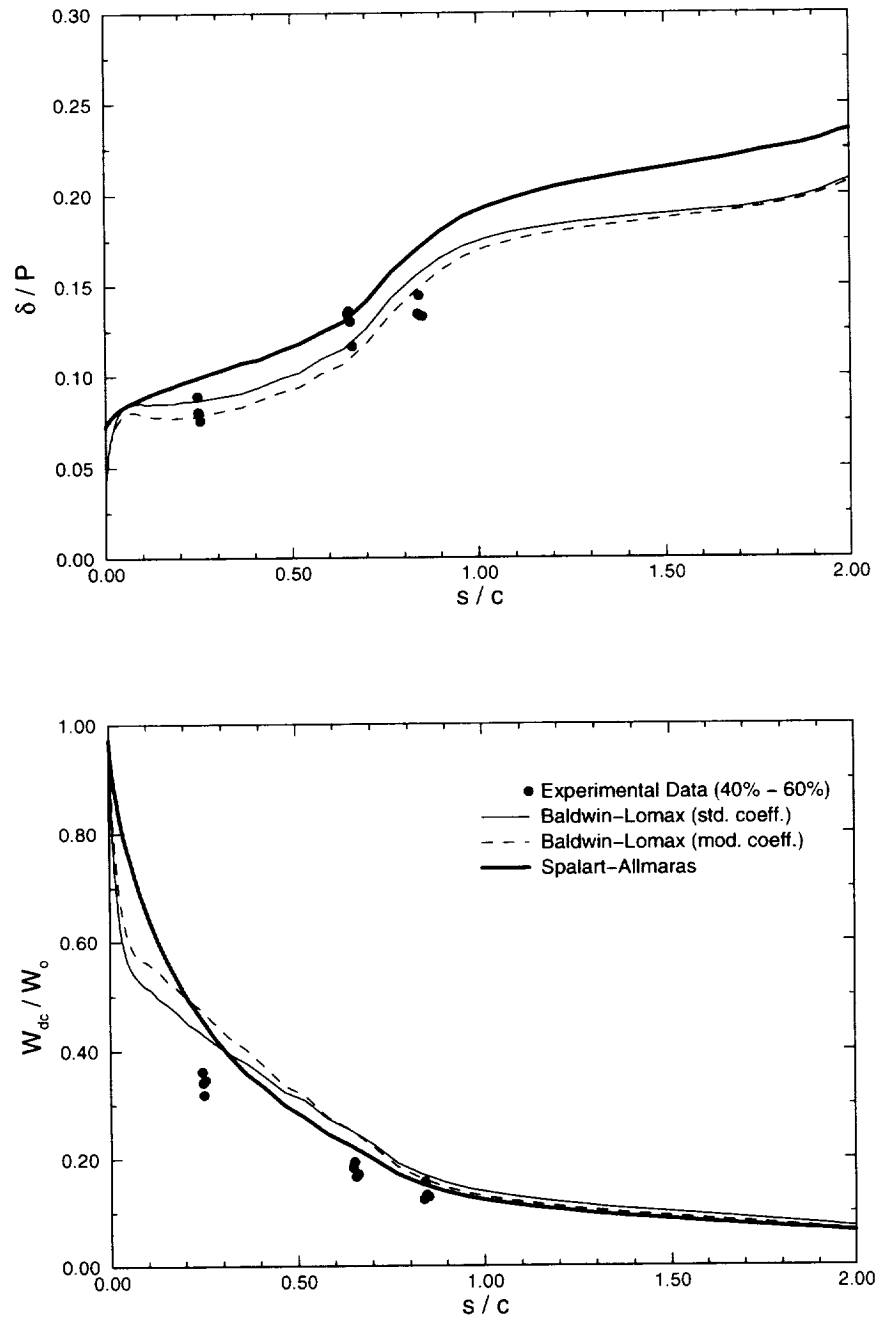


Figure 5.57: Wake width and centerline velocity deficit data from approximately 50% span extracted from the experimental LDV data set and the *ADPAC* numerical solutions. (See Figures 5.27, 5.28, and 5.29)

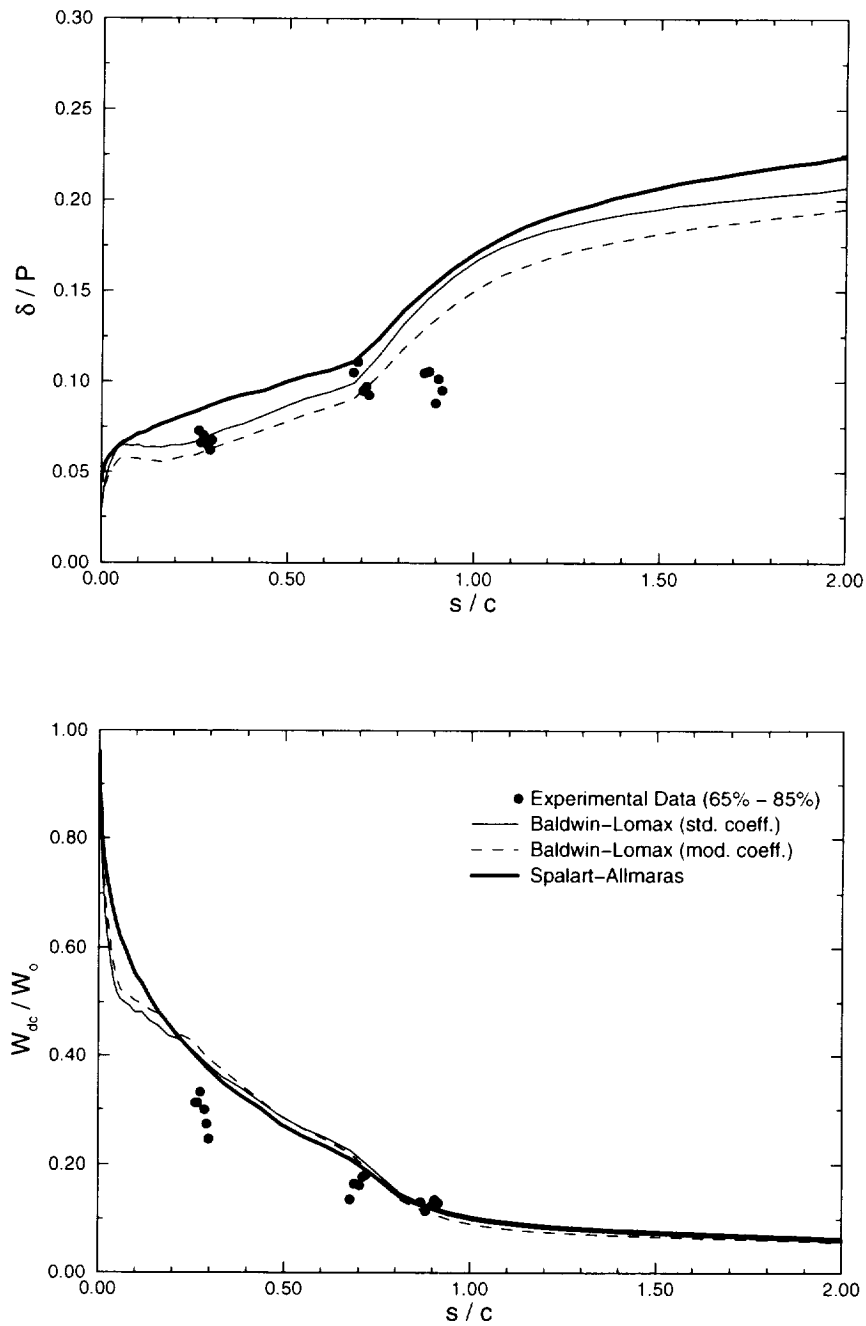


Figure 5.58: Wake width and centerline velocity deficit data from approximately 75% span extracted from the experimental LDV data set and the *ADPAC* numerical solutions. (See Figures 5.30, 5.31, and 5.32)

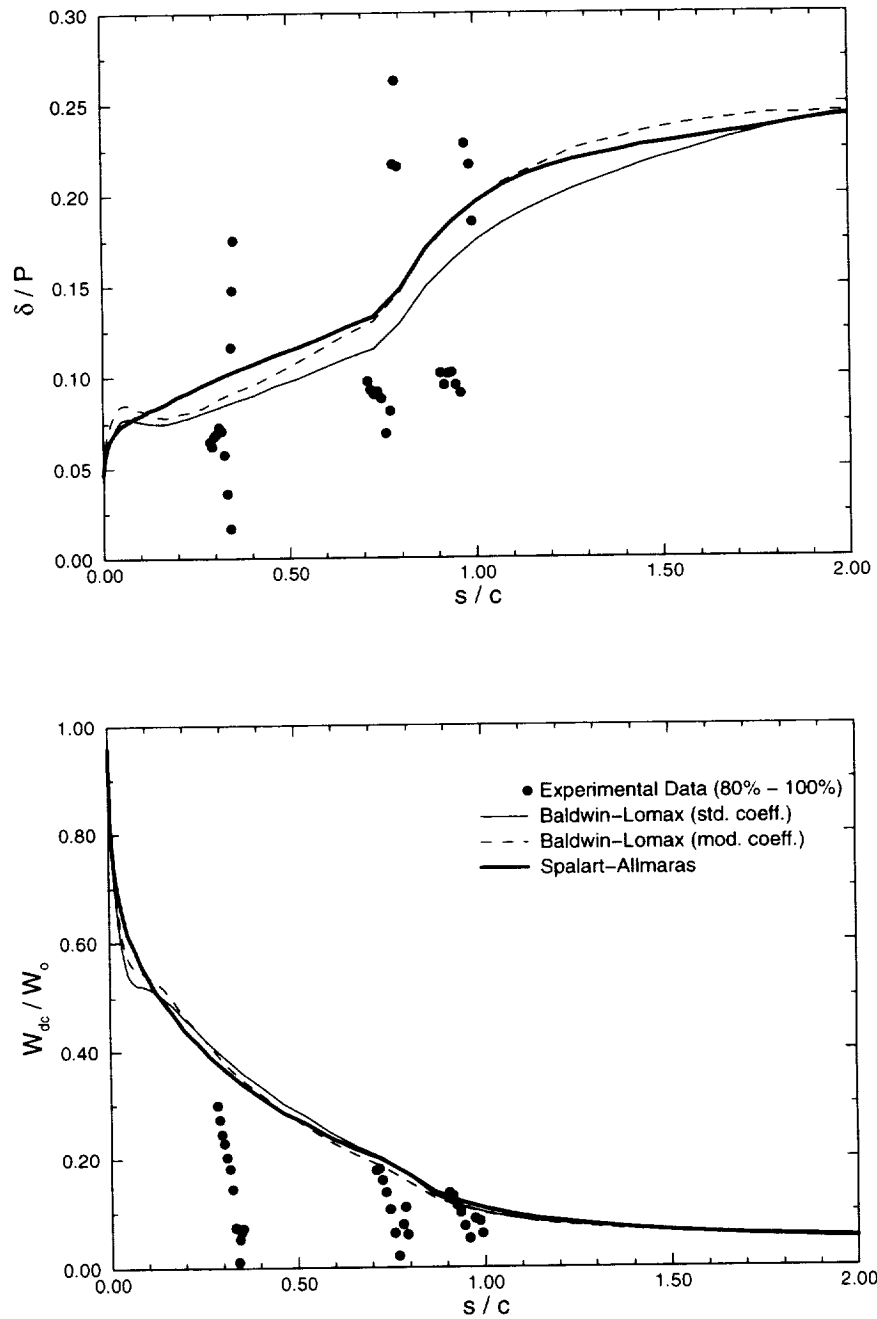


Figure 5.59: Wake width and centerline velocity deficit data from approximately 90% span extracted from the experimental LDV data set and the *ADPAC* numerical solutions. (See Figures 5.33, 5.34, and 5.35)

Wake Width (δ) Correlation Coefficients			
	a	b	c
Baldwin-Lomax (std)	0.1527	0.05465	0.2983
Baldwin-Lomax (mod)	0.1133	0.05247	0.1377
Spalart-Allmaras	0.1331	0.06315	0.2005

Velocity Deficit (W_{dc}) Correlation Coefficients			
	a	b	c
Baldwin-Lomax (std)	0.2509	0.8611	8.8474
Baldwin-Lomax (mod)	0.0051	0.8553	6.1418
Spalart-Allmaras	-0.0964	0.9240	5.6575

$$\text{Correlation Form: } y = \frac{a x + b}{c x + 1}$$

Table 5.1: Values of the correlation coefficients (a, b, c) for the curve fit shown in Figure 5.60.

Wake Width (δ) Correlation Coefficients			
	a	b	c
Baldwin-Lomax (std)	0.09710	0.05472	0.1887
Baldwin-Lomax (mod)	0.07289	0.05250	0.0906
Spalart-Allmaras	0.08543	0.06313	0.1297

Velocity Deficit (W_{dc}) Correlation Coefficients			
	a	b	c
Baldwin-Lomax (std)	0.9554	2.1953	10.4963
Baldwin-Lomax (mod)	0.1824	2.1649	7.7077
Spalart-Allmaras	-0.1628	2.3189	6.1711

$$\text{Correlation Form: } y = \frac{a x + b}{c x + 1}$$

Table 5.2: Values of the correlation coefficients (a, b, c) for the curve fits including the effects of c_d shown in Figure 5.61.

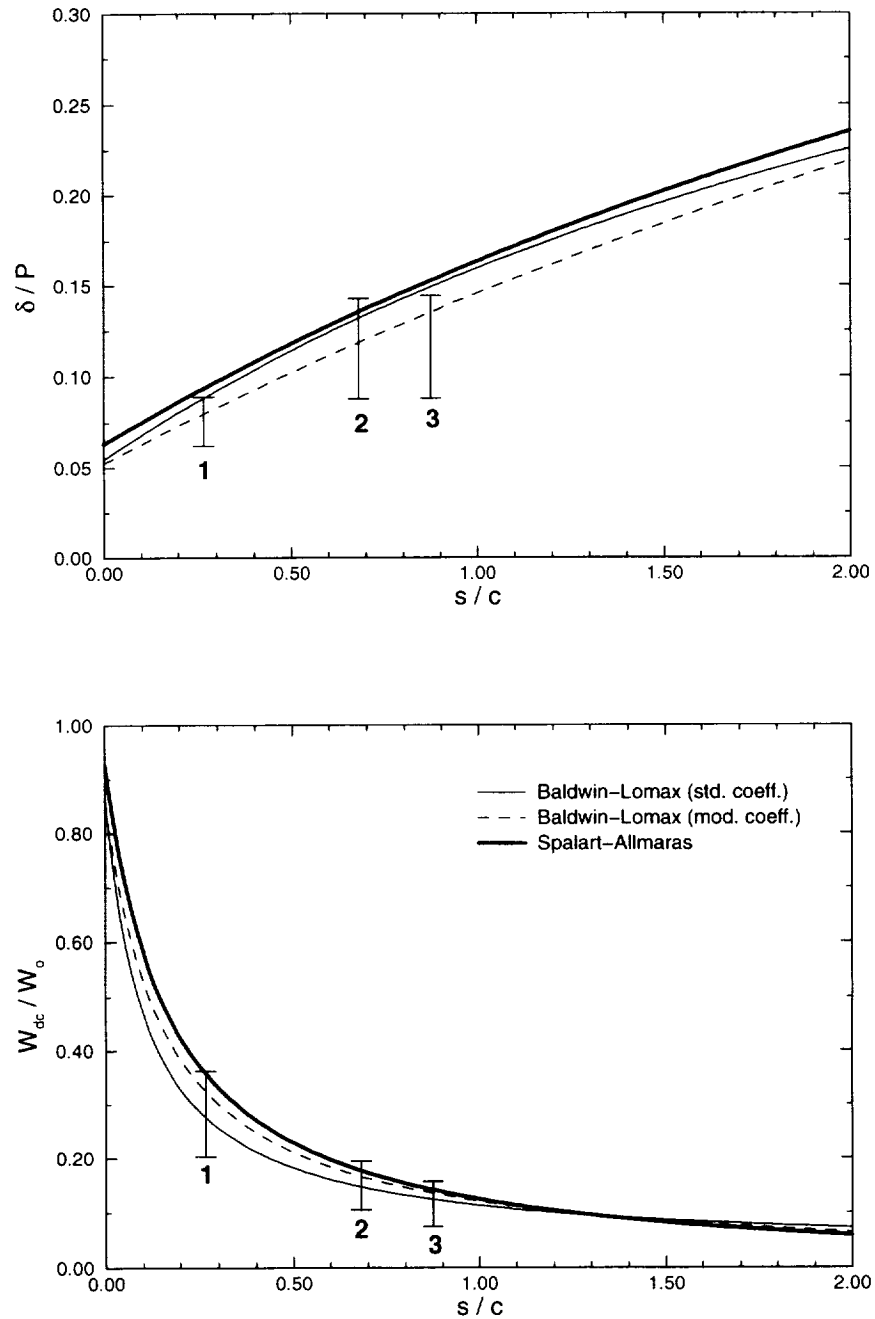


Figure 5.60: Curve fits of the wake width and centerline velocity deficit data from 10% to 90% blade span for each of the three different turbulence models. The ranges of experimental data from each of the NASA measuring stations are also included.

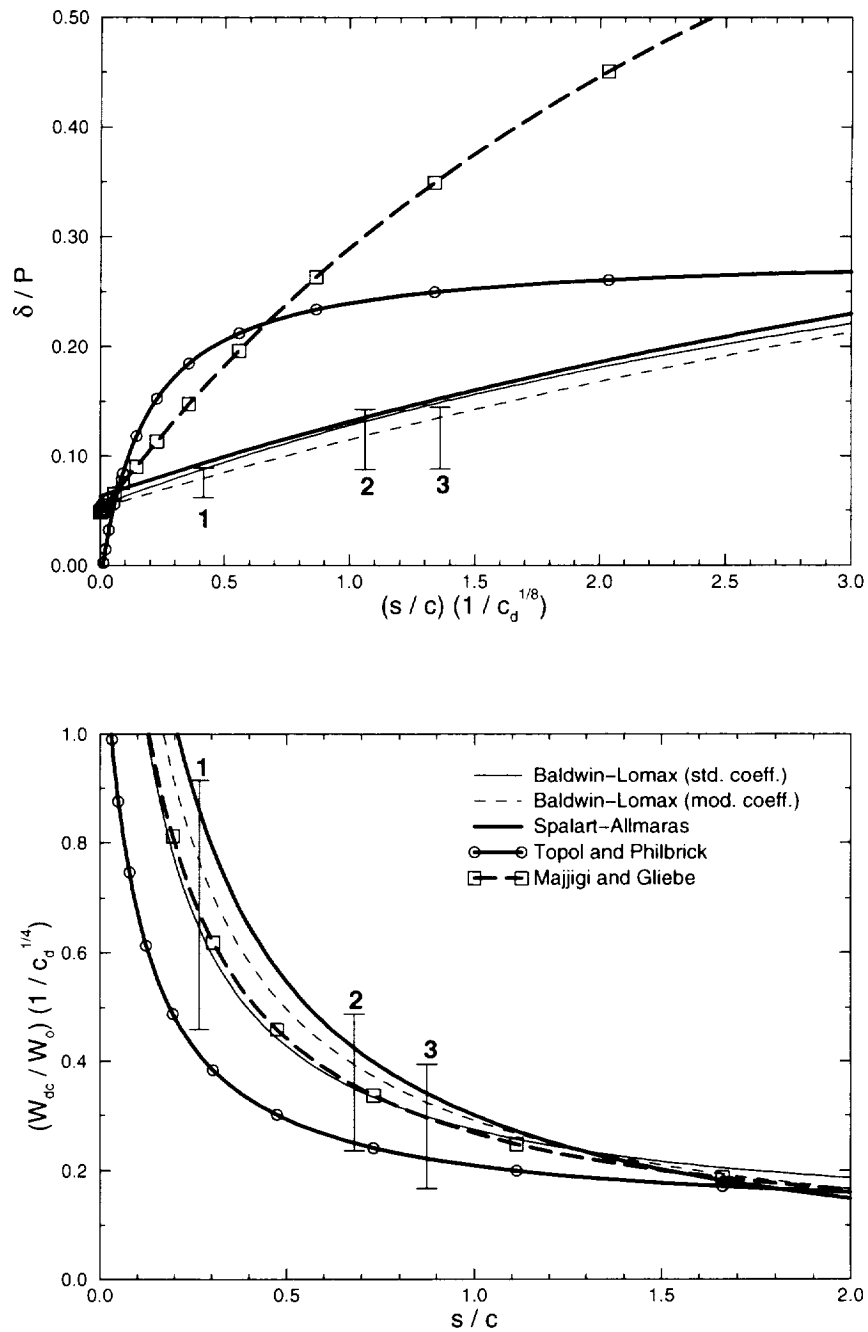


Figure 5.61: Curve fits of the wake width and centerline velocity deficit data from 10% to 90% blade span including the effects of c_d . The ADPAC solutions using the three different turbulence models are compared with correlation curves from the literature. The ranges of experimental data from each of the NASA measuring stations are also included.

5.7.3 Similarity Profiles

In addition to the single-value measurements of wake width (δ) and centerline velocity deficit (W_{dc}), the overall shape of the wake profiles can be compared through the proper nondimensionalization process. The velocity profile can be normalized by:

$$\frac{W_d}{W_{dc}} = \frac{W_o - W}{W_o - W_{min}}$$

and can be plotted against η (defined earlier in Figure 5.53); positive values of η correspond to the pressure side of the wake and negative values of η correspond to the suction side. Through this transformation, it has been shown by several authors [38, 39, 40, 41, 42] that the velocity profiles fall onto a single curve approximated by the following Gaussian function:

$$\frac{W_d}{W_{dc}} = e^{-\ln 2 \eta^2}$$

A examination of the experimental data by 10% spanwise increments was also performed on the similarity profiles shown in Figures 5.62 and 5.63; the data included in these figures are from all three measuring stations. The theoretical Gaussian profile is included in the similarity profile plot for reference. Figure 5.62 includes all the data points and Figure 5.63 includes data from 10% to 70% span only. Again the interaction with the endwall flow regions and tip vortex creates a wider scatter in the data points in the outer span regions; for this reason, the similarity data will be fitted only if it lies between 10% and 70% span. A similar limitation to inner span data was also performed in the literature [36] but to a more severe degree (30% to 60%).

Due to the asymmetry in the profile, caused by differences in the pressure and suction side boundary layers, the symmetric Gaussian form is not appropriate to use as a basis function for the curve fit. Instead a Fourier series approximation can be used, represented by:

$$\frac{W_d}{W_{dc}} = \frac{A_0}{2} + \sum_{n=1}^{NF} \left(A_n \cos \frac{n\pi x}{L} + B_n \sin \frac{n\pi x}{L} \right)$$

where NF is the number of terms used in the curve fit.

Using the experimental LDV data as a test case, a curve fitting analysis was performed to determine the number of frequencies required to adequately model the similarity profile. The results of the analysis are shown Figure 5.64. The upper portion of the figure shows the approximation of the data using an increasing number of harmonic frequencies from 0 to 30. The lower two plots are a measurement of a curve fitting parameter, χ^2 , and a measurement of the profile change resulting from adding one more frequency. From this analysis, fifteen frequencies (thirty Fourier coefficients) will be used to model the similarity profiles.

The similarity profiles from the experimental LDV data and the three *ADPAC* numerical solutions are shown in Figures 5.65, 5.66, 5.67, and 5.68, respectively. The 10%-70% span data in each of these figures have been separated by measuring station location. At Station 1, the two Baldwin-Lomax *ADPAC* solutions are predicting a greater amount of asymmetry than was predicted with the Spalart-Allmaras model or measured experimentally. This difference in asymmetry appears to be more noticeable on the

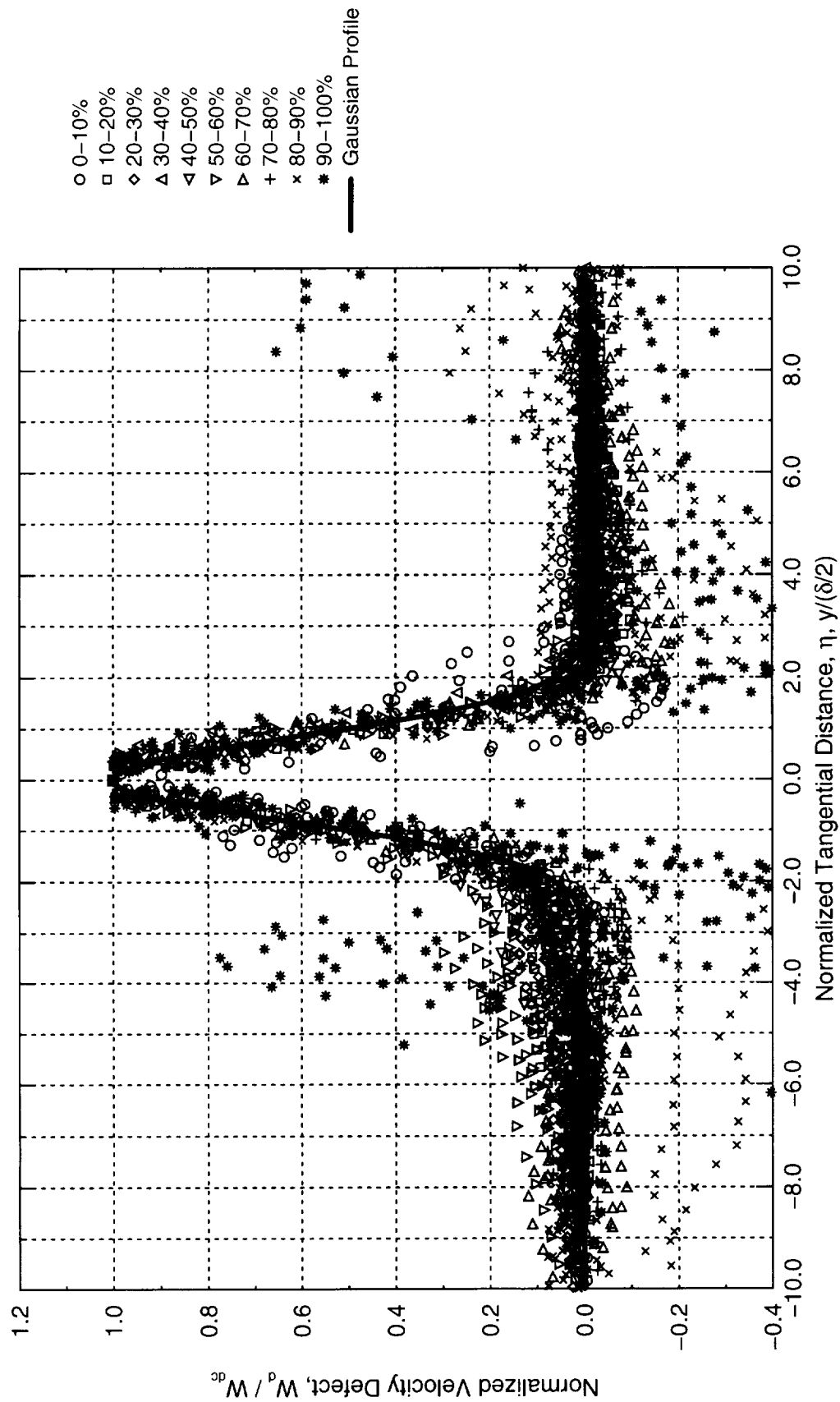


Figure 5.62: Similarity profiles reduced from the experimental LDV data at all three measuring stations, plotted in 10% span intervals.

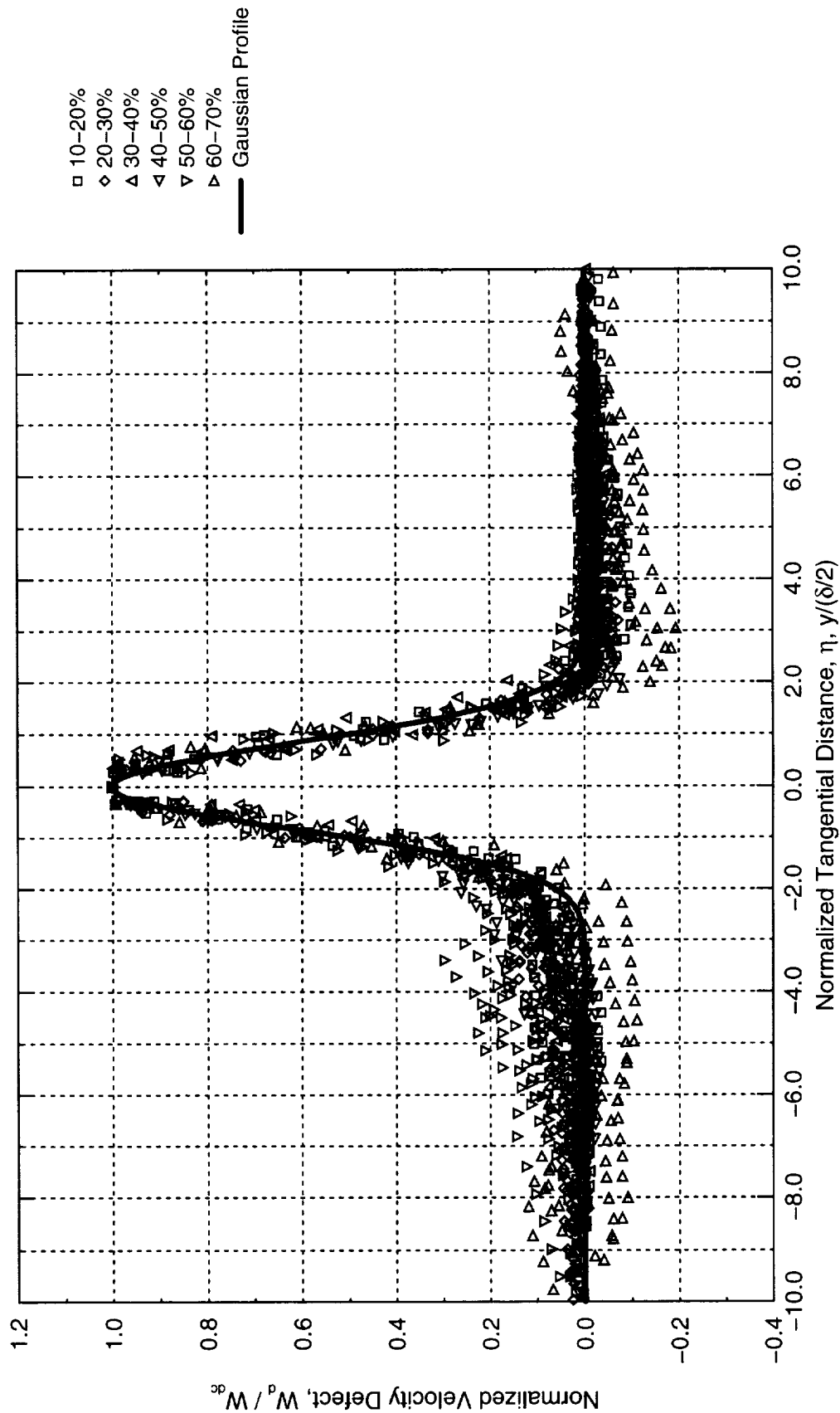


Figure 5.63: Similarity profiles reduced between 10% and 70% from the experimental LDV data at all three measuring stations, plotted in 10% span intervals.

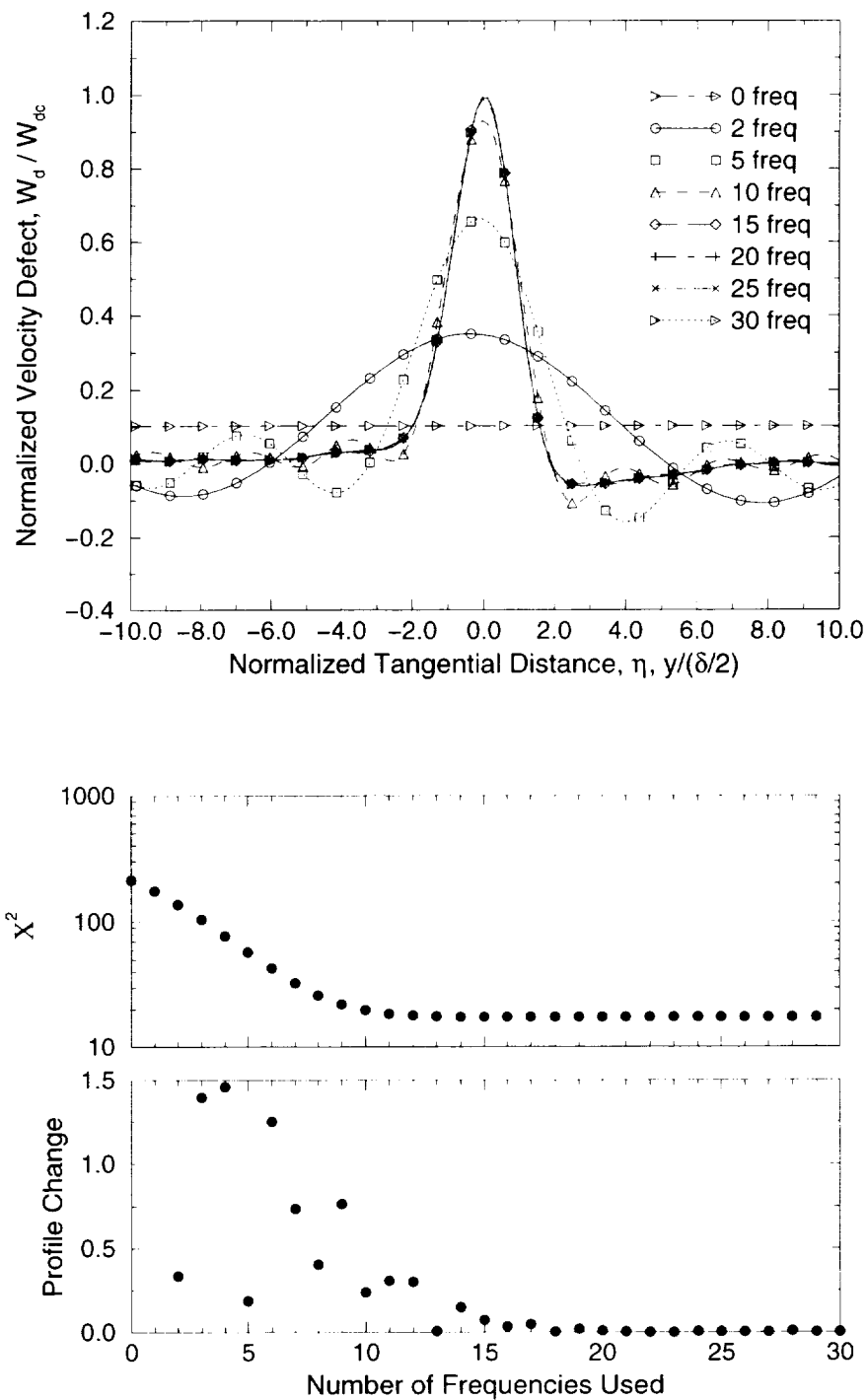


Figure 5.64: Curve fitting analysis used to determine the minimum number of frequencies required to model the similarity profile data using a Fourier series.

suction side of the wake ($-\eta$) and is reduced downstream at Stations 2 and 3. The experimental data also exhibits a large amount of variation in the suction-side wake region with respect to span location than do the *ADPAC* predicted results.

The experimental data and the three *ADPAC* results were curve fit using the above described Fourier series approximation. These curve fits are shown in Figure 5.69 along with the symmetric Gaussian profile. The asymmetry of the Baldwin-Lomax solutions at Station 1 can be seen on the left side of the top plot in the figure. The predicted *ADPAC* solutions match the pressure side of the wake ($+\eta$) experimental data curve fit better than along the suction side of the wake. The experimental data measures a slower decay of the velocity deficit on the suction side. The differences between the experimental data and the numerical solutions at the stations farthest downstream may also be exaggerated due to the extreme stretching performed on the data through the similarity transformation.

The *ADPAC* solution curve fits lie very close to each other and follow the trend of the experimental data curve fit, that the “dip” in the similarity profile on the pressure-side of the wake deepens with distance downstream. The differences in the magnitude of the dip is related to the choice of W_o , as opposed to W_{max} , as the normalizing freestream velocity. The choice of W_o was made to accentuate the asymmetry of the similarity profile when compared to the Gaussian profile. In other work [36, 41], this profile asymmetry has been found to exist as far downstream as $x/c = 0.75$ to $x/c = 4.0$. Other authors [39, 40, 42] have used the different length scales (η_p and η_s shown in Figure 5.53) to account for the asymmetry in the similarity profile.

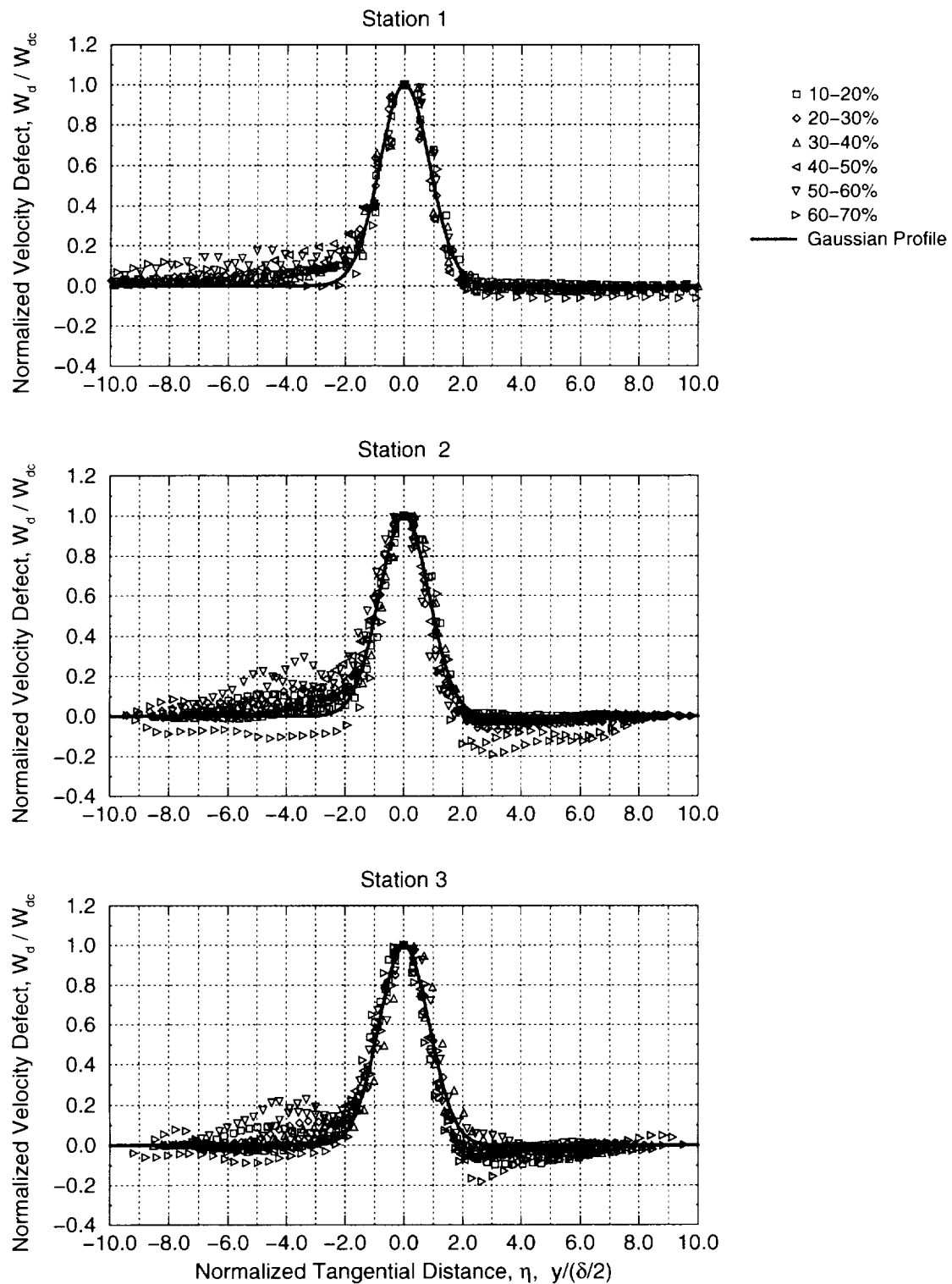


Figure 5.65: Similarity profiles reduced from the experimental LDV data at Stations 1, 2, and 3 and plotted in 10% span intervals.

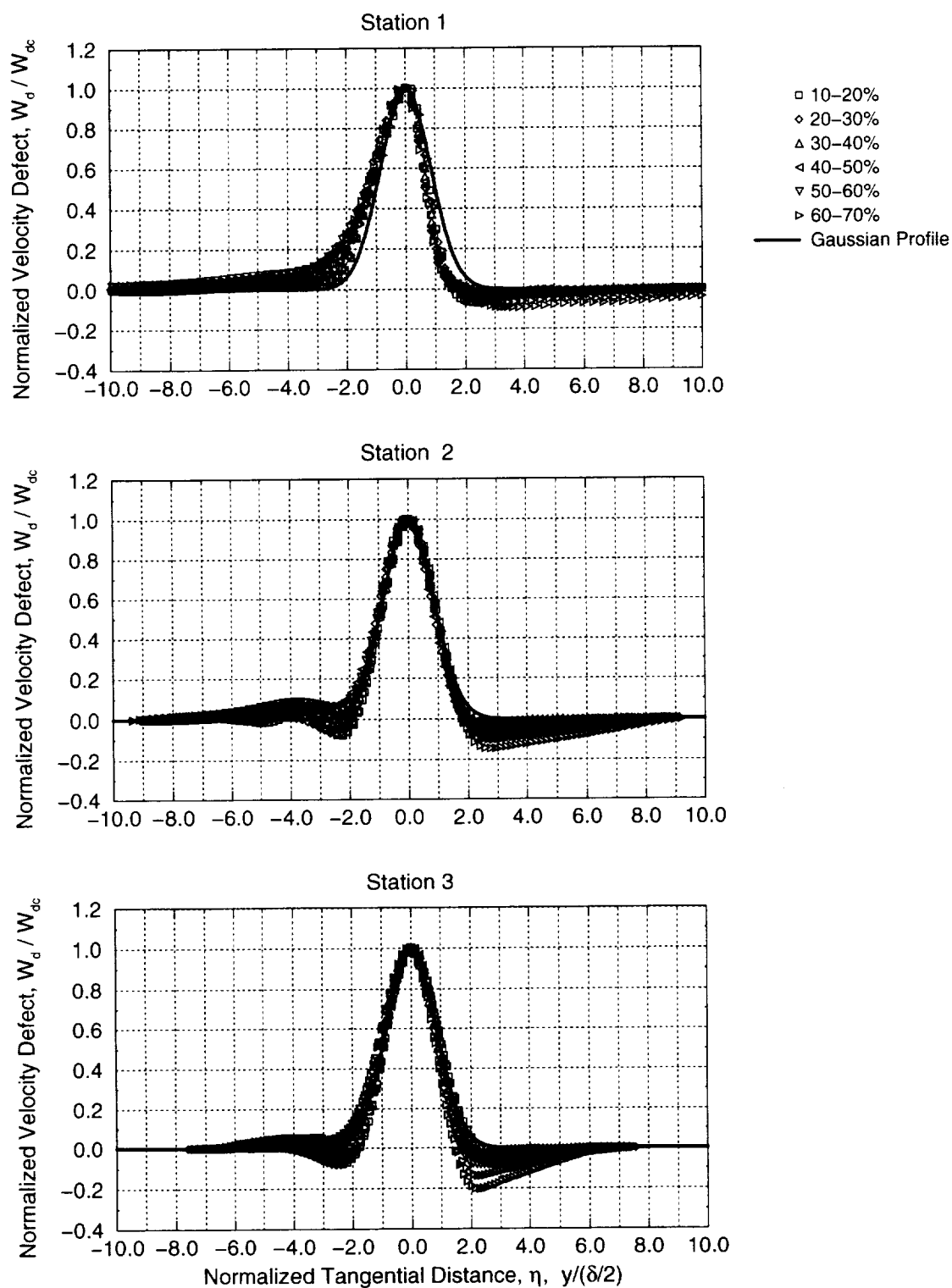


Figure 5.66: Similarity profiles reduced from the *ADPAC* Baldwin-Lomax (std. coeff.) solution at Stations 1, 2, and 3 and plotted in 10% span intervals.

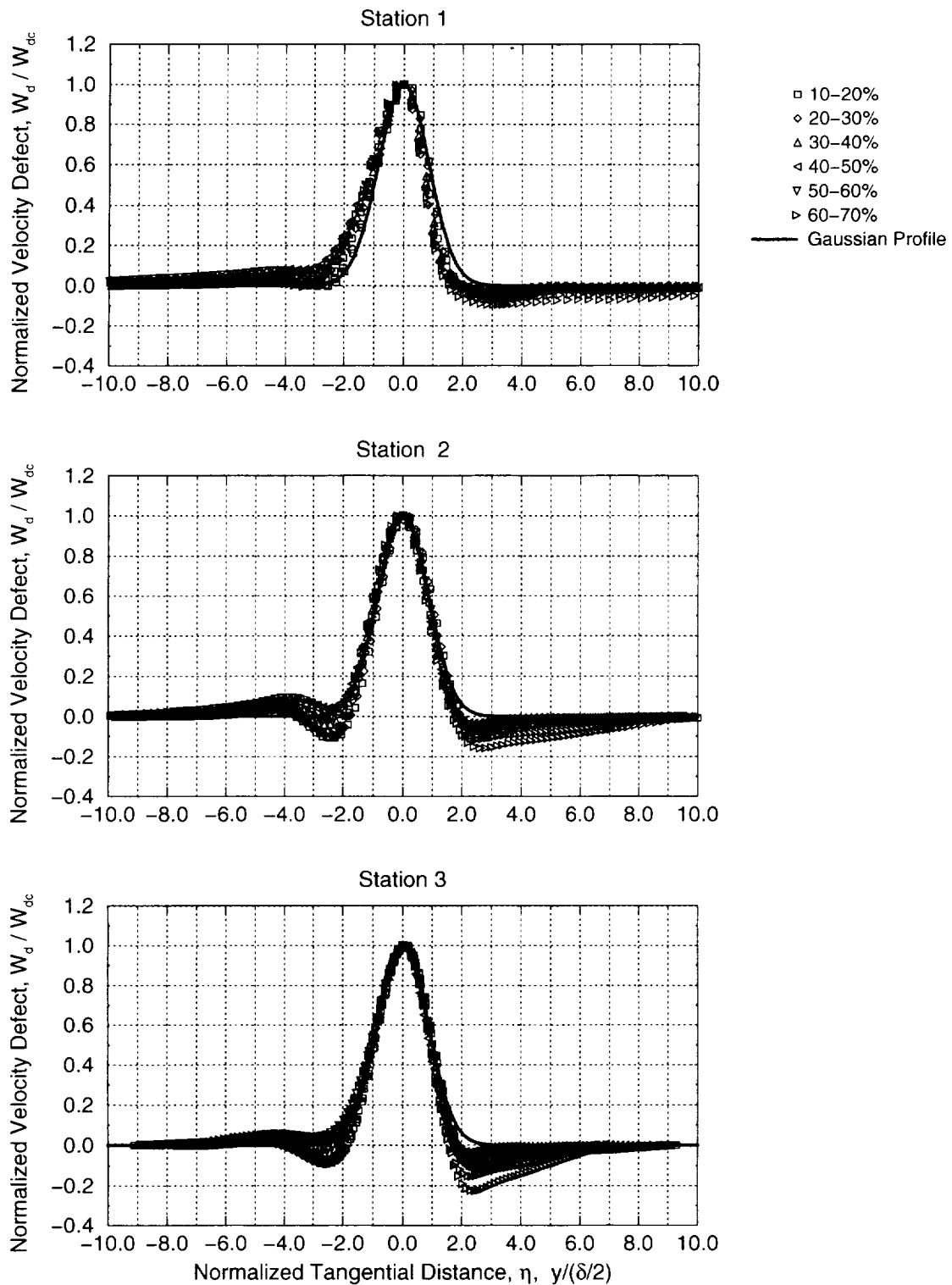


Figure 5.67: Similarity profiles reduced from the *ADPAC* Baldwin-Lomax (mod. coeff.) solution at Stations 1, 2, and 3 and plotted in 10% span intervals.

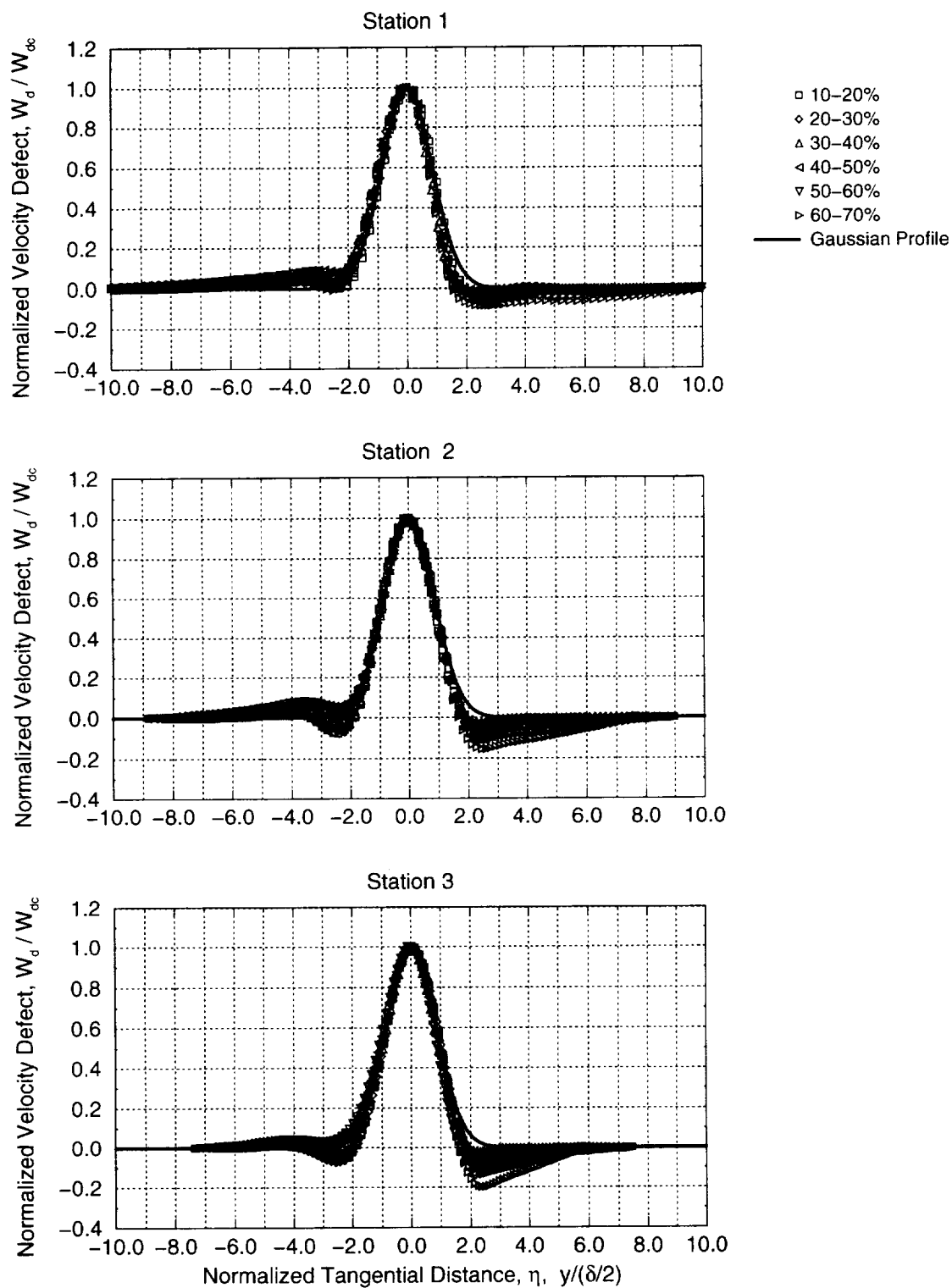


Figure 5.68: Similarity profiles reduced from the *ADPAC* Spalart-Allmaras solution at Stations 1, 2, and 3 and plotted in 10% span intervals.

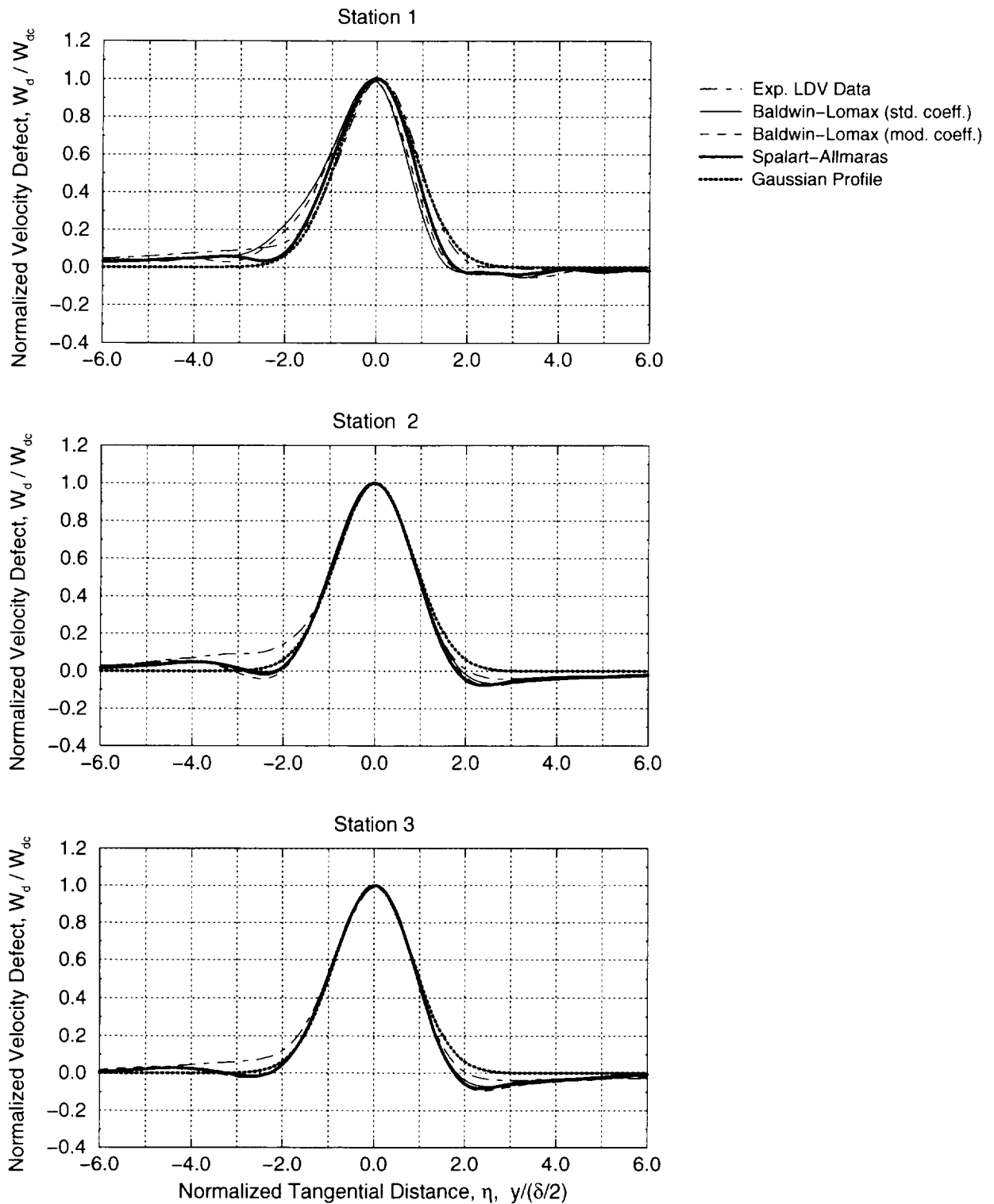


Figure 5.69: Comparison between curve fits of the experimental and numerical similarity profile data at Stations 1, 2, and 3 along with the theoretical Gaussian profile.

Chapter 6

CONCLUSIONS

The work and results compiled in this report were completed as part of the AST project in an effort to support aircraft noise reduction research. As a major contributor to overall engine noise, the interaction of the fan rotor wakes with the bypass stators is one of the primary areas of interest. In order to predict the interaction of the wakes with the bypass stator blade row, an accurate definition of the wake size, shape, and orientation is needed. Using computational fluid dynamics (CFD), the wakes behind the fan blades of a high-bypass turbofan engine were predicted under this program. This study specifically investigated the effect of different turbulence models on the wake prediction capability of a flow solver code.

The aerodynamic predictions for the cases described in this study were obtained using the *ADPAC* analysis code. The *ADPAC* code is a general purpose turbomachinery aerodynamic design analysis tool which has undergone extensive development, testing, and verification. Part of this program focused on incorporating the one-equation Spalart-Allmaras turbulence model into *ADPAC*. A detailed description of the numerical implementation of the model was presented including the implicit discretization of the transport equation and the linearization of the transport equation source term. As several of the terms in the Spalart-Allmaras model are based on the distance to the nearest viscous wall, a “wall-finding” routine was developed and added to *ADPAC*. Due to the flexibility of the multi-block capability and parallelization of *ADPAC*, this task was not as straight forward as might first appear. In order to avoid unnecessary re-computation of the values, the nearest wall distance field is written out as part of the turbulence model restart file.

As part of the Spalart-Allmaras model incorporation into *ADPAC*, several test cases were calculated and compared with the results collected with the algebraic Baldwin-Lomax model. The specific test cases run were a flat plate, a subsonic symmetric airfoil, a transonic bump, and a transonic turbine cascade. The results from the flat plate calculations using the Baldwin-Lomax model and Spalart-Allmaras model did not show significant differences in the prediction of surface quantities such as wall shear stress and friction coefficient. However, a noticeable difference between results was in the prediction of the turbulent eddy viscosity (μ_t) field away from the wall. Due to the split inner/outer nature of the Baldwin-Lomax model, a sharp bend in the μ_t distribution occurred at the crossover point; whereas the Spalart-Allmaras model predicted a much more smooth

distribution of μ_t .

Probably the most interesting and applicable test case calculated with respect to wake prediction was the symmetric airfoil. Detailed measurements of both mean and fluctuating flow quantities in the 2-D wake shed from the airfoil provided a benchmark test case which accentuated the differences between turbulence models when predicting wake shape and decay. In addition to *ADPAC* solutions of the airfoil flow, numerical solution were collected using the *OVERFLOW* flow prediction code using two different turbulence models (Baldwin-Barth and Spalart-Allmaras). Comparisons made with experimental data at thirteen downstream axial stations showed a significant improvement in wake prediction using the Spalart-Allmaras model over the Baldwin-Lomax model. When the centerline velocity distributions were compared, the *ADPAC* Baldwin-Lomax results and the *ADPAC* Mixing-Length results under-predicted the recovery of the velocity magnitude. The Spalart-Allmaras model results from both *ADPAC* and *OVERFLOW* passed through the data points and predicted a more accurate velocity decay rate in the wake region than did the algebraic models. The *ADPAC* Spalart-Allmaras predictions of Reynolds stress distribution also showed an improved capability over the Baldwin-Lomax model.

The final two test cases calculated also showed improvements in the flow prediction using the Spalart-Allmaras model. *ADPAC* results simulating transonic flow over an axisymmetric bump showed closer shock location to experimental data and a more well-defined recirculation region using the Spalart-Allmaras model than the Baldwin-Lomax model. The prediction of recirculating and reversed flow regions becomes very important when modeling the flow around complex turbomachinery geometries. The sensitivity to the inlet turbulence level was evaluated using the Mark II turbine vane geometry. A series of *ADPAC* solutions were collected using the Spalart-Allmaras turbulence model with increasing values of inlet turbulence. The prediction of the surface pressure measurement showed almost no influence from the inlet turbulence levels. However, heat transfer coefficient predictions, which matched well with the experimental data, did show a correlation with the inlet turbulence levels with higher levels of inlet turbulence corresponding to higher values of heat transfer coefficient. It has become standard practice when using the Spalart-Allmaras model in *ADPAC* to set the *initial* value of χ to 20 and the *inlet* value to 1; this higher value of initial turbulence triggers the production terms within the model before they are damped out.

In order to determine the near-wall spacing required to obtain a mesh-independent solution with respect to the turbulence model, two geometries were modeled using a series of meshes with sequentially finer near-wall spacings. The two geometries used were a flat plate and a midspan slice of a compressor stator. The results of this study demonstrated that the first point away from the wall should be within a y^+ value of 5 to obtain mesh-independent turbulence fields. In the 3-D stator midspan case, the wake width and velocity deficit were calculated and compared between the Baldwin-Lomax model results and Spalart-Allmaras results. At the stator trailing edge, both models predicted approximately the same magnitude of velocity deficit; however, the Baldwin-Lomax results showed a much sharper decay in velocity deficit than the Spalart-Allmaras results. The Baldwin-Lomax predicted velocity deficit reached its terminal value at approximately 0.40 chords downstream of the trailing edge, while the deficit predicted using the Spalart-Allmaras model continued to decay up to a full chord downstream. Given the close proximity of neighboring blades in a turbomachine, this difference between the two

turbulence models in the prediction of wake decay immediately behind the stator blade has significant implications on aerodynamic performance, acoustic production, and structural forced response.

Following the incorporation of the Spalart-Allmaras model into the *ADPAC* code and validation, the primary focus of this work was undertaken. Using the geometry of the Allison/NASA Low Noise Fan blade, numerical solutions were collected using *ADPAC* with different turbulence models: the algebraic Baldwin-Lomax model with standard coefficients, the Baldwin-Lomax model with modified coefficients, and the one-equation Spalart-Allmaras model. The only difference between the first two turbulence models used was the values of C_{cp} and C_{Kleb} ; these values were adjusted to compensate for the adverse pressure gradient in fan blade row based on a sensitivity study by Granville. The mesh used to collect the *ADPAC* solutions was an H-grid topology with over 830,000 points. The predicted results were compared with experimental LDV data measured at three axial stations.

The overall performance of the fan was calculated in terms of pressure ratio and efficiency for each of the three *ADPAC* solutions. The *ADPAC* results using the Baldwin-Lomax model with standard coefficients slightly over-predicted both the pressure ratio slightly and efficiency. When the Baldwin-Lomax coefficients were modified, the pressure ratio and efficiency were lowered closer to the experimental values. The Spalart-Allmaras results were even lower, matching most closely of the three numerical solutions with the experimental data; the pressure ratio was very close to the measured value and the efficiency was approximately 0.5 points high. The Spalart-Allmaras results also did not predict an overshoot in total pressure along the hub at the exit profile station as did both the Baldwin-Lomax models; this resulted in a smoother spanwise distribution of calculated efficiency.

Pitchwise distributions of axial velocity at five radial locations were compared between the three *ADPAC* solutions and the LDV data. In general, the *ADPAC* results matched fairly well with the majority of experimental results; however, some differences between the *ADPAC* results and the experimental data and between the different *ADPAC* turbulence model results existed primarily in the endwall regions. Near the outer-most radial span location (90%), all three of the *ADPAC* solutions predicted wider and deeper wakes shapes than the data showed. The modification of the Baldwin-Lomax coefficients was most apparent at the lowest radial span location (10%) where the standard coefficient model under-predicted the velocity deficit by 50% and the modified coefficients predicted a wake shape very similar to the Spalart-Allmaras model and predicted the velocity deficit close to the experimental level.

The orientation of the wake in the $r - \theta$ plane was investigated using wake centerline plots at the three NASA measuring stations. At each radial slice in both the experimental measuring matrix and the numerical mesh, the locations of the minimum velocity were plotted. The *ADPAC* predictions of the location of the wake centerline appeared to be very good, especially in the mid-span of the passage when compared with the experimental LDV data. From the hub to approximately 80% span, there was little difference among the three *ADPAC* solutions. Due to the degradation of a “clean” wake profile near the outer casing, the location of the minimum velocity becomes associated with the blade leading edge tip vortex and not the wake of the blade. This caused a

discontinuity in tangential location of the wake centerline which became more exaggerated farther downstream. By the third and final NASA measuring station, the experimental data displayed this discontinuity at approximately 90% span, whereas the *ADPAC* solutions broke closer to 95% span. There was also a difference between the three *ADPAC* solutions with respect to the tangential location of the tip vortex.

A wake definition study was completed to determine the character of the wake as it traveled downstream from the blade. This information is useful in predicting the intensity of interaction with downstream bypass stator vanes and the related noise propagation. Wake correlation formulations found in previous research were used to define the width and velocity deficit of the wake. Similar to the wake results in the near-wall spacing study, the two versions of the Baldwin-Lomax model results predicted a quick drop in velocity deficit immediately behind the blade, while the Spalart-Allmaras model results predicted a much smoother wake decay. Despite differences in wake decay rates, all three *ADPAC* solutions matched the experimental data fairly well, matching the velocity deficit distribution better than the wake width distribution. When compared with earlier wake correlation functions, the *ADPAC* curve fits and then experimental data aligned significantly better with the correlations defining the velocity deficit than the correlations defining the wake width. The wide variation in the correlations for wake width definition suggests that the current formulation does not completely account for everything impacting the wake such as variation in blade geometry and/or operating conditions. Further study in this area appears to be warranted, but was not included in the scope of the current work.

To evaluate the overall shape of the wake profile, similarity profiles were created through a nondimensionalizing process. A Fourier series approximation was fitted to the normalized wake profiles and compared between the *ADPAC* solutions and the experimental data along with the symmetric Gaussian profile. The asymmetry in the similarity profile due to blade loading as seen in previous studies was seen in both the experimental data and all of the *ADPAC* solutions. The predicted *ADPAC* solutions matched the pressure side of the wake experimental data curve fit better than along the suction side of the wake. The experimental data reflected a slower decay of the velocity deficit on the suction side. Between the wake correlations and the similarity profiles, more significant differences among the results from the three *ADPAC* turbulence models were found in the wake correlations functions than in the similarity profiles.

In summary, this work has successfully incorporated the one-equation Spalart-Allmaras model into the *ADPAC* flow prediction code and demonstrated the significant impact the choice of turbulence models has on the predicted downstream wake definition. The modification of the Baldwin-Lomax coefficients improved the prediction capability using the algebraic turbulence model in adverse pressure gradient flow regions (i.e., fan and compressor regions of a turbofan jet engine). With adequate near-wall mesh resolution, the Spalart-Allmaras turbulence model modeled the free shear regions more realistically than did the wall-bounded Baldwin-Lomax turbulence model. With a better understanding of the effects of different turbulence models, the confidence in using CFD to predict wake structure inputs to acoustic analyses should increase. Due to the possible sensitivity to individual blade geometries shown in the wake correlations, using validated CFD codes to analyze blade designs relatively quickly should be an advantage over extensive experimental testing. By improving the fidelity of the tools used in the engine

design and analysis process, the effort to reduce engine noise in the commercial aircraft industry can take greater strides forward.

References

- [1] NASA Facts, "Making Future Commercial Aircraft Quieter," NASA Lewis Research Center, FS-1997-07-003-LeRC, July 1997.
- [2] Spalart, P. R. and Allmaras, S. R., "A One-Equation Turbulence Model for Aerodynamic Flows," AIAA Paper 92-0439, AIAA 30th Aerospace Sciences Meeting & Exhibit, Reno, NV, January 1992.
- [3] Hall, E. J., Delaney, R. A., and Bettner, J. L., "Investigation of Advanced Counterrotation Blade Configuration Concepts for High Speed Turboprop Systems: Task I - Ducted Propfan Analysis," NASA CR 185217, NASA Contract NAS3-25270, 1990.
- [4] Hall, E. J. and Delaney, R. A., "Investigation of Advanced Counterrotation Blade Configuration Concepts for High Speed Turboprop Systems: Task II - Unsteady Ducted Propfan Analysis - Final Report," NASA CR 187106, NASA Contract NAS3-25270, 1992.
- [5] Hall, E. J. and Delaney, R. A., "Investigation of Advanced Counterrotation Blade Configuration Concepts for High Speed Turboprop Systems: Task V - Counterrotation Ducted Propfan Analysis, Final Report," NASA CR 187126, NASA Contract NAS3-25270, 1992.
- [6] Hall, E. J., Topp, D. A., Heidegger, N. J., and Delaney, R. A., "Investigation of Advanced Counterrotation Blade Configuration Concepts for High Speed Turboprop Systems: Task VIII - Cooling Flow/Heat Transfer Analysis, Final Report," to be published, NASA Contract NAS3-25270, 1994.
- [7] Hall, E. J., Topp, D. A., Heidegger, N. J., and Delaney, R. A., "Investigation of Advanced Counterrotation Blade Configuration Concepts for High Speed Turboprop Systems: Task VII - Endwall Treatment Inlet Flow Distortion Analysis Final Report", NASA Contract NAS3-25270, NASA CR-195468, July 1995.
- [8] Hall, E. J. and Delaney, R. A., "Investigation of Advanced Counterrotation Blade Configuration Concepts for High Speed Turboprop Systems: Task V - Unsteady Counterrotation Ducted Propfan Analysis - Computer Program Users Manual," NASA CR 187125, NASA Contract NAS3-25270, 1993.
- [9] Hall, E. J. and Delaney, R. A., "Investigation of Advanced Counterrotation Blade Configuration Concepts for High Speed Turboprop Systems: Task VIII - Film Cooling/Heat Transfer Analysis - Computer Program Users Manual," NASA CR 195360, NASA Contract NAS3-25270, 1994.

-
- [10] Hall, E. J. and Delaney, R. A., "Investigation of Advanced Counterrotation Blade Configuration Concepts for High Speed Turboprop Systems: Task VII - ADPAC User's Manual", NASA Contract NAS3-25270, NASA CR 195472, July 1995.
- [11] Hall, E. J., Heidegger, N. J., and Delaney, R. A., "Task 15 - ADPAC User's Manual". NASA Contract NAS3-27394, NASA CR 206600, January 1998.
- [12] Jameson, A., Schmidt, W., and Turkel, E., "Numerical Solutions of the Euler Equations by Finite Volume Methods Using Runge-Kutta Time-Stepping Schemes." AIAA Paper 81-1259, 1981.
- [13] Adamczyk, J. J., Celestina, M. L., Beach, T. A., and Barnett, M., "Simulation of Three-Dimensional Viscous Flow Within a Multistage Turbine," ASME Paper 89-GT-152, 1989.
- [14] Jorgensen, P. C. E. and Chima, R. V., "An Unconditionally Stable Runge-Kutta Method for Unsteady Flows," NASA TM 101347, 1989.
- [15] Ameri, A. A. and Arnone, A., "Navier-Stokes Turbine Heat Transfer Predictions Using Two-Equation Turbulence Closures", AIAA Paper 92-3067, 1992.
- [16] Boussinesq, J., "Essai Sur La Théorie Des Eaux Courantes," *Mem. Présentés Acad. Sci.*, vol. 23, Paris, p.46, 1877.
- [17] Spalart, P. R. and Allmaras, S. R., "A one-equation turbulence model for aerodynamic flows," *La Recherche Aéronautique*, no. 1, pp. 5-21, 1994.
- [18] Spalart, P. R., "Improvement in Spalart-Allmaras Model," Boeing Commercial Airplane Company, March 1993.
- [19] Baldwin, B. S. and Lomax, H., "Thin Layer Approximation and Algebraic Model for Separated Turbulent Flows," AIAA Paper 78-257, AIAA 16th Aerospace Sciences Meeting, Huntsville, AL, January 1978.
- [20] Granville, P. S., "Baldwin-Lomax Factors for Turbulent Boundary Layers in Pressure Gradients," *AIAA Journal*, Vol. 25, No. 12, December 1987, p. 1624-1627.
- [21] Turner, M. G. and Jennions, I. K., "An Investigation of Turbulence Modeling in Transonic Fans Including a Novel Implementation of an Implicit $k-\epsilon$ Turbulence Model," *Journal of Turbomachinery*, Vol. 115, April 1993, p. 249-260.
- [22] Anderson, D. A., Tannehill, J. C., and Pletcher, R. H., *Computational Fluid Mechanics and Heat Transfer*, McGraw-Hill, New York, New York, 1984.
- [23] White, F. M., *Viscous Fluid Flow*, McGraw-Hill, Inc., New York, 1991.
- [24] Anderson, J. D. Jr., *Fundamentals of Aerodynamics*, McGraw-Hill Book Company, New York, 1984.
- [25] Wieghardt, K. and Tillman, W., "On the Turbulent Friction Layer for Rising Pressure," NACA TM 1314, 1951.
- [26] Pot, P. J., "Measurements in a 2-D Wake and in a 2-D Wake Merging into a Boundary Layer. Data Report.," NLR TR 79063 U, National Aerospace Laboratory NLR - The Netherlands, 1979.

-
- [27] Goldberg, U. C., "Towards a Pointwise Turbulence Model for Wall-Bounded and Free Shear Flows," *Boundary Layer and Free Shear Flows*, ASME FED-Vol. 184, pp. 113-118, 1994.
- [28] Buning, P. G., Jespersen, D. C., Pulliam, T. H., Chan, W. M., Slotnick, J. P., Krist, S. E., and Renze, K. J., "OVERFLOW User's Manual, Version 1.7r," NASA Ames Research Center, Moffett Field, CA, October 1996.
- [29] Baldwin, B. S. and Barth, T. J., "A One-Equation Turbulence Transport Model for High Reynolds Wall-Bounded Flows," AIAA Paper 91-0610, AIAA 29th Aerospace Sciences Meeting, Reno, NV, January 1991.
- [30] Bachalo, W. D., and Johnson, D. A., "An Investigation of Transonic Turbulent Boundary Layer Separation Generated on an Axisymmetric Flow Model," AIAA 79-1479, 1979.
- [31] Hylton, L. D., Michelc, M. S., Turner, E. R., Nealy, D. A., and York, R. E., "Analytical and Experimental Evaluation of the Heat Transfer Distribution Over the Surfaces of Turbine Vanes," NASA CR-168015, 1983.
- [32] Heidegger, N. J., Hall, E. J., and Delaney, R. A., "Aeropropulsion Technology (APT), Task 23 - Stator Seal Cavity Flow Investigation," NASA CR-198504, 1996.
- [33] Dalton, W. N., Elliott D. B., and Nickols, K. L., "Design of a Low Speed Fan Stage for Noise Suppression," NASA Contractor Report to be released August 1998.
- [34] Podboy, G. G., Bridges J. E., and Krupar, M. J., "LDV and Hot-Wire Rotor Wake Measurements of the Allison Low Noise Fan," NASA Lewis Research Center, to be published 1998.
- [35] Majjigi, R. K. and Gliebe, P. R., "Development of a Rotor Wake/Vortex Model, Volume 1 - Final Technical Report," NASA CR-174849, Contract NAS3-23681, June 1984.
- [36] Topol, D. A. and Philbrick, D. A., "Fan Noise Prediction System Development: Wake Model Improvements and Code Evaluations", Pratt and Whitney Report PWA-6537-1 (an informal report prepared under NASA Contract NAS3-25952 (Task 10), April 1993.
- [37] Press, W. H., Teukolsky, S. A., Vetterling, W. T., Flannery, B. P., *Numerical Recipes in FORTRAN*, Cambridge University Press, Cambridge, 1992.
- [38] Schlichting, H., *Boundary Layer Theory*, 7th ed., McGraw-Hill Book Company, New York, 1979.
- [39] Raj, R. and Lakshminarayana, B., "Characteristics of the wake behind a cascade of airfoils," *Journal of Fluid Mechanics*, Vol. 61, Part 4, 1973, p. 707-730.
- [40] Lakshminarayana, B. and Davino, R., "Mean Velocity and Decay Characteristics of the Guidevane and Stator Blade Wake of an Axial Flow Compressor," *Journal of Engineering for Power*, Vol. 102, January 1980, p. 50-60.
- [41] Hobbs, D. E., Wagner, J. H., Dannenhoffer, J. F., and Dring, R. P., "Experimental Investigation of Compressor Cascade Wakes," ASME Paper 82-GT-299, United Technologies Corporation, 1982.

-
- [42] Hah, C. and Lakshminarayana, B., "Measurement and prediction of mean velocity and turbulence structure in the near wake of an airfoil," *Journal of Fluid Mechanics*, Vol. 115, 1982, p. 251-282.

REPORT DOCUMENTATION PAGE			Form Approved OMB No. 0704-0188	
Public reporting burden for this collection of information is estimated to average 1 hour per response, including the time for reviewing instructions, searching existing data sources, gathering and maintaining the data needed, and completing and reviewing the collection of information. Send comments regarding this burden estimate or any other aspect of this collection of information, including suggestions for reducing this burden, to Washington Headquarters Services, Directorate for Information Operations and Reports, 1215 Jefferson Davis Highway, Suite 1204, Arlington, VA 22202-4302, and to the Office of Management and Budget, Paperwork Reduction Project (0704-0188), Washington, DC 20503.				
1. AGENCY USE ONLY (Leave blank)		2. REPORT DATE February 1999		3. REPORT TYPE AND DATES COVERED Final Contractor Report
4. TITLE AND SUBTITLE Follow-on Low Noise Fan Aerodynamic Study Task 15-Final Report			5. FUNDING NUMBERS WU-538-03-11-00 NAS3-27394 Task 15	
6. AUTHOR(S) Nathan J. Heidegger, Edward J. Hall, and Robert A. Delaney				
7. PERFORMING ORGANIZATION NAME(S) AND ADDRESS(ES) Allison Engine Company P.O. Box 420 Indianapolis, Indiana			8. PERFORMING ORGANIZATION REPORT NUMBER E-11088	
9. SPONSORING/MONITORING AGENCY NAME(S) AND ADDRESS(ES) National Aeronautics and Space Administration Lewis Research Center Cleveland, Ohio 44135-3191			10. SPONSORING/MONITORING AGENCY REPORT NUMBER NASA CR-1999-206599	
11. SUPPLEMENTARY NOTES Project Manager, Christopher J. Miller, Structures and Acoustics Division, NASA Lewis Research Center, organization code 5940, (216) 433-6179.				
12a. DISTRIBUTION/AVAILABILITY STATEMENT Unclassified - Unlimited Subject Category: 02 This publication is available from the NASA Center for AeroSpace Information, (301) 621-0390.			12b. DISTRIBUTION CODE Distribution: Nonstandard	
13. ABSTRACT (Maximum 200 words) The focus of NASA Contract NAS3-27394 Task 15 was to investigate the effects of turbulence models on the prediction of rotor wake structures. The ADPAC code was modified through the incorporation of the Spalart-Allmaras one-equation turbulence model. Suitable test cases were solved numerically using ADPAC employing the Spalart-Allmaras turbulence model and another prediction code for comparison. A near-wall spacing study was also completed to determine the adequate spacing of the first computational cell off the wall. Solutions were also collected using two versions of the algebraic Baldwin-Lomax turbulence model in ADPAC. The effects of the turbulence model on the rotor wake definition was examined by obtaining ADPAC solutions for the Low Noise Fan rotor-only steady-flow case using the standard algebraic Baldwin-Lomax turbulence model, a modified version of the Baldwin-Lomax turbulence model, and the one-equation Spalart-Allmaras turbulence model. The results from the three different turbulence modeling techniques were compared with each other and the available experimental data. These results include overall rotor performance, spanwise exit profiles, and contours of axial velocity taken along constant axial locations and along blade-to-blade surfaces. Wake characterizations were also performed on the experimental and ADPAC predicted results including the definition of a wake correlation function. Correlations were evaluated for wake width and wake depth. Similarity profiles of the wake shape were also compared between all numerical solutions and experimental data.				
14. SUBJECT TERMS Computational fluid dynamics; Stall; Turbomachinery			15. NUMBER OF PAGES 150	
			16. PRICE CODE A07	
17. SECURITY CLASSIFICATION OF REPORT Unclassified	18. SECURITY CLASSIFICATION OF THIS PAGE Unclassified	19. SECURITY CLASSIFICATION OF ABSTRACT Unclassified	20. LIMITATION OF ABSTRACT	